The Development and Engineering Application of a Fiber Reinforced Hybrid Matrix Composite for Structural Retrofitting and Damage Mitigation

by

Hongyu Zhou

A Dissertation Presented in Partial Fulfillment
of the Requirements for the Degree
Doctor of Philosophy

Approved November 2013 by the
Graduate Supervisory Committee:

Thomas Attard, Co-Chair
Apostolos Fafitis, Co-Chair
Marc Mignolet
Samuel Ariaratnam
Benjamin Thomas
Jim Blumsom

ARIZONA STATE UNIVERSITY

December 2013

ABSTRACT

Civil infrastructures are susceptible to damage under the events of natural or manmade disasters. Over the last two decades, the use of emerging engineering materials, such as the fiber-reinforced plastics (FRPs), in structural retrofitting have gained significant popularity. However, due to their inherent brittleness and lack of energy dissipation, undesirable failure modes of the FRP-retrofitted systems, such as sudden laminate fracture and debonding, have been frequently observed. In this light, a Carbon-fiber reinforced Hybrid-polymeric Matrix Composite (or CHMC) was developed to provide a superior, yet affordable, solution for infrastructure damage mitigation and protection. The microstructural and micromechanical characteristics of the CHMC was investigated using scanning electron microscopy (SEM) and nanoindentation technique. The mechanical performance, such as damping, was identified using free and forced vibration tests. A simplified analytical model based on micromechanics was developed to predict the laminate stiffness using the modulus profile tested by the nanoindentation. The prediction results were verified by the flexural modulus calculated from the vibration tests. The feasibility of using CHMC to retrofit damaged structural systems was investigated via a series of structural component level tests. The effectiveness of using CHMC versus conventional carbon-fiber reinforced epoxy (CF/ epoxy) to retrofit notch damaged steel beams were tested. The comparison of the test results indicated the superior deformation capacity of the CHMC retrofitted beams. The full field strain distributions near the critical notch tip region were experimentally determined by the digital imaging correlation (DIC), and the results matched well with the finite element analysis (FEA) results. In the second series of tests, the application of CHMC was

expanded to retrofit the full-scale fatigue-damaged concrete-encased steel (or SRC) girders. Similar to the notched steel beam tests, the CHMC retrofitted SRC girders exhibited substantially better post-peak load ductility than that of CF/ epoxy retrofitted girder. Lastly, a quasi-static push over test on the CHMC retrofitted reinforced concrete shear wall further highlighted the CHMC's capability of enhancing the deformation and energy dissipating potential of the damaged civil infrastructure systems. Analytical and numerical models were developed to assist the retrofitting design using the newly developed CHMC material.

To my parents Yong Zhou, Ying Xu and my fiancée Xinchen Zhang who supported and trusted me along the way.

ACKNOWLEDGMENTS

This thesis and the associated research certainly would not have been completed without the support and help of many people. First of all, I wish to extend an especial acknowledgement to my graduate advisor Dr. Thomas Attard, who not only helped me tremendously in my academic endeavors during the three-and-half years of post-graduate study, but also treated and trusted me like a family. I would also like to acknowledge Dr. Apostolos Fafitis and Prof. Marc Mignolet for their knowledge and advices which contributed significantly to the analytical modeling part. Also, I would like to acknowledge Dr. Benjamin Thomas for his continuous support to our research efforts and for his many advices on the dissertation, and to Dr. Samuel Ariaratnam and Mr. Jim Blumsom for their valuable insights and extensive willingness to help.

An acknowledgement is also extended to Dr. Jy-An Wang, Dr. Yanli Wang, Dr. Donald Erndman at Oak Ridge National Laboratory (ORNL), and Dr. Fei Ren at Temple University for their support and help on my study at ORNL during the summer of 2012. I would also like to thank Dr. Xiang Li, Dr. Bin Zhao, and Dr. Jiangtao Yu at Tongji University for sharing their expertises and for their contributions to many of our experimental efforts. And the experimental assistances from Mr. Kittinan Dhiradhamvit, Mr. Tyler Harries, Mr. Peter Goguen, and Mr. Thomas Cox are also greatly appreciated.

Finally, I wish to thank my parents, Mr. Yong Zhou and Ms. Ying Xu, and my fiancé Xinchen Zhang for their support along all the way.

TABLE OF CONTENTS

Page

LIST OF TABLES

Table Page

LIST OF FIGURES

Figure Page

Chapter 1.

INTRODUCTION

This chapter is an introduction to natural and manmade hazards and the structural damages caused by the disastrous events. The common environmental factors causing structural deteriorations and damages are briefly introduced. The use of engineering composites in structural retrofitting and strengthening, its history, benefits, and drawbacks are presented, as is the problem statement and consequently the scope and aim of this dissertation are presented.

1.1. Natural Hazards and Structural Damages

Civil infrastructures in any geographical location may be subjected to a variety of natural phenomena such as earthquakes, windstorms (tornados and hurricanes), floods, etc. The term "disaster" denotes the occurrence of environmental changes resulting in societal infliction that poses a threat to social, economic, and/ or mortal threats to human life, property, and fundamental functions. Natural disasters can originate from deep inside the earth crust (earthquakes, volcanoes), on or near its surface (landslides/ mudslides, differential settlement); they can also be caused by violent climate changes (flooding, tornadoes/ hurricanes). While a large number of natural disasters comprise natural climates or geological activities, a considerable number of disasters are caused by human activities. i.e., anthropogenic hazards. Such hazards include warfare, terrorist attacks, traffic accidents, etc. In many cases, the successions and interactions of multiple

disasters are possible (earthquake-tsunami, earthquake-landslide, see Figure 1.1.1, and flood-landslide etc.), potentially causing even larger scale damage. To date, the prediction of the type, time, and scale of expected disasters can only be probabilistic [1]. While the occurrence of these incidents cannot be precisely predicted, their impacts should be well understood so that effective hazard mitigation preparedness can be enacted [2]. In this light, the possible impacts of disastrous events on the integrity and safety of civil infrastructures is briefly introduced in the following paragraphs.

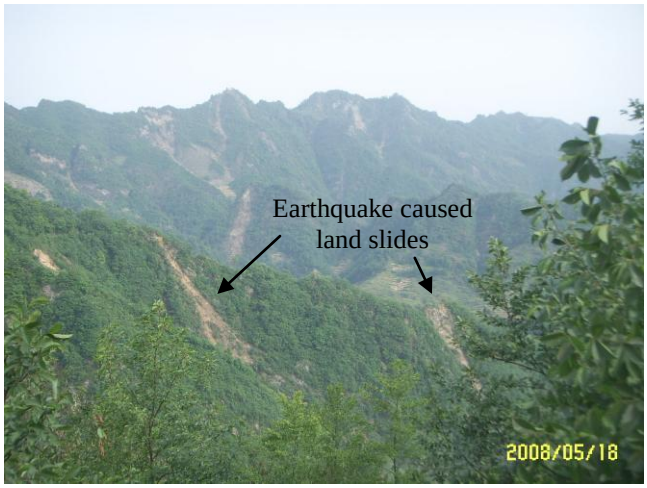

Figure 1.1.1. Earthquake caused landslide (Wenchuan, China, 2008)[1]

Earthquakes

Earthquakes have posed vital threat to human life since the dawn of human history, and they have posed major threats to the general infrastructure of man's cities, his dwellings, and his livelihood, not to mention his mortality. As a result, the potential damage of strong earthquakes has been well understood. Structural design, historically, has often been influenced by the level of desired seismic resistance. Buildings, for

[1] Photo courtesy of Dr. Xiang Li

example, may be designed to withstand nonstructural damage in frequent minor ground trembles, structural damage and minimization of nonstructural damage in occasional moderate ground shaking, and avoidance of collapse or serious damage in rare, yet categorically major, ground shaking. Even though such desired 'performance objectives' may be accomplished through careful design and implementation of structural components, like shear walls, braced frames, base-isolation systems, and energy dissipating devices, structural damage continues to be invariably induced by various earthquake events. For example, the Seismology Committee of the Structural Engineers Association of California (SEAOC) has adopted the philosophy that structural damage is acceptable during rare earthquakes but that collapse is not acceptable in any event [3]. Seismic-induced structural damage are manifested in various forms depending on the type of structure and the characteristics of the geotechnical site and the surrounding seismic waves. For reinforced concrete structures, severe structural damage may be caused by insufficient transverse, or lateral-resistant, reinforcement (large shear wall cracking, see Figure 1.1.2 (a)), inadequate confinement (distress in beam column joints, see Figure 1.1.2 (b) and (c)), insufficient anchorage and connections (slab-column disconnecting that have contributed to collapse [4]), and poor construction and workmanship. Cyclic deterioration in the hysteretic response has been observed in reinforced concrete structures. This form of deterioration is believed to be culpable for damage in buildings that have experienced earthquakes in succession. Buildings that experienced damage during previous earthquakes and were subsequently damaged more severely in following earthquakes have been reported [4]. In many of these cases, the buildings had not been properly repaired, or had received only cosmetic repair following

previous earthquakes. Thus, detailed evaluations of the damage state and implementation of appropriate reparative measures are vital.

Figure 1.1.2. Structural damages caused by earthquake (Wenchuan, China, 2008): (a) seismic induced shear cracks on masonry walls; (b) column-beam joint damage; (c) column damage (top); (d) column damage (bottom)[2]

Tornadoes, Hurricanes, and Typhoons

Hurricanes Hugo (1989) and Hurricane Andrew (1992) were the strongest hurricanes to strike the U.S. East and Gulf coasts since Hurricane Camille struck Louisiana in 1969; as a result, the way that the general public and government, including

[2] Photo courtesy of Dr. Xiang Li.

emergency management agencies regarded the risk of wind storm damage to homes was redefined [5]. The property insurance industry that had once presumed that two $7 billion hurricane disasters would represent the largest expected economic loss due to hurricane catastrophic in a given year, was abruptly shaken by the $26 billion loss following Hurricane Andrew. Losses following Andrew proved that damage attributed to a single hurricane had been severely underestimated. The economic loss caused by some more recent wind storm outbreaks is also substantial. Hurricane Cindy (2005) that struck Louisiana caused five fatalities, with the total economic loss estimated at $320 million. In fact, hurricanes and tropical storms accounted for the majority share of all property insurance losses during the period from 1986 to 1992 [6]. Unlike hurricanes, tornadoes occur over shorter a duration and have a smaller influential density, primarily because of the smaller density populations of where they strike (for example, hurricanes generally attack largely populated coastal cities), however, their occurrence is much more frequent with approximately 1,200 tornadoes recorded annually in the United States alone. Due to the very high wind speed (>250 mph for Enhanced Fujita Level 5, or EF-5, tornado), tornadoes can be extremely destructive, where, for example, the Daulatpur-Salturia Tornado in Bangladesh on April 26, 1989, caused more than 1,300 fatalities. The key strategy to protecting building from high winds caused by tornadoes, hurricanes, and gust fronts is to maintain the integrity of the building envelope, including windows and roofs, and to design the structure to withstand the expected lateral and uplift forces [2]. In this light and similar to earthquakes, careful design and preventive measures do not always preclude structural damage during severe storm outbreaks. Common structural damage imposed by wind storms include roof failures caused by the lack of proper connections

between the roof and exterior walls, wall damage due to poor connections and debris impacts [7;8], and window and door damage caused by windborne debris impacts [9-11] and high wind pressure.

Environmental Induced Deteriorations

Most structural/ construction materials deteriorate naturally with time under normal environmental/ weather conditions. Because of the materials' nature, wood structures, for example, are susceptible to damage from insects and many microorganisms; steel and other metallic structures are prone to corrosion damage since many structural metals oxidize in the presence of water and oxygen. Material deterioration can also originate from the materials themselves, where, for example, alkali-silica reaction (ASR) damage of concrete is caused by the reaction between the hydroxyl ions that exist in the cured cement paste with the reactive silica found in some aggregates, producing an expansive alkali-silica gel. The economic impact of material deterioration is substantial. The original work used to estimate the economic loss caused by metallic corrosion was carried out in 1975 based on an elaborate model involving more than 130 economic sectors, which estimated $82 billion in losses within the United States alone [12]. If infrastructures are properly maintained, however, it normally takes a significantly longer period of time for the materials' natural degradation to occur and cause notable distresses in structures. However, aggressive environments, such as salt/ chemical exposure and the ocean environment, accelerate the deterioration process of structural materials. For instance, steel rebar used as reinforcement for reinforced concrete (RC) structures do not corrode with the protection of the strong alkali

environment of cured concrete (due to the existence of calcium hydroxide as one of the hydration products of Portland cement), unless the PH value of the concrete pore solution decreases to certain levels as a result of concrete carbonation (the reaction between the calcium hydroxide and carbon dioxide in the atmosphere that produces calcium carbonate). Concrete carbonation is a slow process that takes decades to show notable rebar corrosion; however, in the presence of chloride salts (most commonly from deicing products used for highways and bridges), the chloride ions diffuse into the concrete and damage the passive film formed on the rebar surface, resulting in the electrochemical corrosion of steel. Similarly, other types of distresses, such as sulfate attack in concrete, may result from aggressive agents occurring in the environment.

Human-caused Incidents

Besides some of the multiple natural hazards discussed, human-caused (anthropogenic) incidents are also important sources of structural damage, including blast/ explosion, missile strike [13-15], vehicular accidents (truck-impact on low-clearance highway bridges [16], barge-bridge pier collisions [17;18] etc.). According to the database collected from the overheight vehicle detector records and the bridge inspection reports, the frequency of overheight vehicle accidents reported in the state of Maryland increased by 81% between 1995 and 2000 [16]. Nationwide, eighteen out of the twenty-nine states that participated in a statistical survey indicated overheight collisions to be a significant problem. A notable portion of those structures damaged by the anthropogenic incidents require repairs.

1.2. Structural Retrofit and Strengthening Techniques

Although the most effective way to mitigate loss of lives and property is to design structures that are disaster resistant [2]. That said, at least some structural damage is perhaps inevitable following many hazardous events. More importantly, design-based provisions and specifications continue to evolve with society's increasing understanding of natural hazards and their impact on structures. Existing structures designed and constructed according to older code provisions may not necessarily comply with current design standards, and in this light, retrofitting schemes applied to either damaged structures or undamaged structures having insufficient disaster/ hazard resistance is of critical importance so that existing structures are able to meet today's demanding multi-hazards requirements. Various performance objectives can be achieved using structural retrofitting that include increasing the load (strength), deformation (ductility), and energy dissipation capacities of the structure. Conventional, as well as emerging retrofitting, techniques are briefly presented.

Conventional Retrofitting Techniques

Conventional retrofitting techniques include the addition of new structural elements and the enlargement of existing structural members. The addition of structural elements such as shear walls and steel bracing are among the more popular strengthening methods due to their effectiveness and relatively low overall cost. The design of additional shear walls or bracing frames may resist a major portion of possible lateral loads likely to be imparted on a structure (e.g., caused by earthquakes or high winds) to

reduce the demand on various structural components such as the joints, beams and columns. To avoid major architectural changes, an alternative conventional approach to strengthen structures is the section enlargement (or jacketing) of beams and columns. Beam and column jacketing is generally not as effective as element addition, not to mention that the overall project cost may be higher; however, the original functionality of the structure is likely to be retained following a minimal change to the floor plan and allowable space clearance.

Retrofitting Using Base-isolation or Energy Dissipating Devices

To protect structures in the event of earthquake, blast, and impact, it is critical to effectively isolate structures and/ or their components, from the damage source or to enhance their energy dissipation capacity. Seismic base isolation technology involves placing flexible isolation systems between the foundation and the superstructure. By means of their flexibility and energy dissipating capacity, the base isolators reflect/ absorb part of the earthquake energy, reducing the energy dissipation demand on the superstructure. Base isolation significantly increases the effective fundamental period and deformation capacity of the structure; and a major portion of the structural deformation takes place at the isolation level.

A more cost efficient retrofitting strategy is to incorporate supplemental energy dissipation devices, such as viscous fluid dampers and friction dampers [19], for the purpose of implementing structural control (passive, semi-active, or active). The objective of structural control is to reduce structural vibrations for improved safety and/or serviceability under hazards loading, such as wind and seismic loading. Passive control

systems reduce structural vibrations and the associated forces via energy dissipation devices that do not require external power (such as viscous fluid dampers and friction dampers). These devices utilize the motion of the structure to develop counteracting control forces and absorb a portion of the input seismic energy. Active control systems, however, enhance structural response through control forces developed by force delivery devices that rely on external power to operate. Seismic retrofitting of structures using energy dissipation devices such as viscous dampers are intended to increase stiffness, load capacity, and effective damping in structures. However, a concern regarding the use of energy dissipation devices is that the effectiveness of such devices depends on the deformation capacity of the structure. For structures that suffer from inadequate ductility, a feasible solution may be to combine this technique with deformation enhancement measures to ensure their effectiveness.

1.3. Fiber Reinforced Composites for Structural Retrofit and Damage Mitigation

A retrofitting option that has gained popularity is the use of externally bonded polymer matrix composites (PMC) as an alternative to conventional bridge girder retrofitting techniques, such as steel plate patching. Most PMC materials exhibit merits of high strength-to-density ratio, superior durability and ease in-situ applications [20;21]. One particular type of PMC that has drawn significant attention is the advent of fiber reinforced polymers (FRPs) which combine high-strength high-modulus fibers with low modulus polymeric matrices that serve as a binding material to ensure stress transfer between the fibers. A number of fiber types has been used for producing fibrous

composites although the particular application of unidirectional-weaved continuous carbon fibers or glass fibers are ubiquitous in civil infrastructure applications. Because of the increasing demand of polymeric matrix composites in the civil infrastructure industry, research efforts on the utilization of FRPs for new constructions [22] and strengthening or retrofitting damaged structures [23;24] have been extensively carried out since the mid- 1980s. FRP materials were initially used as strengthening materials for reinforced concrete (RC) flexural components [25;26] and were used to provide lateral confinement for RC compression members [27]. The applications of FRPs have since been expanded to masonry [28], wood [29], and concrete/ steel composite structures [30]. Numerous studies have been conducted on fiber reinforced polymers (FRPs) in the repair reinforced concrete and steel structures in experimental [24;31-33] and field applications [34]. Figure 1.3.1 presents some common FRP retrofit techniques for reinforced concrete frame structures, including: (1) flexural strengthening of beams; (2) shear strengthening of beams; (3) flexural strengthening of slabs; (4) strengthening of beams and slabs in the negative moment region; and (5) column wraps to increase the strengths. FRP-strengthening and application of retrofitting techniques of steel structures have also started gaining in popularity in recent years [35]. A recent study by Lam et al. [36] on CFRP strengthened steel notched coupons shows the potential of CFRP to effectively delay or arrest crack growth in the notched steel plate under monotonic load. Additional studies by Attard et al. [37] and Abela and Attard [38] addressed the failure mode alteration in bridge columns using a Ductility-Wrap Envelope (DWE) concept. As for larger- scale structural members, studies conducted by Hmidan et al. [39] and Tavakkolizadeh et al. [40] demonstrated the effectiveness of using CFRP-retrofitting to

restore (and increase) the load capacity and to extend the fatigue life of fatigue-damaged steel girders. Research efforts have also involved the retrofitting of concrete/ steel composite structural members using FRP [41;42]. In a study by Sen et al. [41], six W200×36 SI (W8×24) wide-flange steel bridge girders having a yield strength of 248MPa (A36 steel) were connected to the reinforced concrete bridge deck. The concrete/ steel composite girders were first loaded until the tension-side flange yielded followed by a retrofit of the damaged specimen using carbon fiber reinforced polymer (CFRP) laminates (2 mm and 5 mm thicknesses). After re-testing the six retrofitted girders, a maximum increase in strength of 52% was observed in comparison to the strength of "as-built" members. Furthermore, the elastic stiffness also increased although this gain was reported as modest; more alarming, however, was the fact that debonding of the laminates had occurred for the retrofitted specimens having 5mm laminates. Later work by Tavakkolizadeh et al. [42] examined the effectiveness of using CFRP laminates to retrofit damaged steel-concrete composite girders that had experienced steel section loss. In their study, three large scale steel-concrete composite girders(W355×13.6) were connected to a 75mm thick concrete deck via studs that were notched at mid-span on the tension flange which were used to represent fatigue or corrosion-induced damage. The damage in the three beams was quantified by the reduction of the cross-sectional areas of their tension-side flanges, i.e., 25%, 50%, and 100% reduction, respectively. Following the CFRP retrofit, significant increases in the load capacities were reported, namely 20%, 80%, and 10% using various numbers of laminates for the three girders. In addition, there was full recovery of the elastic stiffness in the three girders of up to 102% of the intact virgin girder. However, the study also brought to light that the CFRP retrofit of

sections having complete loss of tension flange (i.e., 100% reduction) results in minimal ductility, and in similar cases of severe structural damage, current retrofit standards appear to be deficient. As a result, the current study develops a new retrofit scheme for concrete-encased steel flexural members integrated with a mechanism to dissipate energy and to stabilize damage.

While CFRP retrofitting has several advantages, its drawbacks are well documented [43]. Due to the nearly linear elastic nature of the stress-strain behavior of CFRP, the failure of CFRP-retrofitted structural members often occurs in a brittle manner that is induced by the tension rupture of the retrofitting laminate, debonding/ delamination of the composite, or crushing of the concrete in its compression zone, e.g. in the case of CFRP-retrofitted RC flexural members [33;44]. One reasons for these failures is a lack of sufficient damping and energy dissipation which would otherwise enable sufficient ductility. A study by Hamed et al. [45] on the damping properties and viscoelastic dynamic behavior of CFRP-strengthened RC flexural members revealed negligible levels of damping. Studies demonstrated that the lack of a significant energy dissipation mechanism in CFRP-strengthened structures may result in: (1) the lack of significant ductility in the inelastic range, (2) incurred large responses and vibrations in the elastic range, and (3) large acceleration demands in some seismic zones, without an sufficient energy-dissipation mechanism [46-48].

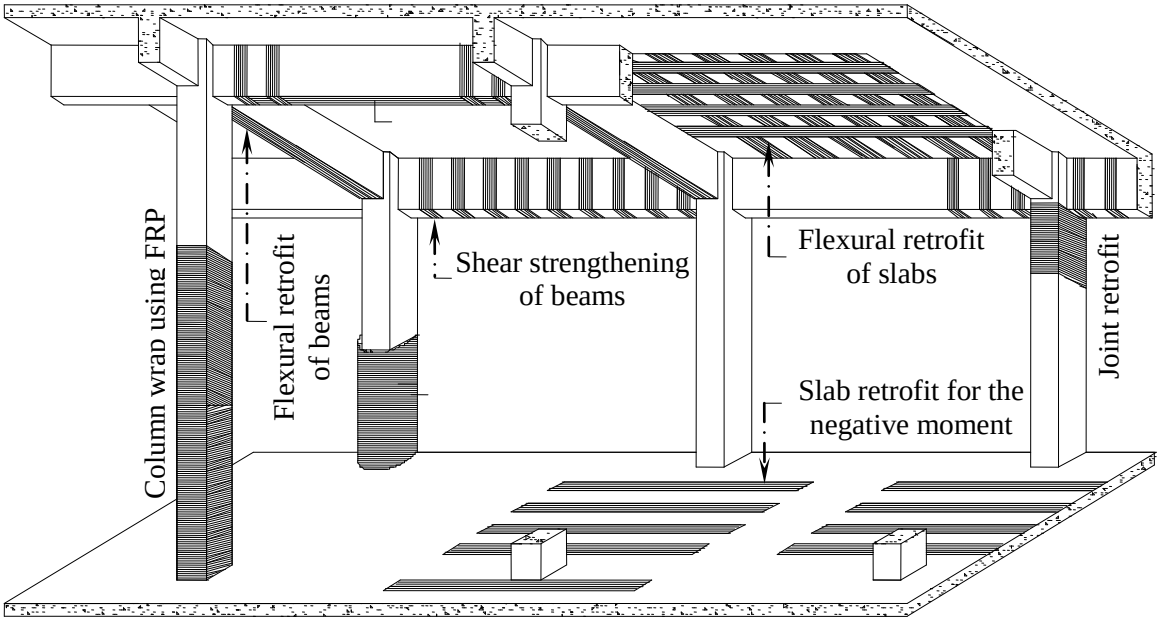

Figure 1.3.1. Illustrative figure showing the structural retrofit for reinforced concrete (RC) frame structures using fiber-reinforced polymer (FRP)

1.4. Problem Statement and Aim of the Study

To date, conventional fiber-reinforced polymer (FRP) technology has proven to have inherent drawbacks, such as low energy dissipation capacity and low ductility, so that it does not provide an ideal solution for 1) protecting civil infrastructures from natural hazards, or 2) repairing damaged structures to restore (or even enhance) their performances. In this light, a new **C**arbon-fiber reinforced **H**ybrid-polymeric **M**atrix **C**omposite (CHMC) that possess a suite of superior physical and mechanical attributes is developed for civil infrastructure applications. The objectives of this research are as follows:

(1) Develop a high-performance, cost-efficient, structural composite that can be used in lieu of conventional carbon fiber reinforced epoxies for the protection and retrofitting of civil infrastructural during hazardous events;

(2) Study the microstructural and micromechanical characteristics of the newly developed material to understand its load-carrying and energy dissipation mechanisms;

(3) Obtain mechanical properties, such as damping, of the newly developed material at macro-scale level and establish preliminary relationships between the macro-scale properties and micro-scale mechanisms;

(4) Explore the feasibility of applying the newly developed CHMC material in various structural applications in lieu of conventional carbon fiber reinforced epoxies.

1.5. Overview of the Dissertation

Chapter 2 introduces the backgrouns of composite development, which includes the properties and physical/ chemical characteristics of various reinforcing fibers and matrix materials; the manufacturing and fabrication process, mechanics and design approaches of engineering composites, particularly the polymeric matrix composites (PMCs); and the toughening mechanisms of advanced fibrous composites.

Chapter 3 proposes a new class of carbon fiber-reinforced hybrid polymeric-matrix composite (CHMC). Its microstructures, micromechanical behaviors and damage mechanisms are investigated using state-of-the-art scanning electron microscopy (SEM) and nano-indentation testing techniques; the proposed multilayered cross-ply texture is evidenced by SEM images. The mechanisms by which the CHMC is able to sustain

damage significantly better than conventional carbon fiber reinforced epoxies is revealed by fractography studies on the fractured composite tensile coupons. And the micromechanical behaviors used to predict laminate stiffness are proposed based on the micromechanical properties tested by the nanoindentation technique.

Chapter 4 presents the dynamic properties and energy dissipation capabilities of carbon fiber reinforced epoxy (CF/ epoxy) versus the CHMC, at the macro-scale level, tested through free and forced frequency vibration tests. The experimental method used to characterize the composite damping is introduced, and the experimental test results are presented. mechanisms by which CHMC is able to possess significantly higher damping than CF/ epoxy and how the material processing parameters - the thickness of the elastomeric phase II, h_p, and the intermittent, t_c, - impact the material damping is discussed from a micro-scale perspective. The physically meaning of the two material parameters will be further introduced in Chapter 3.

Chapters 5 to 7 explore the feasibility of using CHMC in lieu of conventional carbon fiber reinforced epoxies in the structural damage retrofitting applications. Chapter 5 investigates the effectiveness of using CHMC to retrofit notch damaged steel beams under quasi-static bending. The full-field strain distributions near the notch tip were experimentally determined using the digital imaging correlation (DIC) technique. The test results indicate significantly enhanced deformation capability of CHMC- retrofitted beams than those steel beams retrofitted using CF/ epoxy. In chapter 6, the application of CHMC is extended to retrofit full-scale fatigue damaged concrete-encased steel girders. The experimental test results indicate substantially higher post-peak ductility for CHMC retrofitted girders as compared to the one retrofitted by carbon fiber reinforced epoxy.

Analytical models are developed to design CHMC-retrofitted structural members. Finally, chapter 7 discusses the repair of a seismically damaged reinforced concrete (RC) shear wall under bi-axial loading using the newly developed CHMC to provide tremendous confinement capability. The results show 100% strength restoration and significant ductility increase for the retrofitted specimen.

Chapter 2.

CONSTITUENTS, MANUFACTURING, DESIGN, AND TOUGHENING MECANISMS OF STRUCTURAL COMPOSITES

In this chapter the constituent materials, manufacturing process, mechanics and design approaches of engineering composites, particularly the polymeric matrix composites (PMCs), are described in details. The toughened composites and toughening mechanisms together with their merits and drawbacks are discussed .

2.1. Introduction

One important property that differs composites with many other conventional structural materials is their tailorable mechanical and physical properties, i.e. if they are properly designed, the properties and performance of composites can be versatilely altered according to needs. However, it is crucial to have sufficient knowledge of the properties of the constituents, the mechanics, and design approaches of the engineering composites in order to properly design and develop a material that meets the desired performance demands. Recognizing the drawbacks of conventional FRP retrofits discussed in the previous chapter, the challenges encountered by the modern civil infrastructures retrofit and damage mitigation are the increasing demand for materials that possess a suite of superior properties that include high-strength, high-ductility, and good energy dissipation capacity (high damping). Strength, though important, should not be the sole consideration in the design and development of the next generation of materials for civil structural applications, and other important engineering properties such

as energy dissipation and ductility should be sufficiently counted for as well. This chapter introduces the constituent materials of different kinds that have been used to compose structural composites, the manufacturing/ fabrication processes, the mechanics and design approaches that facilitate the design and development of composite materials. The methods used by other researchers to toughen engineering composites are introduced towards the end of this chapter. Their merits and drawbacks are discussed.

2.2. Constituents and Manufacturing Process of Engineering Composites

A composite material is formed by combining two or more distinct materials in order to achieve enhanced properties. The oldest composites are created by nature, such as wood, where the cellulose fibers are embedded in a lignin matrix. The manmade composites date back to ancient Egypt when people started to use the straw-reinforced-clay bricks to construct pyramids and houses. Since 19th century, the evolution of modern technologies often require materials with combinations of properties that cannot be met by conventional structural materials such as metal alloys, ceramics, or polymers. For example, aerospace engineers are increasingly seeking for materials that have a suite of superior properties including low density, high strength and stiffness, good resistance to impact and fatigue, and are not easy to corrode. Such demands for the combined/ and enhanced material properties became the midwifery of modern engineering composites, which use metal, ceramic, or polymer binders reinforced with a variety of fibers, particles, or whiskers.

2.2.1. Classification

Owing to the fact that a large variety of materials can be used as reinforcement and binder to create a composite, a vast number of man-made composites have been developed over the past fifty years, where most among which can be grouped into two major categories:

Particle-reinforced Composites (PRCs), where the reinforcements are particles with random or preferred orientations. Particle reinforced composites are often seen in metallic or ceramic matrix composite, where the particulate reinforcements are added to improve the physical properties, such as hardness and fracture toughness, of the materials. The PRCs are also often subcategorized into the *large-particle reinforced composites* and dispersion-strengthened composites depending on the size of the reinforcing particulate phase, where the later contain much smaller particles (10 - 100 nm in diameter) that interact with the matrix microstructure on the atomic or molecular level [49]. Concrete is an example of large particle reinforced composite, in which case the course aggregates act as particle reinforcements embedded in the cement paste binder.

Fiber-reinforced (Fibrous) Composites (FRCs) use continuous or discontinuous fibers to strengthen the matrix material, and it can be further subcategorized into the following types depending on the configuration of reinforcing fibers: continuous fiber (unidirectional, woven bidirectional, stitched mat etc.) reinforced composites and discontinuous fiber (random orientation, preferential orientation) reinforced composites.

Classifying from matrix materials, most engineering composites can be grouped into the following three types:

Ceramic matrix composite (CMCs) are composed of a ceramic matrix and embedded fiber. Most ceramic matrix composites have good thermal shock resistance (or have low coefficients of thermal expansion) and retain high mechanical performance under elevated temperatures. They are, thus, well-suited to structural applications at high temperatures. The fiber reinforced carbon-carbon (RCC) materials, which consist of carbon fiber reinforcement in a matrix of graphite, retain their mechanical properties above 2000 ℃. Their most well-known applications include the nose cone and wing leading edge of the space shuttle orbiters, and the brake disk of aircrafts and high-end racing cars. However, their lack of impact resistance was highlighted in the Columbia space shuttle disaster, where one of the RCC panels was perforated by a piece of foam insulation from the external fuel tank causing disintegration of the shuttle during its atmospheric re-entry. Due to the difficulty of forming the matrix system of CMCs, their prices are usually very high as compared to other types of composites.

Metallic matrix composites (MMCs) are composed of a metallic matrix (typically aluminum, magnesium, iron, cobalt, or copper) and a dispersed ceramic or metallic phase as reinforcement. Often the surface of reinforcements are coated to prevent chemical with the metallic matrix. Particulate reinforcements, such as diamond or carbide particles, can be included in the metallic matrix to form an isotropic (or pseudo-isotropic) material to achieve enhanced wearing resistance or thermal conductivity. For example, the carbide drills are often made from a tough cobalt matrix with hard tungsten carbide particle. The frequently used continuous reinforcing fibers in MMC include carbon fiber and silicon carbide.

Polymer matrix composites (PMCs) are, to date, the most widely used manmade composites due to their ease of processing and relatively low price. The commonly used reinforcing fibers for PMCs include carbon, glass, aramic (Kevlar), boron and metallic fibers; and the matrix material can be either thermosetting (epoxy, polyester (PET), polyurethane (PUR) etc.) or thermoplastic (polystyrene, polyetheretherketone (PEEK) etc.) polymers. Though, very desirable mechanical properties such as high strength/ stiffness and high fracture roughness, have been achieved by many PMCs, however, because of the low glass-transition temperatures for most polymer materials used as the matrix, the operating temperature of most PMCs are restricted to under 300 ℃.

Some other types of fibrous composites have also gained a lot of popularity over the past two decades, that include the fiber reinforced cementious composite, engineered natural fiber reinforced composites, and many more. However, due to the predominant use of continuous fiber-reinforced polymeric matrix composites (PMCs) in civil infrastructure systems, especially in the field of structural retrofit and strengthening, the context of this dissertation focuses primarily on continuous fiber reinforced polymer matrix composites as externally bonded reinforcements for newly constructed or damaged structures.

2.2.2. Dispersed Phase - Reinforcing Fibers

Most materials have one or two magnitude higher strength in their fibrous form than their bulk forms. A large variety of fibers are utilized for their high strength and high stiffness. For the fibrous composites, the reinforcing fibers provide most of the load bearing capacities. Some commonly used reinforcing fiber materials include: glass (E-

glass, S-glass), carbon (AS4, IM6 ect.), aramid (Kevlar® 29, Kevlar®[3] 49 etc.), silicon carbide (SiC), boron, and basalt. Figure 2.2.2.1 shows a picture of various types of unidirectional and bidirectional woven fiber fabrics that are commonly use for structural composites. Three most commonly used reinforcing fibers are introduced below with sufficient details.

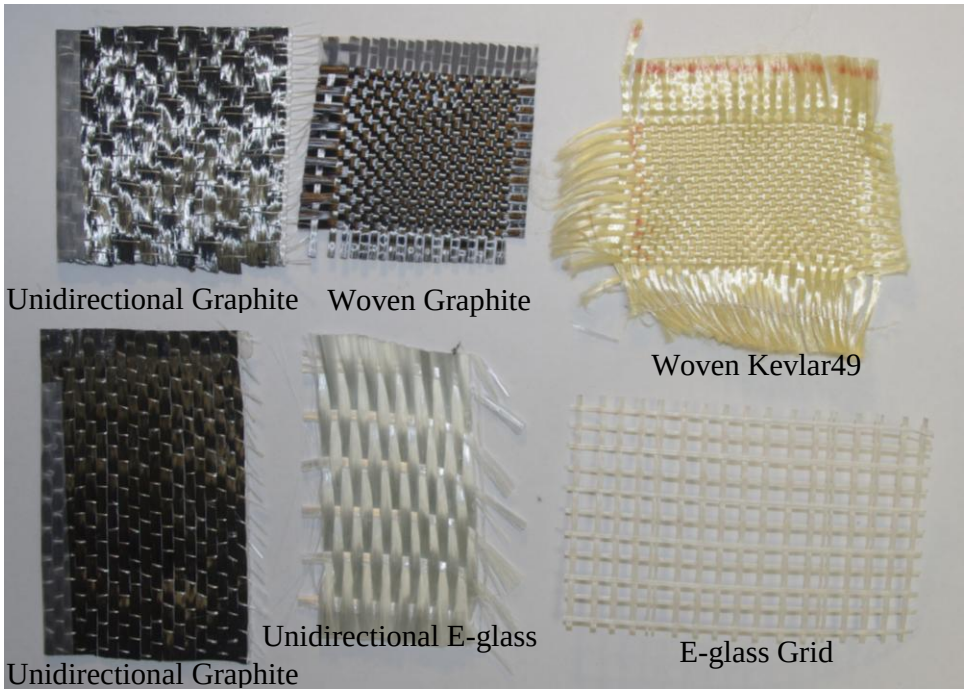

Figure 2.2.2.1. Different types of fiber fabrics used in structural applications

Glass Fiber

Glass fiber is formed by extruding thin strands of silica-based or other formulation glass into fibers with very small diameters (8-25 μm). Unlike glass in its bulk material form, the glass fibers are strong (~3450 MPa for E-glass, ~4600 MPa for S-glass), flexible, and lightweight; and they are relatively inexpensive as compared to other

[3] Kevlar® is a trade mark of DuPont.

types of fibers such as carbon or Aramid. The corrosion resistance of glass fibers depends on the composition of the fiber. For example, the A-glass (alkali-lime glass) is susceptible to alkali corrosion, however, the newer type of E-glass (alumino-borosilicate glass) has good resistance to most common corrosive solutions. The strength of glass fiber is sensitive to humility. Moisture can be easily absorbed and aggravate microcracks and surface defects. Besides the durability issue under aggressive environments, another significant drawback that limits the application of glass fibers in civil infrastructure is their low resistance to creep, i.e. the tensile strength reduces with time under sustained load.

Aramid Fiber

Aramid fiber, which is also often known as its commercial name "Kevlar", is a para-aramid synthetic fiber that was firstly developed at DuPont in 1965. Aramid fibers have high energy absorption upon failure, which make them ideal for impact and ballistic protection. Currently, Kevlar, as a woven fabric, has many applications in personal armors and sports equipment. Because aramid fibers are made of polymeric material, they are sensitive to UV light and creep under sustained load like many other polymers. Similar to glass fibers, aramid fibers also absorb moisture; and their strength varies with humility (or moisture "take-up").

Carbon Fiber

Carbon fiber, also known alternatively as graphite fiber, is composed mostly (more than 90%) by carbon atoms. With its light weight and excellent engineering

properties, in the form of high modulus and high strength fiber materials it was initially developed for aerospace and aircraft use in the 1960s [50]. Carbon fibers are transformed from organic matters, such as polyacrylonitrile (PAN) and pitch, by 1000-1500 ℃ heat treatment. As of today, almost seventy to eighty percent of commercially available carbon fibers are derived from polyacrylonitrile (PAN) polymer [$(CH_2CHCN)_n$]. The early generations of carbon fibers, such as the AS4[4], has diameters of approximately 7-8 micrometer (μm); and later fibers, such as the IM6, have smaller diameters that are approximately 5 μm. The tensile strength of a single carbon fiber filament ranges from 2000-5700 MPa depending on its microstructures structures and flaw distributions. The presence of particulate material and gas bubbles in the carbon fiber filament creates internal and surface flaws that would initiate failure upon loading [50]. Though studies have shown that the single carbon fiber filaments exhibit some extend of non-linearity, namely the increase in Young's modules with increasing load [51], most investigator still consider carbon fibers to be linear elastic because of their apparent linear stress-strain relation at usually rate of tension [50]. The tensile failure of carbon fiber is very brittle and shows very little deformation. Figure 2.2.2.2 presents the fracture surface of a carbon fiber embedded in the epoxy matrix. The rough fracture pattern shows distinct feature of brittle failure. Another unique property of carbon fiber is that the tensile strength does not decrease with increasing temperature up to at least 1300 ℃ [52]. In addition, carbon fibers, in general, have good chemical inertness and do not creep.

[4] AS4 is a carbon fiber product of Hercules.

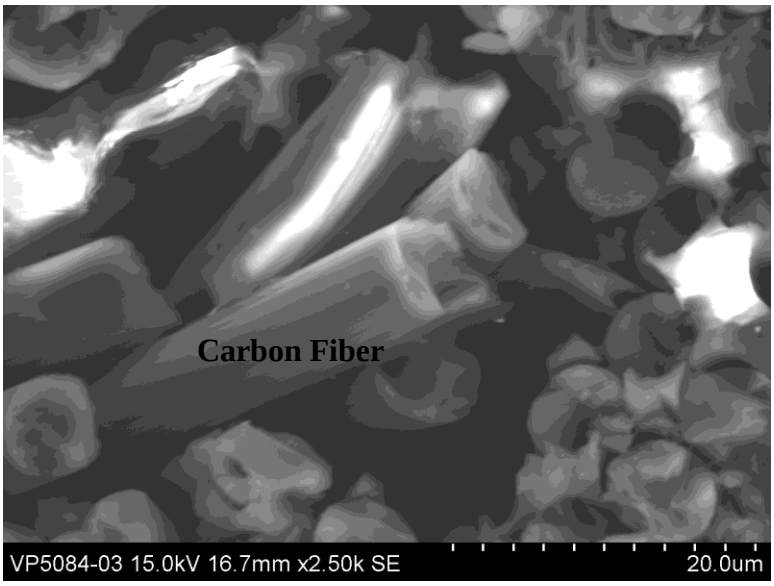

Figure 2.2.2.2. The rough fracture surface of carbon fiber (×2500)

The primary physical and mechanical properties, particularly the specific modulus (Young's modulus / mass density) versus specific strength (tensile strength / mass density), of various fiber materials and conventional metal alloys are compared in Figure 2.2.2.3.

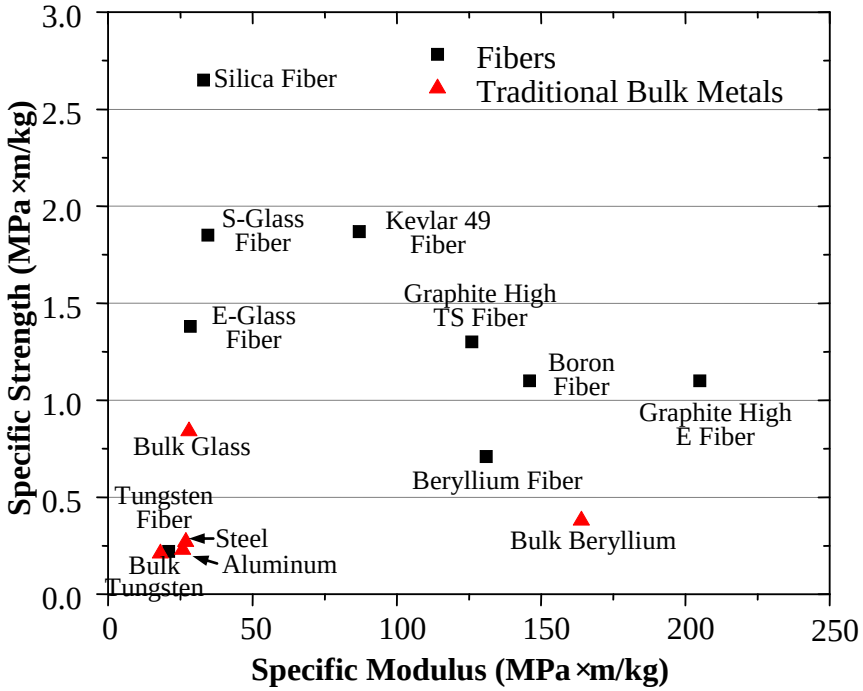

Figure 2.2.2.3. The specific strength versus specific modulus relation of various commonly used fibers for making fibrous composites

2.2.3. Matrix Phase - Polymeric Matrices

The matrix phase of a composite material binds the fibers together, transferring the stresses/ load between fibers. It also carries the transverse and interlaminar shear stresses, and provides protection to the fibers from environmental degradation or mechanical abrasion. Some mechanical properties of the composites, particularly the transverse stiffness and strength, the interlaminar bonding strength, and the in-plane and interlaminar shear stiffness/ strength, are dominated by the properties of matrix. In addition, some matrices also prevents the propagation of brittle cracks from fiber to fiber by the virtue of their high plasticity and ductility, thus preventing catastrophic failure [49].

For the polymer matrix composites (PMCs), both thermoplastic and thermosetting polymers are frequently used as the matrix material.

Thermoplastics

Thermoplastic polymers become viscous liquid and highly "formable" (liquefy) under elevated temperature and form into a hard, dimensionally stable solid when cooled. The liquefy and harden processes of thermoplastic polymers are reversible and can be repeated. Thermoplastics (or thermoplastic polymers) are either amorphous or crystalline at room temperature. They are typically formed by long linear polymer chains folding back on themselves. The polymer chains are associated through intermolecular force, such as the Van der Waals force, which permits thermoplastics to be remolded since the intermolecular interactions increase upon cooling. Most thermoplastic polymers have low elastic modulus, low yield strength, and are usually ductile (except for the amorphous thermoplastics which appear to be brittle under room temperature) due to their linear coiled chain (or lightly branched) molecular structure. The commonly used thermoplastics for making PMCs include polyether ether ketone (PEEK), polyetherimide, polysulfone, and polyphenylene sulfide.

Thermosetting Polymers

In oppose to the thermoplastics, the thermosetting polymers become permanently hard when their cross-linking structure was formed. During the curing process, covalent cross-links are formed between adjacent molecular chains, which prevent the molecular chains from vibrating and rotating at high temperature. If uncontrolled heat is applied to

a cured thermosetting plastic, decomposition will occur before the melting point is reached. Therefore, a thermosetting material cannot be melted and re-shaped after it is cured. Cross-linking of the thermoset polymers is usually extensive where 10-50% of the chain mer units are cross-linked, forming a three-dimensional cross-linked network. Thermosetting polymers are usually harder (have higher stiffness), stronger (have higher strength), and more brittle than thermoplastics. Examples of commonly used thermosetting polymers in composites include epoxy, polyurethane, and Bakelite (phenol formaldehyde).

Lightly Cross-linked Elastomers

Another type of cross-linked polymers has less degree of cross-linking than the thermosetting polymers. Instead of forming a three-dimensional cross-linked network, the elastomers only have a small number of cross-links formed along the molecular chain, generating a lightly cross-linked molecular structure. The long polymer chains are capable of reconfiguring themselves upon loading, see Figure 2.2.3.1 (a), which results in an extremely flexible mechanical behavior. The covalent cross-linkage and long polymer chains allow elastomers to reversibly extend from 5-700% (hyper-elastic), depending on the specific materials. Examples of the lightly cross-linked elastomers include natural and synthetic polyisoprene rubbers, polybutadiene, and Nitrile rubbers. The representative stress-strain curves of thermoplastics, heavily cross-inked thermoset polymers, and lightly cross-linked elastomers are compared in Figure 2.2.3.1 (b).

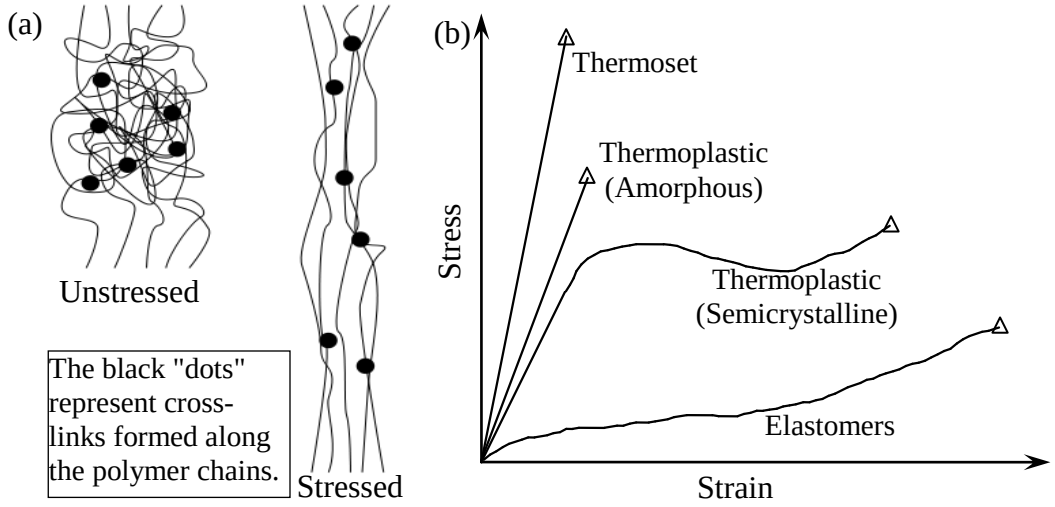

Figure 2.2.3.1. (a) The molecular structures of lightly cross-linked elastomers under stress; (b) the representative stress-strain relations of thermoplastic, thermoset polymers, and elastomers

2.2.4. Fabrication and Manufacturing Processes of Composites

The manufacturing of composites depends largely on the properties of their constituents. For example, continuous protrusion is frequently used for making fiber reinforced thermoplastics, since their thermoplastic matrix can be melted under elevated temperature to form a desired geometry; reaction injection molding is appropriate for manufacturing continuous fiber reinforced epoxy, since the epoxide prepolymer takes certain curing time to react with the hardener to form the cross-linking polymer network. The commonly seen fabrication processes of thermosetting resin matrix composites include: hand lay-up, spray-up, bag molding, resin transfer molding, filament winding, and pultrusion [53].

The hand lay-up technique is the simplest and most commonly used method for the manufacture of both small and large composite products. Spray-up is a partially automated form of hand lay-up, where chopped fibers and resin are deposited simultaneously on an open mold (or surface) [53]. The hand lay-up and spray-up processes have the merits of low equipment requirements, low tooling cost, and flexible for design etc.; however, they are both labor intensive and the quality of the final products depends heavily on the skill of the operators, and thus difficult to control.

Bag molding is also widely used in manufacturing composite parts because of its versatility. During the bag lay-up process, the laminas are laid up in a mold covered with flexible diaphragm or bag and impregnated with wet resin. The curing is usually carried out with heat and pressure. Depending on the pressure and heat applied on the laminates, the general process of bag molding can be sub-divided into pressure bag, vacuum bag, and autoclave. The bag molding process requires some basic tooling such as vacuum pump and autoclave/ oven, however, the quality of the final products can be better controlled than the hand lay-up process.

Other fabrication process like filament winding and pultrution are more suitable for industrialized production due to their higher equipment requirements. Because of the lower tooling cost and high flexibility, to date, the hand lay-up process is predominant in the field of civil infrastructure retrofitting/ strengthening, even the composite products produced by pultrution have been increasingly used as prefabricated laminates in some structural applications.

2.3. Composite Mechanics and Design Approaches

Because of the high compliance of the matrix phase of most polymer matrix composites (PMCs), the design of composite structures is often driven by stiffness. Since the application of continuous fiber reinforced composites has been primarily concentrated in the form of thin plate or shell, the classic lamination theory is used for deriving the stiffness matrix that relates the loads applied on a composite laminate to its deformation. The micromechanics and macromechanics approaches used to assist the stiffness driven design of composite structures is briefly introduced here.

2.3.1. Micromechanics and Lamina Stiffness Determination

Due to the heterogeneous nature of composites, it is difficult, if possible, for the designer to utilize the traditional continuum mechanics principles to guide the analysis and design. Micromechanics studies the interaction of the constituent materials in detail, and allow the designer to represent the heterogeneous composites as equivalent homogeneous materials [54]. There are several approaches available to derive micromechanics formulas, that include “the mechanics of materials approach” which is based on the simple rule of mixtures (ROM) and is used for modeling the fiber and matrix systems within a representative volume element (RVE) either in series or in parallel, depending on the stress and fiber orientations; this approach gives a reasonable prediction of the lamina stiffness and Poisson's ratio in the longitudinal (along fibers), transverse, and in-plane shear directions [55]. Alternatively, “the elasticity approach” established by Paul [56] and improved by Hashin et al. [57;58] provides a more accurate,

yet tedious, approach for stiffness design. Later work by Tsai and Halpin – often referred to as the "Halpin-Tsai approach" [59] – helped to further improve composite stiffness design, resulting in the accurate design of lamina stiffness while using a more feasible methodology. To fix the idea of utilizing micromechanics to homogenization a composite lamina, the equations for calculating the lamina stiffness components that are derived from the simplest mechanics of materials approach is presented here as following:

Longitudinal Modulus $\boldsymbol{E}_1$:

The longitudinal stiffness, or modulus of elasticity in the fiber direction, E_1 can be reasonably well predicted by equation (2.3.1.1), which assume that the strains in the fiber direction are the same in the fiber and the matrix, see Figure 2.3.1.1 (a)

$$E_1 = E_f V_f + E_m \left(1 - V_f\right) \tag{2.3.1.1}$$

where E_f and E_m are the elastic modulus of fiber and matrix, respectively; and V_f is the fiber volume fraction.

Transverse Modulus $\boldsymbol{E}_2$:

The transverse modulus of the lamina is obtained by assuming the fiber and matrix act in "series", see Figure 2.3.1.1 (b), which yields

$$E_2 = \frac{E_f E_m}{\left(1 - V_f\right) E_f + V_f E_m} \tag{2.3.1.2}.$$

In-plane Poisson's Ratio $\boldsymbol{\nu}_{12}$:

The in-plane Poisson's ratio can be similarly determined by the rule of mixtures as

$$\upsilon_{12} = -\frac{\varepsilon_2}{\varepsilon_1} = \upsilon_f V_f + \upsilon_m \left(1 - V_f\right) \tag{2.3.1.3}$$

where v_f and v_m are the Poisson's ratio of the fiber and matrix, respectively.

In-plane Shear Modulus $\boldsymbol{G_{12}}$:

The in-plane shear stress and the resultant deformation on a small lamina element are shown in Figure 2.3.1.1 (c). The mechanics of materials approach yields:

$$G_{12} = \frac{G_f G_m}{G_f \left(1 - V_f\right) + G_m V_f} \tag{2.3.1.4}$$

where G_f and G_m are the shear modulus of the fiber and matrix, respectively. The shear modulus and Poisson's ratio of single fiber filament are rather difficult to measure, due to the fact that many fibers, like carbon fiber, are anisotropic. The experimentally determined shear modulus and Poisson's ratio values for some commercial available fibers can be found in [50].

Finally, note that the elastic stress-strain relation of an orthotropic material under plane stress can be expressed in its principal coordinate system as

$$\begin{Bmatrix} \sigma_1 \\ \sigma_2 \\ \tau_{12} \end{Bmatrix} = \begin{bmatrix} D_{11} & D_{12} & 0 \\ D_{12} & D_{22} & 0 \\ 0 & 0 & D_{66} \end{bmatrix} \begin{Bmatrix} \varepsilon_1 \\ \varepsilon_2 \\ \gamma_{12} \end{Bmatrix} \tag{2.3.1.5}$$

where $D_{i,j}$ are the reduced stiffness components, that can be defined in terms of the engineering constants as:

$$\begin{aligned} D_{11} &= \frac{E_1}{1 - \nu_{12}\nu_{21}}, \; D_{22} = \frac{E_2}{1 - \nu_{12}\nu_{21}} \\ D_{12} &= \frac{\nu_{12} E_1}{1 - \nu_{12}\nu_{21}}, \; D_{66} = G_{12} \end{aligned} \tag{2.3.1.6}$$

with the reciprocal relation:

$$\frac{\nu_{12}}{E_1} = \frac{\nu_{21}}{E_2} \qquad (2.3.1.7).$$

The stress-strain relationship of a composite lamina within the elastic regime can hence be established from equations (2.3.1.1) - (2.3.1.7). The interlaminar properties as shown in Figure 2.3.1.1 (d), which might be critical for many applications, have been left out in this discussion for the sake of simplicity. It is worthy to point out that the mechanics of materials (or rule of mixture) approach over-simplifies the real situation in an engineering composite by ignoring the complex stress states imposed by the fiber-matrix interaction and the critical interfacial layer between fiber and matrix. As a result, the mechanics of materials formulas do not yield accurate predictions for the matrix-dominated properties, such as E_2, and G_{12}. However, it provides a simple base-line approach for the engineers to estimate the engineering properties of the composites, and it is sufficient, herein, to convey the idea of utilizing micromechanics concepts to assist the design of composite structures.

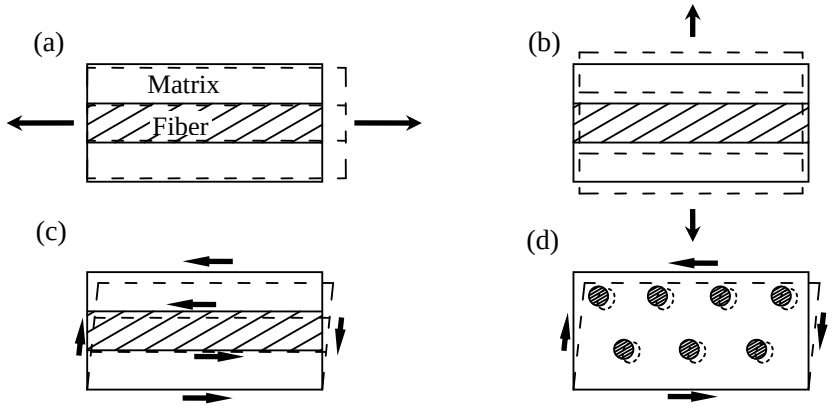

Figure 2.3.1.1. Schematic diagram showing the deformation of the RVE for: (a) longitudinal (along fiber) tension; (b) transverse tension; (c) in-plane shear; and (d) interlaminar shear

2.3.2. Macromechanics of Laminate and Stiffness Driven Design

For a multi-layered composite laminate (with N layers of unidirectional lamina), the deformation is related to the applied load components via:

$$\begin{Bmatrix} N_x \\ N_y \\ N_{xy} \end{Bmatrix} = \int_{-t/2}^{-t/2} \begin{Bmatrix} \sigma_x \\ \sigma_y \\ \tau_{xy} \end{Bmatrix} dz = \sum_{i=1}^{N} \int_{z_{i-1}}^{z_i} \begin{Bmatrix} \sigma_x^i \\ \sigma_y^i \\ \tau_{xy}^i \end{Bmatrix} dz \tag{2.3.2.1}$$

and

$$\begin{Bmatrix} M_x \\ M_y \\ M_{xy} \end{Bmatrix} = \int_{-t/2}^{-t/2} \begin{Bmatrix} \sigma_x \\ \sigma_y \\ \tau_{xy} \end{Bmatrix} z dz = \sum_{i=1}^{N} \int_{z_{i-1}}^{z_i} \begin{Bmatrix} \sigma_x^i \\ \sigma_y^i \\ \tau_{xy}^i \end{Bmatrix} z dz \tag{2.3.2.2}$$

where N_x and N_y are the axial forces per unit width in the x and y directions, respectively; N_{xy} is the in-plane shear force; M_x, M_y, and M_{xy} are the bending moments and torque acting on a unit width of the plate, as shown in Figure 2.3.2.1 (a); and, finally, z_i is defined in Figure 2.3.2.1 (b) [60].

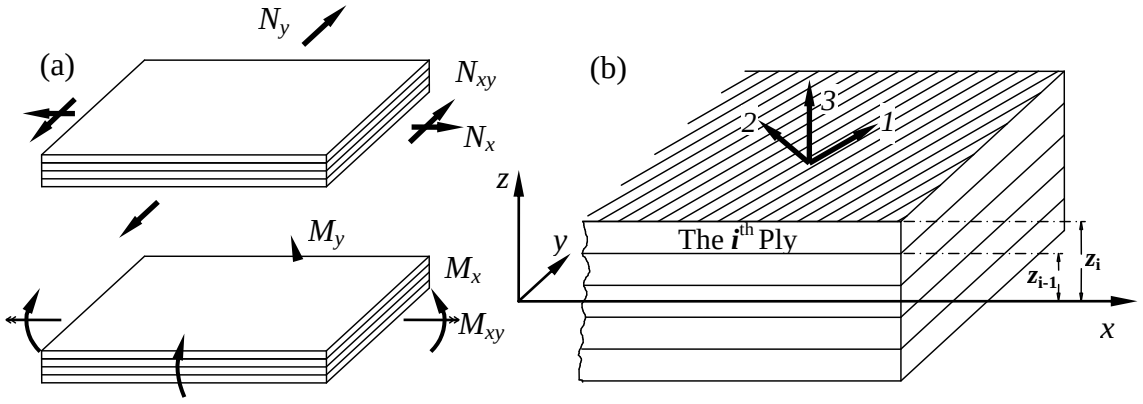

Figure 2.3.2.1. Schematic diagram showing the composite laminates under loading: (a) the free body diagram; (b) figure schematically shows the lamina composition of a composite laminate

Transforming equation (2.3.1.5) from the principle coordinates of the lamina, *1-2-3*, to the global *x-y-z* coordinates yields

$$\{\boldsymbol{\sigma}\} = \left[\overline{\mathbf{D}}\right]\{\boldsymbol{\varepsilon}\} = [\mathbf{T}]^{-1}[\mathbf{D}][\mathbf{T}]^{-T}\{\boldsymbol{\varepsilon}\} \tag{2.3.2.3}$$

or in the expand form of

$$\begin{Bmatrix}\sigma_x\\ \sigma_y\\ \tau_{xy}\end{Bmatrix} = \begin{bmatrix}\overline{D_{11}} & \overline{D_{12}} & \overline{D_{16}}\\ \overline{D_{12}} & \overline{D_{22}} & \overline{D_{26}}\\ \overline{D_{16}} & \overline{D_{26}} & \overline{D_{66}}\end{bmatrix}\begin{Bmatrix}\varepsilon_x\\ \varepsilon_y\\ \gamma_{xy}\end{Bmatrix} \tag{2.3.2.3}$$

where [**T**] is the transformation matrix [60]

$$[\mathbf{T}] = \begin{bmatrix}\cos^2\theta & \sin^2\theta & 2\sin\theta\cos\theta\\ \sin^2\theta & \cos^2\theta & -2\sin\theta\cos\theta\\ -\sin\theta\cos\theta & \sin\theta\cos\theta & \cos^2\theta-\sin^2\theta\end{bmatrix} \tag{2.3.2.4}$$

where θ_i is the fiber orientation of the i^{th} ply, as shown in Figure 2.3.2.1 (b); [**D**] is the stiffness matrix of the lamina expressed in its material principal coordinate, whose components can be determined by equations (2.3.1.1) - (2.3.1.7); and $[\overline{\mathbf{D}}]$ is the stiffness matrix expressed in the global coordinate, and

$$\left[\overline{\mathbf{D}}\right] = \left[\mathbf{T}\right]^{-1}\left[\mathbf{D}\right]\left[\mathbf{T}\right]^{-T} \tag{2.3.2.5}$$

Note that for any specific point cross the thickness of the plate one has

$$\begin{Bmatrix} \varepsilon_x \\ \varepsilon_y \\ \gamma_{xy} \end{Bmatrix} = \begin{Bmatrix} \dfrac{\partial u_0}{\partial x} - z\dfrac{\partial^2 w_0}{\partial x^2} \\ \dfrac{\partial v_0}{\partial y} - z\dfrac{\partial^2 w_0}{\partial y^2} \\ \dfrac{\partial u_0}{\partial y} + \dfrac{\partial v_0}{\partial x} - 2z\dfrac{\partial^2 w_0}{\partial x \partial y} \end{Bmatrix} = \begin{Bmatrix} \varepsilon_x^0 \\ \varepsilon_y^0 \\ \gamma_{xy}^0 \end{Bmatrix} + z\begin{Bmatrix} \kappa_x \\ \kappa_y \\ \kappa_{xy} \end{Bmatrix} \tag{2.3.2.6}$$

where u_0 and v_0 are the displacements of the middle plane in the x and y directions, respectively; w_0 is the mid-plane deflection in the z direction. And κ_x, κ_y, and κ_{xy} are the x, y, and torsional curvature components of the deformed plate. Substitute equations (2.3.2.3) and (2.3.2.6) into equations (2.3.2.1) and (2.3.2.2) yields:

$$\begin{Bmatrix} N_x \\ N_y \\ N_{xy} \end{Bmatrix} = \sum_{i=1}^{N} \begin{bmatrix} \overline{D_{11}} & \overline{D_{12}} & \overline{D_{16}} \\ \overline{D_{12}} & \overline{D_{22}} & \overline{D_{26}} \\ \overline{D_{16}} & \overline{D_{26}} & \overline{D_{66}} \end{bmatrix}_i \left[\int_{z_{i-1}}^{z_i} \begin{Bmatrix} \varepsilon_x^0 \\ \varepsilon_y^0 \\ \gamma_{xy}^0 \end{Bmatrix} dz + \int_{z_{i-1}}^{z_i} \begin{Bmatrix} \kappa_x \\ \kappa_y \\ \kappa_{xy} \end{Bmatrix} z dz \right] \tag{2.3.2.7}$$

and

$$\begin{Bmatrix} M_x \\ M_y \\ M_{xy} \end{Bmatrix} = \sum_{i=1}^{N} \left[\begin{matrix} \overline{D_{11}} & \overline{D_{12}} & \overline{D_{16}} \\ \overline{D_{12}} & \overline{D_{22}} & \overline{D_{26}} \\ \overline{D_{16}} & \overline{D_{26}} & \overline{D_{66}} \end{matrix} \right]_i \left[\int_{z_{i-1}}^{z_i} \begin{Bmatrix} \varepsilon_x^0 \\ \varepsilon_y^0 \\ \gamma_{xy}^0 \end{Bmatrix} z dz + \int_{z_{i-1}}^{z_i} \begin{Bmatrix} \kappa_x \\ \kappa_y \\ \kappa_{xy} \end{Bmatrix} z^2 dz \right] \qquad (2.3.2.8)$$

Thus, the basic stiffness driven design approach that relates the applied load to the composite layout and properties of the constituents is established.

2.3.3. Failure Criteria and Strength Driven Design

The failure criteria of single ply composite laminas are often derived based on the biaxial loading results for two primary reasons: 1) most fiber-reinforced composites are general anisotropic or orthotropic (the failure stress/ load depends heavily on the loading directions), such that the uniaxial test results in one particular loading direction could not fully depict the failure of a composite under complex stress conditions; and 2) the fibrous composites are mostly used as thin laminates (or shells), where the plane-stress condition holds valid and the consideration of tri-axial stress state failure is usually not necessary. Some of the most widely used bi-axial strength criteria of composite laminas, including the maximum stress and maximum strain failure criteria [55], the Hoffman criterion [61], and the Tsai-Wu tensor criterion [62], is briefly discussed in the following paragraphs.

The maximum stress criterion assumes that a lamina fails when at least one of the stresses in the material coordinates exceeds the corresponding strength. The criterion states that failure occurs if any one of the following is true

$$\begin{aligned}
&\sigma_1 > F_{1t} \text{ if } \sigma_1 > 0 \\
&\sigma_1 < F_{1c} \text{ if } \sigma_1 < 0 \\
&\sigma_2 > F_{2t} \text{ if } \sigma_2 > 0 \\
&\sigma_2 < F_{2c} \text{ if } \sigma_2 < 0 \\
&\left|\sigma_6\right| > F_6
\end{aligned} \tag{2.3.3.1}$$

where F_{1t}, F_{1c}, F_{2t}, F_{2c} are the experimental determined tensile and compressive strengths in the longitudinal (along fiber) and transverse directions; and F_6 is the in-plane shear strength. In the principal stress space, the maximum stress criterion is a "rectangular" envelop. Similarly, the maximum strain criterion assumes that the failure of the lamina occurs when one of the strains in the material principal coordinates exceed its limiting value. Since the maximum strain criterion is well-introduced in numerous materials [54;60], it would not be redundantly described here for the sake of simplicity.

The Hoffman criterion [61], on the other hand, considered the coupling of different stress components and the different strengths of composites in tension and compression by expressing the failure criterion as

$$\begin{aligned}
&C_1\left(\sigma_2-\sigma_3\right)^2 + C_2\left(\sigma_3-\sigma_1\right)^2 + C_3\left(\sigma_1-\sigma_2\right)^2 + \\
&+C_4\sigma_1 + C_5\sigma_2 + C_6\sigma_3 + C_7\tau_{23}^2 + C_8\tau_{31}^2 + C_9\tau_{12}^2 = 1
\end{aligned} \tag{2.3.3.2}$$

where C_1 - C_9 are model parameters determined by the experiments. And note that under plane stress condition, the components σ_3, τ_{23}, and τ_{13} equal to zero.

The later work of Tsai and Wu [62] expanded the preceding models into a very general tensorial form of

$$F_i\sigma_i + F_{ij}\sigma_i\sigma_j = 1 \qquad i, j = 1, 2, \cdots, 6 \tag{2.3.3.3}$$

where F_i and F_{ij} are model parameters determined by the experiments. The Tsai-Wu criterion, as expressed by equation (2.3.3.3) is obviously very adaptive to the experimental data by incorporating many terms in the equation, however, it is also complicated.

2.3.4. Energy Dissipation Mechanisms and Damping

Another important consideration in the design of composite structures is its energy dissipation capability, especially in the dynamic loading conditions such as vibration and impact. However, a limited number of efforts [63-67] have been directed towards damping design, where the damping properties of structural composites are tailored to satisfy certain performance metrics. Previous studies, see [65;67] and [63], investigated the influence of the fiber orientation and hysteretic damping of constituent fibers and matrices on the overall composite damping but not at the cohesive interfacial level. That said, the energy dissipation mechanisms associated with fiber- reinforced polymer (FRP) composites, at least from a micro-mechanics perspective, typically result from the: 1) hysteretic damping of fibers; 2) hysteretic damping of matrices; and 3) the inter-phase interactions. Because of the nearly elastic behavior of most reinforcing fibers, the damping contributed by the fiber components is often neglected, thus the overall damping properties of composite material systems are predominantly assumed to originate from the viscous matrices and the constituent interphase interactions. For damaged composites, in which fibers begin to debond from the matrix, the friction between the debonded fibers and the matrix can become an important source of material internal energy dissipation [63]. For a multi-phased matrix composite, the deformation of

the constituent interfaces may play a prominent and practical role, serving as an important source of energy dissipation.

2.4. The Toughened Composites and the Toughening Mechanisms

The toughness and ductility of fibrous composites are closely related to the ability of the matrix phase to effectively transfer stresses between reinforcing fibers and sufficiently sustain a certain level of damage, so that the micro-scale level damage initiated at low stress stage do not propagate unstably causing failure of the material. The highly cross-linked thermosetting polymers are generally brittle at room temperature, though they possess properties desired by many structural applications, such as high strength and high stiffness. Several methods to toughen the otherwise brittle thermosetting polymer matrix are introduced and their merits and limitations are discussed.

2.4.1. Toughening of Polymer Matrices by Incorporating Elastomer Particles

One way to improve the fracture toughness of the bulk polymer material is to incorporate a small amount of elastomer in the form of well-bonded and well-dispersed second-phase particles [68]. Two types of rubber particles - the reactive liquid rubber (CTBN) and core-shell rubber (SCR) are often used for improving the toughness of highly cross-linked polymers such as epoxy [69]. For the CTBN toughened epoxy, the grafted rubber phase is generated by the reaction of a function liquid polybutadiene with the epoxide prepolymer. Prior to the gelation of the epoxy cross-linked network, the

rubbery polybutadiene-epoxy oligomers become incompatible with the forming epoxy network and phase separation occurs [68]. The resulting product is a epoxy-rich matrix filled with the rubber-rich domains, i.e. particles. On the other hand, the core-shell rubber (SCR) is particle that typically consists of a glassy shell (such as PEEK) and a rubber core [70]. The dispersed CSR particles in the matrix would enhance the plastic deformation in front of a formed crack tip, and hence improve the fracture toughness of the matrix material. The incorporation of the elastomer phase has been proved to be effective in improving the fracture toughness and the ability to resist impact. However, one distinct drawback of adding rubber particles into polymeric reins is the drastic reduction of stiffness due to the formation of the "soft" discontinuous phase, i.e. the rubber particles.

In addition, as being pointed out by Yee [71], the increased toughness of bulk polymers may not be directly translatable to the composites, i.e. the attempts to toughen composites by using high toughness matrix do not always meet the expectations, for two possible reasons:

1) Because of the existence of the fibers, the plastic zone formed in the polymeric matrix phase is confined to the inter-fiber space ahead of the crack tip, as shown in Figure 2.4.1.1. The reduction in the plastic zone size, as compared to bulk polymer, would result in a reduction in fracture energy.

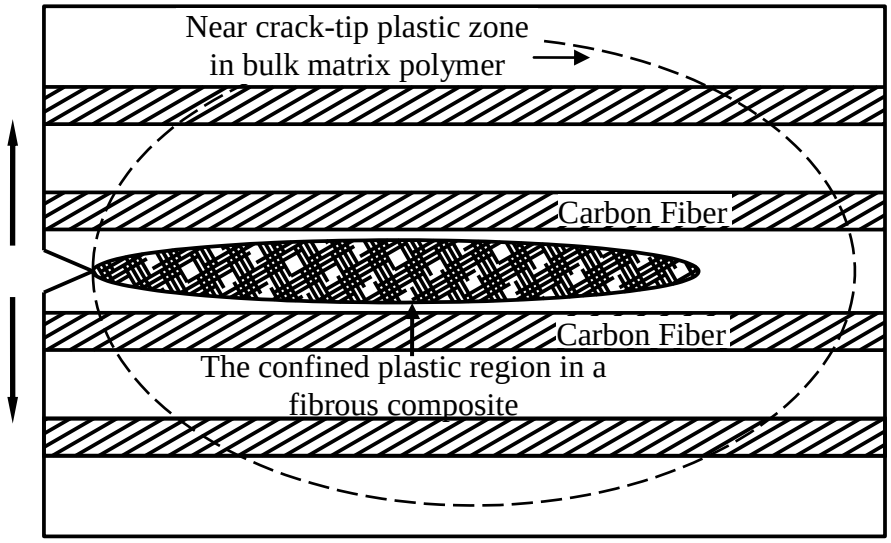

Figure 2.4.1.1. A schematic diagram showing the size of the plastic zone in the polymeric matrix reduced by the closely spaced reinforcing fibers

2) The second possible reason is that the relatively rigid fibers pose constrain to the polymeric resin phase, creating a high hydrostatic tensile stress state. The hydrostatic tensile component tends to promote voiding and crazing, and hence causes brittle fracture of the otherwise ductile polymer [71].

2.4.2. Composite Toughening through Fiber Hybridization

A second method to increase the toughness of a composite is through the fiber hybridization, which is usually accomplished by either 1) blending short whiskers or microfibers (such as carbon nanotubes) into the matrix phase [72]; or 2) using different types of continuous fibers simultaneously in the same laminate as the reinforcements [73;74].

The toughening mechanism of incorporating whisker or microfibers into the matrix is similar to that of the rubber particle toughened composites as discussed in the previous section, where the toughness of the matrix phase is improved. However, instead of creating a "porous" matrix phase like the elastomer particles do, the whiskers/ or microfibers arrest the micro-cracks initiated in the matrix polymer at early loading stages, as shown in Figure 2.4.2.1. Besides, since the whiskers/ or microfibers phase usually have higher elastic modulus than the polymeric matrices, the stiffness of the short fiber toughened composites would not significantly decrease as the volume fraction of the short fibers increases. However, the addition of whisker/ or micro-fiber to the matrix resin may rheologically affect the mixture by increasing the viscosity and thixotropy of the matrix phase [72]. Therefore, from a processing and manufacturing standpoint, it may not be feasible to displace a large amount of short fibers in the matrices.

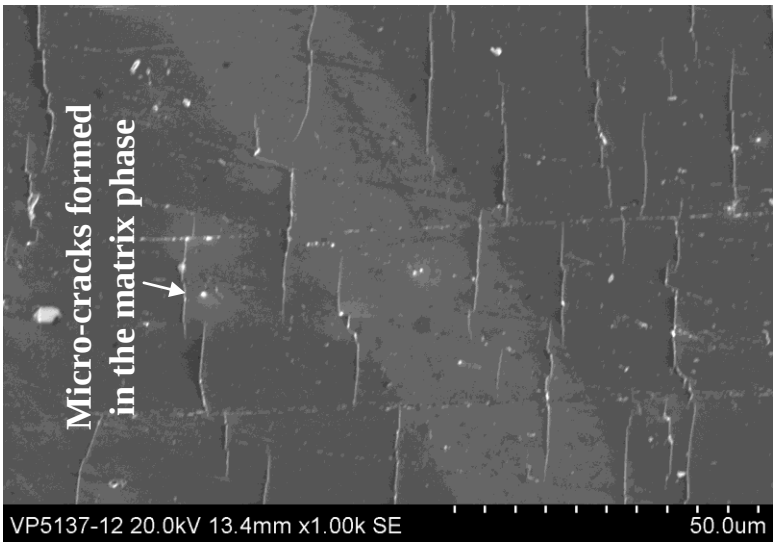

Figure 2.4.2.1. SEM image showing the micro-cracking of the epoxy matrix in a graphite/ epoxy composite (×1000)

The hybridization of the fiber reinforcements, on the other hand, utilize the different failure strains of the various fiber types that are hybridized in the composite laminate acting in parallel, where the failure of fiber strands having lower fracture strain can be arrested by the tougher fibers that have higher failure strains. The hybrid composite laminates would exhibit, at a macroscopic level, certain level of "strain hardening", as a result of the sequent failures of fibers that having different fracture strains. The "strain-hardening" effect caused by the fiber hybridization is shown in Figure 2.4.2.2. There have been a number of successful applications of the hybrid fiber reinforced composites in both producing the pultruded composite structural members [73;74] and in strengthening/ or retrofitting existing structures as well [75]. The more "gradual" failure of the hybrid composite laminates provided extra ductility to the retrofitted systems, as had been observed in the experimental studies of Bakis et al. [73] and Hai et al. [74].

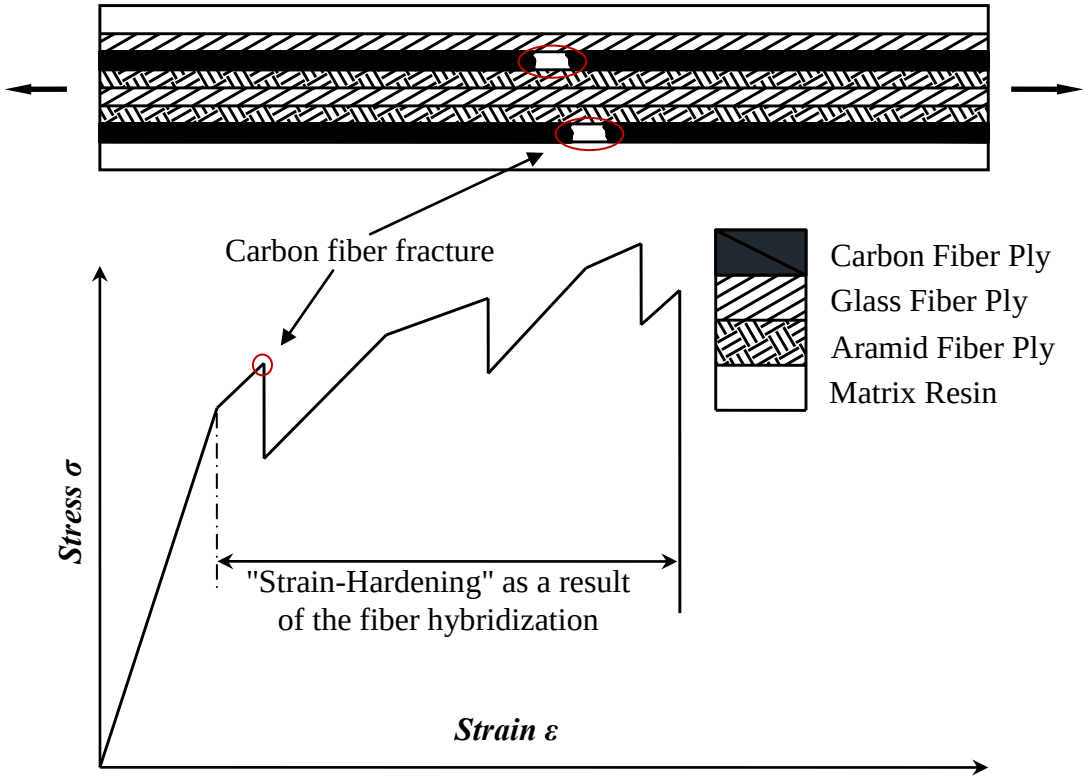

Figure 2.4.2.2. Figure schematically showing the hybridization of the reinforcing fiber and the "hybrid effect" on the stress-strain relations of a composite laminate

2.4.3. Drawbacks of the Existing Toughening Mechanisms

Besides the technical limitations as aforementioned for each of the toughening methods, another important factor limits the use of toughen composites in civil infrastructure is their high cost. Even though many advanced PMCs that exhibit superior toughness and ductility have been developed for structural applications, their high costs have constrained their usage in high-end aerospace and automobile applications. For instance, the matrix toughening using carbon nanotubes often encounter the agglomeration problems where the Van der Waals force between the mircrofibers tends

to making the dispersion of nanotubes difficult and costly. And the in the case of fiber hybridization, the fibers having lower stiffness contribute very little to the pre-damage stiffness and strength of the composite laminate. And because the current unit price of the composites is mostly controlled by the fiber phase, the fiber hybridization may not be economically effective in infrastructure applications. In this light, a new class of composites that possess superior properties but at a reasonably cheap price are highly desirable for civil structural applications.

2.5. Summary

This chapter discussed the classifications, constituent materials, and the manufacturing processes of engineering composites. The mechanics and three design approaches driven by stiffness, strength, and damping for laminated composites are briefly introduced. Some commonly used toughening mechanisms of composite materials are introduced and their merits and drawbacks are discussed. Though composites with superior properties have been developed for high-end aerospace and automobile applications, however, their high price have limited the usage in the civil infrastructures. Thus, a new type of structural composites that have both enhanced properties and low cost are desirable for civil infrastructure retrofitting and damage mitigation applications.

Chapter 3.

MICROSTRUCTURES, DAMAGE MECHANISMS, AND MICROMECHANICAL PROPERTIES OF THE CARBON-FIBER REINFORCED HYBRID POLYMERIC-MATRIX COMPOSITE

A carbon fiber-reinforced hybrid polymeric-matrix composite (CHMC) is proposed in this chapter, its microstructure, damage mechanisms, and micromechanical properties are investigated using state-of-an-art testing techniques, such as scanning electron microscopy and nano-indentation. The primary experimental study results are reported, and the mechanisms by which the CHMC is able to exhibit higher damage tolerance and energy dissipation capacity than traditional graphite/ epoxy composite are discussed.

3.1. A carbon fiber-reinforced hybrid polymeric-matrix (CHMC) composite

Based on the discussions of the previous two chapters, the motivation to develop a new class of high-performance, yet affordable and easy-to-process, composite materials that possess a suite of superior properties including high strength, high ductility, and good energy dissipation for civil infrastructure applications has become obvious. While the strength and stiffness of most continuous fiber reinforced composites are governed by the fiber properties, however, the matrix phases in a composite material provides the stress transferring paths for reinforcing fibers; thus, the matrix phase, to some extent, affects the fracture toughness of the composites [53]. Most thermosetting polymers, such as epoxy, fracture at a relatively low strain range; as a result, damage that is initiated in

the reinforcing fibers or at the fiber-matrix interface quickly bridge together via matrix cracking causing catastrophic failure of the material system. One solution proposed in the current work is to develop a hybrid matrix system that combines the high stiffness and good saturation to fiber fabrics of epoxy-based polymers with the high damping and extremely high fracture toughness produced by conjoined cohesive epoxy-to-lightly-crosslinked elastomers, such that the micro-damage initiated in the more brittle phases, such as the fiber to matrix interface and epoxy based matrix, can be stabilized and exhibit more ductile and tougher mechanical behaviors in the macro-scale sense. The basic design philosophy and cross-ply structure of this hybrid matrix system and how it is combined with the reinforcing fibers is introduced in the following section.

3.1.1. Design Philosophy and Cross-ply Texture of the CHMC Composite

The matrix phase of the carbon-fiber reinforced hybrid-polymeric matrix composite (CHMC) system is created by saturating the reinforcing carbon fiber into an epoxy-based polymeric phase I; then a second lightly crosslinked elastomer is applied to the surface of the polymeric phase I before the curing reaction of the phase I polymer is completed, as shown in Figure 3.1.1.1. A chemically bonded interface would form between the phase I and phase II polymers, providing the bonding strength (and a source of internal damping) between the two distinct matrix phases. The chemical reaction taking place at the polymeric interface layer and how it would affect the mechanical performance of CHMC will be elaborated upon later in greater detail. The "multi-layered" cross-ply texture of CHMC is schematically illustrated in Figure 3.1.1.1, where the reinforcing carbon fibers are "embedded" in the polymeric matrix phase I, and the

polymeric phase II is coated on both sides or one side of the laminate (lamina), depending on whether the CHMC is used as a "stand-alone" structural material system or as a retrofitting system adhered to a substrate.

The CHMC can be used either as a "stand-alone" structural material system to manufacture mechanical components or sports equipments, such as fishing rods and helmets, or as the retrofitting laminate (or patching) to a damaged/ or undamaged substrate, such as concrete and steel. When the CHMC is used as a "stand-alone" material, the polymeric phase II can be coated to both sides of the composite laminate (lamina), as illustrated in Figure 3.1.1.1 (a); and when it is used as a retrofitting material, only one side of the laminate (lamina) can be coated by the polymeric phase II, as shown in Figure 3.1.1.1 (b), since an adhesive layer has to be applied between the laminate and the substrate.

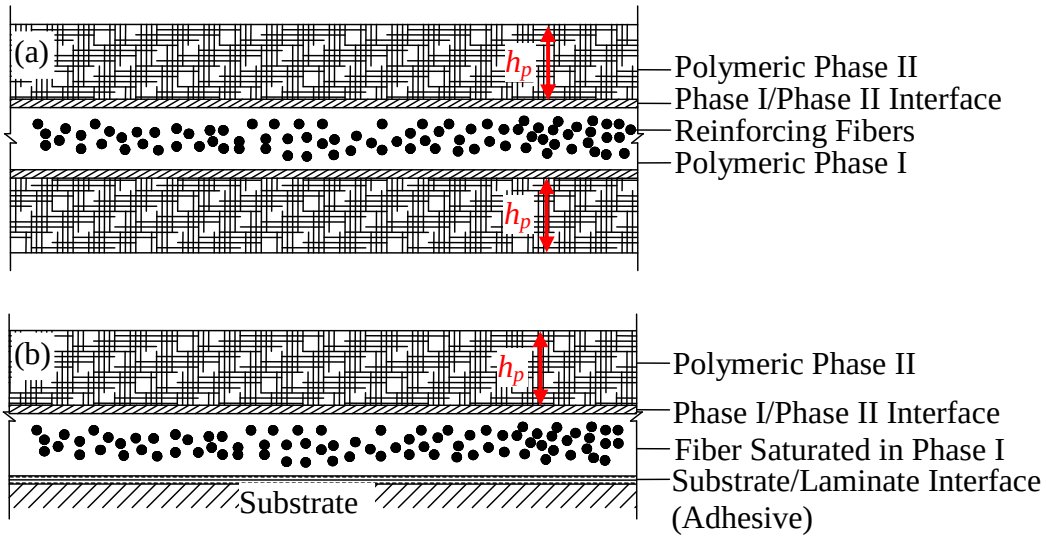

Figure 3.1.1.1. The illustrative figure showing the cross-ply layout of the CHMC: (a) used as a stand-alone system; (b) used as a retrofitting system to a substrate

Two design, or processing, parameters that would affect the mechanical and physical properties of CHMC - 1) the thickness of the polymeric phase II - h_p, see Figure 3.1.1.1, and 2) the intermittent curing time - t_c are induced into the design and manufacturing of the CHMC systems. After the reinforcing fibers are saturated with an epoxy-based two-component matrix phase I, a curing reaction would take place in the matrix phase I. The addition of the second elastomer phase would "interrupt" the curing reaction of phase I via the reaction between the elastomer molecules with one of the prepolymer of phase I. Thus, t_c, which is the reaction time of matrix phase I before the process is "interrupted" by the addition of the phase II elastomer, becomes a critical design parameter of CHMC that affects the interfacial bonding strength of the two polymeric phases and also damping. The chemical reactions taking place during the "time-sensitive" curing process of the hybrid matrix system are elaborated in greater details in the following section.

3.1.2. A "Time-Related" Reaction of the Two Polymeric Phases

The interface between the two polymeric phases I and II, as shown in Figure 3.1.1.1, is formed through the chemical reaction of the two matrix constituents. The extent of the chemical reaction is a function of the intermittent curing time t_c, i.e. the curing reaction of polymeric phase I occurs for a certain time t_c before the it is "interrupted" by the addition of polymeric phase II; the polymeric phase II, which is a lightly cross-linked elastomer formed by a step-growth polymerization process.

The polymeric phase I, which is an epoxy-based resin, is most commonly formed from the reaction of *bisphenol A* with *epichlorohydrin* to form the *bisphenol-A diglycidyl ether* (or DGEBA) shown as (3.1.2.1) below

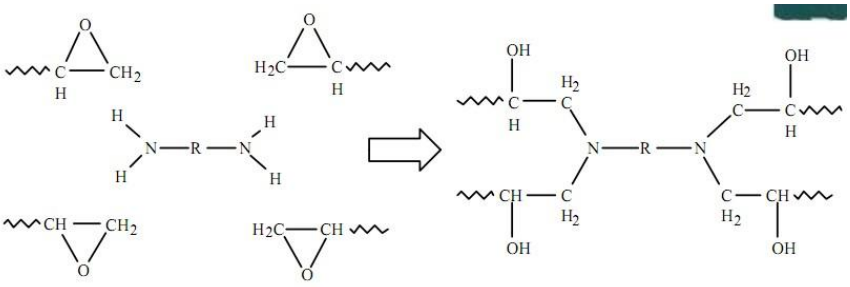

(3.1.2.1)

The completely cured epoxy resin possess a highly crosslinked 3D network molecular structure that yields high elastic modulus and strength under room temperature.

The polymeric phase II is a type of elastomer that is derived from the reaction product of an isocyanate component and a synthetic resin blend component through step-growth polymerization. The prepolymer, or quasi-prepolymer, can be made of an amine-terminated polymer resin, which would yield the general polymerization reaction as follows:

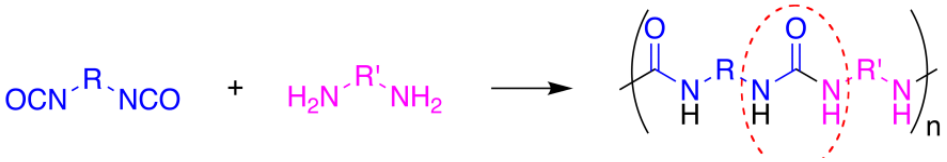

(3.1.2.2)

In the polymeric phase II, alternating monomer units of isocyanates and amines react with each other to form the polymer chains. The same type of linkage can also be formed from the reaction of isocyanates and water which forms a carbamic acid intermediate. The carbamic acid quickly decomposes by splitting off carbon dioxide and leaving behind an amine. This amine then reacts with another isocyanate group to form the polymer chains. The resin blend may also contain additives, or non-primary

components, that may alter the physical and mechanical properties of the final formed polymer. These additives may contain hydroxyls, such as pre-dispersed pigments in a polyol carrier.

During the "two stage" formation of CHMC's hybrid matrix system, the formation of the epoxy-based polymeric phase I in chemical reaction (3.1.2.1) is "interrupted" by the addition of matrix phase II that results in the reaction (3.1.2.3) at the interface of these two polymeric phases [76] (see Figure 3.1.1.1)

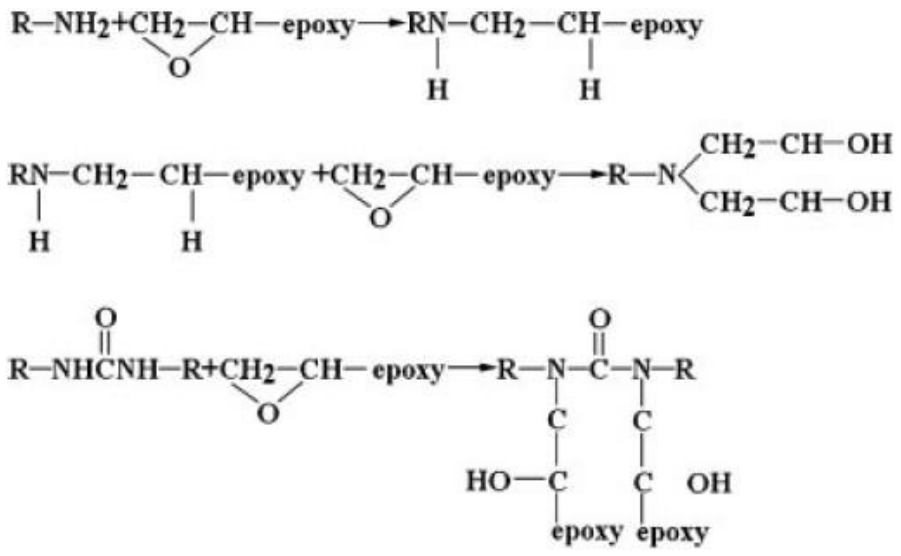

(3.1.2.3)

The interface of the partially reacted matrix phase I (i.e., the epoxy-based phase) and the interfering phase II (i.e., elastomeric phase) copolymer is presumed to lead to discernible material properties as a function of the intermittent curing time - t_c - and the volume fraction of the polymeric phase II, as will be evidenced in the microstructural and mechanical property studies of the CHMC in the following section and also in Chapter 4.

3.2. The Microstructures and Fractography of the CHMC

3.2.1. Microstructures

Due to the heterogeneous nature of fibrous composites, the physical and mechanical properties of many composite materials are governed by their microstructures. For instance, the stiffness and strength of the composite laminate depend significantly on the volume fraction, orientation of the laminate, and distribution of the reinforcing fibers. And as previously discussed in Chapter 2, the microstructure and morphology of each individual constituent, such as the matrix and its porous or solid constituency, would dramatically affect its mechanical properties, such as the fracture toughness. Another important factor that impacts the performance of an engineering composite is the density and distribution of the manufacturing defects, such as the air voids trapped in the matrix during the manufacturing processes. These defects often act as stress risers in the material due to the stress concentration near discontinuities, and initiate damage in the composite laminate even at very low stress levels, as shown in Figure 3.2.1.1. In this light, the microstructure of the newly developed CHMC and the carbon fiber reinforced epoxy composite is investigated using scanning electron microscopy (SEM). The cross-ply morphology of the CHMC laminate (lamina) are presented; and how the CHMC's unique multilayered cross-ply texture could contribute to its superior capability to sustain damage would be discussed.

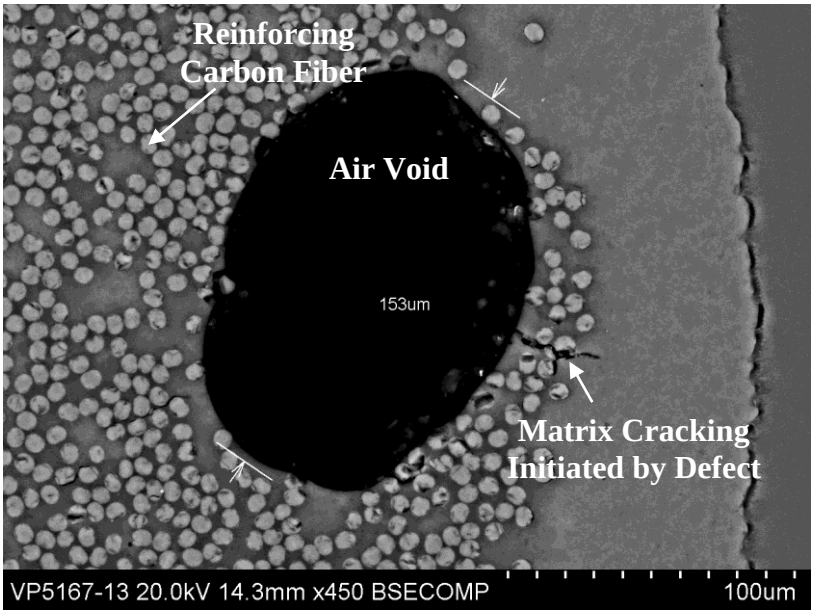

Figure 3.2.1.1. Damage (matrix cracking) initiated by a trapped air void

The microstructures of the newly developed CHMC were investigated using scanning electron microscopy (SEM). The material samples were casted in the epoxy resin with the laminates cross-section facing upwards, as shown in Figure 3.2.1.2. Then the samples were grinded and polished in order to expose the laminate cross-ply section and to create a smooth surface for the impending SEM analysis. Since most polymers do not conduct electricity, the electron beams from the electron microscope tend to build up on the sample surface causing the so-called "electron charging" that would generate very bright spots on the SEM images and disrupt the quality of the pictures. To avoid the electron charging for non-electrical conductive polymers, all sample were "carbon-coated" using a carbon coater, as shown in Figure 3.2.1.3 (a), where the carbon vapor was deposited on the specimen surface in the vacuum environment creating a thin (8-15 nm) carbon film. The thin carbon film acted as a "conductive" layer on the polymer surface to

reduce charging. The HITACHI S-3400 scanning electron microscope, as shown in Figure 3.2.1.3 (b), was used to conduct both the microstructural analysis and fractography study that will be elaborated in the latter sections of this chapter.

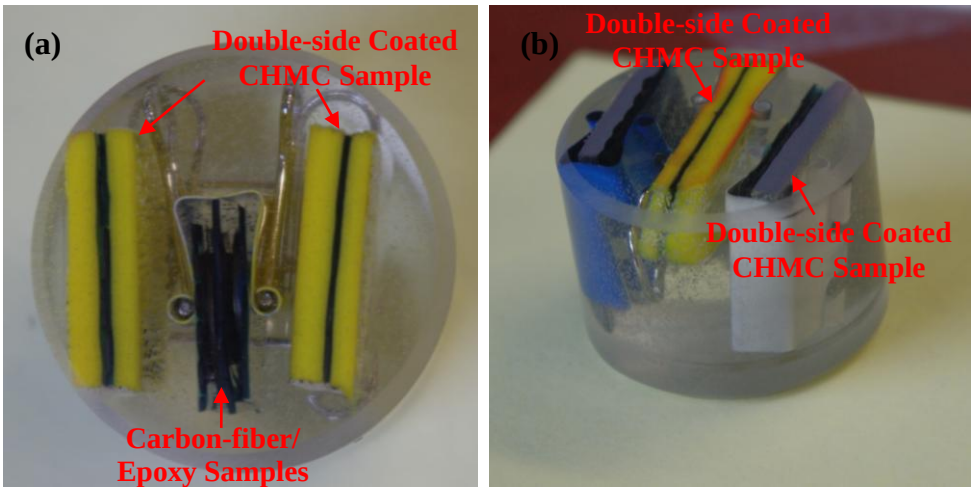

Figure 3.2.1.2. Polished samples used for microstrucutral characterization of CHMC and CFRP: (a) top-view (double-side coated CHMC and CFRP laminates); (b) perspective view (double-side coated CHMC and single-side coated CHMC)

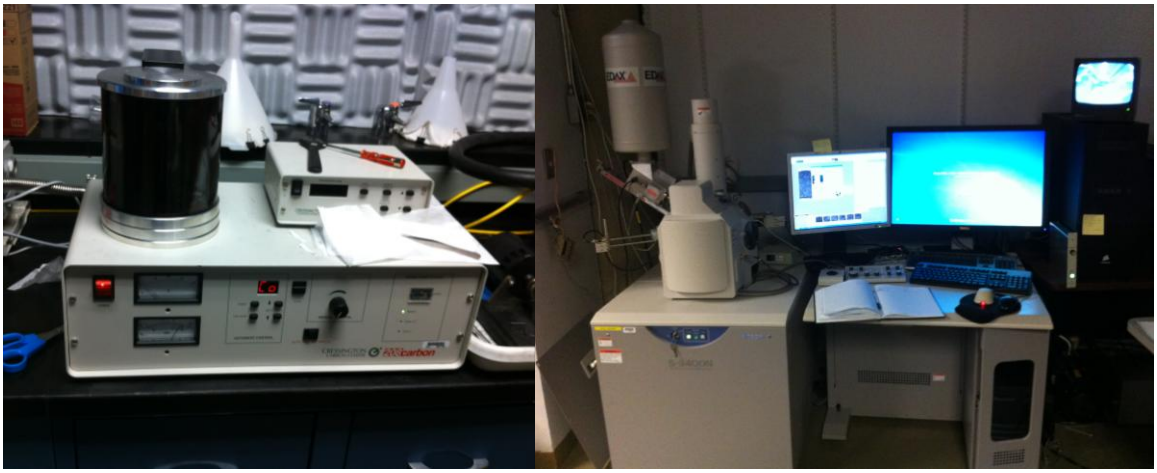

Figure 3.2.1.3. (a) Carbon coater; (b) The HITACHI S-3400 electron scanning microscope used for the microstructural study

The SEM images showing the microstructures of the CHMC laminas (lamina) are presented in Figure 3.2.1.4. The "multi-layered" cross-ply texture of the CHMC composite as introduced in Section 3.1.1, see Figure 3.1.1.1 (a), is evidenced in the SEM image shown in Figure 3.2.1.4, where the center layer is the reinforcing carbon fiber saturated in the epoxy based polymeric phase I and the polymeric phase II elastomer is coated on both side of the lamina, see Figure 3.2.1.4 (a). A "zoomed-in" view of the central region of the laminate is presented in Figure 3.2.1.4 (b) with higher magnification, where reinforcing fiber bundles are clearly distinguishable from the epoxy-based polymeric phase I. The phase II elastomer shows a porous morphology, where the brighter regions in the polymeric phase II as shown in Figure 3.2.1.4 (b) are the air bubbles trapped in the polymeric phase II during its formation process. There are evidences, from the fracture energy perspective, showing that the porous morphology of a material would dramatically increases its fracture toughness as compared to its continuous bulk solid form. Not to mention the lightly crosslinked molecular structure of the elastomeric phase II polymer provides a high level of mobility to its polymer chains resulting in highly ductile stress-strain behavior, as discussed in Chapter 2, also see Figure 2.1.3.2. As a result, the phase II polymer that is used to form the CHMC's hybrid matrix system exhibits extremely high fracture toughness, i.e. 450% -600% elongation upon fracture. The highly tough and ductile property of the phase II polymer would be crucial for the CHMC system to sustain micro-scale level damages. The reinforcing carbon fibers (Torayca®, TORAY) that was used to provide the base-line strength of the CHMC have an average diameter of approximately 7 micrometers, see Figure 3.2.1.4 (c).

The nominal thickness of fiber bundles depends on the manufacturer's specifications for their various products [77]. The interface region image obtained from unpolished CHMC samples, as shown in Figure 3.2.1.4 (d), shows signs of chemical reaction between the two polymeric phases that compose the matrix system of CHMC.

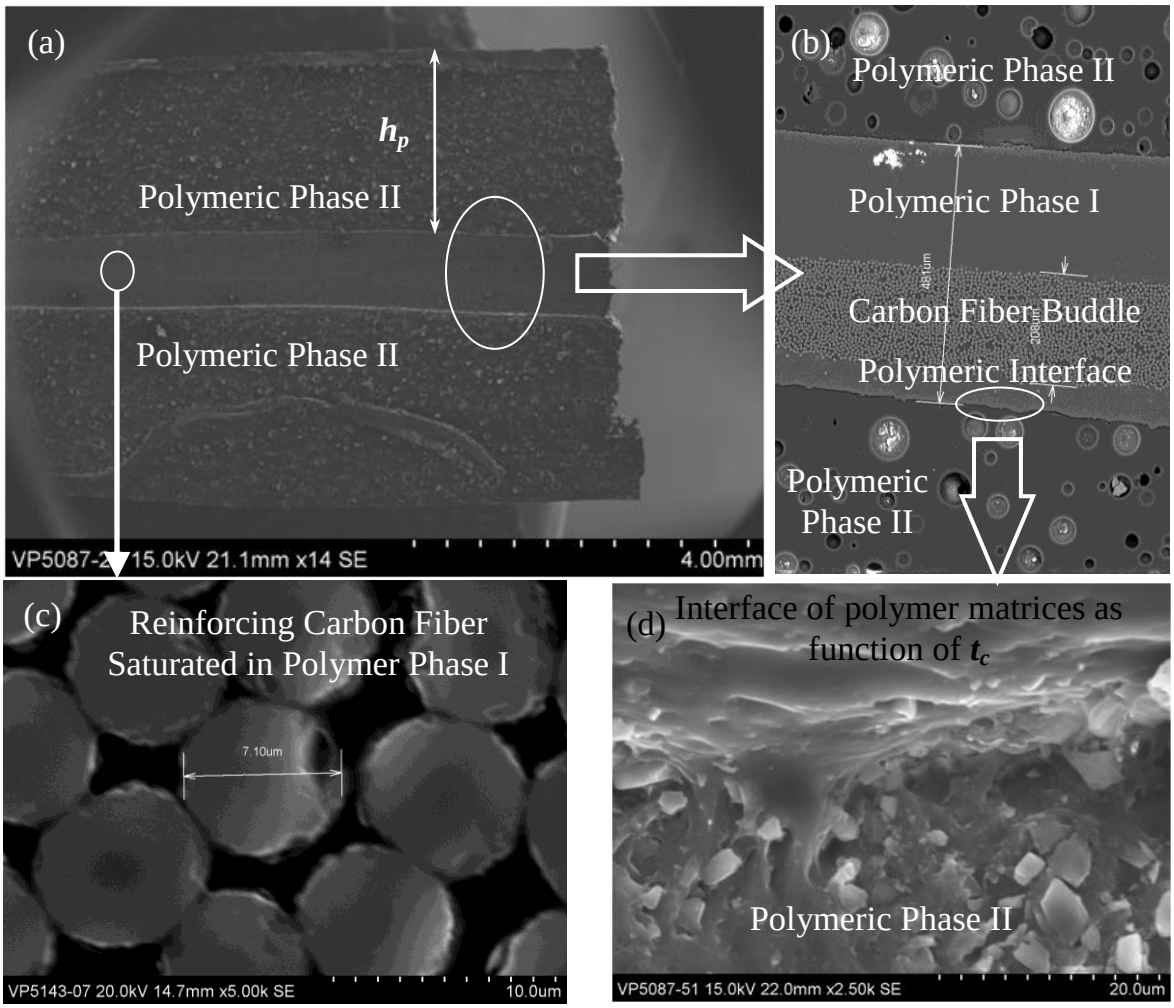

Figure 3.2.1.4. The SEM image showing the microstructures of the CHMC laminate (a) SEM image of carbon fiber reinforced epoxy lamina (low magnification); (b); (c) SEM image of the CHMC lamina (low magnification)

A closer examination of the interface region between the matrix phase I and phase II reveals the different morphologies as a function of the intermittent curing time - t_c - as shown in Figure 3.2.1.5 and Figure 3.2.1.6. The interface of the partially reacted polymeric phase I (i.e., the epoxy-based polymeric phase) and the interfering phase II elastomeric copolymer is presumed to lead to discernible material properties, such as damping and impact resistance, as a function of the epoxy curing time. More specifically, as the intermittent curing time of the phase I (t_c) decreases (i.e., there is less elapsed time before the reactive phase II elastomer is applied), the chemical reaction (3.1.2.1) is "less complete," leaving a larger quantity of "reactive" epoxy prepolymer to react with the polymeric phase II. As a result, a lower the reaction time t_c, implies a "wider" interface region (9.92 micrometers vs. 4.44 micrometers) between the interrupted epoxy-based phase I and interfering phase II elastomer, see Figure 3.2.1.6, which will be evidenced later as a precursor to higher impact-resistance and more damping.

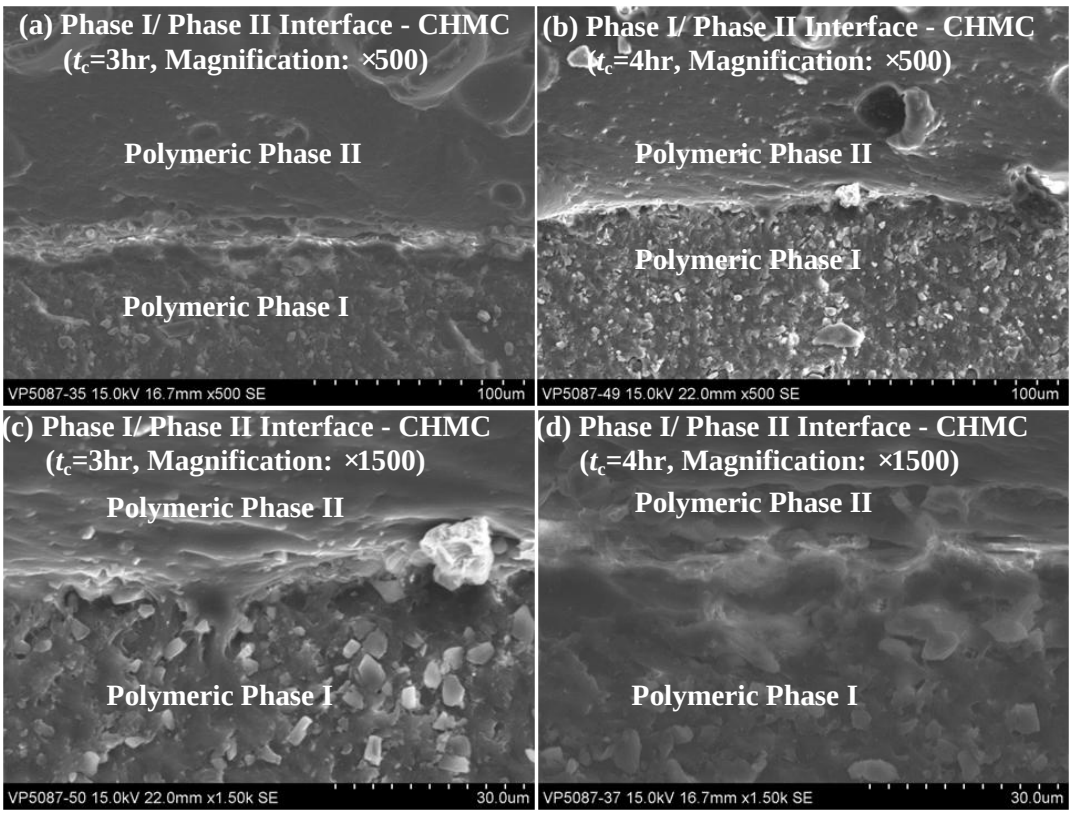

Figure 3.2.1.5. The SEM images obtained from the unpolished samples showing the interfaces between polymeric phase I and phase II for CHMC laminate having various t_c: (a) t_c=3hr., ×500; (b) t_c=4hr., ×500; (c) t_c=3hr., ×1500; (d) t_c=4hr., ×1500

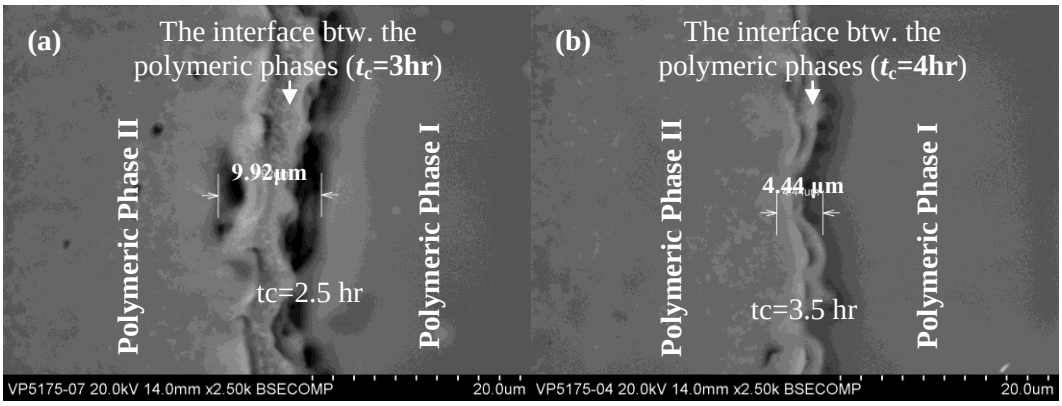

Figure 3.2.1.6. The various interface thicknesses as a function of t_c (a) t_c=3hr.; (b) t_c=4hr.

3.2.2. Fractography and Failure Mechanisms of CHMC versus Carbon-fiber/ Epoxy

One unique property of composite materials is their evolutionary failure characteristic. The non-homogeneity of the microstructure provides numerous paths in which load may be redistributed around a damaged region. Because of the non-homogeneity of the microstructure of composites, the integrity and response of the composite are affected more by the effective accumulated subcritical damage than by any single damage event (unless the single damage event is excessively large), see Figure 3.2.2.1 (a) for the example of micro- matrix cracking originated from the fiber-matrix interface. For laminated composites reinforced by continuous long fibers, this subcritical damage may be manifested as shown in Figure 3.2.2.1 (b) as: (1) matrix cracking; (2) fiber-matrix debonding which is also depicted as in Figure 3.2.2.1 (a); (3) fiber breakage or fracture; (4) fiber pullout; and (5) inter-lamina delamination (which is not applicable to single-ply laminates). Thus, in the design of a damage-tolerant composite material, a microscopically weak structure must be integrated into a macroscopically strong solid in order to ensure that any single damage event results only in minimal harm. In the case of a unidirectional fibrous composite, such as CFRP and CHMC as proposed herein, under tensile loading, the carbon fibers do not all snap at once in one fracture plane but instead, snap in a sequential manner because of the variability in flaw size along their length. Consequently, the fiber-epoxy matrix interface fails by de-adhesion, see 3.2.2.1 (a), and, in doing so, this blunts the tip of any small matrix crack that may be present which then effectively dissipates the energy that would have otherwise been used to further

propagate that crack, wherein the fibers bridging that crack remain intact and can thus carry the load.

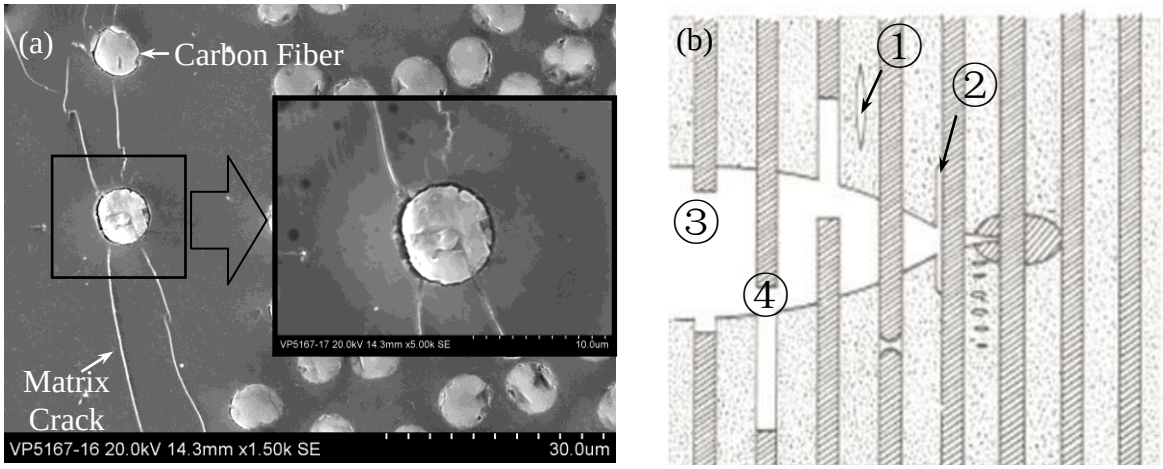

Figure 3.2.2.1. (a) The typical damage mechanisms of a laminate fiber composite [44]: ①matrix cracking, ②fiber-matrix debonding, ③fiber breakage, and ④fiber pullout

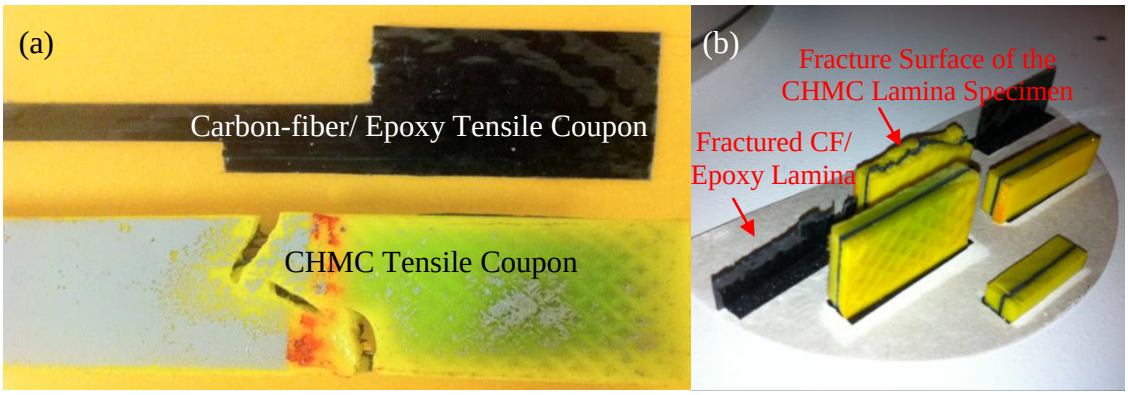

Figure 3.2.2.2. (a) Damaged tensile tests coupon specimens for carbon fiber reinforced epoxy and the CHMC; (b) Specimens used for fractography studies

Because of the evolutionary failure characteristic and non-homogeneous micro-structure of structural composites, the internal damping and energy dissipation quantities may also play a significant role on the damage and failure of the composite material by allowing stress redistribution and by creating a damage mitigation path. A fractography, or what is loosely referred to as a fracture surface morphology, was performed on the damaged carbon-fiber reinforced epoxy composite and the CHMC tensile coupons as presented in Figure 3.2.2.2. The samples to perform the fractography studies on both CHMC and CFRP were cut from the tensile test coupons used for the uniaxial tension tests per ASTM D3039 specifications, see Figure 3.2.2.2 (a). The fractography reveals many of these failure modes and may further prove that failure of the composite system is a chain of damage events rather than a single event although one or more failure modes may dominate. In a carbon-fiber/ epoxy matrix composite that had been loaded in tension, the damage often initiates at the fiber-matrix interface because of the relatively low interfacial fracture toughness and highly mismatched fiber/ matrix properties, such as mismatches in the elastic modulus and Poisson's ratio [63], also see Figure 3.2.2.1 (a). Several weakened fiber-matrix interfaces may cause stress concentrations on adjacent fibers leading to fiber fracture and pullout until enough damage events are bridged together to cause failure, see Figures 3.2.2.3 (b) and (c), e.g., along the fiber/ epoxy interface. By incorporating damping via the unique multi-phase matrix system, which will be quantified in the nanoindentation and vibration studies, see Figure 3.2.2.3 (e), the damage path is blunted and turned away, thus releasing energy and preventing stress concentrations, where: (1) the crack does not readily propagate due to internal stress/ force redistribution, (2) the crack location remains ‘localized,’ where the

occurrence of the formation of other similar cracks is reduced, and (3) subsequent dominant failure modes are dispersed since damage events are not bridged together. Consequently, the CHMC system not only exhibits desirable macro-mechanical features, such as vibration suppression and high-impact resistance, but it also fails in a very ductile energy-releasing fashion with much higher damage tolerance. The mechanical performance of the CHMC system at the macro-scale level will be discussed in greater details in Chapter 4.

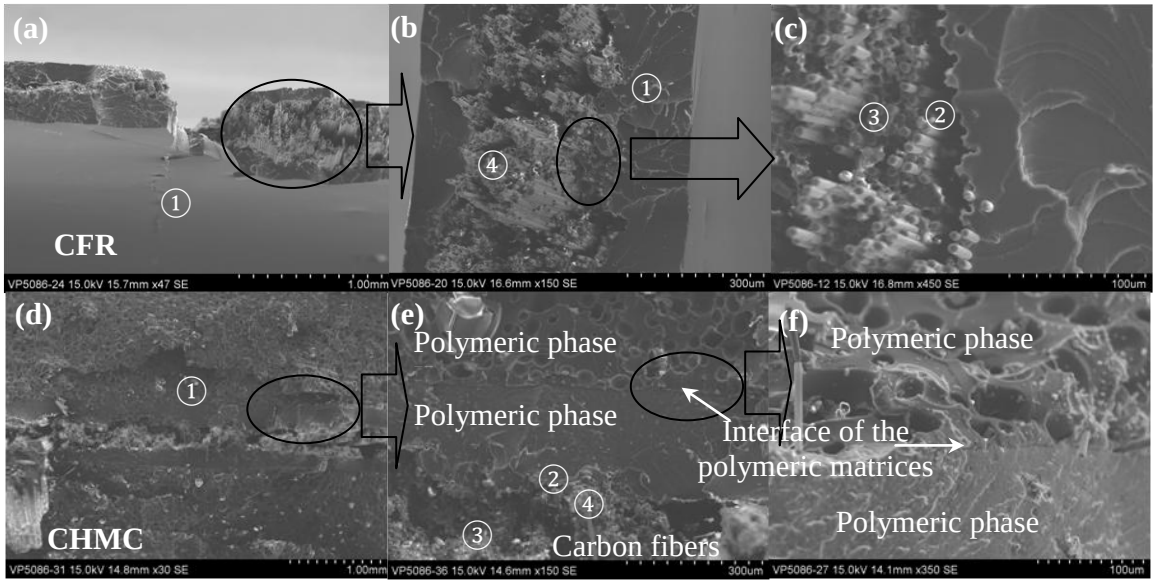

Figure 3.2.2.3. The microstructures and fracture surface morphology for CFRP and CarbonFlex composites: (a) fracture surface of a carbon fiber/ epoxy laminate, x47 SE; (b) x150 SEM; (c) x450 SEM image showing fiber- matrix debonding in CFRP; (d) The fracture surface of CHMC, x30 SE; (e) x150 SEM image showing the matrix fracture, fiber fracture etc. of a CHMC laminate; (f) x350 SEM image showing the polymeric interface in CHMC

3.3. The micromechanics and micromechanical behavior of the constituents

3.3.1. Micromechanics

The micromechanics of laminate composites have been briefly introduced in Chapter 2, where the micromechanics formulas based on the representative volume element (RVE) and basic rule of mixture were derived for calculating the lamina stiffness as functions of the fiber volume fraction and properties of the constituents. In this section, the simple rule of mixture method will be extended to the multi-layered CHMC laminate to derive the equations used to predict the tension and flexural stiffness of the laminates. The prediction results will be later compared to the experimental test results presented in Chapter 4.

Tension Stiffness of the CHMC Laminates

Since the simple rule of mixture formulas are accurate [60] in predicting the along-fiber direction modulus E_1, this method is extended to predict the primary elastic modulus (along-fiber direction) of the CHMC.

Recall the CHMC's "multilayered" cross-ply texture as introduced in Figure 3.1.1.1, the deformed shape of CHMC laminate used as a potential "stand-alone" structural material or as retrofitting laminates applied to a damaged/ or undamaged substrate under along-fiber direction tension are shown in Figure 3.3.1.1 (a) and (b), respectively. Despite the actual dispersion of reinforcing fibers as shown in Figure 3.2.1.4 (b), the reinforcing fibers are assumed to uniformly distribute within an equivalent fiber layer having a nominal thickness of h_f, see Figure 3.3.1.1. Upon tension, the

laminate is assumed to deform uniformly, i.e. the strains within all constituent layers are identical

$$\varepsilon_f = \varepsilon_{m1} = \varepsilon_p \tag{3.3.1.1}$$

where ε_f, ε_{m1}, and ε_p are the strains in the reinforcing fibers, matrix phase I, and matrix phase II, respectively. Thus, the homogenized equivalent tension modulus E_1 of the "stand-alone" composite laminate, as shown in Figure 3.3.1.1 (a), can be expressed in terms of the constituent modulus and the laminate thickness as

$$E_1 = \frac{h_f}{h_c} E_f + 2\frac{h_{m1}}{h_c} E_{m1} + 2\frac{h_p}{h_c} E_p \tag{3.3.1.2}$$

where E_f, E_{m1}, and E_p are the elastic modulus of the strains in the reinforcing fibers, matrix phase I, and matrix phase II, respectively; and h_c is thickness of the composite laminate and h_{m1} and h_p are the thickness of the polymeric matrix phase I and phase II, respectively, as illustrated in Figure 3.3.1.1.

Similarly, the equivalent tension modulus for the retrofitting laminate within the linear elastic range can be expressed as

$$E_1 = \frac{h_f}{h_c} E_f + \frac{h_{m1}}{h_c} E_{m1} + \frac{h_p}{h_c} E_p \tag{3.3.1.3}$$

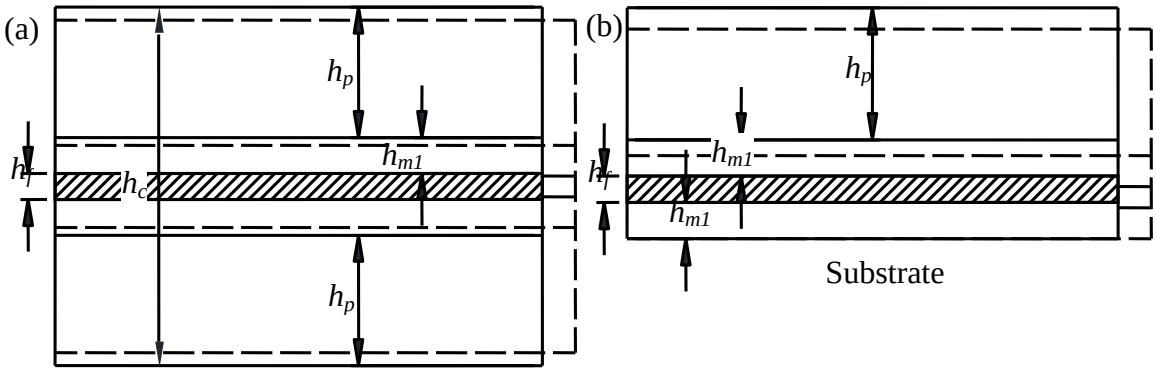

Figure 3.3.1.1. The CHMC laminate under along-fiber direction tension: (a) the "stand-alone" laminate with polymeric phase II coated on both sides of the laminate; (b) the CHMC laminate used as the retrofitting system for a substrate

Flexural Modulus of the CHMC Laminates

In the case of bending, the homogenized modulus tested via flexural tests are usually significantly lower than those predicted by equation (3.3.1.2) or (3.3.1.3) for the possible reasons that the high stiffness reinforcing fibers are distributed near the center of the laminate where the location is close to the neutral axis, see Figure 3.3.1.2 (a). The strains within the reinforcing fibers would be low during the flexural deformation as compared to those in the matrix polymers, however, equations (3.3.1.2) and (3.3.1.3) assume that the laminate deforms uniformly cross the ply thickness, which obviously over estimated the contribution of reinforcing fibers to the flexural stiffness of the composite laminate. Thus, the formulas that can more accurately predict the bending modulus of the CHMC laminates are derived in this section as follows.

Several assumptions and simplifications are adopted in the formula derivation that: 1) the analysis assumes that plain section remains plain after deformation (Euler-

Bernoulli beam theory), which implies the strain compatibility of each adjacent constituent layer(s) and the strain will be linearly distributed across the ply-thickness direction, as shown in Figure 3.3.1.2 (a); 2) the reinforcing fibers are assumed to uniformly distributed within a equivalent fiber layer; and 3) the shear deformation is ignored. The bending stiffness of a stand-alone CHMC laminate as shown in Figure 3.3.1.2 (a) may be expressed as

$$E_{flexural} I_c = \frac{h_f^3}{12} E_f + 2[\frac{h_{m1}^3}{12} E_{m1} + \frac{h_p^3}{12} E_p + h_{m1} E_{m1} \left(\frac{1}{2} h_{m1} + \frac{1}{2} h_f \right)^2 + h_p E_p \left(\frac{1}{2} h_f + h_{m1} + \frac{1}{2} h_p \right)^2] \quad (3.3.1.4)$$

where $E_{flexural}$ is the homogenized equivalent flexural modulus of the laminate, and I_c is moment of inertia of a unit width of the composite laminate

$$I_c = \frac{1}{12} h_c^3 \quad (3.3.1.5)$$

And the flexural stiffness for the retrofitting laminate as shown in Figure 3.3.1.2 (b) is expressed as

$$E_{flexural} I_c = \frac{h_f^3}{12} E_f + \frac{h_{m1}^3}{6} E_{m1} + \frac{h_p^3}{12} E_p + E_{m1} h_{m1} \left[\left(D - \frac{1}{2} h_{m1} \right)^2 + \left(D - h_f - \frac{3}{2} h_{m1} \right)^2 \right] + E_f h_f \left(D - h_{m1} - \frac{1}{2} h_f \right)^2 + E_p h_p \left(D - h_f - 2h_{m1} - \frac{1}{2} h_p \right)^2 \quad (3.3.1.6)$$

where D is the distance from the neutral axis to the substrate, and can be expressed as

$$D = \frac{E_f h_f \left(h_{m1} + \frac{1}{2} h_f \right) + E_{m1} h_{m1} \left(h_f + 2h_{m1} \right) + E_p h_p \left(2h_{m1} + h_f + \frac{1}{2} h_p \right)}{2E_{m1} h_{m1} + E_f h_f + E_p h_p} \quad (3.3.1.7)$$

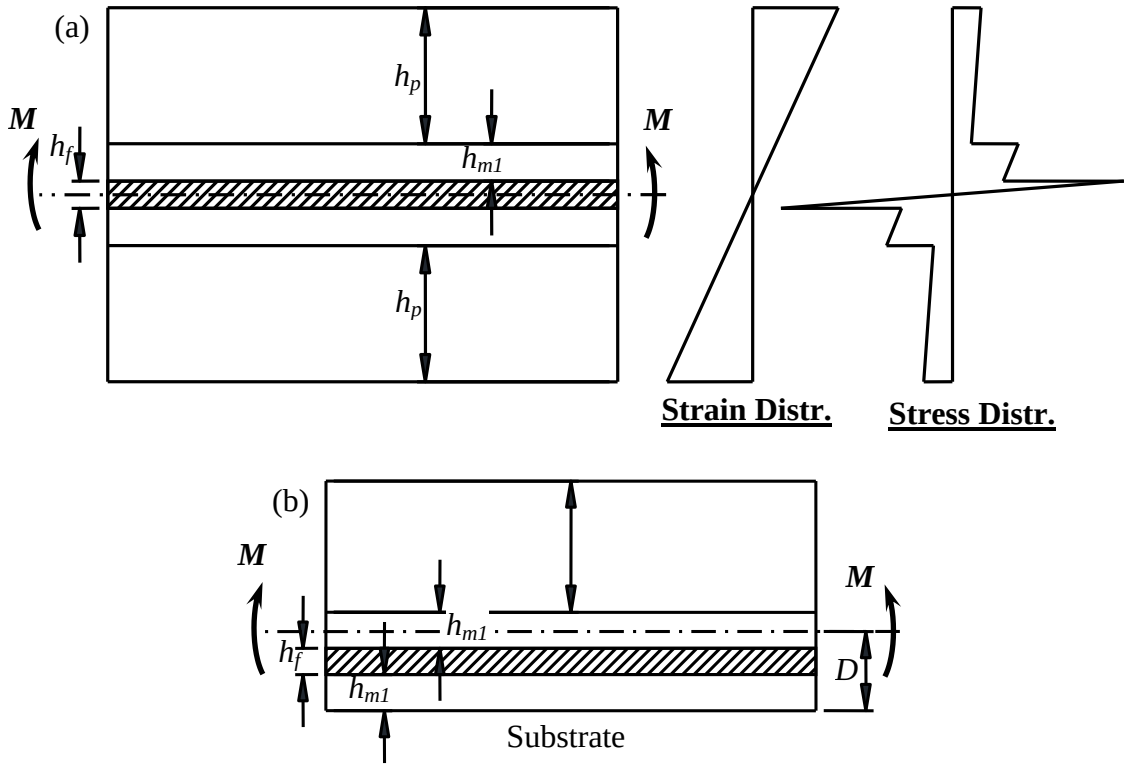

Figure 3.3.1.2. Illustrative figure showing the CHMC laminates under bending: (a) self-supported system; (b) retrofitting laminate on a substrate

It may be worthwhile to point out that for many retrofitting applications, where the substrate thickness is much greater than the thickness of retrofitting laminate (such as the case of retrofitting a damaged reinforced concrete beam), the stress distribution within the thin retrofitting laminate is close to that in pure tension. Equations (3.3.1.1) and (3.3.1.2) are suitable for calculating the homogenized elastic modulus of the composite laminates. However, if the substrate is thin (comparable to the thickness of the retrofitting laminate), such as the cases of being used as a stand-alone structural material and retrofitting a thin-walled pipeline or pressurized vessel, the stress distribution across the composite ply is no longer uniform. Thus, the location of the neutral axis and its

influence on the flexural stiffness have to be taken into account, i.e., formulas that are similar to equations (3.3.1.4) and (3.3.1.6) should be used to predict the equivalent modulus of the composite laminate. Moreover, several limitations of equations (3.3.1.4) and (3.3.1.6) should be mentioned here: 1) the analysis assume that plane sections remain plane, therefore, the deformation caused by shear is ignored. Caution must be taken when the modulus of the matrix phase I - E_{m1} is significantly lower than the other two phases, where the shear deformation of the phase I may dominate the bending behavior of the laminate as shown in Figure 3.3.1.3 (a). In such case, the equations developed by Ross, Ungar, and Kerwin (or often being referred as to the RKU equations) [78] should be used; 2) strain compatibility was assumed for all adjacent constituent layers, so that the deformation within the interfaces is also omitted in the analysis. Thus, care should also be taken when analyzing laminates having weak, or very soft, interfaces, see Figure 3.3.1.3 (b).

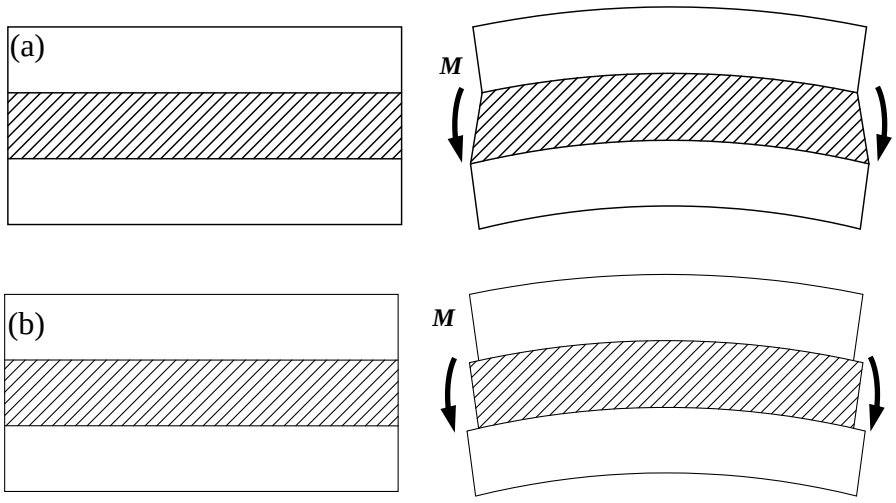

Figure 3.3.1.3. The flexural deformation of composite laminate dominated by (a) the shear deformation of the center "soft" layer; (b) soft interface

3.3.2. Characterization of Micromechanical Properties using Nanoindentation

Nanoindentation, which was initially developed in the mid-1970s, is an indentation hardness test applied to very small volumes. In a nanoindentation test, a very small (having a size of several micrometers or even nanometers) and hard indenter tip whose mechanical properties are pre-known is pressed into a material sample whose material properties are unknown. The indentation load (in μN or nN) versus penetration depth (in nm) curves are recorded. A typical nanoindentation curve is schematically shown in Figure 3.3.2.1. The analysis of the load-penetration curves is often based on the work of Oliver and Pharr [79], where the slope of the unloading curve was termed as the contact stiffness, *S*, and is given by equation (3.3.2.1) as

$$S = \frac{dP}{dh_{cont}} = \frac{2\beta}{\sqrt{\pi}} E_r \sqrt{A_p\left(h_{cont}\right)} \tag{3.3.2.1}$$

where P is the load; $A_p(h_{cont})$ is the projected area of tip-sample contact at the contact depth h_{cont}; β is a factor that counts for the geometrical shape of the indentor tip; and E_r, the reduced Young's modulus, is a function of the stiffness of both sample material and the indentor tip and is expressed as

$$\frac{1}{E_r} = \frac{\left(1-\upsilon_s^2\right)}{E_s} + \frac{\left(1-\upsilon_i^2\right)}{E_i} \tag{3.3.2.2}$$

where E_s and E_i are the Young's modulus of testing sample and the indenter tip, respectively; and v_s and v_i are the Poisson's ratio of the sample and indenter tip materials. For the indentor tips that are made from diamond, E_i is 1140 GPa and v_i is 0.07. The tip shape function, $A_p(h_{cont})$, may be determined using a polynomial fit of the form [80]

$$A_p\left(h_{cont}\right) = C_0 h_{cont}^2 + C_1 h_{cont} + C_2 h_{cont}^{1/2} + C_3 h_{cont}^{1/4} + \ldots \quad (3.3.2.3)$$

where $C_0 \sim C_i$ are constants determined by curve fitting; and h_{cont} is the contact depth, see Figure 3.3.2.2. For the materials that exhibit some extend of plasticity, the contact depth h_{cont} does not equal to the maximum indentation depth h_{max} since the material surface tends to "concave down" due to the plastic deformation, as illustrated in Figure 3.3.2.2. The relationship between h_{cont} and h_{max} may be estimated by equation (3.3.2.4) as

$$h_{cont} = h_{max} - \frac{\chi P_{max}}{S} \quad (3.3.2.4)$$

where χ is a function of the particular tip geometry [80].

The contact stiffness at the maximum load point can be expressed as a function of the maximum penetration, h_{max}, and residual penetration, h_r, as shown in Figure 3.3.2.1, as

$$S|_{P_{max}} = \alpha m\left(h_{max} - h_r\right)^{m-1} \quad (3.3.2.5)$$

where the α and m are parameters related to the geometric shape of the indenter tip. Thus, the relationship between the reduced elastic modulus E_r and the unloading curve is established as

$$E_r = \frac{\sqrt{\pi}}{2\beta}\frac{S|_{P_{max}}}{\sqrt{A_p\left(h_{cont}\right)}} \quad (3.3.2.6)$$

where A_p, h_{cont}, and $S|_{Pmax}$ are obtained from the nanoindentation unloading curve and equation (3.3.2.3), (3.3.2.4), and (3.3.2.5), respectively. And the hardness of the tested material is defined as

$$H = P_{max} / A_p \quad (3.3.2.7)$$

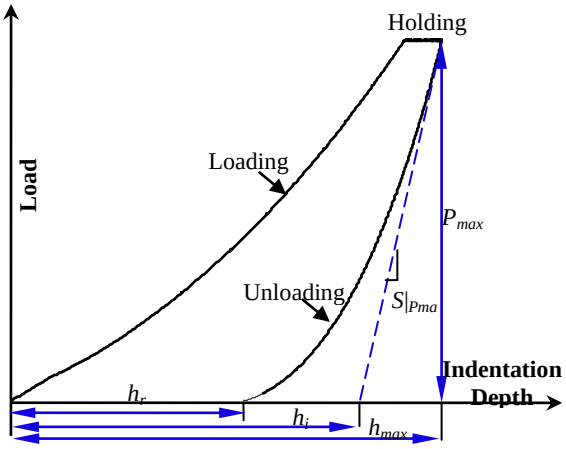

Figure 3.3.2.1. (a) The load profile used in this study;(b) a typical load-penetration curve in which several important parameters used in the Oliver and Pharr method are illustrated

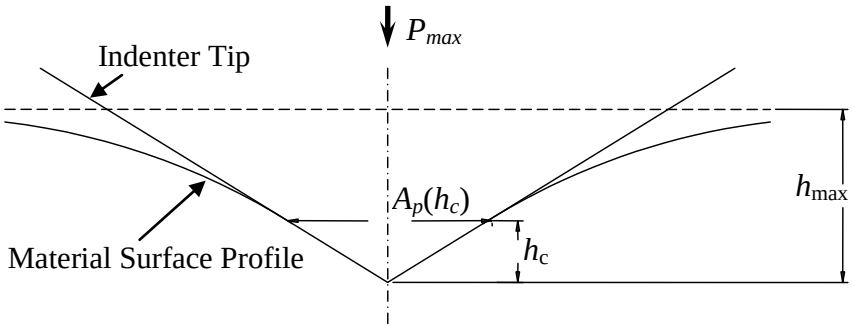

Figure 3.3.2.2. Illustrative figure showing the deformed material surface at maximum load

3.3.3. Nanoindentation Tests on the CHMC Constituents

The nanoindentation tests were performed at the High Temperature Materials Laboratory (HTML) at Oak Ridge National Laboratory. The HYSTRON TriboIndentor

as shown in Figure 3.3.3.1 were used to perform the indentation tests on the constituent fiber and matrix polymers of the CHMC. The test samples were cast in the epoxy resin and polished to expose a smooth surface on the laminate cross-ply section. Five indentation areas, each having a dimension of 100 micrometers (μm) by 100 micrometers (μm), were selected from the center (reinforcing fiber) to the edge (polymeric phase II) of the CHMC laminate cross-section, see Figure 3.3.3.2. The nanoindenter was programmed to produce a five by five indent matrix within each of the five indentation areas where the spacing of each row and column was 25 micrometers. The indentation areas, together with their atomic force microscopy (AFM) images, were presented as the red boxes shown in Figure 3.3.3.2. A Berkovich tip, which has a three-edge pyramid shape, was used for the indentation tests. The indentation tests were load-controlled to reach the maximum load of 500 micro-Newton (μm) at constant loading rate and the maximum load was held for 5 sections before unloading. The load profile used is shown in Figure 3.3.3.3.

Figure 3.3.3.1. (a) The HYSITRON TriboIndenter used for the nano-indentation study; (b) the specimen and key components of the nano-indentor

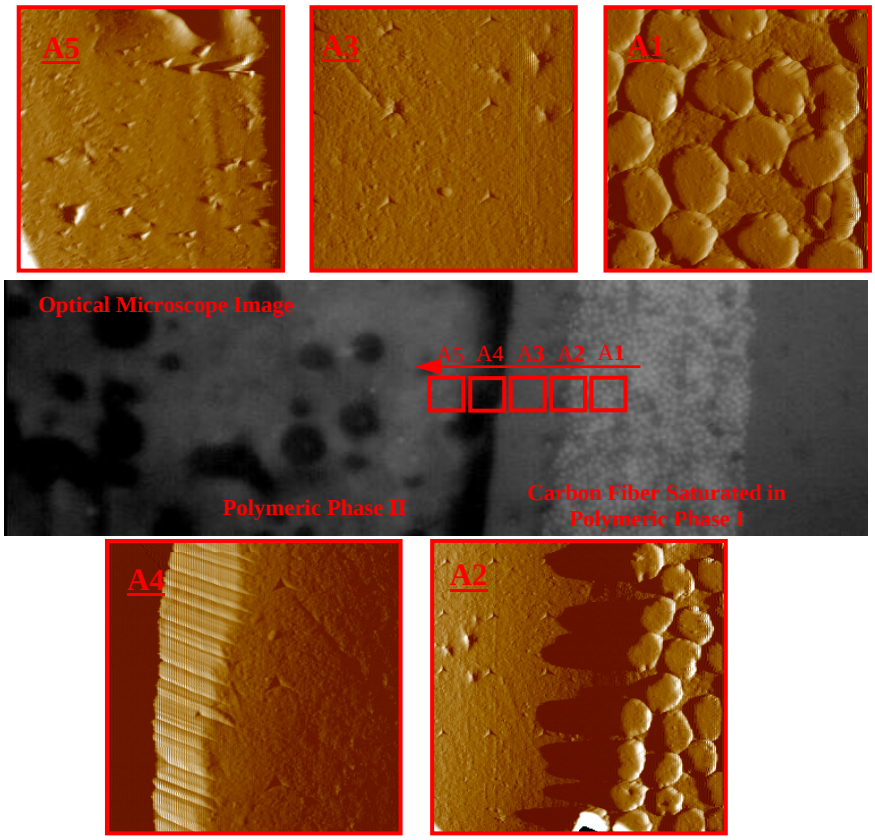

Figure 3.3.3.2. Optical microscope and atomic force microscopy (AFM) images showing the indentation areas tested on the CHMC

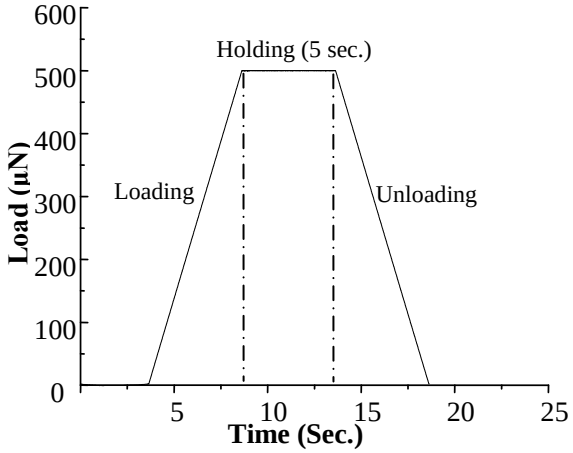

Figure 3.3.3.3. The load profile used in the nanoindentation tests

The load versus penetration depth curves obtained within each of the indentation area are shown in Figures 3.3.3.4 - 3.3.3.7, and the nanoindentation results for all tests, including the nano-hardness H and reduced elastic modulus E_r, are summarized in Appendix A. Area A1, which was located in the center region of the laminate cross-section (see Figure 3.3.3.2), consists of reinforcing carbon fiber and the polymeric phase I. The nanoindentation tests within this area were mostly on the carbon fibers with a few on the epoxy-based polymeric phase I and the fiber-phase I interface, see Table A1. Area A2 was located at the interface between the carbon fiber bundle and polymeric matrix phase I, see Figure 3.3.3.2. The indents within this area were landed mostly on the polymeric phase I with a few landed on the carbon fibers, see Table A2. The load-indentaiton depth curves are plotted in Figure 3.3.3.4, where the curves on fibers are clearly distinguishable from those on the polymeric I and exhibit very stiff and nearly purely elastic behavior, i.e., there was almost no residual deformation after unloading. The nanoindentation curves for the epoxy-based polymeric phase I, on the other hand, indicate much smaller stiffness (elastic modulus) than carbon fiber and a high level of plastic deformation, which was signified by the large residual displacement - h_r, as defined in Figure 3.3.2.1. The indents within area A3 all landed on the polymeric I, producing a series of stable indentation curves with small variation. Area A4 was located at the polymeric phase I - phase II interface, thus, a portion of the indents within this area landed on the polymeric phase I, and some landed on the phase II elastomer. It is obvious from the Figure 3.3.3.6 that the phase II elastomer exhibits much "softer" behavior as compared to the phase I polymer. Under the same peak load, the penetration depths on the phase II elastomer were much greater (about six times greater) than those

on phase I polymer. It was also noted that the indents landed within the interface region resulted in strange curve shape, with very small loading stiffness at initial loading and the stiffness suddenly increases after certain displacement level, see Figure 3.3.3.6. A reasonable explanation might be the surface condition of the polished samples used for the indentation tests. Since the elastic modulus of the three primary material phases within CHMC are significantly different as evidenced by the nanoindentation tests, the mechanical polishing of the sample surface will result in a non-smooth surface, leaving the stiffer material phases slightly higher than the softer ones. As a result, if the indenter tip lands on the interface between two material phases, it will be in partial contact with stiffer material phase; and as the displacement increase, the indenter tip will also be in contact with the softer material phase, producing the "jagged" curve shape as shown in the interface region of Figure 3.3.3.6. Lastly, the area A5 was located on the elastomeric phase II, producing a series of stable indentation curves that signify the properties of the phase II elastomer.

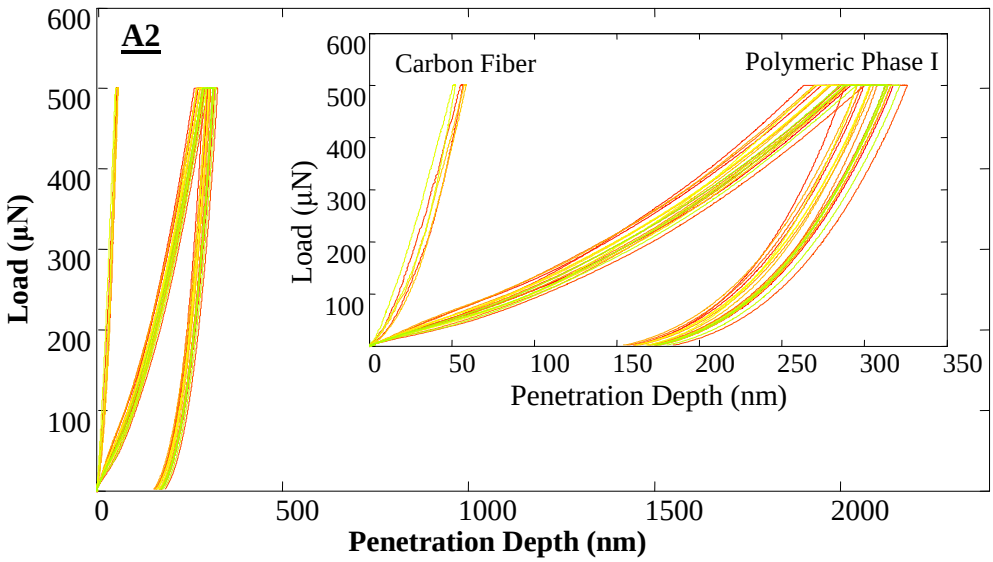

Figure 3.3.3.4. The nanoindentation curves obtained within area A2

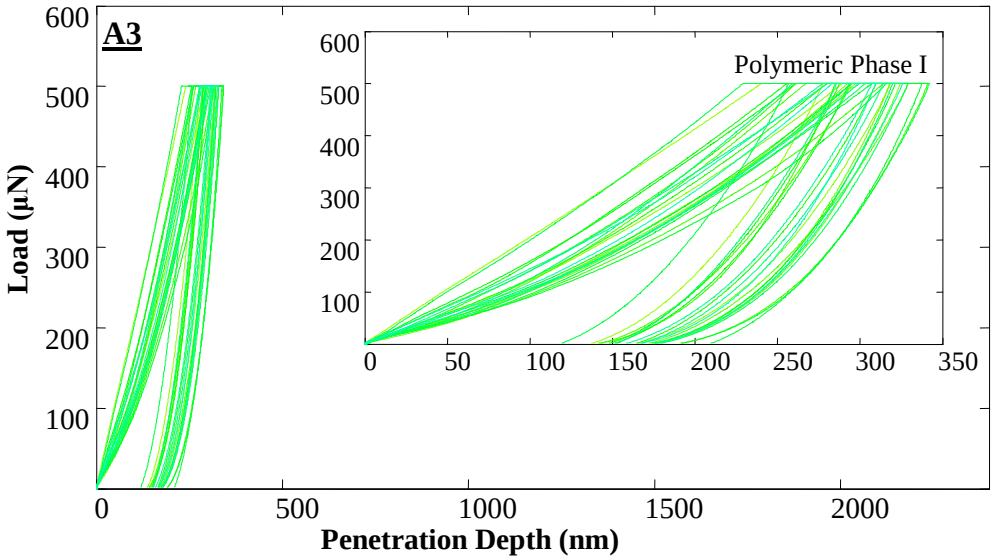

Figure 3.3.3.5. The nanoindentation curves obtained within area A3

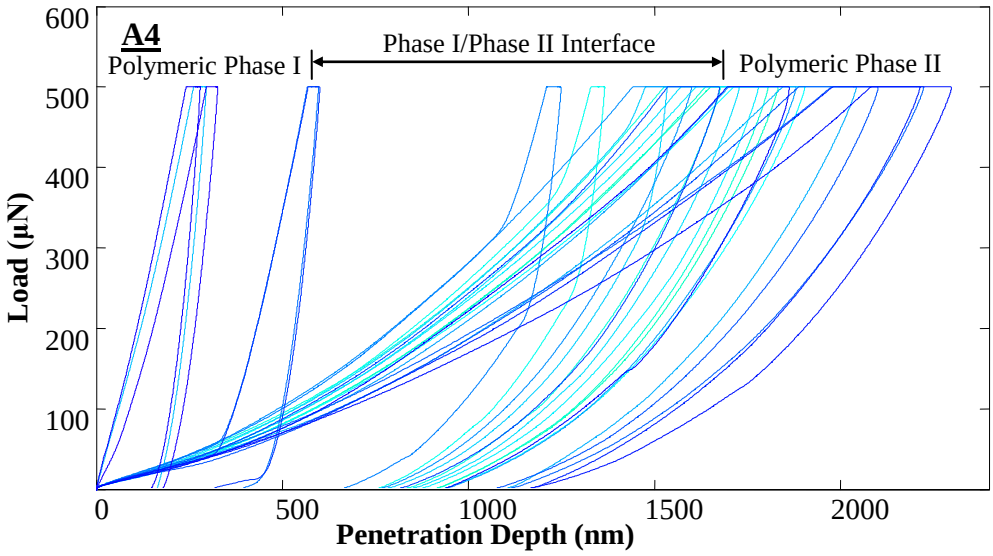

Figure 3.3.3.6. The nanoindentation curves obtained within area A4

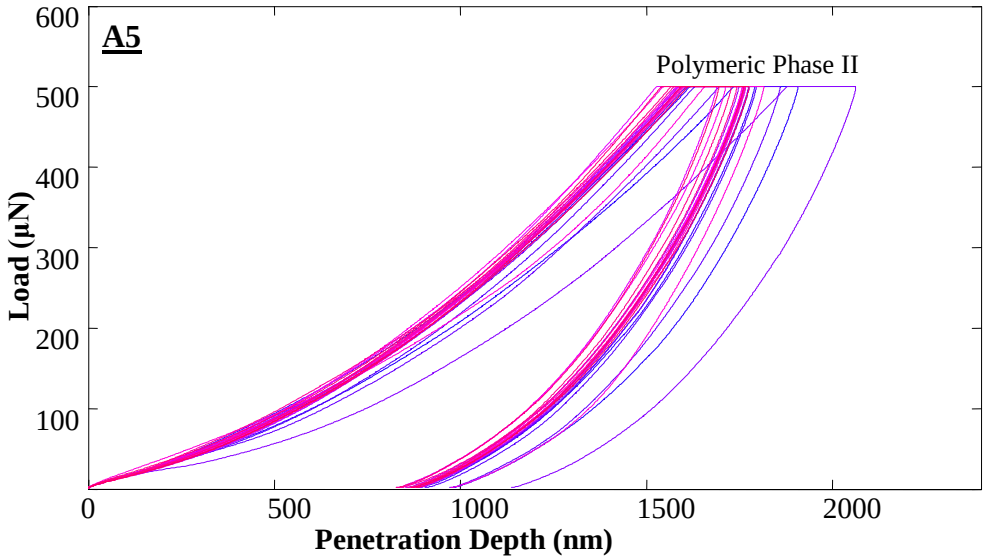

Figure 3.3.3.7. The nanoindentation curves obtained within area A5

The relationships between stress-strain curves, load-indentation depth (or penetration depth) curves, and the residual impressions of indentation for typical a) ideally elastic, b) rigid perfect-plastic, and c) elasto-plastic materials are schematically shown in Figure 3.3.3.8 [81]. For an ideally-elastic solid, the sample surface deforms elastically during the loading-and-unloading process. Upon the load removal, the impressions made by the indenter tip fully recover leaving no traceable residual impression on the sample surface, see Figure 3.3.3.8 (a). A rigid-perfectly plastic solid, on the other hand, deform permanently once the yield stress is reached. No recovery takes place upon unloading, leaving the impressions unchanged and are identical to the shape of the indenter tip, see Figure 3.3.3.8 (b). In the case of an elasto-plastic solid, the indentation deformation has both elastic and plastic components, as shown in Figure 3.3.3.8 (c). The elastic deformation recovers during the unloading process, however, the

plastic component of deformation is permanent, leaving a partially recovered impression mark as shown in Figure 3.3.3.8 (c). In addition, for the materials that exhibit time-dependent behavior in addition to the elastic and plastic material response (e.g. polymers, elastomers, or bitumen), the indentation curves would exhibit viscoelastic or viscoplastic characteristic, such as the creep plateau as shown in Figure 3.3.2.1 created by the load holding regime as the one shown in Figure 3.3.3.3 [82].

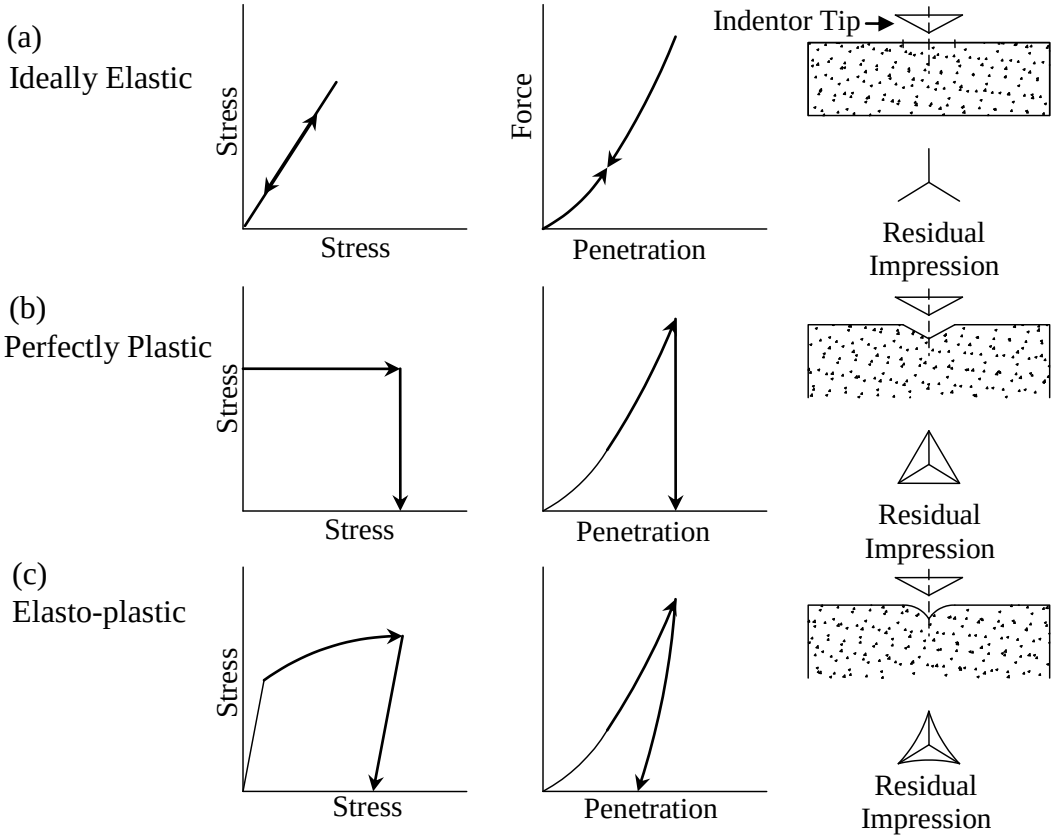

Figure 3.3.3.8. Schematics showing the relationship between stress-strain relations, typical indentation curves, and residual impressions of the indentation for (a) perfectly elastic; (b) rigid, perfectly plastic; and (c) elasto-plastic solids

The representative nanoindentation curves for each of the three primary constituent phases that compose the CHMC are presented in Figure 3.3.3.9 (a), and the displacement time-history responses of carbon fiber, the epoxy-based polymeric phase I, and the elastomeric phase II, together with the load time history schemes used for each test were presented in Figure 3.3.3.9 (b), (c), and (d), respectively. The solid black curve in Figure 3.3.3.9 (a) indicates high stiffness (elastic modulus) of carbon fiber and very little plastic deformation during loading and unloading, i.e. the loading the unloading curves nearly overlapped showing almost ideally elastic behavior; the epoxy-based matrix phase I, which is shown as the solid blue curve in Figure 3.3.3.9 (a), exhibits mediate level of plastic deformation as signified by the residual deformation; and the polymeric phase II shows much greater level of plastic/ viscoplastic deformation than both carbon fiber and epoxy. As far as the time-dependent properties of the three constituents are concerned, the deformation caused by material creep during the five-second load holding is signified by the plateau encountered at maximum load. Carbon fiber shows almost no viscous component in its deformation diagram, see Figure 3.3.3.9 (a). This is also substantiated by the deformation time-history response presented in Figure 3.3.3.9 (b). And the two polymeric phases both exhibit a level of viscoelastic/ or viscoplastic behavior, see Figure 3.3.3.9 (c) and (d). The areas encompassed by the hysteresis loops represent the amount of energy dissipated via both viscous damping and plastic deformation during each loading-unloading cycle, which clearly indicate the superior hysteric damping of the elastomeric phase II. The viscoelastic/ viscoplastic properties of the constituent materials are important for identify damping of the composites, which would be discussed later in Chapter 4, since the hysteric damping of

the constituents is an important damping source in engineering composites. This will be later evidenced by the dependency of the damping coefficient of CHMC laminate to the thickness of elastomeric phase II, or h_p. It should also be noted that if the unloading rate is very slow, the viscoelastic properties of the materials would have large influence on the unloading contact stiffness, and deviate the modulus estimated by the Oliver and Pharr method from the actual values [83]. The loading and unloading rates used in this study are considered to be within the "reasonable" range to produce accurate modulus readings for the polymeric materials [83].

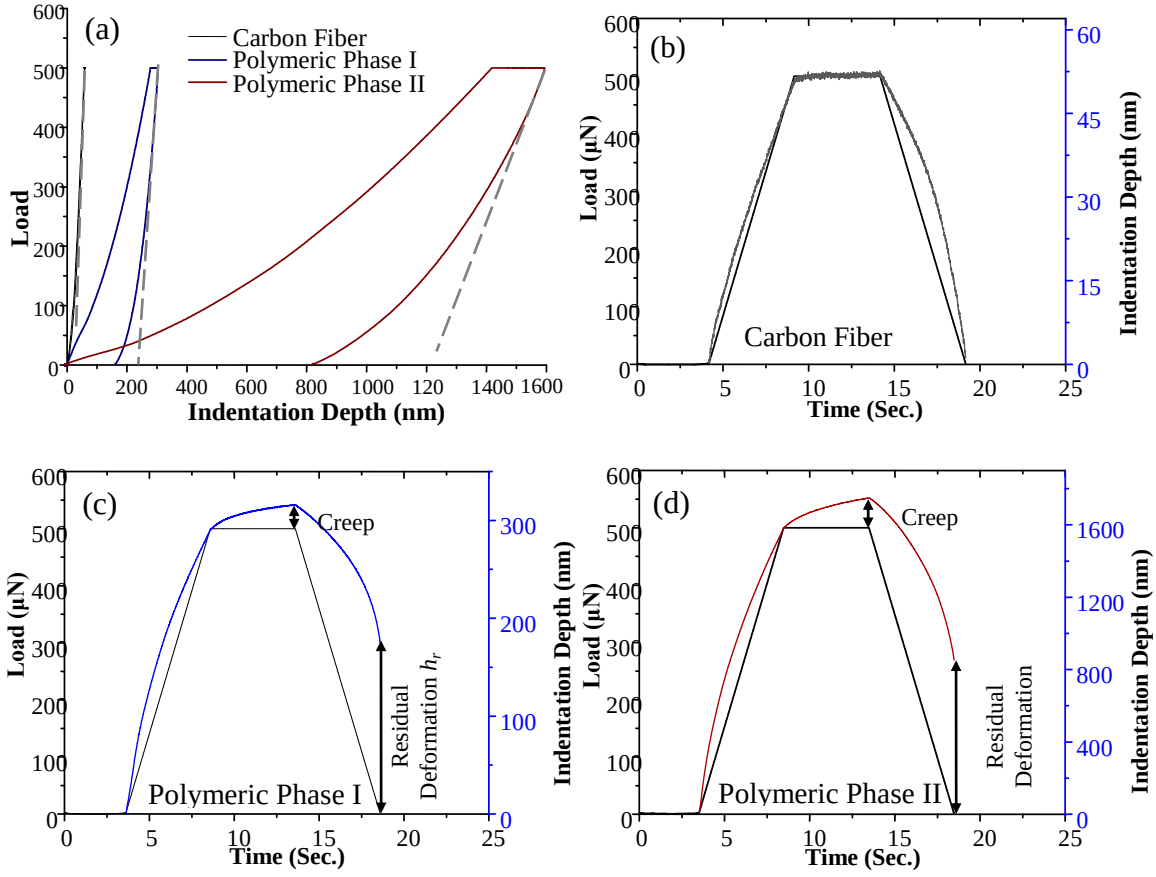

Figure 3.3.3.9. (a) Typical indentation curves for the three primary phases in CHMC; and the load and deformation time-histories of (b) carbon fiber; (c) polymeric phase I; and (d) polymeric phase II

The reduced modulus of the three primary constituents and their interfaces, that was calculated based on equation (3.3.2.6) and the unloading contact stiffness of the nanoindentation curves, is summarized in Table 3.3.3.1 and Figure 3.3.3.10 (a); and the nano-hardness obtained by using equation (3.3.2.7) is summarized in Table 3.3.3.2 and Figure 3.3.3.10 (b). The elastic modulus of the three primary phases span three orders of magnitude with the average reduced modulus of carbon fiber to be 55.15 GPa, 4.39 GPa for the polymeric phase I, and 0.13 GPa for the elastomeric phase II. The data for the interface region exhibits a large extent of scatterness, possibly because of the "unstable" testing within these regions as had been previously discussed.

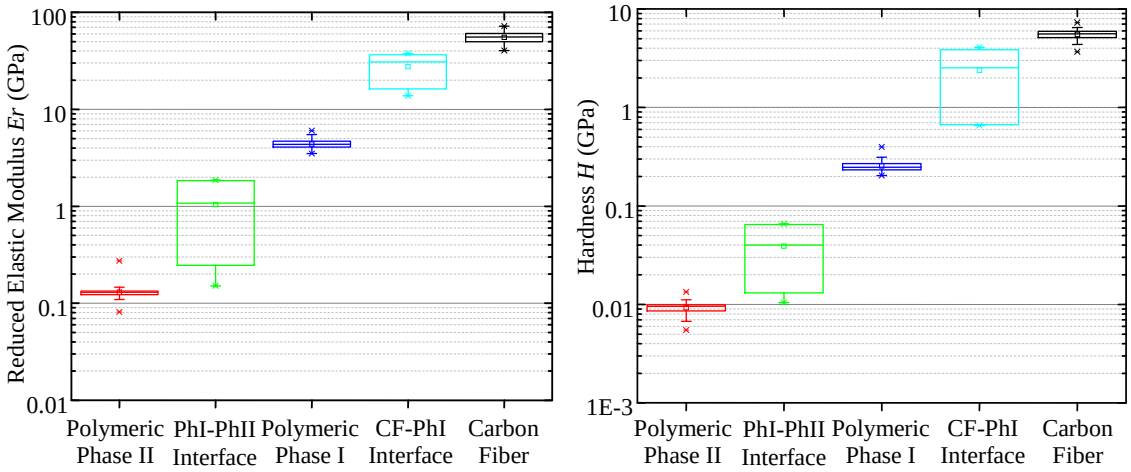

Figure 3.3.3.10. The box charts showing the (a) reduced modulus E_r, and (b) nano-hardness H of the material phases within CHMC

Table 3.3.3.1.

The nanoindentation results of the constituents of CHMC - Reduced Modulus E_r (GPa)

	# of indents	Mean	Std. Dev.	Var.	Min	Max
Polymer Phase II	41	0.130	0.0304	9.24E-4	0.0812	0.2737
Pha. I-Pha. II Interface	4	1.041	0.9225	0.851	0.1511	1.8601
Polymeric Phase I	47	4.385	0.4945	0.244	3.5066	6.0390
Fiber-Phase I Interface	6	27.621	10.691	114.3	13.778	37.711
Carbon Fiber	18	55.153	8.1182	65.90	40.332	71.850

Table 3.3.3.2.

The nanoindentation results of the constituents of CHMC - Hardness H (GPa)

	# of indents	Mean	Std. Dev.	Var.	Min	Max
Polymer Phase II	41	0.0093	0.0015	2.34E-6	0.0055	0.0134
Pha. I-Pha. II Interface	4	0.0390	0.0299	8.96E-4	0.0104	0.0655
Polymeric Phase I	47	0.2547	0.0359	0.00129	0.2032	0.3968
Fiber-Phase I Interface	6	2.3833	1.6692	2.786	0.6534	4.0719
Carbon Fiber	18	5.5285	0.8409	0.707	3.6774	7.2952

The stiffness profile in the cross-ply direction of the CHMC laminate is plotted in Figure 3.3.3.11, where the stiffness transition from the center of the laminate (reinforcing fibers) to edge (polymeric phase II) can be clearly seen from the plot. Knowing the distribution of the elastic modulus cross the laminate, now it is possible to utilize the micromechanical equations developed in Section 3.3.1 to predict the laminate stiffness.

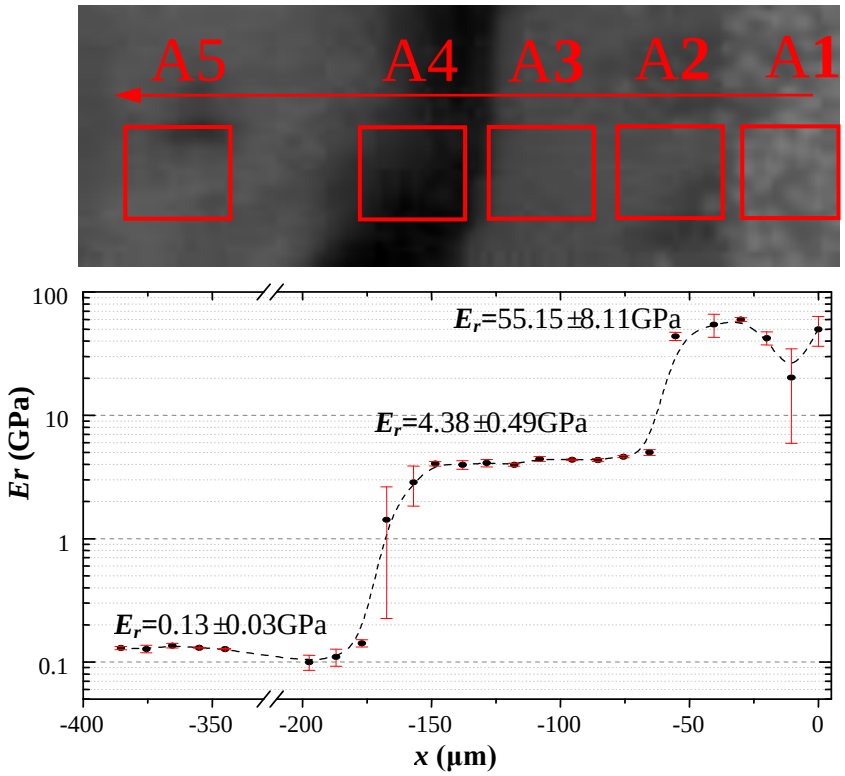

Figure 3.3.3.11. The modulus profile of the CHMC laminate

3.4. Summary and Conclusion

This chapter discusses the design philosophy, cross-poly morphology, microstructures, and micromechanical properties of the carbon-fiber reinforced hybrid-polymeric matrix (CHMC) composite. The scanning electron microscopy (SEM) images showing the microstructures of the CHMC are presented. The multilayered cross-ply texture proposed in the beginning of this chapter was evidenced by the SEM images. The mechanisms by which CHMC is able to better sustain damage than conventional carbon fiber reinforced epoxies was revealed by performing the fractography studies on the fractured composite tensile coupons. And lastly, the micromechanical formulas to

predict laminate stiffness was proposed and the micromechanical properties of all constituents were studied using the nanoindentation technique. The nanoindentaiton results were presented and discussed, and the cross-ply modulus profile of the CHMC laminate was obtained.

Chapter 4.

MECHANICAL PERFORMANCE OF CARBON-FIBER REINFORCED HYBRID POLYMERIC-MATRIX COMPOSITE AT MACROSCALE - DAMPING

The dynamic properties and energy dissipation capabilities of carbon fiber reinforced epoxy (CF/ epoxy) and the CHMC, at the macro-scale level, were investigated by free and forced frequency vibration tests. The experimental results are presented in this chapter. The mechanisms by which the CHMC is able to possess significantly higher damping than CF/ epoxy and how the material processing parameters - h_p and t_c - have impact the material damping are discussed from micro-scale perspectives.

4.1. Introduction

Damping is an important property that influences the dynamic behavior of fiber-reinforced composite structures including the minimization of resonance and the suppressing of near-resonant vibrations. Damping mechanisms in composite materials differ from those observed in conventional structural materials such as metals and alloys. At the constituent level, the energy dissipation in fibrous composites is induced by 1) the viscoelastic/ viscoplastic nature of fiber and matrix materials; 2) the interaction between different materials phases, e.g., friction between the fiber and matrix; and 3) the damping due to damage if exist [78]. At the laminate level, the damping of fibrous composites depends not only on the constituent lamina (or ply) properties, but also on the ply orientations and inter-laminar effects [84].

The early experimental studies on the damping properties of fiber-reinforced composite include the work by Adams and his colleagues [64;65]. Beams were excited by a coil/ electromagnet driver transducer, where the coil was mounted at the mid-span point of the beam. The input signal was tuned to the fundamental natural frequency of the beam, and the damping was evaluated over a frequency range of 100-800Hz. Gibson and Plunkett [66], Suarez et al. [67;85], and Crane and Gillespie [86] developed the impulse method to test the damping of composite materials, where the impulsive excitation was induced to the flat cantilever beam specimens using an electromagnetic hammer. The transverse displacement of the beam was measured as a function of time using a non-contact eddy current probe positioned near the tip of the beam. The frequency response function was obtained by performing the Fourier transform of the measured data; and curve fitting to the Fourier transform was used to obtain a loss factor and the complex modulus. Hadi and Ashton [87] evaluated the damping of glass fiber reinforced epoxies from the logarithmic decrement of the free vibration of cantilever beams. More recently, the damping of more advanced composite materials, such as the carbon nanotube composites [88;89] was evaluated using free and forced vibration tests. In this chapter the dynamic properties of the newly developed CHMC and conventional carbon fiber reinforced epoxies that were obtained using both free vibration and forced vibration tests are presented and discussed. The "stand-alone" CHMC laminates, as introduced in Chapter 3, were tested using self-supported beams; and the laminates, which constituted the retrofitting system, were tested using the Oberst beam method and the modified Oberst beam method.

4.2. Identification of the Energy Dissipation Capacity of CHMC via Beam Vibration Tests

4.2.1.Vibration of Continous Beams - Fundamentals of the Dynamic Mechanical Analysis

Equation of Motion (EOM)

A thin continuous beam subjected to a transverse force is shown in Figure 4.2.1.1. The general equation of motion of a un-damped beam in transverse vibration may be written in the form of equation (4.2.1.1) as [90]

$$\rho A(x)\frac{\partial^2 w}{\partial t^2}(x,t) = -\frac{\partial^2 M}{\partial x^2}(x,t) + f(x,t) \qquad (4.2.1.1)$$

where ρ is the mass density of the material; $A(x)$ is the cross section area of the beam, as a function of x; $w(x,t)$ is the transverse deflection of the beam as a function of the location x along the beam, and time t; $M(x,t)$ is the bending moment as shown in Figure 4.2.1.1; and $f(x,t)$ is the external excitation force.

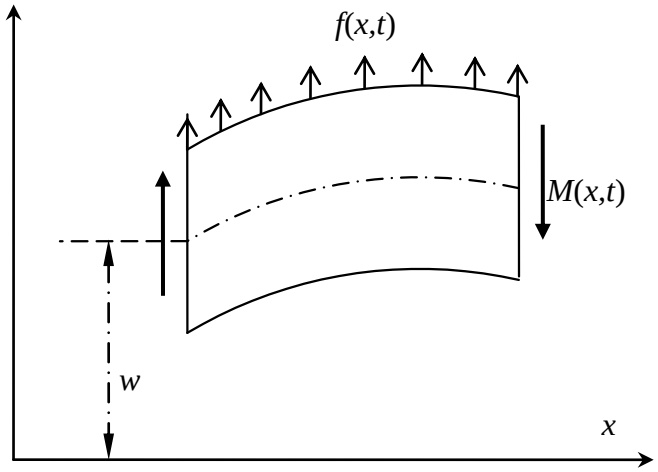

Figure 4.2.1.1. Free body diagram of a continuous beam subject to transverse loading

For the Euler-Bernoulli beam theory, the relationship between the bending moment M and the deflection w can be expressed as

$$M(x,t) = EI(x)\frac{\partial^2 w}{\partial x^2}(x,t) \tag{4.2.1.2}$$

where E is the Young's Modulus of the beam material, and $I(x)$ is the moment of inertia of the beam as a function of x, see Figure 4.2.1.1.

Substituting equation (4.2.1.2) into equation (4.2.1.1) yields

$$\frac{\partial^2}{\partial x^2}\left[EI(x)\frac{\partial^2 w}{\partial x^2}(x,t) \right] + \rho A(x)\frac{\partial^2 w}{\partial t^2}(x,t) = f(x,t) \tag{4.2.1.3}.$$

In the case of a uniform beam with a clamped-clamped boundary condition (which was used in the experiments), where the moment of inertia I and the cross-section area A remain constant and are independent of x, the following common equation may be obtained

$$EI\frac{\partial^4 w}{\partial x^4}(x,t) + \rho A\frac{\partial^2 w}{\partial t^2}(x,t) = f(x,t) \tag{4.2.1.4}$$

or

$$c^2\frac{\partial^4 w}{\partial x^4}(x,t) + \frac{\partial^2 w}{\partial t^2}(x,t) = \frac{1}{\rho A} f(x,t) \tag{4.2.1.5}$$

where

$$c = \sqrt{\frac{EI}{\rho A}} \tag{4.2.1.6}$$

having boundary condition of

$$w(0)=0,\ \frac{\partial w}{\partial x}(0)=0$$
$$w(L)=0,\ \frac{\partial w}{\partial x}(L)=0 \qquad (4.2.1.7)$$

Free Vibration of Thin Beams Clamped (Fixed)at Both Ends

In the case of free vibration, the equation of motion of a beam (4.2.1.5) is written as

$$c^2\frac{\partial^4 w}{\partial x^4}(x,t)+\frac{\partial^2 w}{\partial t^2}(x,t)=0 \qquad (4.2.1.8)$$

The solution of equation (4.2.1.8) can be found using the method of variables by assuming

$$w(x,t)=W(x)T(t) \qquad (4.2.1.9)$$

Substituting equation (4.2.1.9) into (4.2.1.8) yields

$$\frac{c^2}{W(x)}\frac{\partial^4 W(x)}{\partial x^4}+\frac{1}{T(t)}\frac{\partial^2 T(t)}{\partial t^2}=0 \qquad (4.2.1.10)$$

In order for equation (4.2.1.10) to hold true for any *x* and *t*, the two terms in equation (4.2.1.10) remain constant, with opposing signs. Thus, equation (4.2.1.10) can be rewritten into two equations. Rearranging terms

$$\frac{\partial^4 W(x)}{\partial x^4}-\frac{k}{c^2}W(x)=0 \qquad (4.2.1.11)$$

$$\frac{\partial^2 T(t)}{\partial t^2}+kT(t)=0 \qquad (4.2.1.12)$$

The solution of equation (4.2.1.12) is

$$T(t) = A\cos\left(\sqrt{k}t\right) + B\sin\left(\sqrt{k}t\right) \tag{4.2.1.13}$$

where A and B are constants that depend on the initial condition. Setting $k=\omega^2$ yields

$$T(t) = A\cos\left(\omega t\right) + B\sin\left(\omega t\right) \tag{4.2.1.14}$$

The solution of equation (4.2.1.11) can be obtained by assuming $W(x)$ has an exponential function form as

$$W(x) = Ce^{sx} \tag{4.2.1.15}$$

where C and s are constants. Substitute equation (4.2.1.15) into (4.2.1.11) and recall $k=\omega^2$, we have

$$s^4 Ce^{sx} - \frac{\omega^2}{c^2} Ce^{sx} = 0 \tag{4.2.1.16}$$

Thus, the four roots of equation (4.2.1.16) are given as

$$s_1 = \sqrt{\frac{\omega}{c}},\ s_2 = -\sqrt{\frac{\omega}{c}},\ s_3 = i\sqrt{\frac{\omega}{c}},\ s_4 = -i\sqrt{\frac{\omega}{c}} \tag{4.2.1.17}$$

And the solution of equation (4.2.1.11) becomes

$$W(x) = C_1 e^{\sqrt{\frac{\omega}{c}}x} + C_2 e^{-\sqrt{\frac{\omega}{c}}x} + C_3 e^{i\sqrt{\frac{\omega}{c}}x} + C_4 e^{-i\sqrt{\frac{\omega}{c}}x} \tag{4.2.1.18}$$

where C_1, C_2, C_3, and C_4 are constant that can be determined by the boundary conditions. Note the Euler's formula

$$e^{ix} = \cos x + i\sin x \tag{4.2.1.19}$$

equation (4.2.1.18) can be then written as

$$W(x) = C_1\cosh(\sqrt{\frac{\omega}{c}}x) + C_2\sinh(\sqrt{\frac{\omega}{c}}x) + C_3\cos(\sqrt{\frac{\omega}{c}}x) + C_4\sin(\sqrt{\frac{\omega}{c}}x) \tag{4.2.1.20}$$

The function $W(x)$ is often known as the *normal mode*, or *characteristic function*, of the beam; and ω is the *natural frequency*. If the natural frequency of the i^{th} mode is ω_i, and the corresponding normal mode is denoted as $W_i(x)$, and recall equations (4.2.1.9) and (4.2.1.14), then the total free vibration response of the beam can be expressed as

$$w(x,t)=\sum_{i=1}^{\infty}W_i(x)\left[A_i\cos\left(\omega_i t\right)+B_i\sin\left(\omega_i t\right)\right] \tag{4.2.1.21}$$

where A_i and B_i are constant that can be determined from the initial condition.

For the case of clamped-clamped beam, equation (4.2.1.20) is more conveniently rewritten as

$$\begin{aligned}W(x)=C_1\left[\cosh(\sqrt{\frac{\omega}{c}}x)+\cos(\sqrt{\frac{\omega}{c}}x)\right]+C_2\left[\cosh(\sqrt{\frac{\omega}{c}}x)-\cos(\sqrt{\frac{\omega}{c}}x)\right]\\ +C_3\left[\sinh(\sqrt{\frac{\omega}{c}}x)+\sin(\sqrt{\frac{\omega}{c}}x)\right]+C_4\left[\sinh(\sqrt{\frac{\omega}{c}}x)-\sin(\sqrt{\frac{\omega}{c}}x)\right]\end{aligned} \tag{4.2.1.21}$$

Applying the first two boundary conditions of equation (4.2.1.7), namely $W(0)=0$ and $dW(0)/dx=0$, to equation (4.2.1.21) leads to

$$C_1=C_3=0 \tag{4.2.1.22}$$

Substituting $W(L)=0$ and $dW(L)/dx=0$ into equation (4.2.1.21) leads to

$$C_2\left[\cosh(\sqrt{\frac{\omega}{c}}L)-\cos(\sqrt{\frac{\omega}{c}}L)\right]+C_4\left[\sinh(\sqrt{\frac{\omega}{c}}L)-\sin(\sqrt{\frac{\omega}{c}}L)\right]=0 \tag{4.2.1.23}$$

and

$$C_2\left[\sinh(\sqrt{\frac{\omega}{c}}L)+\sin(\sqrt{\frac{\omega}{c}}L)\right]+C_4\left[\cosh(\sqrt{\frac{\omega}{c}}L)-\cos(\sqrt{\frac{\omega}{c}}L)\right]=0 \tag{4.2.1.24}$$

In order for equations (4.2.1.23) and (4.2.1.24) to have non-trivial solutions, the determinant of the coefficients of C_2 and C_4 is set equal to zero, which then yields

$$\left[\sinh^2(\sqrt{\frac{\omega}{c}}L)-\sin^2(\sqrt{\frac{\omega}{c}}L)\right]+\left[\cosh(\sqrt{\frac{\omega}{c}}L)-\cos(\sqrt{\frac{\omega}{c}}L)\right]^2=0 \qquad (4.2.1.25)$$

Or

$$\cos(\sqrt{\frac{\omega}{c}}L)\cosh(\sqrt{\frac{\omega}{c}}L)=1 \qquad (4.2.1.26)$$

where c is constant expressed as equation (4.2.1.6). The i^{th} root of equation (4.2.1.26) gives the natural angular frequencies of the i^{th} mode of vibration. The equation (4.2.1.26) is also called the *frequency equation*. The mode shapes of a continuous beam that is clamped (fixed) at both ends are plotted in Figure 4.2.1.2 for the first three vibration modes.

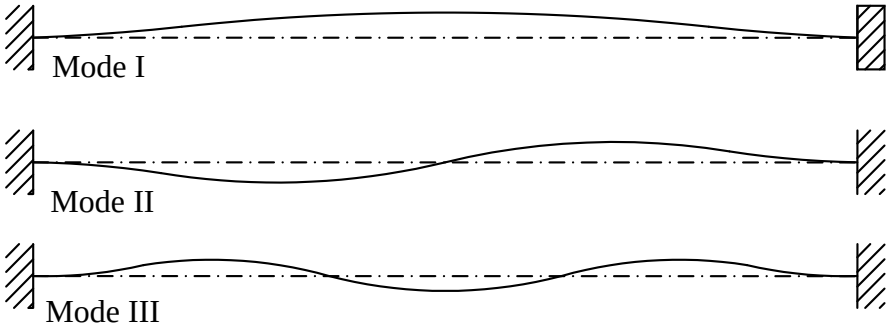

Figure 4.2.1.2. The first three mode shapes of the fixed-fixed beam in transverse vibration

Forced Vibration

The equation of motion of a beam subjected to a distributed transverse force is given by equation (4.2.1.3) and equations (4.2.1.4) for a uniform beam. Similar to

equation (4.2.1.8) for the free vibration case, if we write the solution of equation (4.2.1.4) as a linear combination of the normal modes of the beam

$$w(x,t)=\sum_{i=1}^{\infty}W_i(x)\eta_i(t) \tag{4.2.1.27}$$

where $W_i(t)$ are the normal modes obtained by solving equation (4.2.1.21) together with the four boundary conditions; and $\eta_i(t)$ are the modal participation coefficients that may be obtained by substituting (4.2.1.27) into equation (4.2.1.4), which yields

$$EI\sum_{i=1}^{\infty}\frac{d^4W_i(x)}{dx^4}\eta_i(t)+\rho A\sum_{i=1}^{\infty}\frac{d^2\eta_i(t)}{dt^2}W_i(x)=f(x,t) \tag{4.2.1.28}$$

Recall equation (4.2.1.6) and (4.2.1.11), and $k=\omega^2$

$$\frac{\partial^4W(x)}{\partial x^4}=\frac{\omega^2\rho A}{EI}W(x) \tag{4.2.1.29}$$

Substituting equation (4.2.1.29) into (4.2.1.28) yields

$$\rho A\sum_{i=1}^{\infty}\omega_i^2W_i(x)\eta_i(t)+\rho A\sum_{i=1}^{\infty}\frac{d^2\eta_i(t)}{dt^2}W_i(x)=f(x,t) \tag{4.2.1.30}$$

where ω_i is the natural frequency of the i^{th} vibration mode. Multiplying every term in equation (4.2.1.30) by $\int_0^L W_i(x)dx$, and recalling the orthogonality condition for normal modes, where

$$\begin{aligned}&W_i(x)W_j(x)=0,\ \text{for } i\neq j\\&W_i(x)W_j(x)=1,\ \text{for } i=j\end{aligned} \tag{4.2.1.31}$$

Equation (4.2.1.30) then becomes

$$\frac{d^2\eta_i(t)}{dt^2}+\omega_i^2\eta_i(t)=\frac{1}{\rho A}\int_0^L f(x,t)W_i(x)dx \tag{4.2.1.32}$$

If we set

$$q_i(t) = \frac{1}{\rho A}\int_0^L f(x,t)W_i(x)dx \qquad (4.2.1.33)$$

then the complete solution of equation (4.2.1.32) contains a complementary component obtained by solving the homogeneous equation (4.2.1.12) and a particular component, and it may be expressed as

$$\eta_i(t) = \left(A_i \cos\omega_i t + B_i \sin\omega_i t\right) + \frac{1}{\omega_i}\int_0^t q(\tau)\sin\omega_i\left(t-\tau\right)d\tau \qquad (4.2.1.34)$$

where A_i and B_i are constants that can be obtained from the initial condition.

Consideration of Damping

Unlike the simple single or multiple degree(s) of freedom (SDOF or MDOF) systems with a finite lumped mass, the modeling of damping in a continuous damped system has been challenging. The actual energy dissipation mechanisms of a fibrous composite, which will be discussed in greater details later, may be induced by various sources such as the viscous nature of the constituent materials (such as matrix and fiber), damages occuring at the micro-scale level, the interaction between matrix and fiber (often in the form of friction), and also the interaction between the matrix phases in the case of the CHMC and some other toughened composites. Regardless of the complicated actual damping mechanism, there are two commonly used approaches for including damping in continuous vibrating systems: one is to replace the damping forces of a complicated nature using mathematically simplified equivalent viscous damping. In the case of a uniform viscously damped beam, the governing equation of motion may be written as

$$EI\frac{\partial^4 w}{\partial x^4}(x,t)+\rho A\frac{\partial^2 w}{\partial t^2}(x,t)+c_s A\frac{\partial w}{\partial t}(x,t)=f(x,t) \qquad (4.2.1.35)$$

where c_s is the coefficient of viscous damping by unit volume. Equation (4.2.1.35) can be expressed in a more concise format using the previous notation as

$$c^2\frac{\partial^4 w}{\partial x^4}(x,t)+\frac{\partial^2 w}{\partial t^2}(x,t)+\frac{c_s}{\rho}\frac{\partial w}{\partial t}(x,t)=f(x,t) \qquad (4.2.1.36)$$

where ρ is the mass density of the material; . Similar to the solution of equation (4.2.1.5), if the total deflection response is, again, assumed to be a combination of the normal modes as in equation (4.2.1.27), the equation of motion for the damped beam may then be similarly expressed in normal co-coordinates as [84]

$$\frac{d^2\eta_i(t)}{dt^2}+2\xi_i\omega_i\frac{d\eta_i(t)}{dt}+\omega_i^2\eta_i(t)=q_i(x) \qquad (4.2.1.37)$$

for the i^{th} mode of vibration, where ξ_i is the modal damping coefficient, which is defined by equation (4.2.1.38) as

$$2\xi_i\omega_i=\frac{c_s}{\rho} \qquad (4.2.1.38)$$

In addition to including the viscous damping term in the equation of motion and since the viscoelastic material both store and dissipate energy during vibration in the elasticstate, an alternative approach to modeling damping is to express the elastic moduli of materials as complex quantities

$$E_\omega^*=E_\omega^{'}\left(1+i\eta_\omega\right) \qquad (4.2.1.39)$$

where E^*_ω is the complex Young's modulus of the beam material at frequency ω; η_ω is the loss factor associated to the dynamic Young's modulus (or storage moduli) E'_ω at frequency ω. Recall the frequency equation (4.2.1.6) of an un-damped beam fixed at both ends, the solution of equation (4.2.1.6) can be approximated by equation (4.2.1.40) with relatively decent accuracy as

$$\omega_n = 2\pi f_n = \frac{1}{\zeta_n^2}\sqrt{\frac{EI}{\rho A L^4}} \tag{4.2.1.40}$$

where

$$\zeta_n = (2n+1)\pi/2 \tag{4.2.1.41}$$

Thus, the storage modulus can be expressed as a function of the natural frequency of mode *i* as

$$E'_\omega = \left(\frac{2\pi f_n L^2}{\zeta_n^2}\right)^2 \frac{\rho A}{I} \tag{4.2.1.42}$$

where f_n is the resonant (natural) frequency of mode *i* for the vibrating beam, expressed in Hz. Since damping is assumed to have only a minimal influence on the natural frequencies (for damping <0.2), equation (4.2.1.42), which is derived based on the un-damped system, can be used here to estimate the storage elastic moduli for lightly damped systems. And the loss moduli, which indicate the ability of an elastic vibrating system to dissipate energy, can then be expressed in terms of the storage moduli and loss factor for lightly damped beams as

$$E''_\omega = E'_\omega \tan\eta_i = 2E'_\omega \xi_i \tag{4.2.1.43}$$

where η_i and ξ_i are the loss factor and damping coefficient of mode *i*, respectively.

Experimental Determination of the Damping Parameters

The experimental measurements of the modal damping coefficient, ξ_i, or loss factor, η_i, can be carried out via both free vibration and forced vibration tests. In the case of free vibration, if a clearly distinguishable first-mode vibration response can be determined, as shown in Figure 4.2.1.3, the damping coefficient of the system can be determined by the logarithm decrement method as expressed by equation (4.2.1.44) as

$$\xi = \left[\frac{1}{\omega_n (n-1) T_d} \right] \ln \frac{x_1}{x_n} \tag{4.2.1.44}$$

where x_1 are x_n are the amplitudes of the first and n^{th} vibration cycles that are used for the logarithm decrement calculation; ω_n is the natural angular frequency of the system, expressed in rad/ sec; and T_d is the period of vibration of the first cycle of the damped response.

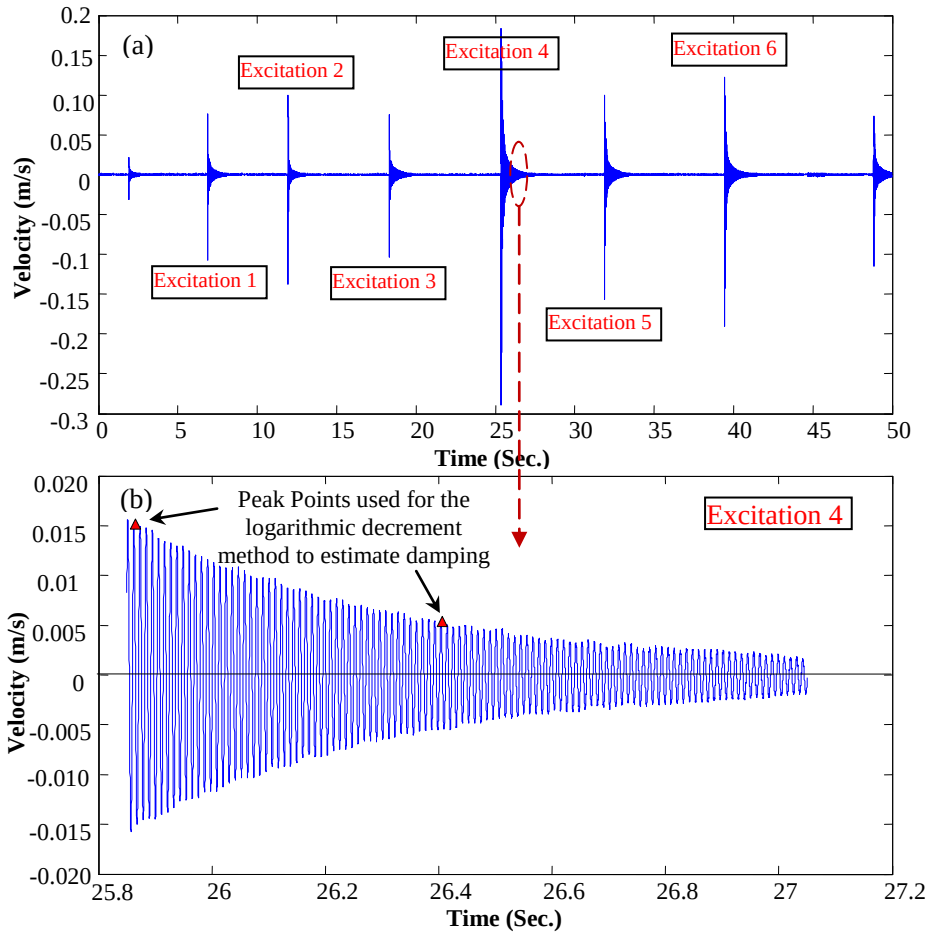

Figure 4.2.1.3. Example of the time history velocity response of a test beam in free vibration condition obtained by the laser vibrometer (thick steel beam)

However, for a beam composed of a fibrous composite, if the material principal axes, i.e., the directions of reinforcing fibers and in the transverse direction, do not coincide with the geometrical axes of the beam, or if the laminate is not symmetric with respect to its own mid-plane, the first mode vibration will be coupled with the higher modes of vibration such as the in-plane and interlamina shear and torsion modes, as shown in Figure 4.2.1.4 (a), thus making ascertaining of the peak response very difficult, if even possible. In such a case, a "half-power bandwidth" method that utilizes the

response data transformed to the frequency domain, as expressed by equation (4.2.1.45) and schematically shown in Figure 4.2.1.4 (b), is more suitable for determining the modal damping coefficient.

$$\xi = \frac{\Delta f}{2 f_n} \tag{4.2.1.45}$$

where f_n is the resonance frequency in Hz; and $\Delta f = f_2 - f_1$ is the frequency difference between the half-power points, as presented in Figure 4.2.1.4.

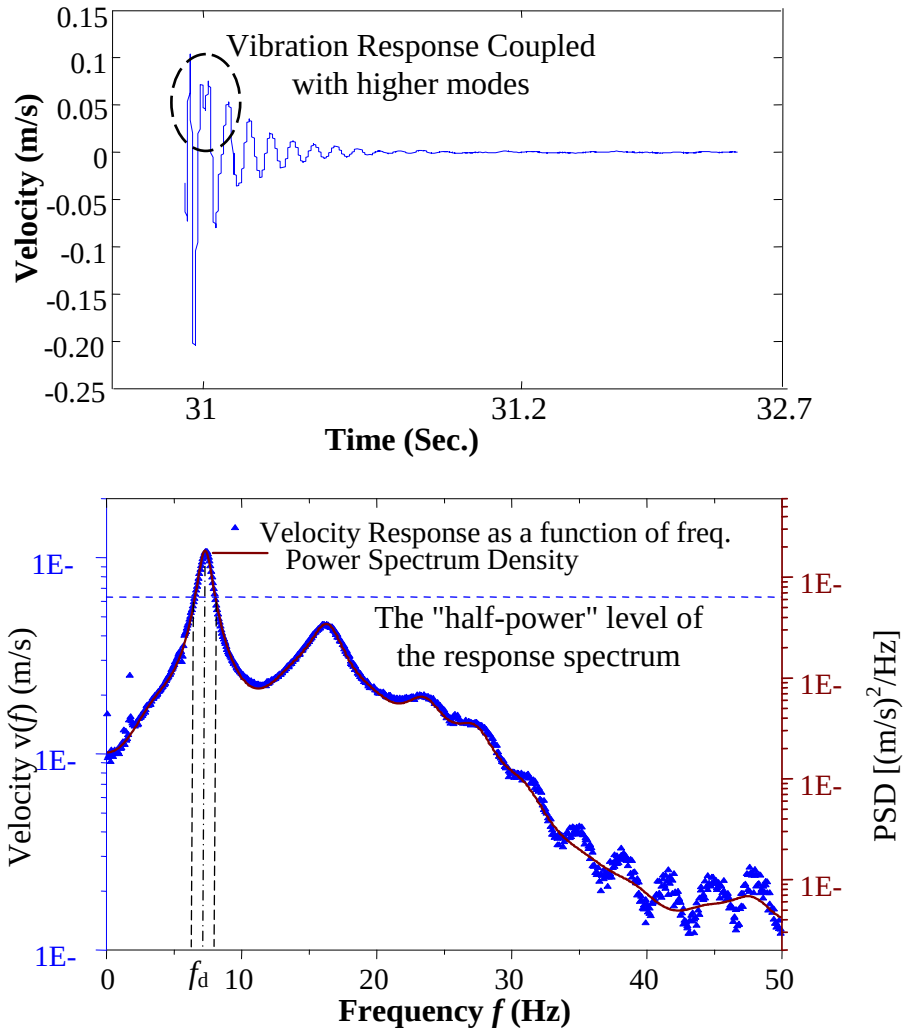

Figure 4.2.1.4. Example of the response (velocity) spectrum (obtained by FFT) and the power spectral density (PSD) obtained using the Auto-Regression (AR) process and the damping ratio estimated using the "half-power bandwidth" method

The damping properties of a system are also tested using the forced vibration, where a limited bandwidth white noise excitation signal within a certain frequency range is input into the system. The corresponding response is recorded by a laser vibrometer or using accelerometers, see Figures 4.2.1.5 (a) and (b). The recorded time-history

responses were then converted to frequency responses via Fast Fourier Transform (FFT), see Figures 4.2.1.5 (c) and (d).

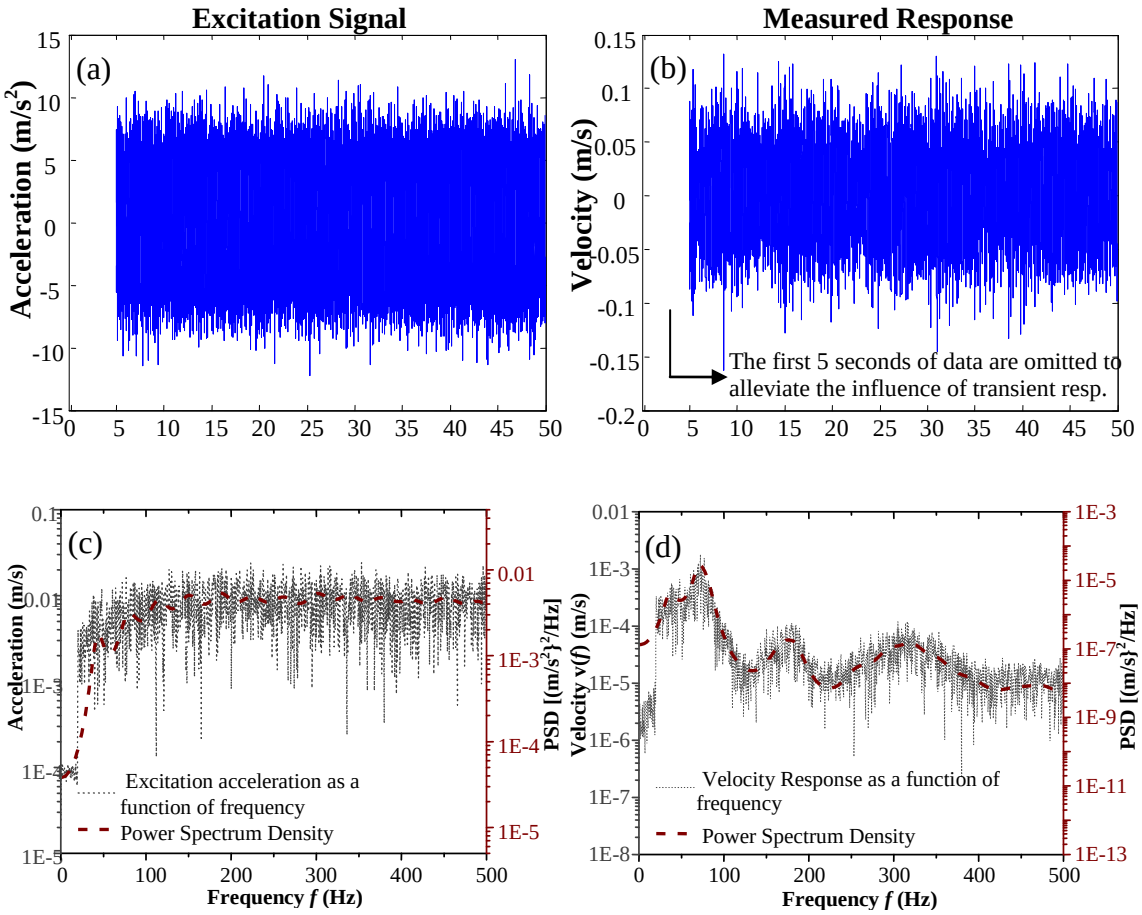

Figure 4.2.1.5. The forced vibration excitation signal and responses: (a) excitation acceleration (time-history); (b) response velocity (time-history); (c) excitation acceleration (PSD); (d) response velocity (PSD)

The power spectral density (PSD) of a random signal gives the power carried by the signal per unit frequency. The term "power" of a signal here does not necessarily refer to the actual physical power, but in a more general and convenient sense, it can be defined as the squared value of the signal. In this sense, the power P of a signal $w(t)$, i.e.

vibration responses (acceleration or velocity) in the current case, is defined as the following time average

$$P = \lim_{T\to\infty} \frac{1}{2T} \int_{-T}^{T} w(t)^2 dt \tag{4.2.1.46}$$

To analyze the frequency content of $w(t)$, one can perform the truncated Fourier transformation on the signal, where the signal is integrated over a finite time interval [0, T]

$$\overline{w}(\omega) = \frac{1}{\sqrt{T}} \int_0^T w(t) e^{-i\omega t} dt \tag{4.2.1.47}$$

Then the power spectral density (PSD) is defined as

$$S_{ww}(\omega) = \lim_{T\to\infty} \mathbf{E}\left[\left| \overline{w}(\omega) \right|^2 \right] \tag{4.2.1.48}$$

where $\mathbf{E}(\bullet)$ denotes the expected value. Substitute equation (4.2.1.47) into (4.2.1.48), one may have

$$S_{ww}(\omega) = \lim_{T\to\infty} \frac{1}{T} \int_0^T \int_0^T \mathbf{E}\left[w^*(t) w(t+\tau) \right] e^{-i\omega\tau} dt d(t+\tau) \tag{4.2.1.49}$$

Thus for a stationary random process, the power spectral density $S_{ww}(\omega)$ and the autocorrelation of the signal are a Fourier transformation pair. Explicitly, we have

$$S_{ww}(\omega) = \lim_{T\to\infty} \int_0^T R_{ww}(\tau) e^{-i\omega\tau} d\tau \tag{4.2.1.50}$$

where $R_{ww}(\tau)$ is the autocorrelation function of the signal $w(t)$

$$R_{ww}(\tau) = \mathbf{E}\left[w^*(t) w(t+\tau) \right] \tag{4.2.1.51}$$

For the random vibration response signals collected by the laser vibrometer or accelerometers (as shown in Figure 4.2.1.5), the power spectral density (PSD) of the signal is estimated using the Yule-Walker autoregression (AR) method, which is briefly summarized here for the sake of clarity.

In an AR model of a time series, the current value of the series, $w(n)$, is expressed as a linear function of the previous values plus an error term

$$w(n) = -\sum_{k=1}^{p} a(k)w(n-k) + e(n) \tag{4.2.1.52}$$

where p is the order of the model. Rearranging the terms in equation (4.2.1.52), the error term may be expressed as

$$e(n) = w(n) + \sum_{k=1}^{p} a(k)w(n-k) \tag{4.2.1.53}$$

The measure of the total error over all samples may then be given by the mean squared error defined as

$$Err = \frac{1}{N}\sum_{n=1}^{N} e^2(n) = \frac{1}{N}\sum_{n=1}^{N}\left[w(n) + \sum_{k=1}^{p} a(k)w(n-k) \right]^2 \tag{4.2.1.54}$$

The optimal value of each parameter in equation (4.2.1.52) is obtained by setting the partial derivative of equation (4.2.1.54) with respect to the model parameter to zero, which subsequently yields

$$\frac{\partial Err}{\partial a(k)} = \frac{1}{N}\sum_{n=1}^{N}\left[w(n) + \sum_{k=1}^{p} a(k)w(n-k) \right] w(n-k) = 0 \tag{4.2.1.55}$$

Rearranging terms in equation (4.2.1.55) yields

$$\frac{1}{N}\sum_{n=1}^{N}\left[\sum_{k=1}^{p}a(k)w(n-k)\right]w(n-k)=-\frac{1}{N}\sum_{n=1}^{N}w(n)\,w(n-k) \quad (4.2.1.56)$$

Note that the autocorrelation function of discrete data series may be expressed as

$$R_{ww}(-j)=R_{ww}(j)=\lim_{N\to\infty}\frac{1}{N}\sum_{n=1}^{N}w(n)\,w(n-k) \quad (4.2.1.57)$$

Rewriting equation (4.2.1.56) into matrix form yields

$$\begin{bmatrix} R_{ww}(0) & R_{ww}(1) & \cdots & R_{ww}(p-1) \\ R_{ww}(1) & R_{ww}(0) & \cdots & R_{ww}(p-2) \\ \vdots & \vdots & \vdots & \vdots \\ R_{ww}(p-1) & R_{ww}(p-2) & \cdots & R_{ww}(0) \end{bmatrix}\begin{Bmatrix} a(1) \\ a(2) \\ \vdots \\ a(p) \end{Bmatrix}=-\begin{Bmatrix} R_{ww}(0) \\ R_{ww}(1) \\ \vdots \\ R_{ww}(p) \end{Bmatrix} \quad (4.2.1.58)$$

or

$$\mathbf{R}_{ww}(k-j)\mathbf{a}(k)=-\mathbf{R}_{ww}(k) \quad (4.2.1.59)$$

Thus, the parameters in equation (4.2.1.52) are calculated as

$$\mathbf{a}(k)=-\mathbf{R}_{ww}^{-1}(k-j)\mathbf{R}_{ww}(k) \quad (4.2.1.60)$$

Then the model parameters estimated by equation (4.2.1.59) and the error function (4.2.1.54), may be inserted into the equation of power spectral density (4.2.1.48) to obtained the autoregressive power spectrum density, see Figure 4.2.1.5 (c) and (d).

The PSD estimated using the autocorrelation method, plotted as red dashed lines in Figure 4.2.1.5 (c) and (d), has practical significance in analyzing the vibration data collected in this section, since it generates smooth, yet accurate, spectrum curves that can be readily used for determining the modal damping coefficient of the system using the half-power bandwidth method, while the spectrum obtained by the direct Fast Fourier

Transformation (FFT), as plotted in grey dot line in Figure 4.2.1.5 (c) and (d), are more difficult to interpret due to large variations in the response amptilide.

4.2.2. Testing the Composite Damping Properties using a High Frequency Vibration Tester

Specimen Configurations

In order to test the dynamic properties of the CHMC (and the carbon fiber reinforced epoxy as a control group) both as the stand-alone and retrofitting systems, three types of beam specimen were manufactured: 1) the self-supported beam specimen, where the sample beams were made using composite laminates that are symmetrical to the beam's mid-plane, i.e., for the CHMC beams, the polymeric phase II is applied to both sides of the laminate, as shown in Figure 3.1.1.1 (a); 2) the composite beams having a steel base beam and the composite laminates, as the retrofitting layer, attached to one side of the steel base beam; 3) the composite beams having a steel base beam and composite laminates attached to both sides. Beam types 2) and 3) are also termed as the "Oberst Beam" and "Modified Oberst Beam," if they are tested as cantilever beams. The configurations of the three types of beam specimens are schematically shown in Figure 4.2.2.1, and the pictures showing the self-supported and (modified) Oberst beams are presented in Figure 4.2.2.2. The composite laminates were prepared using a hand lay-up process for TORAY Torayca® carbon fibers having a nominal single-ply thickness of 0.33 mm. The epoxy resin used to make the carbon fiber reinforced epoxy samples was the BASF MBrace® Saturant. The micromechanical properties of the constituent

materials are reported in Chapter 3, and the properties reported by the manufacturers can be found from the manufacture's data sheets [77;91].

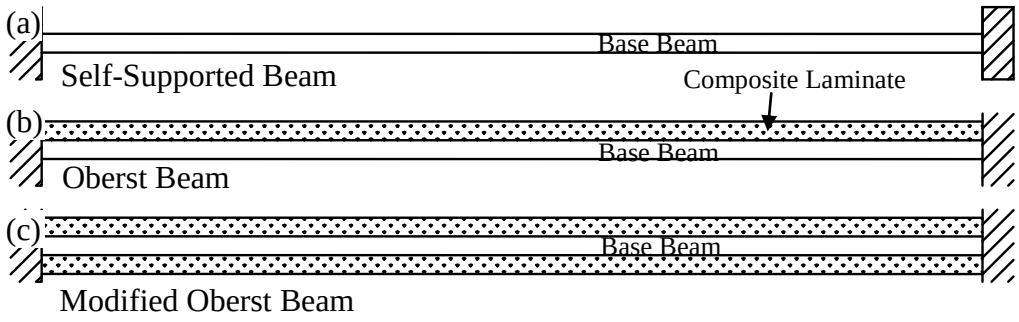

Figure 4.2.2.1. Illustrative diagram showing the various types of beams used for damping characterization

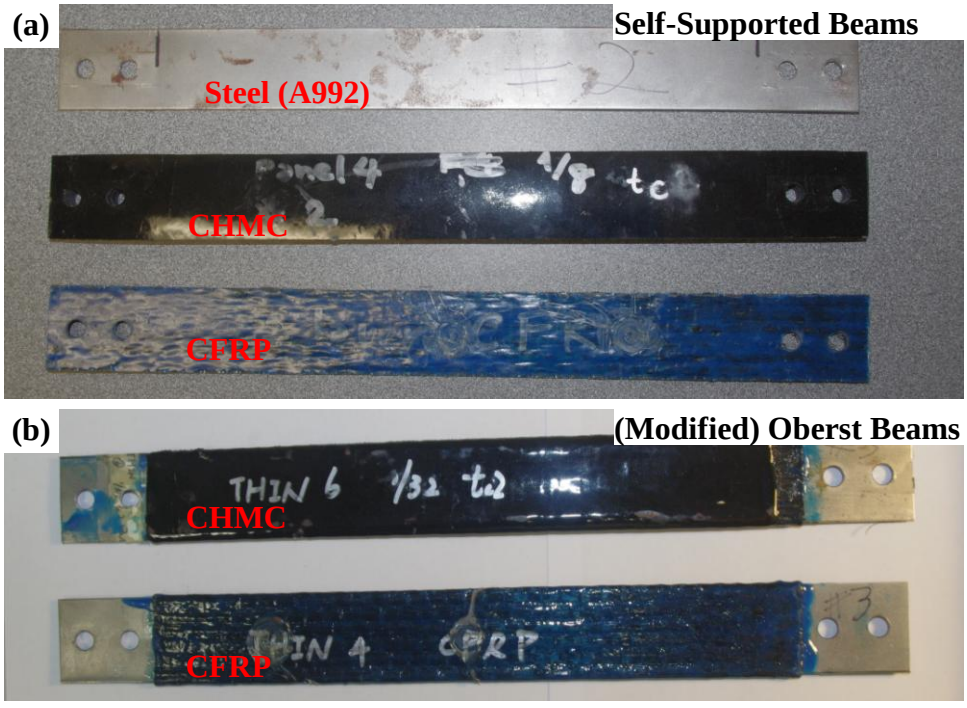

Figure 4.2.2.2. Specimens used for the vibration tests: (a) the self-supported specimens; (b) the (modified) Oberst beam specimens

Test Setup and Instrumentations

The experimental equipment used for the vibration tests is shown in Figure 4.2.2.3. The specimens are supported horizontally as fixed-fixed beams. A laser vibrometer and two accelerometers mounted at the mid-span and the quarter point of the specimen were used to measure the velocity and acceleration responses of the test beams. The free vibrations of the beams were excited through pulse loading induced by a hammer (six times for each specimen). The beam responses were detected by the laser vibrometer and accelerometers, and the signals were processed using a MatLab code developed herein to obtain both the response time-histories and frequency spectrums for each excitation, where the resonance frequencies can be determined and the logarithm decrement and half-power bandwidth methods as described by equations (4.2.1.44) and (4.2.1.45), respectively, can be readily used for estimating the damping coefficient for the fundamental vibration mode, ξ, of the tested beams, see Figures 4.2.1.3 and 4.2.1.4.

The forced vibration tests were performed using a high frequency shaker, as shown in Figure 4.2.2.3 (b). The random excitation signals, as shown in Figure 4.2.1.5 (a) (time-history) and (c) (frequency spectrum), with peak acceleration amplitude of 0.3g and 3g were used to determine the frequency-dependent dynamic properties of the tested beams. In a fashion similar to the free vibration tests, the beam responses were detected by the laser vibrometer and accelerometers as shown in Figure 4.2.2.3 (a) and (b). Two additional accelerometers were mounted on the shaker base to ensure that the actual excitation signal complies with the desired input signal. The measured time-history responses were converted into frequency spectrums via Fast Fourier Transformation (FFT). And the power spectral density (PSD) distributions for each forced vibration test

were estimated using the "pyulear" tool box in MatLab, which is based on the Yule-Walker autoregressive method [92] as briefly described by equations (4.2.1.52) - (4.2.1.60). An example of the PSD obtained by the autoregression process is plotted together with the measured response data in the frequency domain in Figure 4.2.1.5 (d), where three prominent peaks can be determined in the frequency range of 0 to 500Hz. Then the damped natural frequencies of the first n^{th} vibration modes are determined and the modal damping coefficient, ξ_i, are calculated using equation (4.2.1.45).

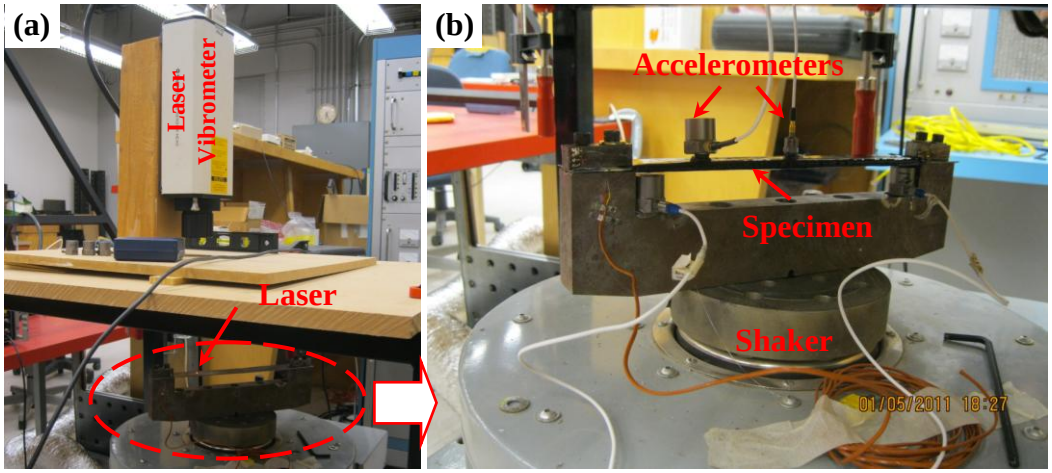

Figure 4.2.2.3. (a) The test setup showing the vibrator and the laser vibrometer used to measure the velocity response; (b) a closed-up view of the instrumentations on the specimen

4.2.3. Results of the Self-supported Beams

When used as the stand-alone structural material in the case of manufacturing mechanical components, the CHMC is manufactured by coating both sides of the laminates (lamina) with the polymeric phase II, as shown in Figure 3.1.1.1 (a). The

macro-scale preliminary dynamic properties of the stand-alone, or "double-side coated", CHMC beams are ascertained using the self-supported beams as shown in Figure 4.2.1.1 (a).

Free Vibration Responses

The typical free vibration time-history responses of the steel, carbon fiber reinforced epoxy, and CHMC1 (t_c=2.5 hr.) self-supported beams with similar initial conditions are plotted in Figure 4.2.3.1 (a). It is obvious that damping of the vibration responses of the CHMC beams is significantly larger than both Carbon fiber/ epoxy and steel beams. And the damping coefficients of the fundamental vibration mode for the five types of the beams tests, i.e. steel, carbon fiber reinforced epoxy, and three types of the CHMC beams having various t_c, are compared in Figure 4.2.3.1 (b). The damping coefficients of the self-supported CHMC beams, as calculated using the free vibration responses, are significantly higher than those of steel (about 13 times higher) and carbon fiber/ epoxy (3.2 times higher) beams. It can also be observed from Figure 4.2.3.1 that, as the intermittent curing time - t_c - increases, the damping coefficients of the self-supported beams decrease. This may be explained by the fact that the damping component had originated from the polymeric interfacial region as first introduced in Section 3.2.1. The source of internal damping of fibrous composite materials include: 1) the hysteretic damping from the constituent materials, i.e., reinforcing fiber and matrix; 2) the interaction between different material phases, e.g., the friction between the fiber and matrix; and 3) micro-scale level damage. Figure 3.2.1.6 (a) and (b) presents the different sizes and microstructures of the polymeric interfacial regions (between phase I and phase

II) produced with various t_c values, i.e. t_c = 3 hr. versus t_c = 4 hr. A comparison of the time-dependent interfacial cohesion layers shows the former has a significantly 'rougher' pattern due to a lower chemical processing cure time, i.e., t_c = 3 hr, possibly indicating a more compliant interfacial covalent molecular bond of the hybridized polymer structure, resulting in higher mobility of the polymeric molecular chain, that thus enables the internal friction between the molecules to produce higher damping [93].

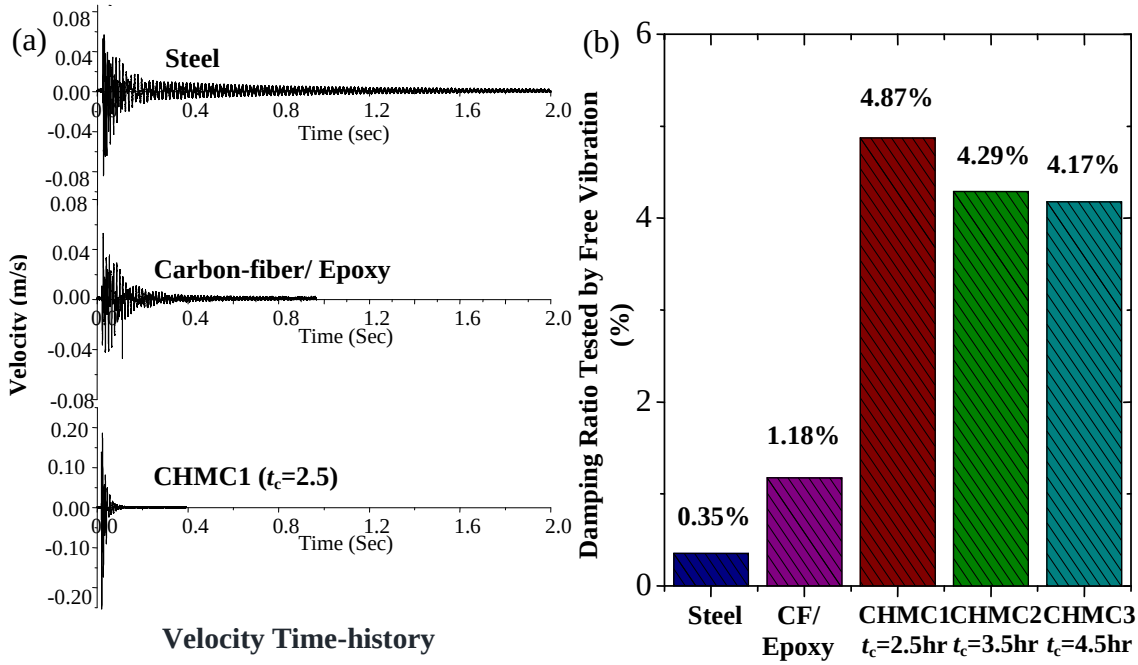

Figure 4.2.3.1. Free vibration responses and damping ratio of the "stand-alone" systems: (a) time-history responses of steel, carbon fiber reinforced epoxy, and CHMC with similar initial conditions; (b) damping ratio calculated from the free vibration responses

Forced Vibration (Random Excitation)

The forced vibration responses of the self-supported beams are obtained by exciting the specimens by band-limited white noise as shown in Figure 4.2.1.5 (a) and (c). Two peak excitation accelerations (PEA), i.e., 0.3g and 3g, were used to excite the beams

and the velocity responses are measured using the laser vibrometer. The power spectral density (PSD) of the beams made from steel, carbon fiber reinforced epoxy, and CHMC1 (t_c=2.5 hr.) for PEA equal to 0.3g and 3g are plotted in Figure 4.2.3.2 (a). The PSD indicates the energy (in a general sense) distribution of a response signal as the function of frequency. It is evident from Figure 4.2.3.2 (a) that, under the same excitation condition, the energy contained in the velocity response signal of the CHMC beam is significantly lower as compared to the energies in the steel and carbon fiber reinforced epoxy beams, especially for the higher modes of vibration. The increased suppression of higher modes of vibration is critical for applications that are sensitive to higher frequency vibrations. The damped resonance frequencies detected from the PSD curves and the modal damping coefficients calculated by the half-power bandwidth method for the first three vibration modes of the carbon fiber reinforced epoxy and the three types of the CHMC are listed in Table 4.2.3.1., and are plotted in Figure 4.2.3.2 (b). The dependency of the modal damping confidents to the intermittent curing time - t_c - for the first three vibration modes generally follows the same trend as the free vibration test results, i.e., damping coefficients decrease as t_c increases, see Table 4.2.3.1. And the modal damping coefficient, in general, appears to slightly increase at higher frequencies, see Figure 4.2.3.2 (b). This is consistent with the observation of the PSD curves as shown in Figure 4.2.3.2 (a) that the spectrum peaks of higher modes of vibration were "flattened out" because of the higher damping in the higher frequency range.

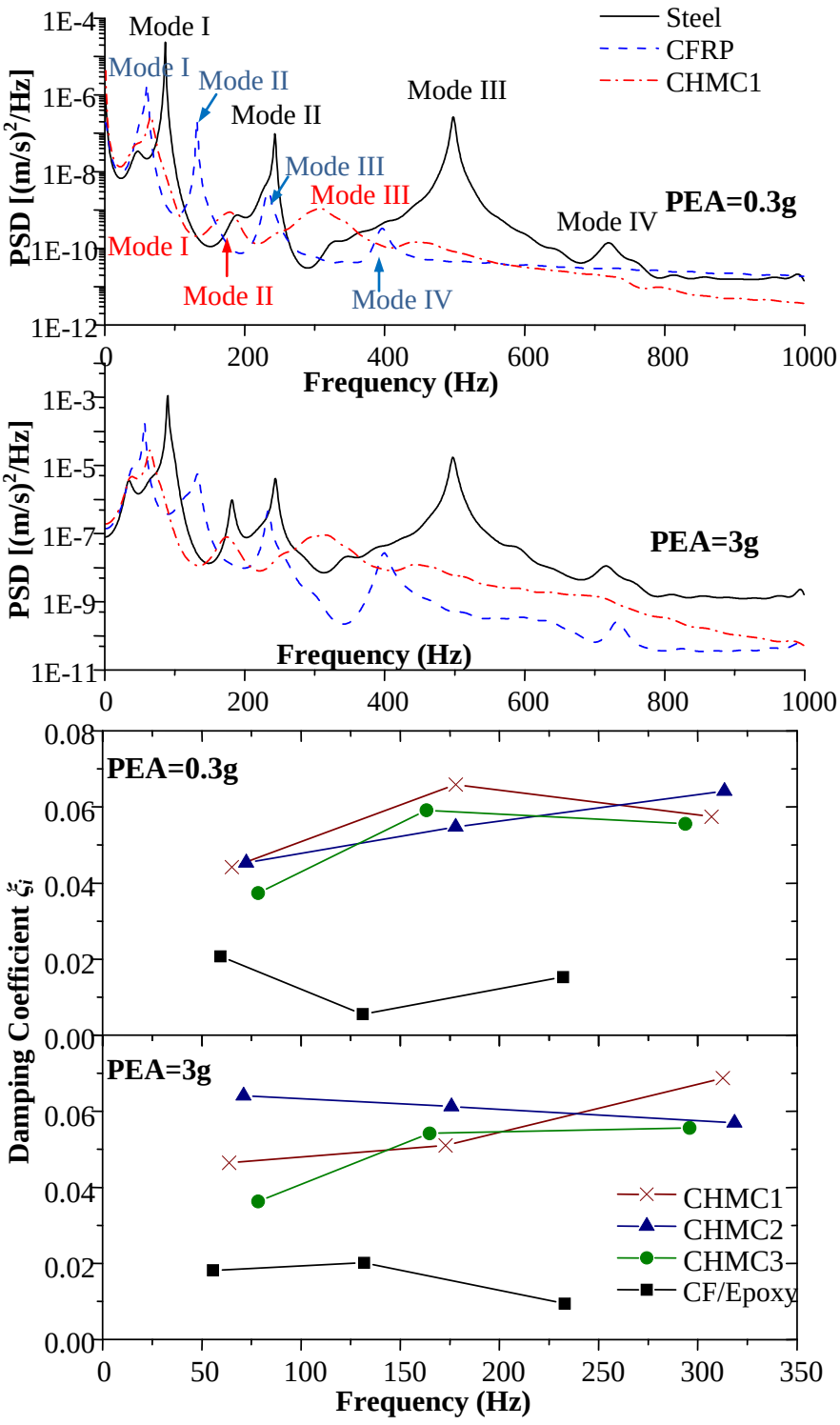

Figure 4.2.3.2. The forced vibration responses of the self-supported beams: (a) Power spectral density (PSD); (b) damping coefficients for the first three vibration modes

Table 4.2.3.1.

The resonance frequencies and damping coefficients of the first three vibration modes

Spec#	Mater. Type	t_c *hr.*	f_{n1} Hz	f_{n2} Hz	f_{n3} Hz	ξ_1	ξ_2	ξ_2
1	CF/Epoxy	n.a.	57.495	131.470	232.544	0.019	0.013	0.012
2	CHMC1	2.5	64.453	175.415	309.814	0.045	0.058	0.063
3	CHMC2	3.5	71.777	176.880	316.040	0.045	0.055	0.061
4	CHMC3	4.5	78.369	164.063	294.800	0.040	0.057	0.056

The homogenized equivalent flexural modulus of the self-supported composite beams can be calculated based on the dynamic (resonance frequency), physical (mass density), and geometrical (cross-section area, moment of inertia, and beam length) properties of the beam by equation (4.2.1.42). For the four types of composites tested here, the equivalent flexural modulus calculated by equation (4.2.1.42) using the measured beam dynamic properties, E'_{meas}, and the tension (E_1) and flexural modulus ($E_{flexual}$) predicted by equations (3.3.1.2) and (3.3.1.4), respectively, that were developed in Chapter 3 are compared in Table 4.2.3.2. The error was calculated between the measured flexural modulus and the modulus predicted by equation (3.3.1.4). A good match (within 15% of error) is found between the measured modulus and that calculated by equation (3.3.1.4), where it is apparent that equation (3.3.1.2) over estimates the bending stiffness of the laminate by more than 10 times if it is used to calculate the tranverse flexural stiffness of a stand-alone laminate, since the fiber layer is mostly concentrated in the center region of the laminate, where it is very close to the neutral axis. The storage and loss moduli of the CF/ epoxy and CHMC were plotted in Figure 4.2.3.3.

Table 4.2.3.2.

The modulus measured by the forced vibration tests as compared to the model prediction

Spec#	Mater. Type	t_c *hr.*	h_f mm	h_{m1} mm	h_p mm	E_1 GPa	$E'_{meas.}$ GPa	$E_{flexual}$ GPa	err %
1	CF/Epoxy	n.a.	0.330	0.708	n.a.	55.454	5.065	5.704	12.62
2	CHMC1	2.5	0.456	0.384	3.435	11.795	0.195	0.180	8.05
3	CHMC2	3.5	0.456	0.384	3.325	12.096	0.179	0.154	13.93
4	CHMC3	4.5	0.456	0.384	3.158	12.626	0.164	0.162	1.48

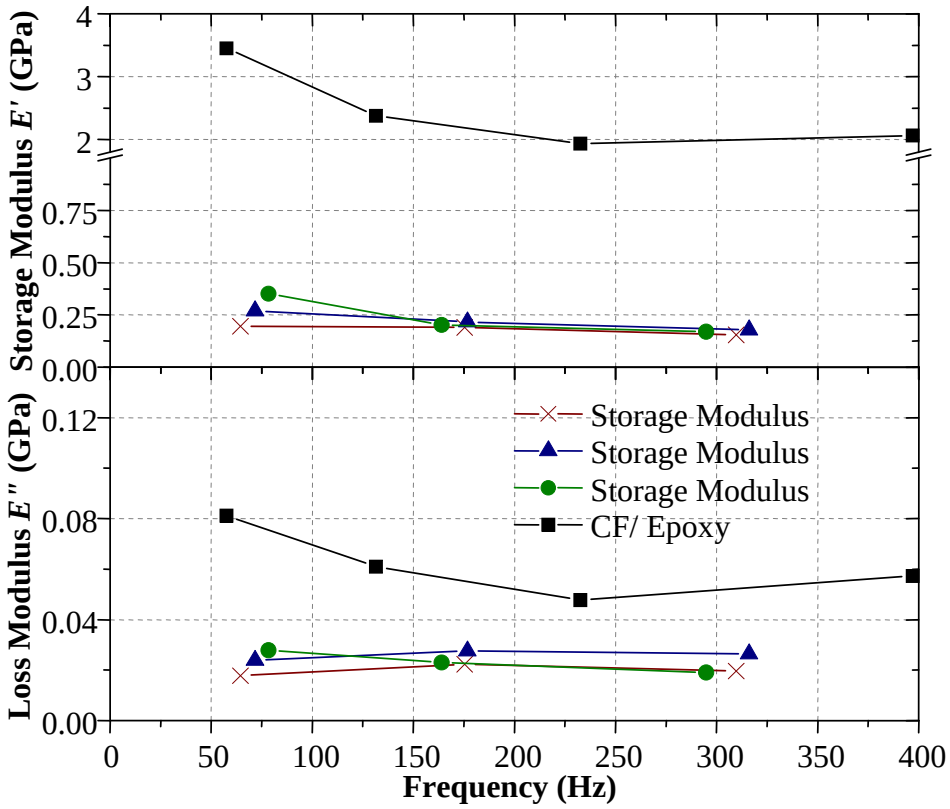

Figure 4.2.3.3. The storage and loss moduli of composites tested as self-supporting systems: (a) storage modulus as a function of frequency; (b) loss modulus

4.2.4. Results of the Oberst Beam and Modified Oberst Beam Tests

When materials are used as the retrofitting systems for a substrate, such as steel or concrete, they are often applied as thin laminates (or coating). It is often not feasible to test the dynamic properties of the retrofitting material system as a self-supported system. In such cases, the retrofitting material can be attached to one side (Oberst) or both sides (modified Oberst) of a base beam, as shown Figure 4.2.2.1. The properties of the retrofitting laminate, such as the (equivalent) Young's modulus and damping coefficient (or loss factor), can be determined from the dynamic responses of the composite beam and the base beam. The fundamental theoretical frame work of the Oberst analysis is briefly introduced followed by presentation of the results.

Composites Attached to One Side of the Steel Base Beam (Oberst Beam)

The analysis of the Oberst beams, i.e., steel base beam with the composites laminate attached on one side as shown in Figure 4.2.1.1 (b), follows the classical beam theory (Euler-Bernoulli) [78;94], which does not include the rotational inertia and shear deformation. The analysis assumes that plane sections remain plane after deformation. If the Young's modulus of the base beam and composite laminate are E_b and E, respectively; the thickness of the base beam and the laminate are H_b and H; the resonance (natural) frequencies of the composite beam (base beam attached with composite laminates) and the laminate are f_c and f_n; and if the loss factors of the composite beam and the laminates are η_c and η, respectively, then the elastic modulus and loss factor of the laminate may be calculated using equations (4.2.4.1) and (4.2.4.2) as

$$E = \frac{E_b}{2T^3}\left[(\alpha-\beta)+\sqrt{(\alpha-\beta)^2-4T^2(1-\alpha)}\right] \tag{4.2.4.1}$$

$$\eta = \eta_c\left[\frac{(1+MT)\left(1+4MT+6MT^2+4MT^3+M^2T^4\right)}{MT\left(3+6T+4T^2 2MT^3+M^2T^4\right)}\right] \tag{4.2.4.2}$$

where M is the Young's modulus ratio of the laminate and base beam material

$$M = \frac{E}{E_b} \tag{4.2.4.3}$$

T is the thickness ratio

$$T = \frac{H}{H_b} \tag{4.2.4.4}$$

and

$$\alpha = \left(\frac{f_c}{f_n}\right)^2\left(1+D_\rho T\right) \tag{4.2.4.5}$$

$$\beta = 4+6T+4T^2 \tag{4.2.4.6}$$

where D_ρ is the density ratio of the laminate and the base beam material

$$D_\rho = \frac{\rho}{\rho_b} \tag{4.2.4.7}$$

where ρ and ρ_b are the mass density of the laminate and base beam materials, respectively.

Note that due to the heterogeneous microstructure of composites as discussed in Chapter 3, the Young's modulus of composite laminate, *E*, here refers to the homogenized equivalent modulus which treats the laminate as a homogenous material. The first-mode resonance frequencies and damping coefficients of the composite beam, f_{c1} and ξ_{c1}, and base beam, f_{b1} and ξ_{b1}, together with the calculated damping coefficient of

the retrofitting laminate, ξ_1, based on equation (4.2.4.2) for each of the Oberst beam tested are summarized in Table 4.2.4.1. The damping coefficients of the CHMC used as retrofitting laminates are lower than the self-standing laminate possibly due to the constrain from the base beam and the smaller volume fraction of the high damping constituent - polymer phase II, i.e. smaller h_p, and the phase II elastomer could only be applied to one side of the retrofitting laminate. Comparing the first mode damping coefficients of laminates having the same t_c, i.e., specimen #5 to #8, see Table 4.2.4.1, one can find that the damping coefficient is higher with a greater thickness of the polymeric phase II, i.e. h_p. The damping coefficients of the retrofitting laminate as the function of frequency are plotted in Figure 4.2.4.1. The dependence of frequency on the damping coefficients of the CHMC-retrofitted beams follows the same trend as the stand-alone laminates, i.e., damping increases as the frequency increases, see Figure 4.2.4.1. This observation may be concluded using the viscous properties of the composite constituents, particularly the elastomeric matrix phase II, applied to the steel substrate beams.

Table 4.2.4.1.

The resonance frequencies and damping coefficients of the first three vibration modes

Spec#	Mater. Type	t_c	h_p	f_{c1}	f_{b1}	ξ_{c1}	ξ_{b1}	ξ_1
		hr.	mm	Hz	Hz			
5	CHMC4	2.5	1.765	115.356	60.059	0.014	0.006	0.018
6	CHMC5	3.5	1.012	121.216	60.059	0.011	0.006	0.014
7	CHMC6	4.5	0.499	140.625	60.059	0.006	0.006	0.008
8	CHMC4	2.5	1.575	153.809	60.059	0.011	0.006	0.013
9	CHMC5	3.5	0.829	164.429	60.059	0.009	0.006	0.012
10	CHMC6	4.5	0.625	116.455	60.059	0.010	0.006	0.013

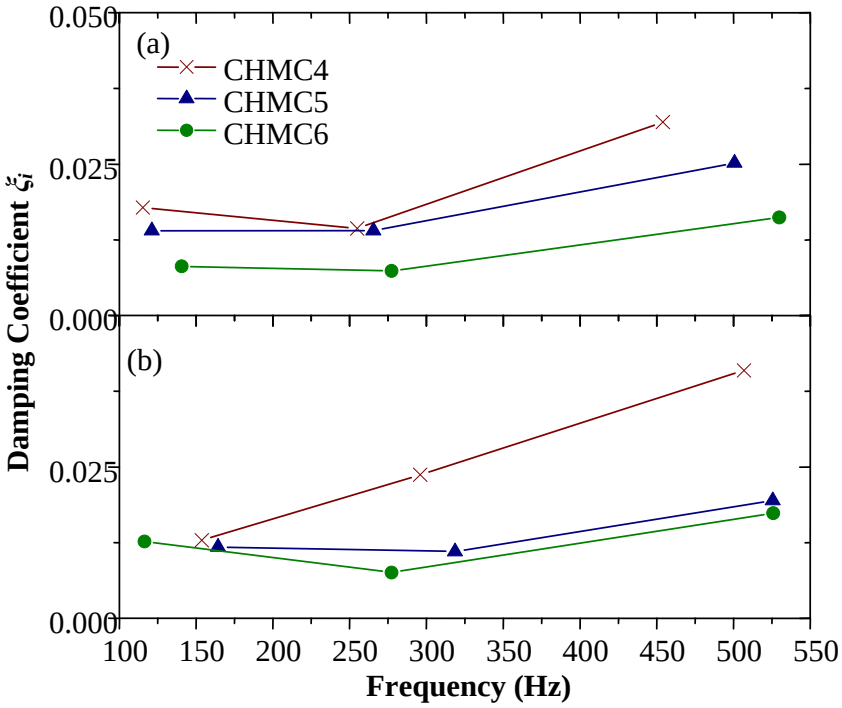

Figure 4.2.4.1. The modal damping coefficients of the Oberst beams: (a) specimens 5-7; (b) specimens 8-10

The flexural modulus may be calculated using equation (4.2.4.1), and the forced vibration responses of the single-side coated (Oberst) steel beams are compared to the tensile and flexural modulus as predicted by equations (3.3.1.3) and (3.3.1.6) in Table 4.2.4.2. The prediction results of the second specimen group, i.e., specimen #8 - #10, indicate a relatively large discrepancy using the measured values, which possibly results from the non-uniformity of the cross-section along the specimen length due to specimen preparation error. The storage and loss moduli obtained via the Oberst-type tests plotted in Figure 4.2.4.2 as functions frequency.

Table 4.2.4.2.

The modulus measured by the forced vibration tests as compared to the model prediction

Spec#	Mater. Type	t_c	h_f	h_{m1}	h_p	E_1	$E'_{meas.}$	$E_{flexual}$	err
		hr.	mm	mm	mm	GPa	GPa	GPa	%
5	CHMC4	2.5	0.550	0.384	1.765	36.296	1.866	1.700	8.89
6	CHMC5	3.5	0.550	0.384	1.012	47.989	3.976	3.546	10.80
7	CHMC6	4.5	0.550	0.384	0.499	61.513	7.870	7.213	8.36
8	CHMC4	2.5	0.550	0.384	1.575	38.671	3.160	1.991	36.99
9	CHMC5	3.5	0.550	0.384	0.829	52.077	7.585	4.463	41.16
10	CHMC6	4.5	0.550	0.384	0.625	57.512	5.888	5.932	0.75

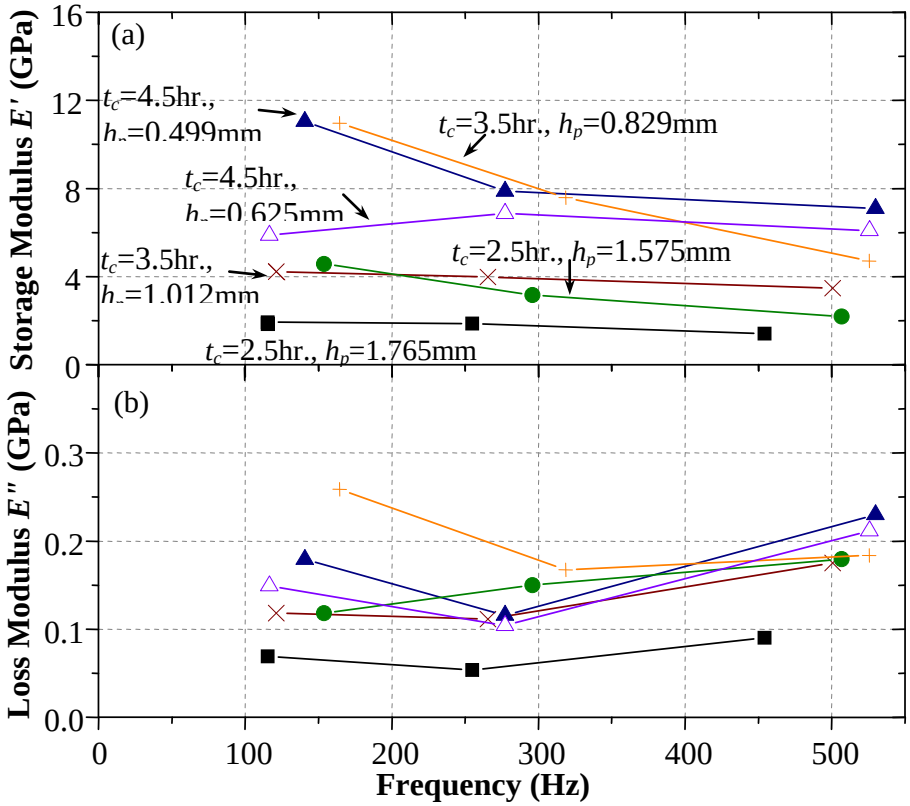

Figure 4.2.4.2. The storage and loss moduli of the CHMC as functions of frequency tested via the Oberst-type method: (a) storage modulus, *E'*; (b) loss modulus, *E''*

Composites Attached to Both Side of the Steel Base Beam (Modified Oberst Beam)

The analysis of symmetric free-layer beams, i.e., steel base beam with both sides attached with the composites laminates as shown in Figure 4.2.1.1 (c), is similar to that of the Oberst beams. The flexural stiffness of the composite beam expressed in term of the complex elastic moduli as

$$E_c I_c \left(1+i\eta_c\right) = 2EI\left(1+i\eta\right) + E_b I_b \tag{4.2.4.8}$$

where I_c, I, and I_b are the moment of inertia of the composite beam, laminate, and base beam, respectively. Equating both the real and imaginary parts of the LHS and RHS of equation (4.2.4.8) yields

$$E = E_b \frac{\left[\left(f_c / f_n\right)^2 \left(1+2D_\rho T\right) - 1\right]}{\left(8T^3 + 12T^2 + 6T\right)} \tag{4.2.4.9}$$

$$\eta = \eta_c \left[1 + \frac{E_b}{E\left(8T^3 + 12T^2 + 6T\right)}\right] \tag{4.2.3.10}$$

Thus, the properties of the composite laminates, i.e. CF/ epoxy and CHMC, can be readily calculated from the dynamic responses of the composite beam.

The first-mode damping coefficients tested via modified Oberst beams (both sides attached with the composite laminates) are consistent with the results obtained by the Oberst Beams (one side attached with composite laminate), as listed in Table 4.2.4.3. Table 4.2.4.4 compares the tensile and flexural modulus predicted based on equations (3.3.1.3) and (3.3.1.6) for the Modified Oberst Beams with the flexural modulus calculated by equation (4.2.4.9) using the measured vibration responses. Large discrepancies are observed between the predicted results and the measured modulus for

specimens #16 - #20, in which cases thicker base, or substrate, beams (1.32 mm) were used. Since the analysis of the symmetric free layer (or Modified Oberst) beams is based on planes sections remaining plane, attention must be given when using equations (4.2.4.9) and (4.2.4.10) if the retrofitting laminate thickness is not much greater (about four times) than that of the metal beam [78;94]. The ratios of the thickness of the composite laminate to the thickness of the bases for #16 - #20 range from 0.92 to 2.14. As a result, the modulus calculated from the dynamic responses of the composite beams may not be accurate. Other possible sources of error include 1) the actual fiber distributions for every laminate, as shown in Figure 4.2.4.4, may be different from the nominal thickness of the fiber layer used in the calculation; 2) the distribution of reinforcing fibers may not be perfectly symmetric about the laminate mid-plane; and 3) the beam cross-section along the beam length direction may not be perfectly uniform. Similarly, the storage and loss muduli tested by the modified-Oberst type tests were plotted in Figure 4.2.4.3.

Table 4.2.4.3.

The resonance frequencies and damping coefficients of the first three vibration modes

Spec#	Mater. Type	t_c	h_p	f_{c1}	f_{b1}	ξ_{c1}	ξ_{b1}	ξ_1
		hr.	mm	Hz	Hz			
11	CF/Epoxy	n.a.	n.a.	191.162	60.059	0.009	0.006	0.010
12	CHMC7	2.5	0.889	152.344	60.059	0.015	0.006	0.016
13	CHMC8	3.5	0.614	156.738	60.059	0.018	0.006	0.019
14	CHMC4	2.5	1.415	166.260	60.059	0.017	0.006	0.018
15	CHMC5	3.5	1.437	123.047	60.059	0.015	0.006	0.017
16	CF/Epoxy	n.a.	n.a.	172.852	87.524	0.007	0.007	0.009
17	CHMC7	2.5	0.889	174.683	87.524	0.012	0.007	0.015
18	CHMC8	3.5	0.582	192.993	87.524	0.011	0.007	0.012
19	CHMC4	2.5	1.894	183.838	87.524	0.016	0.007	0.019
20	CHMC5	3.5	1.493	189.331	87.524	0.012	0.007	0.014

Table 4.2.4.4.

The modulus measured by the forced vibration tests as compared to the model prediction

Spec#	Mater. Type	t_c *hr.*	h_f mm	h_{m1} mm	h_p mm	E_1 GPa	$E'_{meas.}$ GPa	$E_{flexual}$ GPa	err %
11	CF/Epoxy	n.a.	0.550	0.306	n.a.	95.846	32.438	25.146	22.48
12	CHMC7	2.5	0.550	0.384	0.889	50.664	4.937	4.129	16.37
13	CHMC8	3.5	0.550	0.384	0.614	57.859	7.053	6.036	14.42
14	CHMC4	2.5	0.550	0.384	1.415	40.927	3.883	2.305	40.64
15	CHMC5	3.5	0.550	0.384	1.437	40.606	1.938	2.258	16.54
16	CF/Epoxy	n.a.	0.550	0.333	n.a.	91.612	35.562	22.456	36.85
17	CHMC7	2.5	0.550	0.384	0.889	51.427	12.235	4.129	66.26
18	CHMC8	3.5	0.550	0.384	0.582	58.821	19.842	6.332	68.09
19	CHMC4	2.5	0.550	0.384	1.894	39.575	8.117	2.257	72.19
20	CHMC5	3.5	0.550	0.384	1.493	46.104	11.563	3.332	71.19

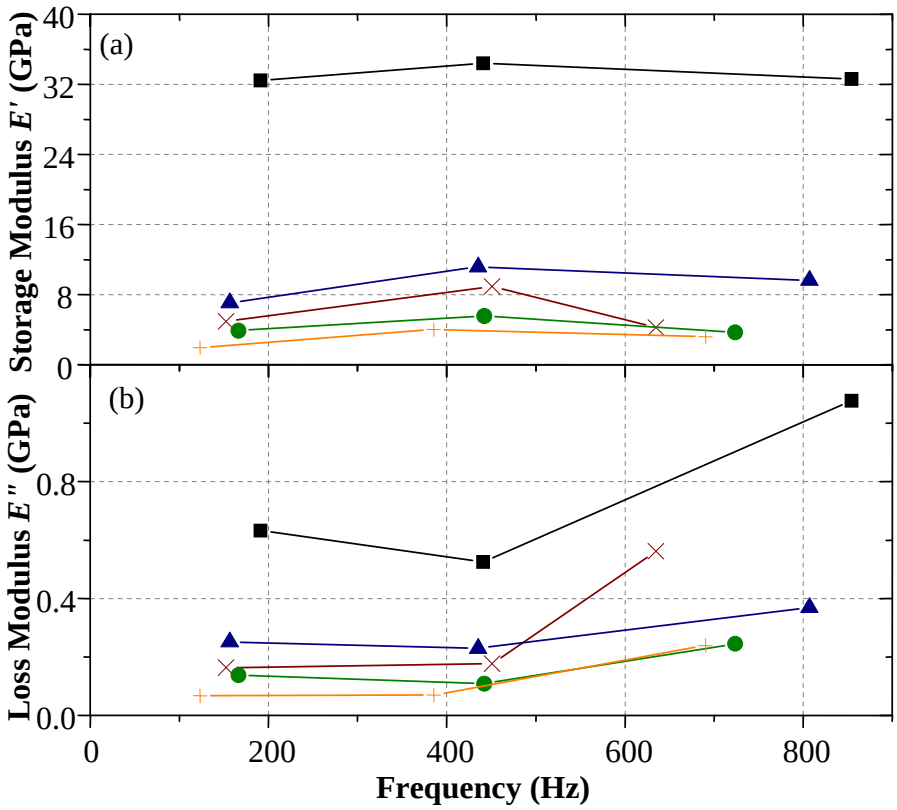

Figure 4.2.4.3. The storage and loss moduli of the CHMC as functions of frequency tested via the Modified Oberst-type method: (a) storage modulus, *E'*; (b) loss modulus, *E''*

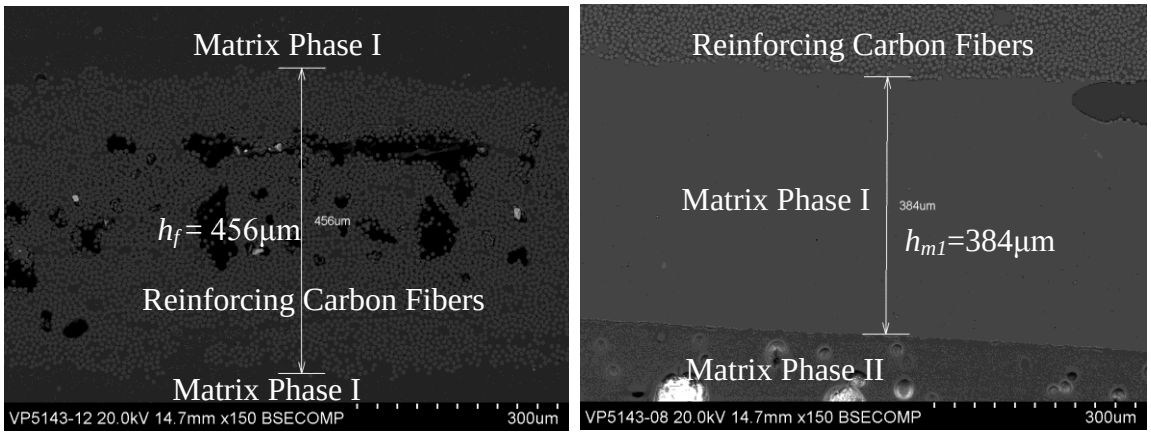

Figure 4.2.4.4. The actual fiber distribution in a CHMC laminate

4.3. Summary and Conclusions

The methodology used to characterize the dynamic performance and damping property of composite materials is presented and discussed in this chapter. The dynamic properties of the CHMC and conventional carbon fiber reinforced epoxies (CF/ epoxy) are investigated using free vibration and forced vibration tests. The natural frequencies and damping coefficients were calculated for the materials based on vibration responses of tested beams. The CHMC exhibits significantly greater damping and vibration suppression properties than the conventional CF/ epoxy as both a stand-alone structural material and as a retrofitting system. Generally, the observed damping is higher when used as a stand-alone laminate than as a retrofitting material. This may be attributed to the single-side coated lay-up of the retrofitting laminates and the constraint of the substrates and also because of the greater damping the CHMC provides over the steel substrate beam. The influence of the two material processing parameters - h_p and t_c - on the material damping was investigated, and the results reveal that, generally, the damping

coefficients increase with greater h_p and smaller t_c although the influence of h_p is greater than that of t_c. The damping based design of the newly developed CHMC material is facilitated by thoroughly understanding how the material processing parameters, such as the matrix phase II thickness - h_p - and intermittent curing time - t_c, - impact the properties of the composite laminates.

Chapter 5.

REHABILITATION OF NOTCH DAMAGED STEEL BEAMS USING THE CHMC

The retrofit of notch damaged steel beams is investigated in this chapter via the experimental testing of nine wide flange steel beam specimens and finite element simulation. Three notch configurations representing various damage levels were identified, and the beam specimens were retrofitted using both carbon fiber reinforced polymer (CFRP) laminates and the Hybrid-polymeric Matrix Composite (CHMC). A Digital Imaging Correlation (DIC) technique is employed into the experiments to measure the full field strain distribution at critical locations. Finite element models were developed to investigate the strain/ stress distributions near the notch tips, and the results were compared to those obtained by DIC.

5.1. Introduction

With the understanding of the impending demands of developing a new generation of materials that possess not only high strength but also high ductility and superior damping properties for civil infrastructure retrofitting, and the design philosophy, microstructures, and the mechanical performance of the newly developed CHMC at both micro- and macro- scale levels that have been thoroughly discussed in the previous chapters, this chapter explores the feasibility of using the CHMC to repair and retrofit severely damaged structural members at the scaled component level.

Despite the significant amount of research and applications of FRPs in reinforced concrete (RC) and masonry structures as has been introduced in chapter 1, efforts to utilize FRP materials to retrofit and strengthen steel structures have been limited [95]. In the mid- 1990s, Mertz and Gillespie [96] tested six 1525mm long steel beams (W200x15 section) strengthened with five different lay-ups. The increases in elastic stiffness of the five strengthened steel beams in comparison to the control beam ranged from 11% to 30%; and the strengths of the members increased by 41-71%. As part of that same study, Mertz and Gillespie also retrofitted and tested two full-scale corrosion damaged bridge girders; the test results show that CFRP strengthening significantly increased the stiffness and moment capacity of the corroded girders, where one of the retrofitted girders, the elastic stiffness of which had degraded to approximately 87% of its un-corroded condition, showed full recovery of its flexural stiffness and load capacity. Over the past decade, more experimental [97] and analytical [98] work have been performed to study the effectiveness of FRPs on strengthening and retrofitting steel structural members. Besides, research efforts have also been made to extending the fatigue life of steel structures. Experimental studies conducted by Tavakkolizadeh and Saadatmanesh [40], Wu et al. [99], and Jiao et al. [100] demonstrated the effectiveness of using a CFRP-retrofit scheme to extend the fatigue life of damaged and intact steel girders. Hmidan et al. [39], Kim and Harries [101], on the other hand, investigated the CFRP repair strategies for steel beams having experienced notched damages. The influence of notch configurations was studied using a finite element analysis to obtain the J-integral versus displacement relationships of the repaired and unrepaired beams with varying notch profiles. It is worthy to point out that due to the higher strength and stiffness of steel, the

failure modes and mechanisms of FRP-retrofitted steel structural systems are generally different than those of concrete – FRP systems [12]. For example, debonding of the retrofitting laminates, if it occurs, often initiates at the steel – adhesive interface, thus mandating careful surface preparation prior to applying the laminates [20].

This chapter discusses the experimental test results of nine notch damaged steel beams retrofitted using both CFRP and the newly developed CHMC. Three unrepaired steel beams with various notch configurations were labeled as the control group (NB-1 ~ 3) and tested under static three-point bending. Three notched (damaged) specimens were retrofitted with CFRP (CB-1 ~ 3) and three other notched specimens were retrofitted using the CHMC (CFB-1 ~ 3); the six retrofitted beams were then tested quasi-statically under the same three-point bending configuration. The experimental test results of the nine specimens are subsequently presented. In addition to the experimental study, finite element models were also developed to analyze the bending behavior of the as-is and retrofitted notched beams, including the failure mechanisms and the stress/ strain distributions around critical regions. The numerical analysis results were then compared to the experimental results obtained by the digital imaging correlation (DIC) technique. The experimental phase of this research was performed at Oak Ridge National Laboratory (ORNL).

5.2. Experimental Program

5.2.1. Specimen Configurations and Retrofitting Schemes

An experimental program was developed to investigate the performances of the notch damaged steel beams with and without the composite laminate retrofits. Three types of notch configurations were used to represent prescriptive damage levels in the steel beams. The three damage levels are (1) total loss of the tension-side flange of the steel beam; (2) total loss of the flange plus 25% web loss; and (3) total loss of flange plus 50% web loss as presented in Figure 5.2.1.1. Since the fracture and crack propagation of steel can be highly dependent on the sharpness of the crack tip, the width of the notch was controlled to be 1.27 mm (50 mils) in all cases. American Institute of Steel Construction (AISC) W100x19 SI (W4×13), hot rolled sections were used in the study in order to accommodate the test machine configuration and dimensions. The sections were made of A992 grade steel having a nominal yield strength of 344.7 MPa (50 ksi). The specimens were subjected to three-point bending under static load conditions and with a span length of 304.8 mm (12 in.). The specimens were categorized into three groups. Specimens NB-1 - 3 are the non-retrofitted control beams having three different notch configurations (Figure 5.2.1.1 (a)). Specimens CB-1 - 3 are retrofitted using conventional CFRP. Specimens CFB-1 - 3 are the notched beams having been retrofitted using the CHMC laminates externally bonded to the tension-side of the flanges. Preparation of the steel beams included sand-blasting the bottom surfaces of the tension flanges and applying an acetone cleanser to improve the bond strength between the laminates and the substrate steel by removing any rust and residual grease prior to

applying the epoxy-based primer adhesive. Laminate debonding has been proven to be one of the dominant failure modes of FRP retrofitted/ or strengthened steel structural members [95] even though careful surface preparations may had been performed [39;102]. In addition, the existence of a geometric discontinuity, e.g., at the mid-span notch in this case, would impose significant interfacial shear stress concentrations in this vicinity, which would initiate the progressive laminate debonding at early loading stages. In order to preclude the undesired total detachment of the retrofitting laminates and to maintain the partial function of the laminates following adhesive failure, mechanical anchorages were used, as has been the case in several retrofitting practices [103-105]. In the current experimental program, a mechanical anchorage system, as shown in Figure 5.2.1.1 (b), was used to ensure the failure mode of the retrofitted beam are controlled by laminate rupture such that a fair comparison between the performances of CFRP and the newly developed CHMC (or CarbonFlex) was achieved. The CFRP used to retrofit CB-1 - 3 was the MBrace® CF130 system produced by BASF™ having a nominal laminate strength of 3,800 MPa [77]. The TORAYCA® unidirectionally weaved carbon fiber having a nominal thickness of 0.165 mm/ply constituted the reinforcing fiber of the CHMC and provides the baseline strength. Different from conventional CFRP composite, the CHMC incorporates a multilayered matrix with higher damping and fracture toughness, as aforementioned in the previous chapters, to provide the load bearing fiber a more stable media for stress transfer, and thus, enhances the damage tolerance of the entire composite system. Details of the test specimens, including the notch configurations, the retrofitting materials that were used, and the laminate thickness, are summarized in Table 5.2.2.1.

Table 5.2.2.1.

Specimen geometric and retrofitting details

Spec. #	Notch Profile[5]	Retrofitting Material	Laminate Thickness[6] (mm)
NB-1	100%F+50%W	None	N.A.
NB-2	100%F+25%W	None	N.A.
NB-3	100%F+0%W	None	N.A.
CB-1	100%F+50%W	CFRP	0.330
CB-2	100%F+25%W	CFRP	0.165
CB-3	100%F+0%W	CFRP	0.165
CFB-1	100%F+50%W	CHMC	0.330
CFB-2	100%F+25%W	CHMC	0.165
CFB-3	100%F+0%W	CHMC	0.165

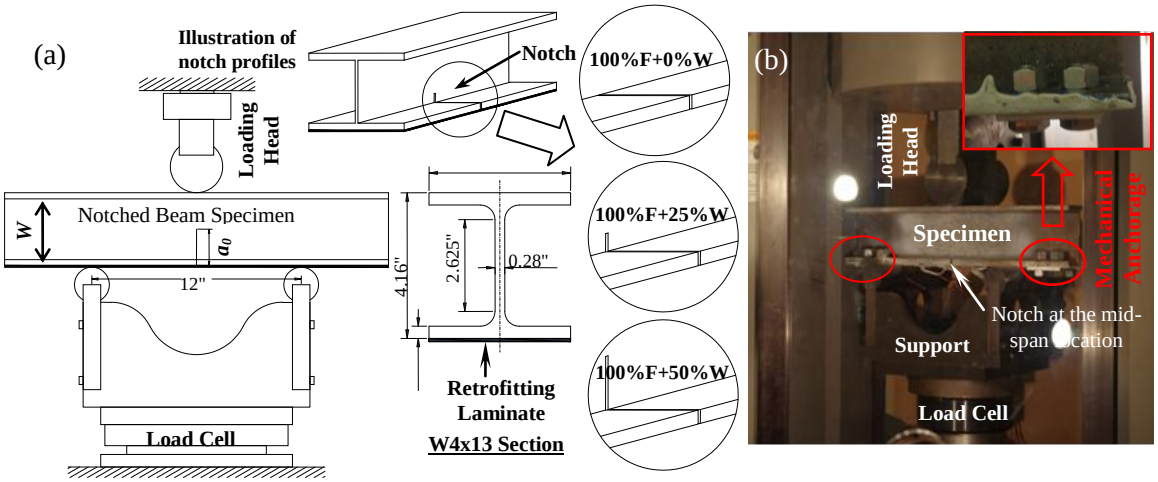

Figure 5.2.1.1. (a) Illustrative figure showing the specimen and test setup; (b) Picture of test setup [106][7]

[5] see Figure 5.2.1.1.
[6] Due to the difficulty of controlling the over-all thickness of the retrofitting laminate on-site, the laminate thickness was taken as the nominal thickness of the dry fiber.
[7] Original figures provided by the author and reprint under the license permission of Elsevier.

5.2.2. Instrumentations

Testing was performed using the Test Machine for Automotive Crashworthiness (TMAC) at Oak Ridge National Laboratory (ORNL). The maximum static load capacity of the TMAC is 490 kN having a closed-loop hydro-servo control system; the test set-up and specimens are shown illustratively in Figure 5.2.1.1 (a), and the test set-up itself is shown in Figure 5.2.1.1 (b). The loading rate was 0.04 mm/sec via displacement control; Six electrical-resistance strain gauges (with a gauge length of 6.35mm, or 0.25 in.) were spaced 25.4 mm (1 inch) apart and mounted along the center-line of the tension flange, starting at the mid-span notch, see Figures 5.2.2.1 (a) and (b); an additional gauge was mounted on the compression flange, and a second gauge was mounted at the mid-span on the outside of the laminate to measure the tensile strain of the retrofitting laminate during loading. In addition, a three-dimensional digital imaging correlation (3-D DIC) system was used to monitor the strain fields on the specimen webs near the crack tip. The 3-D DIC system is composed of an image acquisition and analysis system and two high-definition cameras at an angle to the specimen surface. As shown in Figure 5.2.1.1 (c), the area of interest, was polished and a random speckle pattern was created on the specimen surface. During loading, the movements of the speckles painted on the specimen surface were captured by the cameras simultaneously and these sequential images were analyzed by the image correlation software, VIC-3D (Correlated Solutions, Inc.) to obtain the Lagrangian strain fields, as well as the crack mouth opening distances (CMODs) for each notched specimen. A closer details on the working principles of the

DIC technique will be introduced in the following section. A picture showing the experimental instrumentations including the DIC system is presented in Figure 5.2.1.1.

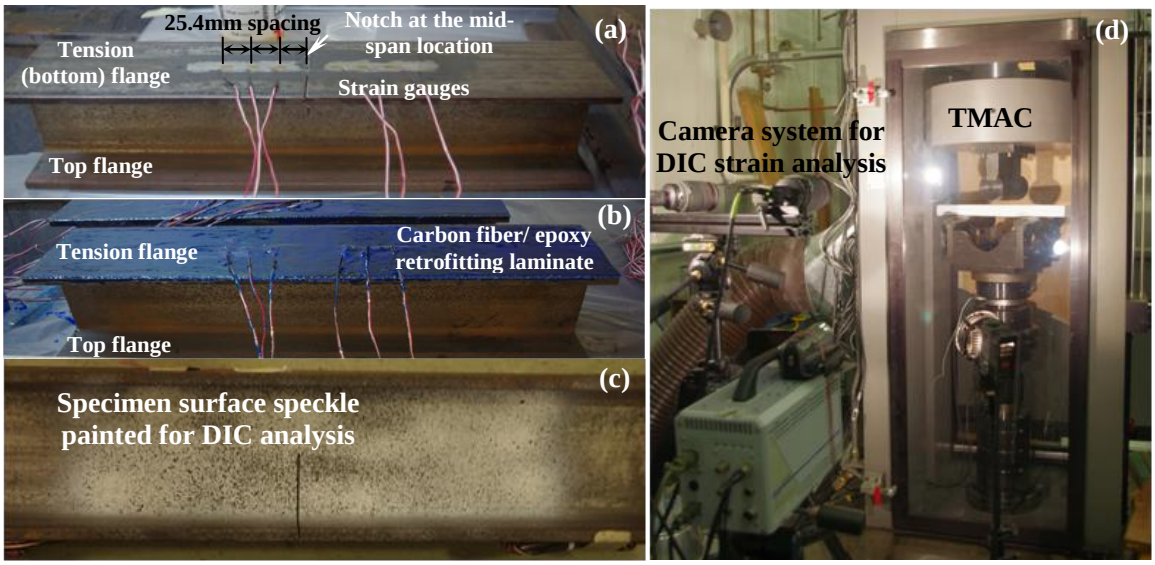

Figure 5.2.2.1. Pictures showing the experimental instrumentations (a) strain gauges installed along the center line of the tension flange; (b) the application of the CFRP (BASF MBrace® CF130) retrofitting laminate; (c) the speckle pattern created on the specimen web surface for DIC analysis; (d) the digital imaging correlation (DIC) setup [106][8]

5.2.3. The Digital Imaging Correlation (DIC) Technique for Strain Field Measurement

Digital Image Correlation (DIC), which has been firstly used by researcher for mechanical testing at University of South Carolina in the early 1980s [107-109], is an

[8] Original figures provided by the author and reprint under the license permission of Elsevier.

optical method that employs tracking and image registration techniques for accurate 2D and 3D measurements of changes in images. It is often used to measure displacement, deformation, and strain in engineering applications. The concept of using correlation to measure shifts in datasets has been known for a long time, and it was applied to digital images at least as early as 1975 [110]. It is now widely used in the field of experimental mechanics to provide full-filed displacement and strain measurement by comparing the digital images of a test object surface acquired before and after deformation [111]. The basic work principle of the digital imaging correlation is based on the maximization of a correlation coefficient, that is determined by examining the pixel intensity array subset on two or more corresponding images. For the subset as shown in Figure 5.2.3.1, the similarity degree between the reference subset and the deformed subset is evaluated by a correlation coefficient, such as the cross correlation coefficient r_{ij} in form of equation (5.2.3.1)

$$r_{ij} = 1 - \frac{\sum_i \sum_j \left[f\left(x_i, y_j\right) - \overline{f} \right] \left[g\left(x_i^{'}, y_j^{'}\right) - \overline{g} \right]}{\sqrt{\sum_i \sum_j \left[f\left(x_i, y_j\right) - \overline{f} \right]^2 \sum_i \sum_j \left[g\left(x_i^{'}, y_j^{'}\right) - \overline{g} \right]^2}} \qquad (5.2.3.1)$$

where $f(x_i,y_j)$ is the pixel intensity or gray scale value at point (x_i,y_j) in the un-deformed image, see Figure 5.2.3.1; $g(x_i^{'},y_j^{'})$ is the pixel intensity at point $(x_i^{'},y_j^{'})$ in the deformed image; $\overline{f}$ and $\overline{g}$ are the mean values of the intensity matrices. The position of the deformed subset can thus be determined by searching the peak position of the distribution of correlation coefficient.

The coordinates of point $\boldsymbol{Q}(x_i,y_j)$ around the subset center $\boldsymbol{P}(x_0,y_0)$ in the un-deformed subset can be mapped to point $\boldsymbol{Q}'(x'_i,y'_j)$ in the deformed subset by the shape function

$$\begin{aligned} x_i^{'} &= x_i + \xi\left(x_i, y_j\right) \\ y_i^{'} &= y_i + \eta\left(x_i, y_j\right) \end{aligned} \tag{5.2.3.2}$$

where the shape function may be expressed in the first order in terms of the transition, rotation, shear, and normal strains as

$$\begin{aligned} \xi\left(x_i, y_j\right) &= u + \frac{\partial u}{\partial x}\Delta x + \frac{\partial u}{\partial y}\Delta y \\ \eta\left(x_i, y_j\right) &= v + \frac{\partial v}{\partial x}\Delta x + \frac{\partial v}{\partial y}\Delta y \end{aligned} \tag{5.2.3.3}$$

where u and v are transition displacements of the center $\boldsymbol{P}(x_0,y_0)$ of the subset in the x and y directions, respectively, see Figure 5.2.3.1; and Δx and Δy are the distances from Point $\boldsymbol{Q}(x_i,y_j)$ to the subset center.

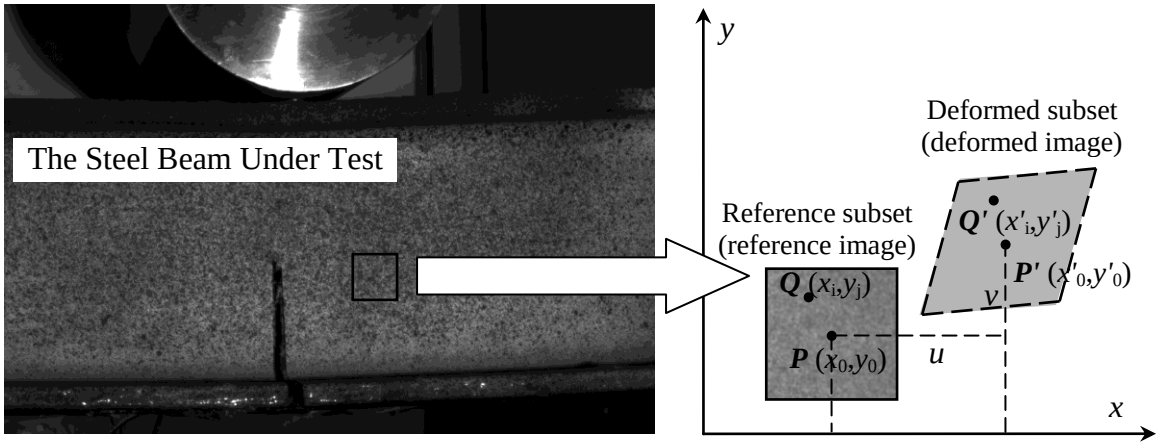

Figure 5.2.3.1. Schematic illustration of a square reference subset and a deformed subset after deformation

In the current work, a commercially available digital imaging correlation (DIC) software - VIC-3D (Correlated Solutions, Inc.) is employed, in lieu of traditional strain gauges, to analyze the digital images captured consecutively at 2 frames per second, so that the full strain filed at particular import locations of the specimen, such as the notch tip region, can be obtained. The obtained results will be later compared to the numerical results obtained by finite element analysis to validate the merits of using CHMC, as a candidate retrofitting material, to repair damaged steel structures.

5.2.4. Experimental Results and Discussion

The experimental test results of the notch damaged steel beams are summarized in Table 5.2.4.1, and the load-deflection responses of the nine notched beams (with and without retrofit) are presented in Figures 5.2.4.1 - 5.2.4.3. Failure of the non-retrofitted beams is indicated by the cracks initiated at the notch tips, propagating towards the compression flanges, wherein the load carrying capacity of the beams decreased due to increased section loss. The damaged beams had relatively low flexural stiffness. In the beams retrofitted by CFRP and CHMC, the failure modes were generally governed by rupture of the laminates, see Table 5.2.4.1. When the measured tensile strains of the composite laminates had reached the ultimate strains, the laminates started to fracture, albeit each having varying characteristics; consequently, this affected the overall flexural performance of the retrofitted beams. Due to the brittle nature of the CFRP constituents, i.e., the carbon fiber and the epoxy resin matrix, the CFRP laminates fractured in a very brittle manner, see Figure 5.2.4.4 (a), resulting in sharp load drops immediately following the laminate rupture whereby the strain energy stored in the laminate had been suddenly

released thus causing further damage to the substrate structures in the form of crack formation. This is also evidenced by the near-crack-tip strain fields measured by the DIC system (to be discussed later) and the finite element (FE) analysis executed out in the next section. On the contrary, however, the CHMC system failed in a much more ductile manner, which enabled the stored strain energy to not only be gradually released via damage accumulation of the laminate but also dissipated by the high internal damping of the CHMC laminate. As a result, the CHMC retrofitted beams, had shown increased ductility as opposed to the counterpart CFRP-retrofitted beams, see Table 5.2.4.1. Fracture of the CHMC laminate is presented in Figure 5.2.4.4 (b).

Table 5.2.4.1.

The primary experimental test results of the notched steel beams

Spec. #	**Peak Load** (kN-m)	**Disp. Ductility**[9] (mm/mm)	**Elastic Stiffness** (kN/mm)	**Failure Mode**[10]
NB-1	8.57	4.86(8.60/1.77)	31.42	Crack propagation
NB-2	13.84	2.78(7.81/2.81)	41.29	Crack propagation
NB-3	16.82	2.08(7.45/3.59)	52.93	Crack propagation
CB-1	12.25	2.18(4.20/1.93)	51.76	Laminate rupture
CB-2	14.37	2.09(5.58/2.67)	56.30	Laminate rupture
CB-3	18.20	2.46(6.24/2.54)	71.19	Laminate rupture
CFB-1	14.13	2.84(7.27/2.56)	35.42	Laminate rupture
CFB-2	15.89	2.66(9.62/3.62)	39.37	Laminate rupture
CFB-3	17.98	3.11(10.47/3.37)	51.12	Laminate rupture

[9] The Displacement Ductility is defined as the ratio of the peak-load-displacement to the displacement at yielding. The values for both the peak-load-disp. and the yield disp. are shown in the bracket for each specimen

[10] The failure mode is designated as the first significant load drop, the actual sequences of failure events were presented in Figure 5.2.4.1-3.

One significant difference between the CFRP and CarbonFlex retrofitted beams is their deformation capabilities. In beam CB-1, the peak load corresponds to a mid-span deflection of 5 mm which is 41.9% less than the peak-load deflection of the un-retrofitted NB-1; however, the peak load of CFB-1 occurs at a mid-span deflection of 7.47 mm, implying that the energy dissipated by CFB-1 prior to the laminate rupture is 43.8% higher the that dissipated by CB-1. The ductility of structures is critical considerations in extreme load events, such as earthquakes. For the group of beams having the most severe damage, i.e. 100% flange + 50% web loss, both the CFRP and the CarbonFlex retrofits effectively restored the load capacity and elastic stiffness of the beams. The increases in load capacity for CB-1 and CFB-1 were 42.9% and 84.9%, respectively, as compared to the non-retrofitted beam, NB-1; and the elastic flexural stiffness values in each retrofitted beam were improved by 94.2% and 46.6% in CB-1 and CFB-1, respectively. Figure 5.2.4.2 presents the load-deflection curves obtained for beams NB-2, CB-2, and CFB-2, which had experienced a damage level of "100% flange + 25% web loss." The load-carrying capacities of CB-2 and CFB-2 had increased by 3.8% and 14.8%, respectively, in comparison to NB-2. The loading curves also indicate that the peak loads generally occur at larger deflections in the beams having experienced less damage. Two possible explanations to this observation are: (1) the lower neutral axis position in the less damaged beams, it was necessary for those beams to deflect more in order for the tensile strain in the retrofitting laminate to reach the ultimate strain value. Thus, the deflections corresponding to the peak load of the retrofitted specimens would be higher than the more severely damaged ones; (2) the fiber thickness of the laminates used for the less-damaged beams was only 0.165 mm, or half of the thickness used in the most severely

damaged beams, see Table 5.2.2.1. These observations also hold true for the group of beams which had only 100% flange loss, see Figure 5.4.2.3. The increases in load capacity and stiffness, as compared to the un-retrofitted NB-3, were 8.2% and 54.2%, respectively for CB-3, and 6.9% and 4.5% for CFB-3.

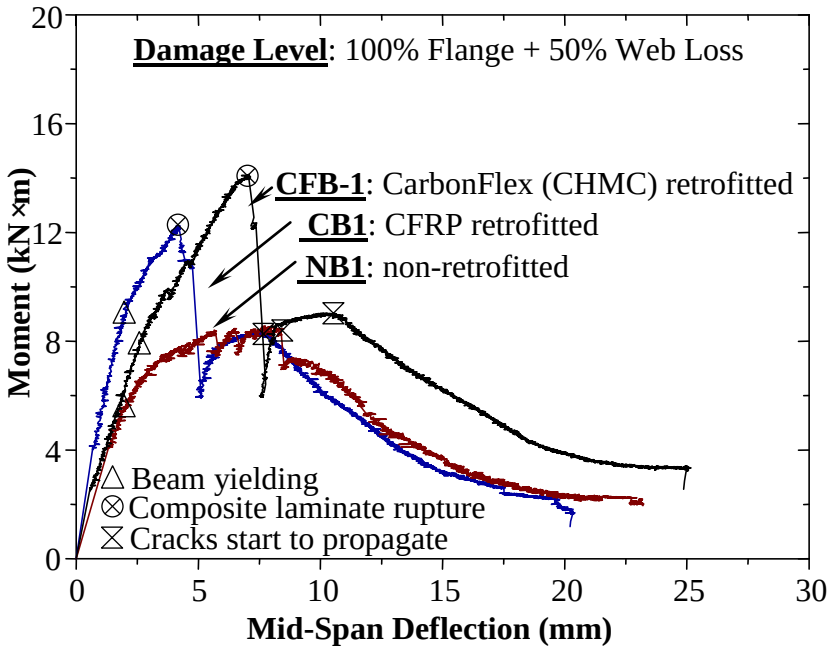

Figure 5.2.4.1. The load-deflection of beams with 100%F + 50%W notch damage

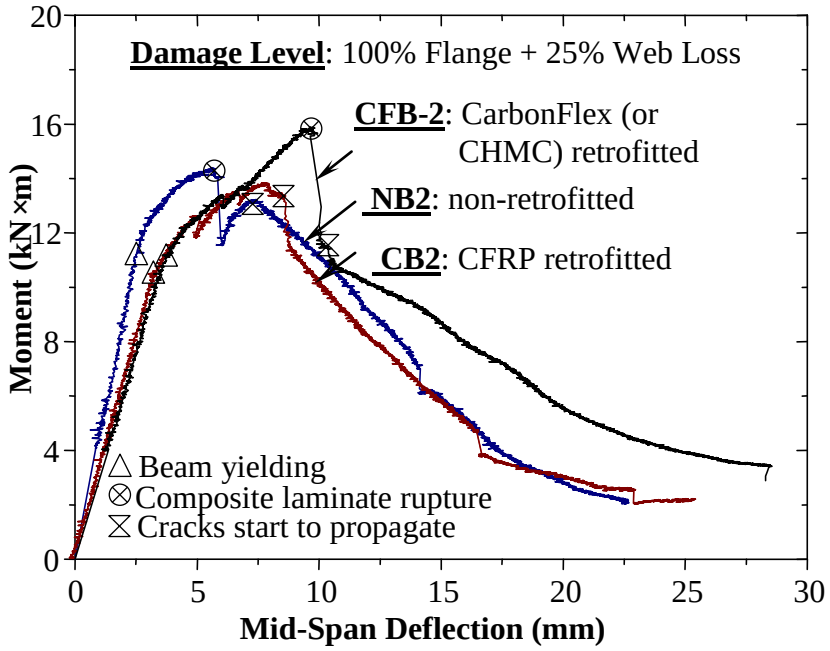

Figure 5.2.4.2. The load-deflection of beams with 100%F + 25%W notch damage

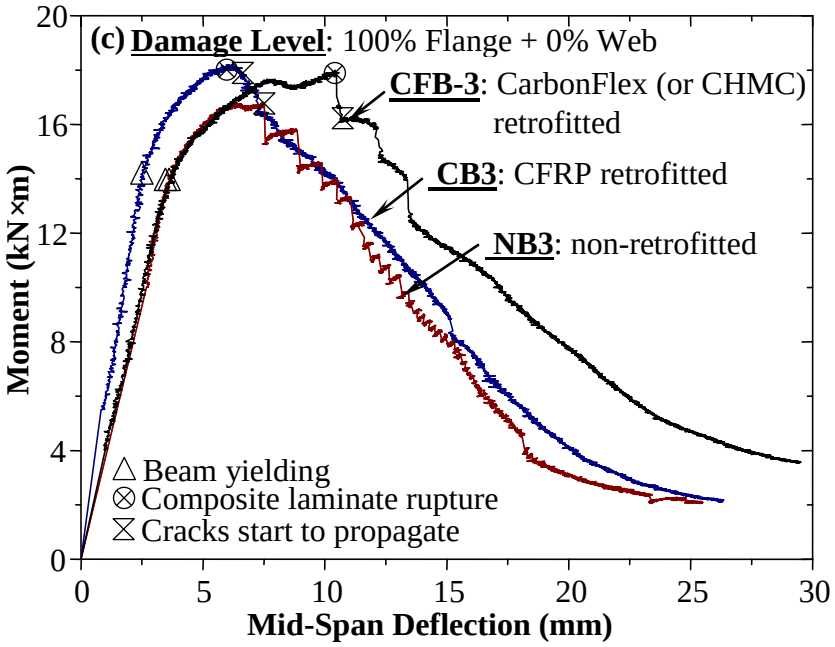

Figure 5.2.4.3. The load-deflection of beams with 100%F + 0%W notch damage

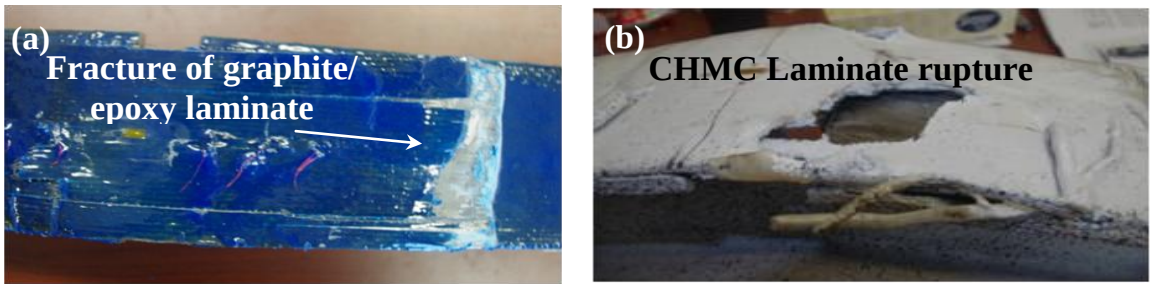

Figure 5.2.4.4. (a) Rupture of graphite/ epoxy laminate; (b) rupture of the CHMC laminate [106][11]

5.3. Finite Element Analysis of the Steel Beams With/ and Without the Composite Retrofit

5.3.1. Finite element models

Three dimensional finite element (FE) models were developed using the general purpose finite element analysis program, ABAQUS [112], see Figure 5.3.1.1 (a). Geometric and material nonlinearities were both taken into account in modeling the flexural behaviors of the retrofitted and un-retrofitted beams and the stress/ strain distributions at critical locations. Ten-node quadratic tetrahedron elements with modified formulation (C3D10M) [112] were used to model the W4×12 steel sections. The mesh was refined near the notch area in order to better capture the stress concentrations caused by the notch geometric discontinuity. A simple convergence study was carried out to obtain an appropriate mesh density, and the result has been presented in Figure 5.3.1.2. The loading head of the TMAC system was modeled using a four-node bilinear rigid element, and a frictionless contact was defined between the loading head and the top

[11] original figures provided by the author and reprint under the license permission of Elsevier

surface of the steel beam. For the retrofitted beams, the CFRP or CHMC laminate was modeled using the four-node S4R shell element (plane stress) and was connected to the bottom surface of the tension flange throughout the beam length via a set of spring elements (SPRINGA) [112]. The spring stiffness, k, can be calculated using equation (5.3.1.1), which is a function of: 1) the bonding area represented by each spring element, 2) the adhesive thickness δ, and 3) the elastic properties of the cured adhesive as

$$k = \frac{S}{\Delta x} = \frac{\int_{\Delta A} \tau dA}{\int_{\delta} \gamma d\delta} \tag{5.3.1.1}$$

where S is the shear force acting on the bonding-area, ΔA, represented by the spring element; Δx is the relative displacement between the retrofitting laminate and the substrate steel; τ is the interfacial shear stress and γ is the shear strain within the adhesive layer. The spring element model together with the variables in equation (5.3.1.1) is also shown schematically in Figure 5.3.1.1 (b). If ΔA and δ are small enough such that the interfacial shear stress can be assumed to be uniformly distributed within each represented area and the shear deformation is constant along the adhesive thickness, equation (5.3.1.1) can be rewritten as

$$k = \frac{\tau \Delta A}{\gamma \delta} = \frac{E_{ad.} \Delta A}{2(1+\upsilon_{ad.})\delta} \tag{5.3.1.2}$$

where Young's modulus $E_{ad.}$, Poisson's ratio $v_{ad.}$, and the thickness δ of the cured adhesive can be found in the manufacture data sheet [91]; and ΔA is determined based on the density of the spring elements assigned to the model. In addition, and as has been previously indicated in the experimental study, the interfacial cracks were initiated near the notch location, causing progressive laminate debonding until it was arrested by the

mechanical anchor, at which locations the relative displacements between the nodes on the laminate and the nodes on the substrate steel flange were fully constrained. The laminate debonding process has an influence on the flexural stiffness of the retrofitted beam, and the numerical simulation of the debonding process will be discussed in greater detail later.

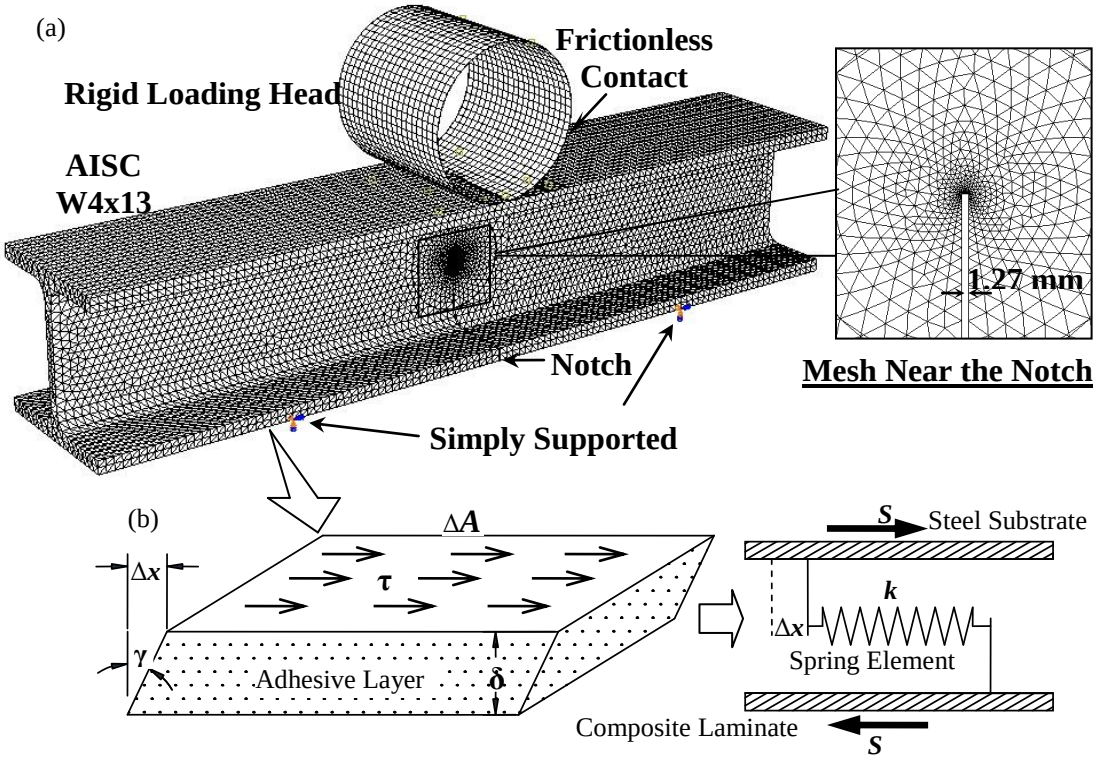

Figure 5.3.1.1. (a) The finite element mesh used in the numerical study; (b) figure schematically showing the spring element used to model the adhesive layer

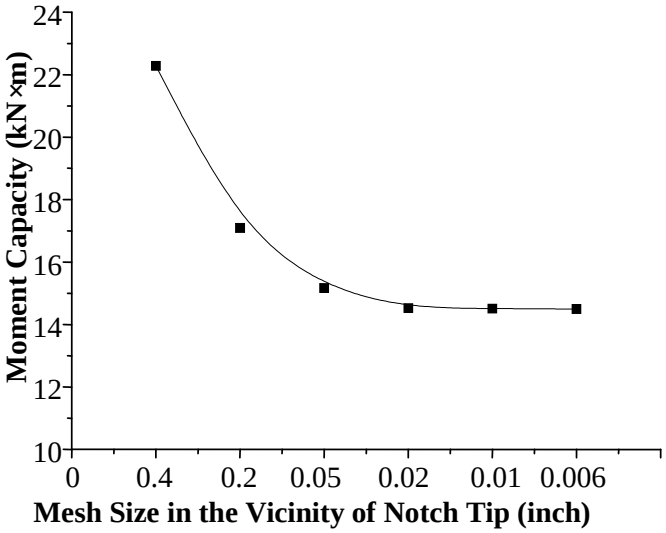

Figure 5.3.1.2. The convergence study result (in term of mesh size near notch tip)

5.3.2. Boundary Conditions and Material Constitutive Models

The modeling effort included beams having a hinged support on one side and a roller support at the other side, with a span length of 304.8 mm, or 12 inches, as per the experimental setup. The static load was applied incrementally in a displacement-controlled mode by imposing a displacement on the rigid loading head.

The A992 steel was assumed to follow elastic-perfectly plastic stress-strain behavior, and a linear elastic stress-strain relationship for the CFRP laminate was incorporated into the FE model because of the brittle nature of the CFRP composite. The elastic modulus of the CFRP laminate was set to be 144 GPa in tension, and the ultimate tensile strength was 2548 MPa. However, because of the high damage tolerance exhibited by the CarbonFlex (or CHMC) composite [30;113], its constitutive relationship exhibits a strong nonlinear tendency, see Figure 5.3.2.1. In the unidirectional tension coupon tests - according to ASTM D3039 specifications [113], the CarbonFlex (or

CHMC), behaved linearly elastically below approximately 25% of its ultimate strength, followed by a nonlinear segment until the material reached its peak strength of 2497 MPa. For most continuous-fiber reinforced composite materials, the damage and failure are typically attributed to the sequential breakage of the reinforcing fibers and the progressive microcracking in the matrix or matrix-fiber interfaces. The non-linearity of the stress-strain relationship of CHMC may be a result of the high energy dissipation capability of the newly developed multi-layered polymeric matrix system that helps to stabilize this crack growth and subsequent fiber damage during loading, resulting in substantial fracture toughness. Though the damage in the CHMC system is attributable to a series of crack initiations and propagations at the microscopic scale (as had been discussed in the previous chapters), the retrofit laminate was treated as a continuum media in the present FE modeling effort for computational ease; the stress-strain relationship of the CHMC was implemented by defining the material inelasticity [112], where the true stress-plastic strain relationship was calculated using the data shown in Figure 5.3.2.1. Finally, initial imperfections or residual stresses caused by the manufacturing process were not included in the modeling.

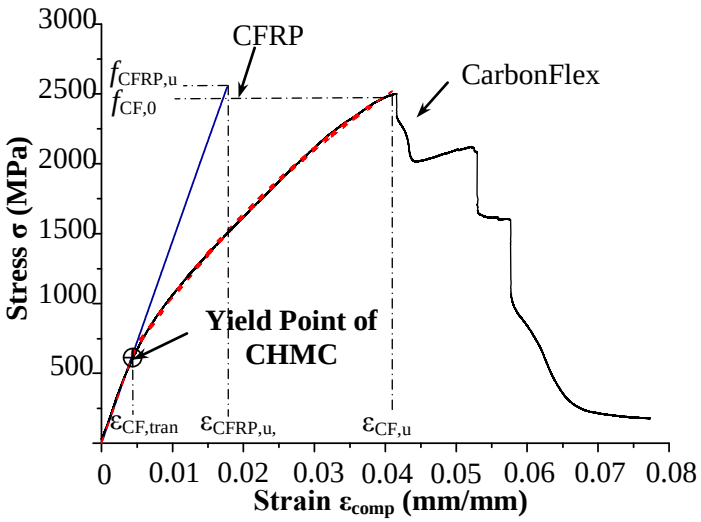

Figure 5.3.2.1. The finite element mesh used in the numerical study

5.3.3. Interfacial Stress and Debonding of the Retrofitting Laminate

In order to prevent the complete laminate debonding during loading, mechanical anchors were installed at the two ends of the retrofitted beams, see Figure 5.2.1.1 (b) (the "zoomed-in" view). However, due to the geometrical discontinuity at the notch location, stress concentrations occur in the vicinity of the notch as a result of the interfacial shearing that occurs between the retrofitting composite laminate and the substrate steel. Consequently, as the interfacial shear stress reaches the shear strength of the epoxy adhesive, interfacial cracks initiate, see Figure 5.3.3.1, and propagate towards the beam ends. Figure 5.3.3.2 shows a plot of the FEA results of CFB-1 with both assumptions of: (1) no debonding occurs, see the solid line in Figure 5.3.3.2; or (2) the laminate is held solely by the mechanical anchor (in the event of complete adhesive fracture), see the dash line in Figure 5.3.3.2, as compared to the experimental data. The experimental load-

deflection relation of CFB-1 was located somewhere between these two conditions, indicating a progressive debonding process that gradually decreased the flexural stiffness of the retrofitted beams. The study carried out by Gunes et al. [114] indicated that the total energy dissipated by the retrofitted system as a result of the debonding process may be determined by calculating the change in the potential energy:

$$\Delta \mathscr{D} = -\Delta \Pi = \frac{P_1^2}{2K_1} - \frac{P_2^2}{2K_2} \tag{5.3.3.1}$$

where P_1 is the load prior to the progress of debonding; P_2 is the load after the progress of debonding; and K_1 and K_2 are the corresponding elastic stiffness values calculated prior to and after the progression of debonding [114], also see Figure 5.3.3.2. Therefore, in the current study, the energy dissipated by the debonding process may also be expressed as

$$\Delta \mathscr{D} = \int \boldsymbol{\sigma}_{steel} d\boldsymbol{\varepsilon}_{steel}^{p} + \int \boldsymbol{\sigma}_{comp.} d\boldsymbol{\varepsilon}_{comp.}^{inelast.} + \int G_{ad.} dA_{de.} \tag{5.3.3.2}$$

where is $\int \boldsymbol{\sigma}_{steel} d\boldsymbol{\varepsilon}_{steel}^{p}$ is the energy that is dissipated by the plastic deformation of steel, see Figure 5.3.3.3 for the plastic zone near the crack-tip captured by DIC; $\int \boldsymbol{\sigma}_{comp.} d\boldsymbol{\varepsilon}_{comp.}^{inelast.}$ is any possible energy dissipation due to the inelastic deformation of the retrofitted composite during the debonding process; and $\int G_{ad.} dA_{de.}$ is the energy dissipated by the adhesive fracture, where $G_{ad.}$ is the fracture energy of the adhesive, and $dA_{de.}$ is the debonded area in incremental form. If the interfacial crack grows uniformly along the beam width, then equations (5.3.3.1) and (5.3.3.2) yield:

$$K_2 = \frac{K_1 P_2^2}{P_1^2 - 2K_1 \left(\Delta \mathscr{D}_{inelast.} + G_{ad.} W \Delta L_d \right)} \tag{5.3.3.3}$$

where $\Delta \mathscr{D}_{inelast} = \int \boldsymbol{\sigma}_{steel} d\boldsymbol{\varepsilon}^{p}_{steel} + \int \boldsymbol{\sigma}_{comp.} d\boldsymbol{\varepsilon}^{inelast.}_{comp.}$ is the energy dissipation due to material inelasticity; W is the beam width; and L_d is the laminate debonding length as shown in Figure 5.3.3.4. Thus, the stiffness of the retrofitted beam is related to the debond length, L_d, and the inelastic behavior of the materials via equation (5.3.3.3).

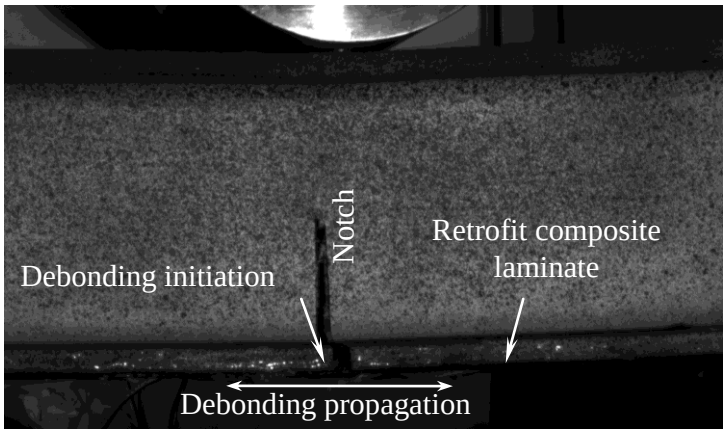

Figure 5.3.3.1. Picture showing the debonding initiation and propagation on the retrofitted steel beams

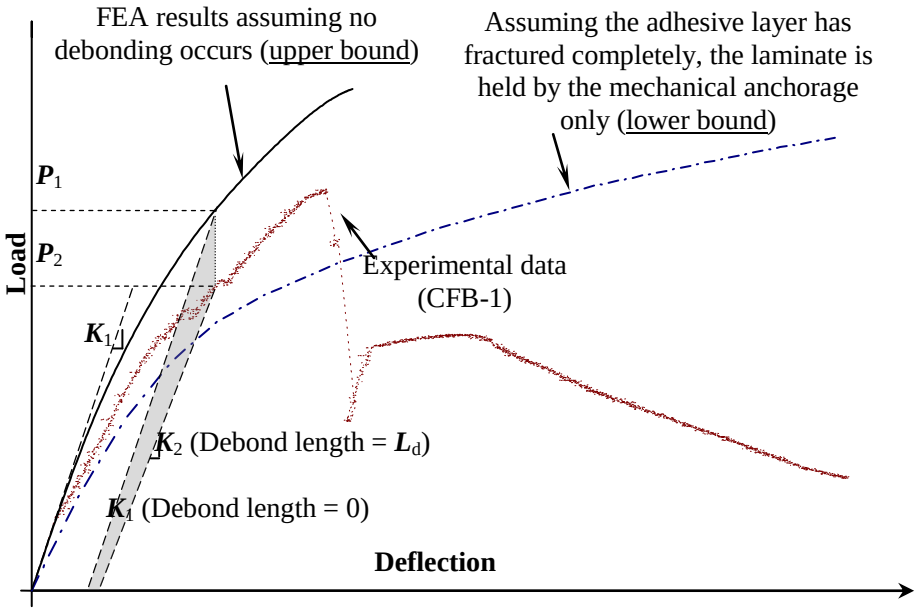

Figure 5.3.3.2. The influence of debonding on the flexural stiffness of retrofitted specimen

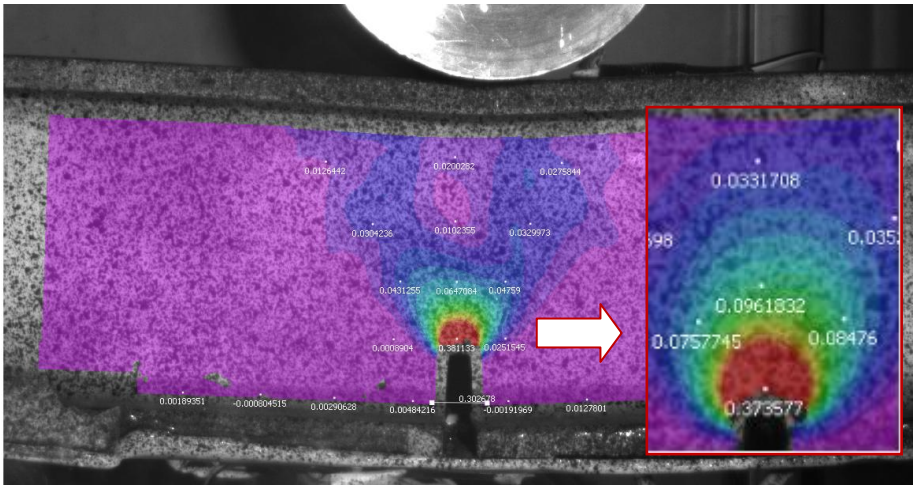

Figure 5.3.3.3. The near notch tip (principal) strain field obtained by DIC

Laminate debonding was assumed to propagate when the interfacial shear stress reached the shear strength of the adhesive, wherein the stiffness of the interfacial springs was assumed to be zero. The propagation of the debonding process was then modeled incrementally in the FE models, as shown in Figure 5.3.3.4. Figure 5.3.3.5 shows a plot of the interfacial shear stresses at the laminate-steel interface versus the distance to the notch for the CHMC retrofitted CFB-1 beam. The results indicate that the interfacial stress reaches the adhesive shear strength at very low load levels, i.e., $\boldsymbol{M} \leq 4.8$ kN×m, because of the resulting large stress concentrations near the notch, see curve ① in Figure 5.3.3.5. Laminate debonding initiated at this point. Stress distribution curves ①, ②, ③, and ④ in Figure 5.3.3.5 corresponds to the interfacial stress distributions when the maximum shear stresses reached the critical adhesive shear strength while the debond length $\boldsymbol{L}_d$ equal to 0 mm, 25.4 mm, 50.8 mm, and 76.2 mm; the load levels associated to the four curves are $\boldsymbol{M} = 4.8$ kN×m, $\boldsymbol{M} = 9.5$ kN×m, $\boldsymbol{M} = 12.0$ kN×m, and $\boldsymbol{M} = 13.1$ kN×m,

respectively. Consequently, the installed mechanical anchors stopped the debonding cracks at the anchors, thus enabling the beams to fail by laminate rupture as observed by the experiments, see Table 5.2.4.1.

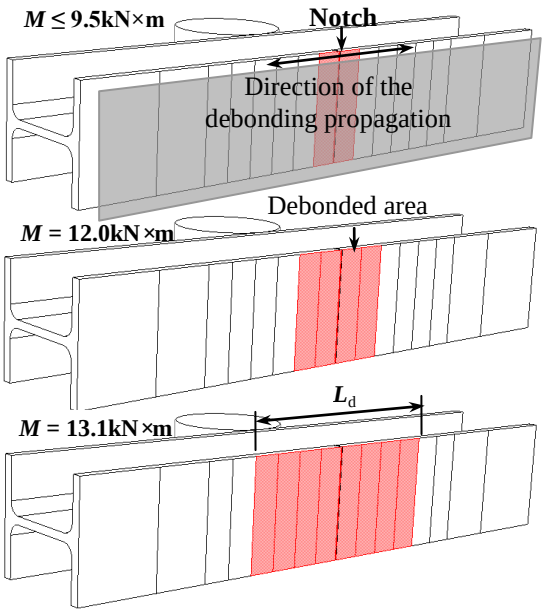

Figure 5.3.3.4. Debonding propagation in the finite element model

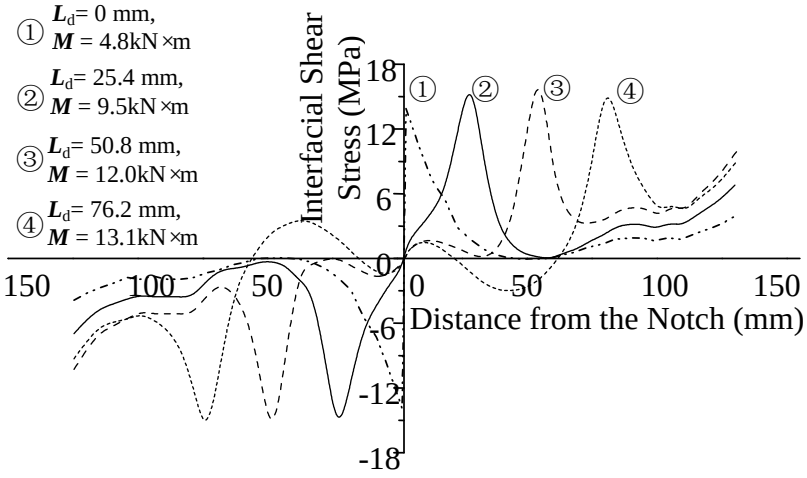

Figure 5.3.3.5. Interfacial shear stress distributions at various load levels

5.3.4.Results and Discussion

The Unretrofitted Beams

The load-deflection relationships that were obtained experimentally and that were computed using an FE analysis for the three notched beams NB-1, NB-2, and NB-3 are compared in Figure 5.3.4.1. This particular group of specimens was not retrofitted and served as the control group in order to quantitatively determine the effectiveness of the composite retrofit. The load-deflection curves of the notched beams predicted by FE models matched closely to the experimental test results, see Figure 5.3.4.1. Both the elastic stiffness and the load-carrying capacities of the non-retrofitted beams decrease as the damage level increases. The beams behaved linear elastically at the very beginning of the loading, and the load-deflection curve soon became nonlinear after a short elastic regime. Since the tension flanges of the test beams were notched and could no longer transfer stresses, the nonlinearity of load-deflection behaviors were primarily caused by the material plasticity near the notch tip locations. Figures 5.3.4.2 (a)-(c) presents the strain fields obtained by the DIC system of NB-1 - 3 instantaneously before the crack started to propagate; and the maximum principal strain distributions near the crack tip computed by the finite element analysis is shown in Figures 5.3.4.2 (d)-(f). The strain levels used to plot contours obtained by DIC and FEA are comparable, and the experimental strain values at particular points are presented in the close-up views in Figure 5.3.4.2. A comparison between these two groups of crack tip strain distributions shows excellent matching between the experimental and computational results. Both results indicate that the steel in the vicinity of the notch tip had yielded prior to the time

when the cracks started to propagate, i.e., the plastic zones had formed prior to the initiation of crack growth. Moreover, the size and shape of the crack tip plastic zones varied with the damage levels, i.e., the ratio of a_0/W, where a_0 is the original notch length and W is height of the beam web, see Figure 5.3.4.2. There has been a significant amount of theoretical [115-117], and experimental [118] work conducted on the investigation of the shape and size of the crack tip plastic zones. For ductile metals, such as the structural steel used in this study, where the von Mises yield criterion applies, the elastic-plastic boundary may be expressed in the following form under plane stress condition [119]

$$r = \frac{1}{2\pi}\left(\frac{K_I}{\sigma_Y}\right)\cos^2\left(\frac{\theta}{2}\right)\left[1+3\sin^2\left(\frac{\theta}{2}\right)\right] \qquad (5.3.4.1)$$

where σ_Y is the material yield stress, r and θ are the plastic zone radius and the angle with respect to the symmetric line, see [119]; and K_I is the first-mode stress intensity factor. The crack starts to initiate when K_I reaches a critical value, thereafter, the crack propagation becomes unstable. Under three-point bending, the crack toughness measurements, K_{IC}/σ_Y (measured experimentally) and thus the size of the plastic zone as calculated by equation 5.3.4.1, vary as a function of the ratio of a_0/W, and they peak when a_0/W ranges from 0.15 to 0.35 [120]. This is consistent with the observations shown in Figure 5.3.4.3, where the near crack-tip plastic zone is largest on NB-2 (a_0/W =0.25) at the time of crack initiation. Once cracking on the steel sections had initiated, the load carrying capacities of the specimens decreased continuously due to progressive section loss upon loading increase.

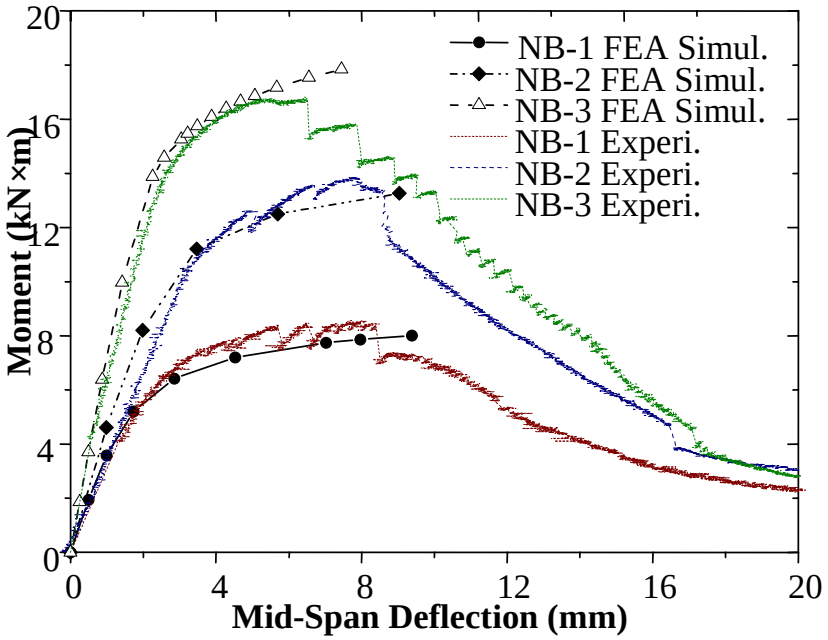

Figure 5.3.4.1. The load-deflection responses obtained by FEA as compared to the experimental results, NB -1 ~ 3

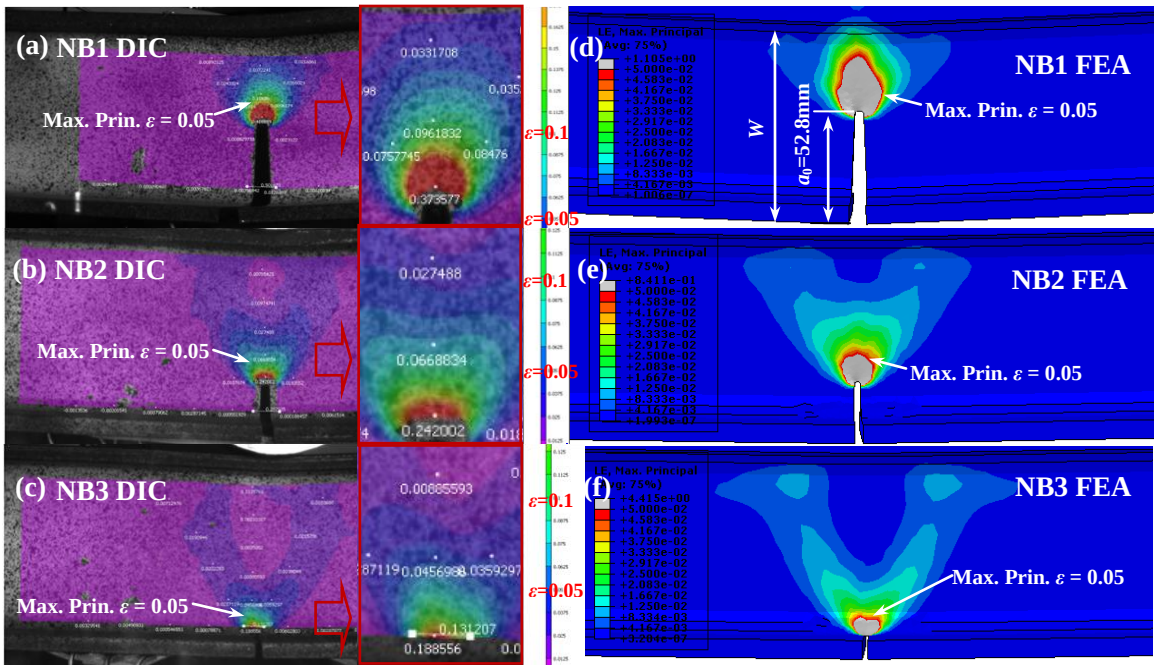

Figure 5.3.4.2. The strain distributions near notch tips DIC vs. FEA

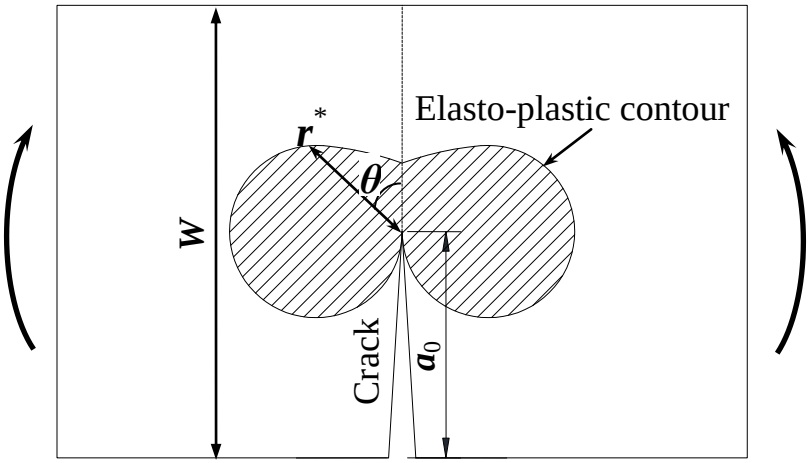

Figure 5.3.4.3. The illustrative figure showing the near crack-tip plastic zone

The CHMC and CF/ Epoxy Retrofitted beams

The computational and experimental load-deflection curves of the two beams retrofitted by CFRP (CB-1) and CHMC (CFB-1) were compared in Figure 5.3.4.4, and the crack-tip strain fields occurring at the time of laminate fracture and obtained by the digital image correlation (DIC) and finite element (FE) analysis are presented in Figures 5.3.4.5 (a)-(d) and Figures 5.3.4.5 (e)-(f), respectively. Because of the lower laminate stiffness of the CHMC with respect to CFRP, see Figure 5.3.2.1, the CHMC retrofitted beam has presented lower bending stiffness soon after the beginning stage of the loading curve, see Figure 5.3.4.4. Following the short elastic range, the load-deflection relation of CFB-1, as calculated by the FE analysis, becomes nonlinear due to a combination of the nonlinearity of the retrofitting composite and yielding of the steel near the crack tip accelerated by the presence of stress concentrations, see Figure 5.3.4.5. Just prior to laminate rupture, i.e., when the maximum tensile strain of the retrofitting CHMC laminate reaches the ultimate strain ε_u, a relatively large plastic zone formed in front of

the crack tip because of the high deformation capability of the CHMC, resulting in greater crack mouth opening distance (CMOD) at the time of laminate rupture as compared to its CFRP-retrofitted counterpart (see Figures 5.3.4.5 (a) and (e) in comparison to Figures 5.3.4.5 (c) and (f)). Following the rupture of the CHMC laminate, the loading curve - as calculated by the FE model - then followed the behavior of notched beam without the composite retrofit, see the dash line in Figure 5.3.4.4. Since the descending branch the stress-strain relation of the CHMC was not incorporated in the FE models, see the red dash line in Figure 5.3.2.1, the load drop on the simulated curve is more abrupt than that of the true experimental result. On the other hand, because of the nearly linear elastic behavior of CFRP, CB-1 had reached its peak load at a much smaller deflection than CFB-1, followed by the sudden load drop as observed in Figure 5.3.4.4. Because the crack propagation process has not been included in the modeling, the descending branches of the load-deflection relations due to crack growth were not captured in the FE simulation results.

In addition, it had been mentioned earlier that the sudden release of the strain energy by the rupture of the composite laminate may cause further damage to the substrate structures. The observations on the crack tip strain field lay evidence to the damage caused by the released energy. Figures 5.3.4.5 (c) and (d) show two adjacent frames of the crack tip strain fields obtained by DIC immediately before and after the CFRP fracture of CB-1. Since the data acquisition frequency of the DIC system was set to be two frames per second and the loading rate was set to be very low (at 0.04 mm/sec) in order to exclude time-related phenomena, the change in the strain field in Figures 5.3.4.5 (c) and (d) is assumed to be caused solely by the laminate rupture. A dramatic

increase in the maximum principle strains has been observed immediately following rupture of the CFRP for CB-1, which clearly indicates the sudden release of strain energy caused by the retrofitting composite fracture, and consequently resulting in the strain increase in the substrate structure. Furthermore, the initiation of a crack at the notch tip, see Figure 5.3.4.5 (d), provides proof of the substrate damage that was caused by the sudden energy release. On the other hand, Figures 5.3.4.5 (a) and (b) present the crack-tip strain field immediately prior to and after the CHMC laminate rupture for beam CFB-1. After comparing the two figures, the strains before and after the facture of the CHMC have not changed prominently; and in contrast to beam CB-1, no obvious damage, such as cracking, has been observed in CFB-1 immediately following the time when the CHMC had reached its ultimate strain. These observations indicate that the rupture of the CHMC progressed in a significantly more prominent ductile manner than CFRP, so that the strain energy stored in the retrofitting laminate was gradually released. The measurements of the CMODs for the two beams immediately prior to and after laminate fracture also support the preceding discussion. For CB-1, the COMD corresponding to Figures 5.3.4.5 (c) and (d) were 0.2066 mm and 0.2663 mm, respectively; and the COMD corresponding to Figures 5.3.4.5 (a) and (b) were 0.2295 mm and 0.2459 mm, respectively, for CFB-1. The increase in CMOD for the former case (0.0597 mm) is approximately 2.64 times larger than the later CHMC retrofitted beam (0.0164 mm).

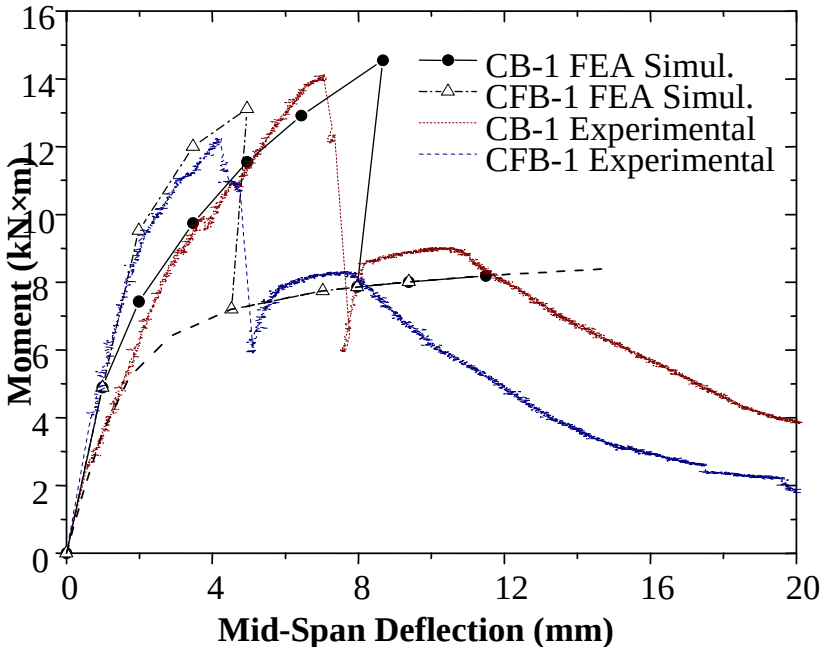

Figure 5.3.4.4. The comparison between experimental and FE analysis results for the retrofitted steel beams CB-1 and CFB-1

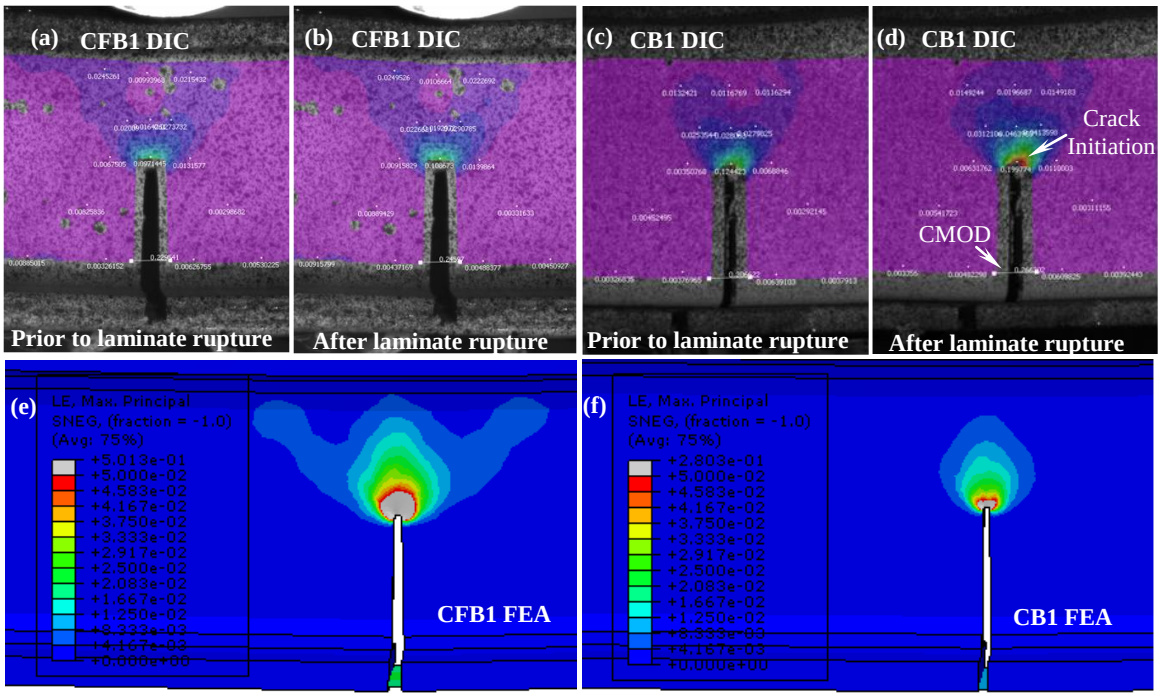

Figure 5.3.4.5. The maximum principal strain fields near notch tip for CFRP and CHMC retrofitted beams: (a) DIC results taken immediately before the CHMC rupture of the CFB-1; (b) DIC results taken immediately after the CHMC rupture of the CFB-1; (c) DIC results taken immediately before the CFRP rupture of the CFRP retrofitted CB-1; (d) DIC results taken immediately after the CFRP rupture of CB-1; (e) FEA results showing the crack tip strain field at the moment of CHMC rupture (CFB-1); and (f) FEA results showing the crack tip strain field at the moment of CFRP rupture (CB-1) [106][12]

5.4. Summary and Conclusion

In this chapter, nine notched wide-flange steel beam specimens were categorized into three groups: unretrofitted beams, carbon fiber reinforced polymer (CFRP)-

[12] Original figures provided by the author and reprint under the license permission of Elsevier.

retrofitted beams, and the Carbon-fiber Hybrid-polymeric Matrix Composite (CHMC) - retrofitted beams. The experimental test results are analyzed and compared to those obtained by finite element analysis. The following conclusions can be drawn:

- The load capacities of the notched steel beams were increased between the following ranges: 3.8% to 42.9% and 6.9% to 84.9% following a retrofit strategy using CFRP and the CHMC laminates, respectively, with respect to the unretrofitted specimens. In addition, the CHMC-retrofitted beam showed marginal increase in strength recovery, which is defined as the increase in peak strength with respect to the unretrofitted beam. However, the strength sustainability and the displacement ductility (related to the material energy-dissipation) of the CHMC-retrofitted beams are significantly larger than those of the CFRP-retrofitted beams. In particular, the increase in the peak-load deflections of the CHMC-retrofitted beams vary between 67.8% to 73.1% than those of the CFRP-retrofitted specimens.
- The maximum principal strain fields obtained by both FE analysis and DIC indicate that:

1. significant yielding of the steel beams had occurred near the crack-tip prior to crack propagation as evidenced by the formation of the crack-tip plastic zones;

2. a comparison between the strain distributions and CMODs immediately prior to and after the rupture of the retrofitting laminates indicates the ability of the CHMC (or CarbonFlex) to sustain some strengths after the damage was initiated, while the complete failure of CFRP occurred in an abrupt manner, as expected.

Chapter 6.

REHABILITATION AND RETROFIT OF FATIGUE DAMAGED CONCRETE ENCASED STEEL GIRDERS USING CHMC

This chapter further explores the feasibility of using the newly developed CHMC to retrofit damaged large-scale infrastructure components, however, in this case three identical concrete-encased steel girders that underwent high-cycle fatigue loading were pre-damaged to the same level. Then the fatigue-damaged girders were repaired using both CHMC and conventional graphite/ epoxy, or CFRP, where the later was acting as a control specimen. The experimental results are presented and discussed, and a computational algorithm - CSRAP-flex was developed based on the "fiber section" analysis method. Equations to evaluate the load capacity of retrofitted beams are derived and validated by the experimental results.

6.1. Introduction

Concrete-encased steel composite structural members, also referred to as steel reinforced concrete (SRC) composite members, are widely used in the design of building columns [121-123] and bridge piers [124]. In the region of high seismicity, they constitute part of the lateral and axial force resistant system due to their superior performance in combining high load-carrying capacity and high ductility. The integration of concrete and a wide-flange steel section provides two distinct advantages: (a) they provide a tremendous increase in concrete confinement via the steel flanges, and (b) they provide a restraint against the buckling of the encased steel section via the

surrounding concrete; moreover, the concrete encasement also protects the steel against fire and environmental-induced deterioration [121;122]. Several design codes and specifications in the United Stated including ACI 318-08 [125] and AISC-LRFD (2005) [126] have evolved to provide the design recommendations for encased composite steel-concrete structural members. Concrete/ steel composite sections are commonly used as bridge girders for middle-span highway bridges in which case the wide-flange steel section is connected to the upper reinforced concrete (RC) deck through connectors such as shear studs. To protect the steel section against corrosion, fire, or possible load-induced buckling, the steel girders, in certain cases, are encased in concrete for new construction or later retrofitting [127].

Bridge girders are particularly prone to experiencing fatigue damage as a result of repeated traffic loads [128;129]. The ASCE Committee on Fatigue and Fracture Reliability reported that 80-90% of failures in steel structures are related to fatigue and fracture [130]. Due to the high cost of reconstruction and the lengthy process of acquiring construction permits, the repair and retrofit of damaged bridge structures is typically recommended. Due to the significant energy dissipation capability and superior ductility that CHMC has exhibited in the study of vibration suppression and steel beam retrofit, the CHMC will be explored, herein, as an alternative retrofitting and strengthening exterior composite used to stabilize the crack growth in damaged concrete-encased steel sections. In this chapter, three large-scale fatigue-damaged concrete-encased steel girders were retrofitted using externally bonded CFRP and CHMC; and the retrofitted specimens were re-tested to failure under quasi-static loading. The experimental results were discussed and analyzed. A computer algorithm named

"CSRAP-Flex" (Concrete Structure Retrofit Analysis Program) was developed based on the "fiber section" analysis method to simulate the mechanical behavior of the retrofitted girders.

6.2. Experimental Program

6.2.1. Configuration and Pre-damage Levels of the Fatigue Damaged SRC Girders

Three fatigue-damaged concrete- encased steel beam specimens (labeled as B1, B2, and B3 in Table 1) were retrofitted using CHMC, whichis also known as CarbonFlex, for specimens B1 and B3, and the carbon fiber reinforced epoxy, that has also been referred to as CFRP, for specimen B2. The dimensions of each beam were 3050mm (length), 220mm (width), and 400mm (depth). The encased steel sections (W250×45 SI, or W10×30) were made of ASTM A572 Grade 50 steel, having an overall height of about 270mm and a half-flange width of 70mm. The three specimens had been initially damaged by fatigue load, resulting in significant cracking in the encased steel. The induced fatigue load was intended to damage the virgin specimens which were tested via four-point cyclical bending with minimum and maximum moment values within the pure bending span of $\boldsymbol{M}_{\min}$ = 22.45 kN × m, and $\boldsymbol{M}_{\max}$ = 96.23 kN × m respectively, having a load range of $\Delta\boldsymbol{M}$ = 73.78 kN × m. The fatigue pre-existing cracks had been initiated in the tension side flange of the encased steel section and had propagated through the width of the flange and approximately half-way into the web. The lengths of the cracks that had propagated into the webs were measured as 122mm, 130mm, and 126mm in beams

B1, B2, and B3, respectively, as shown in Figure 6.2.1.1. The damage levels in the three specimens were nearly identical with an a_0/W ratio of approximately 0.5, where a_0 is the initial length of the fatigue crack and W is the overall height of the web of the encased steel. Concrete had crushed at the mid spans due to excessive deflection during one of the last cycles of the fatigue loading. The damage conditions and thickness of retrofitting composites of the three specimens are summarized in Table 6.2.1.1; material properties and section dimensions are listed in Table 6.2.1.2.

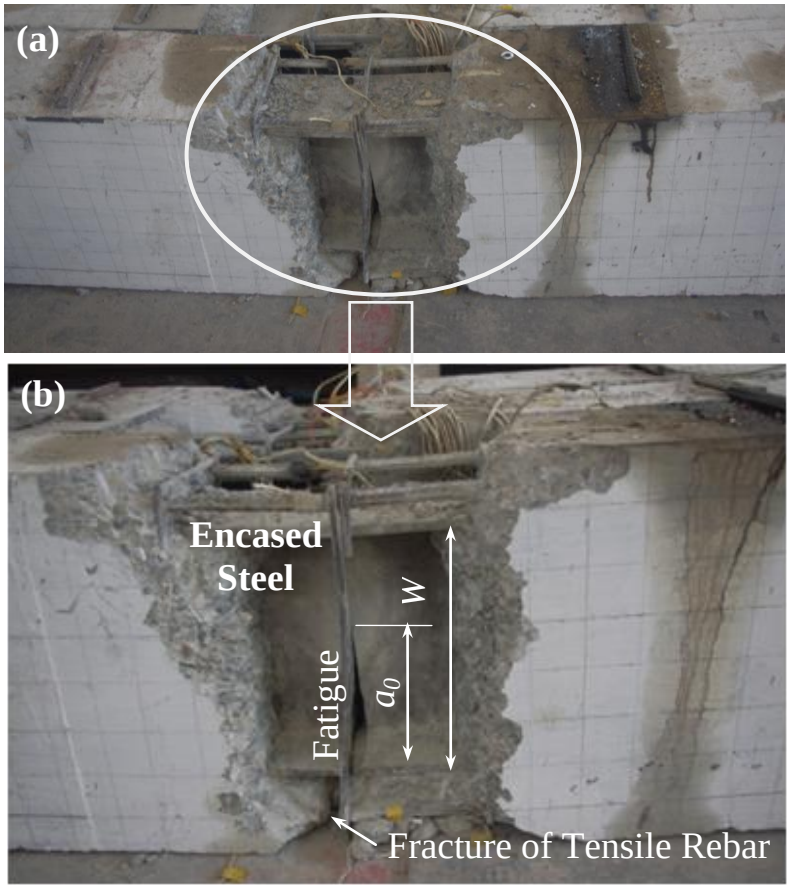

Figure 6.2.1.1. The fatigue damage of concrete- encased steel girders

Table 6.2.1.1.

Damage levels and retrofit composite type of the SRC girders

Spec. #	a0	a0/W	Ten. Reinf.	Crack Welding	Retrof. PMC	Thickness of PMC[13]
B1	122mm	0.452	Fractured	Yes	CHMC	0.501mm
B2	130mm	0.481	Fractured	Yes	CFRP	0.501mm
B3	126mm	0.467	Fractured	No	CHMC	0.501mm

Table 6.2.1.2.

Dimension and material properties of the retrofitted SRC girders

Section Properties	Concrete	Steel(Rein.)	Steel(Shape)	CarbonFlex
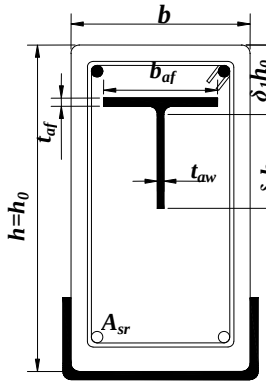	E_c=45.6GPa f_c'=65MPa $\varepsilon_{c,u}$=0.004[14] $\delta_1 h_0$=75mm $\delta_2 h_0$=200mm	E_s=200GPa f_y=385MPa A_{sr}'=307mm^2 A_{sr}=0mm^2 a_{sr}'=32mm	E_s=200GPa f_a=400MPa b_{af}=140mm t_{af}=10mm h_{af}=270mm t_w=8mm	E_{CF}=144GPa $f_{CF,t}$=628MPa $\varepsilon_{CF,t}$=0.0045 $f_{CF,0}$=2500MPa $\varepsilon_{CF,0}$=0.041 t_{comp}=0.501mm b_{comp}=300mm[15]

6.2.2. Repair and Retrofit Procedures for the Damaged Specimens

In order to restore the load capacity of the fatigue damaged girders, several retrofitting steps were carried out, see Figure 6.2.2.1, including:

(1) Applying an orthopedic force to offset the residual deflections of the damaged sections and to "re-shape" the beams to their original shapes.

[13] Due to the difficulty of controlling the thickness of matrix on-site, the thickness of PMC was taken as the thickness of dry fiber according to ACI 440.2R-08.
[14] Ultimate strain of confined concrete.
[15] b_{comp} is a equivalent value considering the flipped over part of strengthening bottom plate.

(2) Welding of the existing fatigue cracks in the webs and tension flanges of the encased steel shapes were welded, see Figure 6.2.2.2. The cracked encased steel shape in specimen B-3 was left un-welded to provide a comparison with specimen B1 and also to simulate the field case when the welding is not accessible.

(3) Grouting repair of the heavily damaged concrete near the mid-span using the rapid-setting cementious grout that had a 3-day strength of 65.2 MPa; and epoxy injection to fill the hair-line cracks and small surface voids. The surface voids were filled with a highly viscous epoxy-based putty to create smooth surfaces for the forthcoming composite laminates. All concrete surfaces were sandblasted and cleaned; and the corners were rounded with a concrete grinder per specifications of ACI 440 [43] to avoid possible stress concentration in the retrofitting composite laminates.

(4) Lastly, beams B1 and B3 were retrofitted using the CHMC (or CarbonFlex), and beam B2 was retrofitted using carbon fiber reinforced epoxy (or CFRP) in order to compare the ability of CHMC to sustain the retrofitted strength and provide ductility in beams that had no effective tensile reinforcements following fracture of the welded steel section.

The repair and retrofit steps of the fatigue damaged SRC girders are summarized in Figure 6.2.2.1. The "U"-jackets were provided to avoid possible debonding of the bottom laminate and delamination of the concrete-cover. Besides, each specimen was also wrapped at its mid-span over a length of 975mm in order to provide confinement to the repaired concrete. The details of the retrofitting schemes are shown in Figure 6.2.3.1 (b).

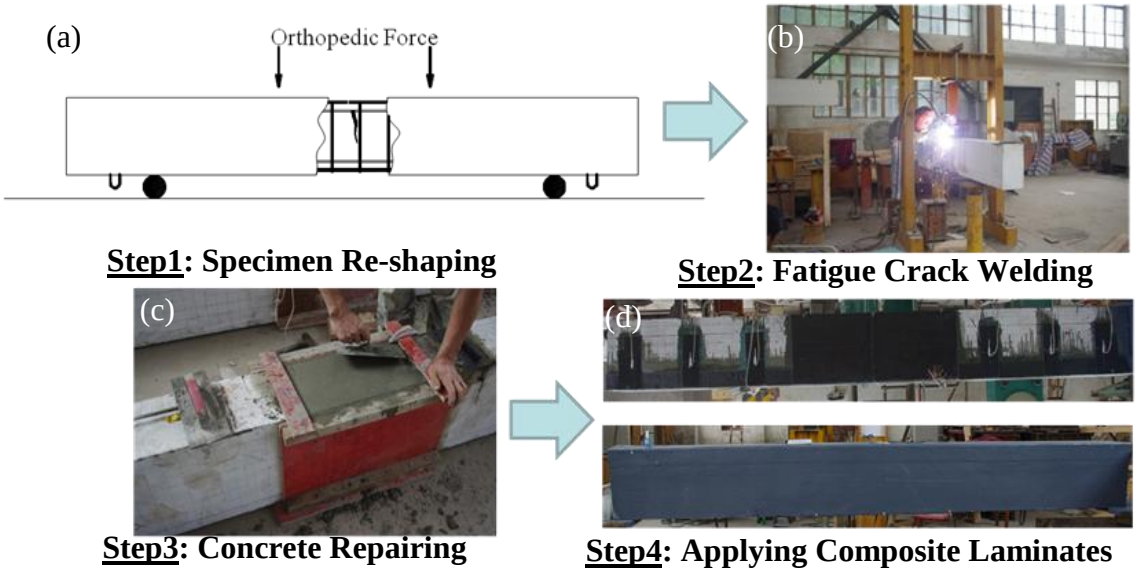

Figure 6.2.2.1. The repairing/ retrofitting steps for the fatigue damaged SRC girders: (a) applying an orthopedic force to compensate the residual plastic deformation; (b) fatigue crack welding ; (c) replacement of damaged concrete; (d) applying the composite wraps

Figure 6.2.2.2. The welded fatigue crack on the encased steel section, crack length shown in centimeters

6.2.3. Experimental Setup and Instrumentation

The experimental test setup is shown schematically in Figure 6.2.3.1. The specimens were simply supported, having a span length of 2900mm, and loaded using a static four-point bending configuration. Two hydraulic actuators, each having capacity of 600 kN, were placed at 800 mm apart. The load, *P*, was incrementally applied using load control as ΔP at 1/20th increments of the calculated yielding moment until the tension flange of the encased steel yielded; then a displacement control scheme was used thereafter. The mid-span deflections were measured using three vertical LVDTs installed at the mid-span and at the supports of the test specimens; the net mid-span deflection was calculated as the average value of the LVDT support readings subtracted from the mid-span LVDT reading, see Figure 6.2.3.1 (a). Electronic resistance strain gauges were mounted on the concrete surfaces, see Figure 6.2.3.1 (b); the tension flanges (gauge numbers S1, S2, and S3 in Figure 6.2.3.1 (c)) and compression flanges (gage number S4) of the encased steel sections in specimens B1 and B2. One strain gauge was mounted near the crack tip at the welding seam in order to capture the welding fracture in beams B1 and B2, see Figure 6.2.3.2. Strain gauges were also installed on the composite wraps: (1) the composite bottom laminate (gauges F3, F4 were mounted at mid-span; F5 and F6 were installed on the bottom surface each at a distance of 800mm from the mid-span), (2) the composite "U"-jackets (gauges F7 - 12), and (3) the center composite wraps (gauge F13 and F14 at the center of the section depth). The picture showing the test setup is presented in Figure 6.2.3.3.

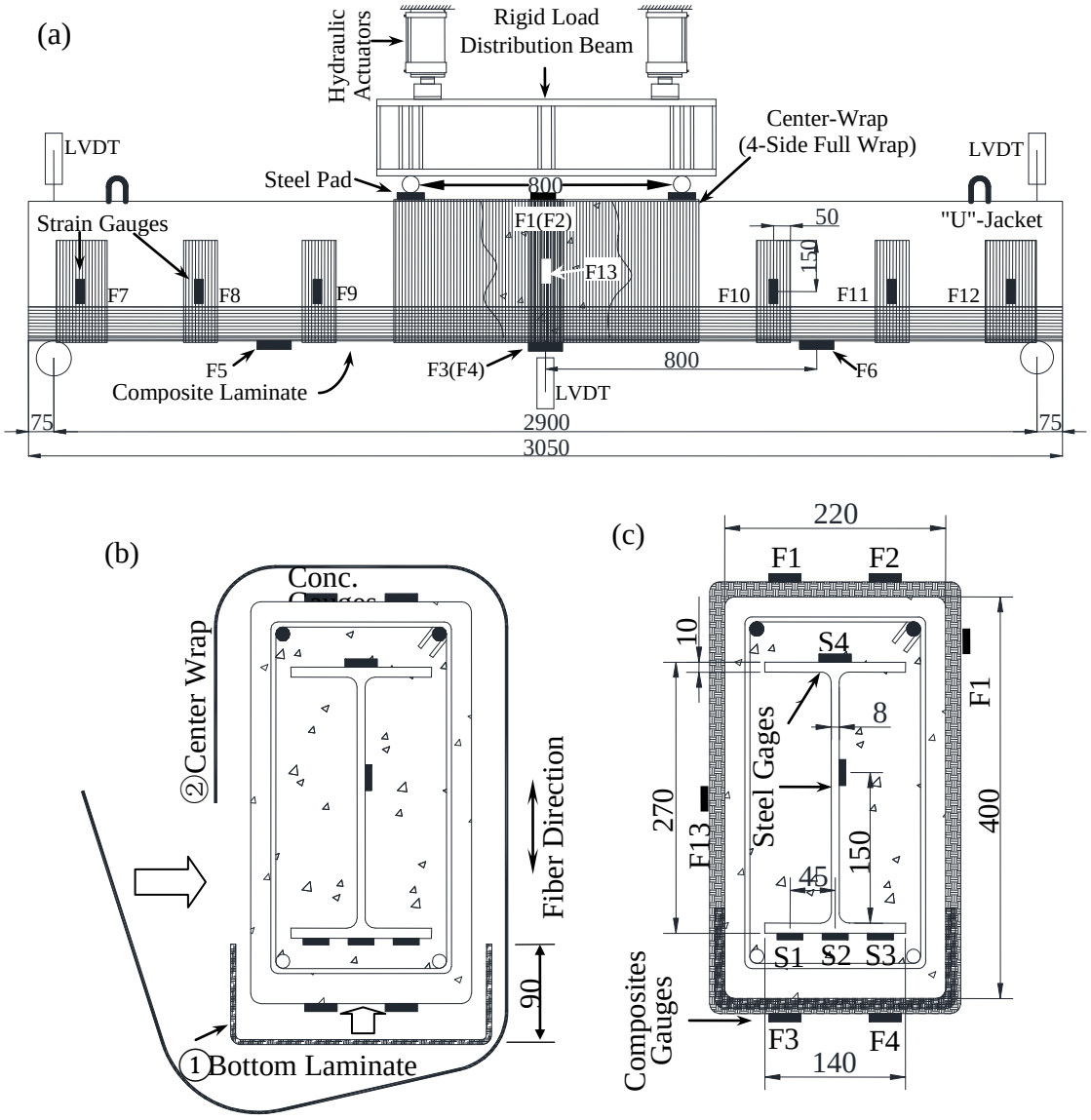

Figure 6.2.3.1. Figures schematically showing the test setup and instrumentation of the (a) Test setup and instrumentation (elevation view) ; (b) locations of strain gauges at mid-span on the SRC specimen and layup procedure of bottom laminate and center wraps; (c) locations of strain gauges at mid-span on the exterior of the laminate [30][16]

[16] Original figure provided by the author, and reprint with the permission of Elsevier.

Figure 6.2.3.2. Strain gauge installed at the fatigue crack tip to monitor the weld fracture

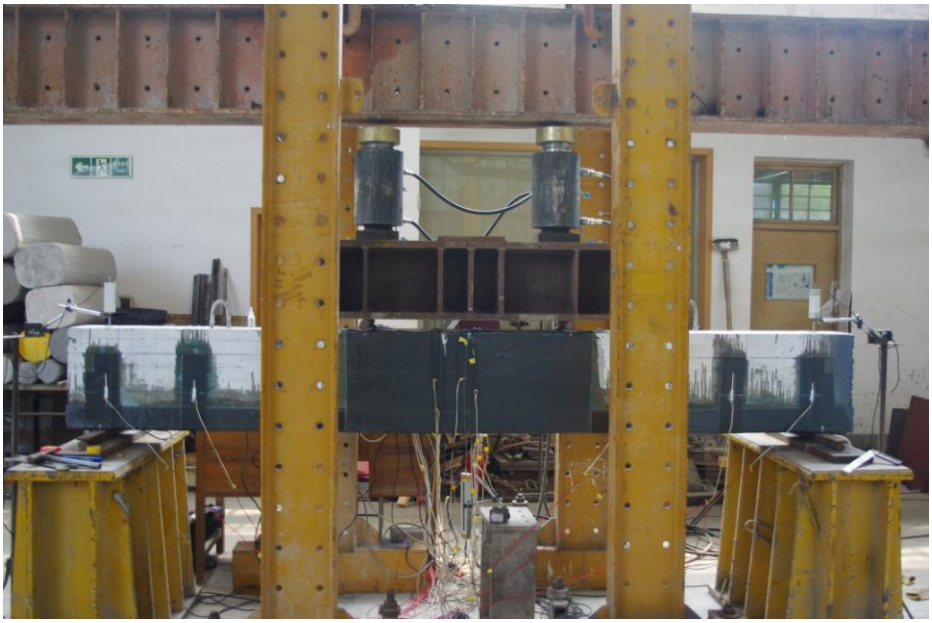

Figure 6.2.3.3. Picture showing the experiment setup (B2 - CFRP retrofitted SRC girder)

6.2.4. Experimental Results and Discussion

The load-deflection responses of the three retrofitted concrete encased steel beams are summarized and presented in Figure 6.2.4.1 (a). The initiation of flexural cracking in the concrete was not visually observable due to the overlying wraps. As a result, the first occurrence of sudden decrease in concrete strain gauge readings on the bottom surface was correlated to the concrete cracking moment, M_{cr}. The load-deflection relationships of the retrofitted beams remained linear until concrete cracking. At this point, since the corresponding strains in the bottom laminate were low with respect to the failure strain of the strengthening composites, i.e. 0.017 for CFRP and 0.041 for CHMC, the concrete cracking moments of the three beams are independent of the retrofitting material (CFRP or CHMC), see Figure 6.2.4.1 (a). The slopes of the load-deflection curves slightly decreased at concrete cracking and remained nearly constant until the tension flange of the encased steel yields, in this case at a load of approximately 375 kN. Since the stress in the bottom composite laminate of each specimen was still low at the point of steel tension flange yielding (nearly 15% of its ultimate strength, which lies within the linear range for both CHMC and CFRP), there was minimal difference between the load-deflection responses of B1 and B2 prior to yielding of the encased steel.

Due to the defects and the residual stresses induced by the welding process, the weld seam on the encased steel fractured before a plastic hinge had formed in the encased steel. Consequently, abrupt drops on the load-deflection curves of B1 and B2 were observed, see Figure 6.2.4.1 (a). The discussion of weldments fracture falls out of the range of this current work, however, various fracture mechanics models, including

simplified linear elastic fracture mechanics (LEFM) models [131] and finite element crack models [132], are available for analyzing the fracture of welded structural steel. At the moment of repairing welds fracture, a sudden release of strain energy in the vicinity of the welds was signified by an abrupt drop in the strain gauge readings on the steel tension flange. The ultimate failure of B2, which was attributed to the sudden rupture of the CFRP tension laminate, occurred soon after the weld had fractured, as shown in Figure 6.2.4.1 (a) and (c). On the other hand, B1 was able to sustain approximately two-thirds of the peak load via the CHMC's ability to dissipate the sudden burst of strain energy released by the weld fracture, resulting in substantial ductility. Complete failure of B1 occurred when the CHMC laminate ruptured, at which point the ultimate deflection in the beam was nearly three times the deflection when the weld had initially fractured, see Figure 6.2.4.1 (a) and (b). One distinction that separates the CHMC- and CFRP-retrofitted systems is the post-peak-load-deflection responses of B1 and B2, where the damping properties of CarbonFlex, which are a function of the cohesive interfacial interaction between the constituent polymers, as has been discussed in previous chapters, help retain a significant portion of the peak strength of the retrofitted beam by dissipating energy that may otherwise rupture the brittle carbon-fiber in a progressive fashion.

Since the fatigue crack in specimen B3 was not welded for the purpose of comparison, an interesting observation was made on the force-deflection responses in specimen B1 and B3. A localized damaged region in the vicinity of fatigue crack on the encased steel was identified as the "fatigue crack affected region," which is a main contributor to the total deflection of specimen B3. For a given mid-span deflection, the corresponding strain as measured in the CHMC laminate is significantly higher in B3

than it is in B1, per the strain gauge readings F3 and F4, see Figure 6.2.3.1 (c). This may be explained by the dramatic upward shift of the neutral axis in B3 at the time of initial concrete cracking, in combination with the strain localization in the "fatigue crack affected region." As a result, the moment capacity and flexural stiffness of B3 was significantly lower than that of B1 and B2 due to the section loss of the encased steel - caused by the pre-exist fatigue crack and crack propagation which had initiated at early load stages.

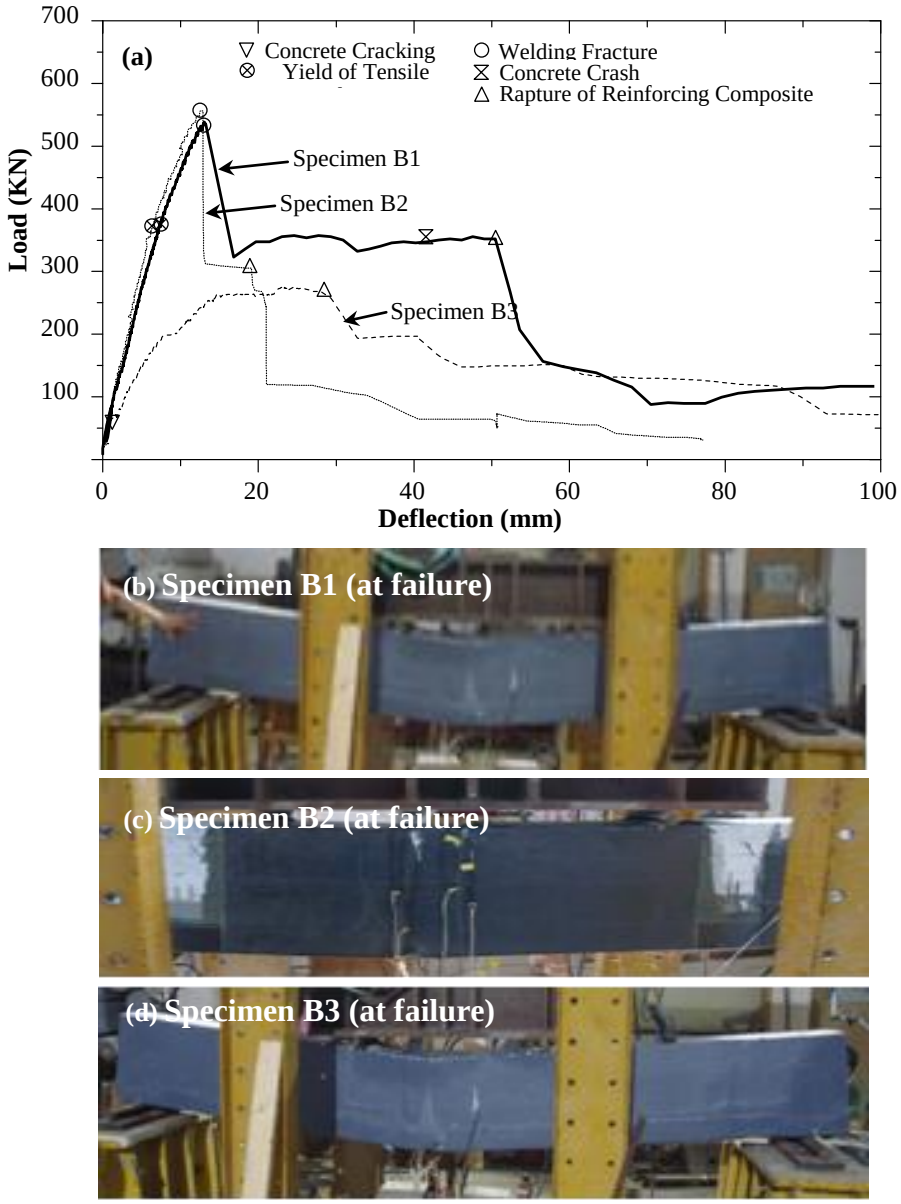

Figure 6.2.4.1. Experimental test results and failure modes of the SRC girders

6.3. Numerical Model and Analysis Results

6.3.1. Development of the CSRAP-flex Model for Analyzing Damaged SRC Girders

A non-linear iterative program called CSRAP-Flex was developed to analyze the flexural behavior of already-damaged concrete-encased steel beams retrofitted using

externally bonded composite materials (e.g., CFRP or CHMC) where the existing crack on the encased steel may or may not have been welded and repaired. CSRAP-Flex is developed using a fiber section analysis method [122;133], as illustrated in Figure 6.3.1.1 (a), assuming that plane sections remain plane and that the nonlinear response of concrete is dependent on the degree of confinement. According to Figure 6.3.1.1 (a), CSRAP-Flex model incorporates fully-confined and partially confined concrete models where the former is confined by the encased steel and center wrap laminate, and the latter is confined by just the center wrap. The program is developed assuming that concrete, reinforcing rebar, encased steel section, and the strengthening composite materials are perfectly bonded to their respective adjacent component(s) in order to ensure strain compatibility. The moment-curvature analysis is then executed by increasing the compressive strain variable ε_c in Figure 6.3.1.1 (b), and iteratively determining the location of the neutral axis, *c*, by establishing force equilibrium across the section. Constitutive models of each material are used to obtain the stresses in each "fiber section," $A_{i,j}$ in Figure 6.3.1.1 (a). The moment of the entire section is subsequently calculated by integrating the stress over the section and then repeat at each strain increment.

The load-deflection responses of B1 and B2 were obtained by integrating the curvature distribution along the beam for every load step before the welds had fractured [134]. The loading function used during experimental testing was incrementally modeled in CSRAP-Flex, and at each load step, the moment was calculated as a function of the cross-sectional strain and the corresponding curvature. It was observed that the repairing welds in specimens B1 and B2 had fractured due to the defects and residual stresses

induced by welding [135]. If the welds were assumed to behave linear elastically prior to fracture and the principles of linear elastic fracture mechanics (LEFM) apply, the welding fracture occurs when the stress intensity factor, K, reaches a critical value [131;136]. Various fracture mechanics models, including simplified LEFM models [131] and two- and three- dimensional finite element crack models [132], have been used to analyze the fracture mechanics of welded structural steel. However, because of a lack of critical information such as the flaw size and residual stress distribution to calculate the weld fracture moment M_{wf}, the present study utilizes M_{wf} which was determined experimentally and was input into CSRAP-Flex. When the weldments started to fracture, the stress flow was interrupted in the vicinity of the crack because a portion of the encased steel section, namely the tension flange and a portion of the web, could no longer adequately transfer stresses. This region was previously identified as the "fatigue crack affected region," which is illustrated in Figure 6.3.1.1 (f) resulting in the section loss shown in Figure 6.3.1.1 (d). Cross sections outside of this region were identified and modeled as "sections with intact encased steel," see Figure 6.3.1.1 (e). Recent studies by Hmidan et al. [39] on the flexural behaviors of notched W-shape steel beams retrofitted by CFRP were used to approximate the radius of the “fatigue crack affected region” as that of the crack length, a_0, for cases of a_0/W=0.5, where a_0 is approximately L_{ca}, which is the half-length of the idealized region, see Figure 6.3.1.1 (f). Furthermore the particular influence of local stress concentrations specifically near the crack tip were assumed to have minimal influence on the overall calculated moment because: (a) the web thickness of the encased steel section is small to begin with, and therefore, the resultant force at the crack tip is minimal, (b) the location of the crack tip is close to the neutral axis of the

composite section; and (c) the stress near the crack tip is limited by the yield stress of the steel. The moment-curvature relationships of retrofitted sections in the presence of a crack on the encased steel (i.e., within the "fatigue crack affected region") and also outside of this region were calculated. Therefore, once the weld started to fracture, the curvature distribution along the beam abruptly changed at the boundary of the "fatigue crack affected region," which is akin to the behavior of cracked reinforced concrete beams near the plastic hinge region [137].

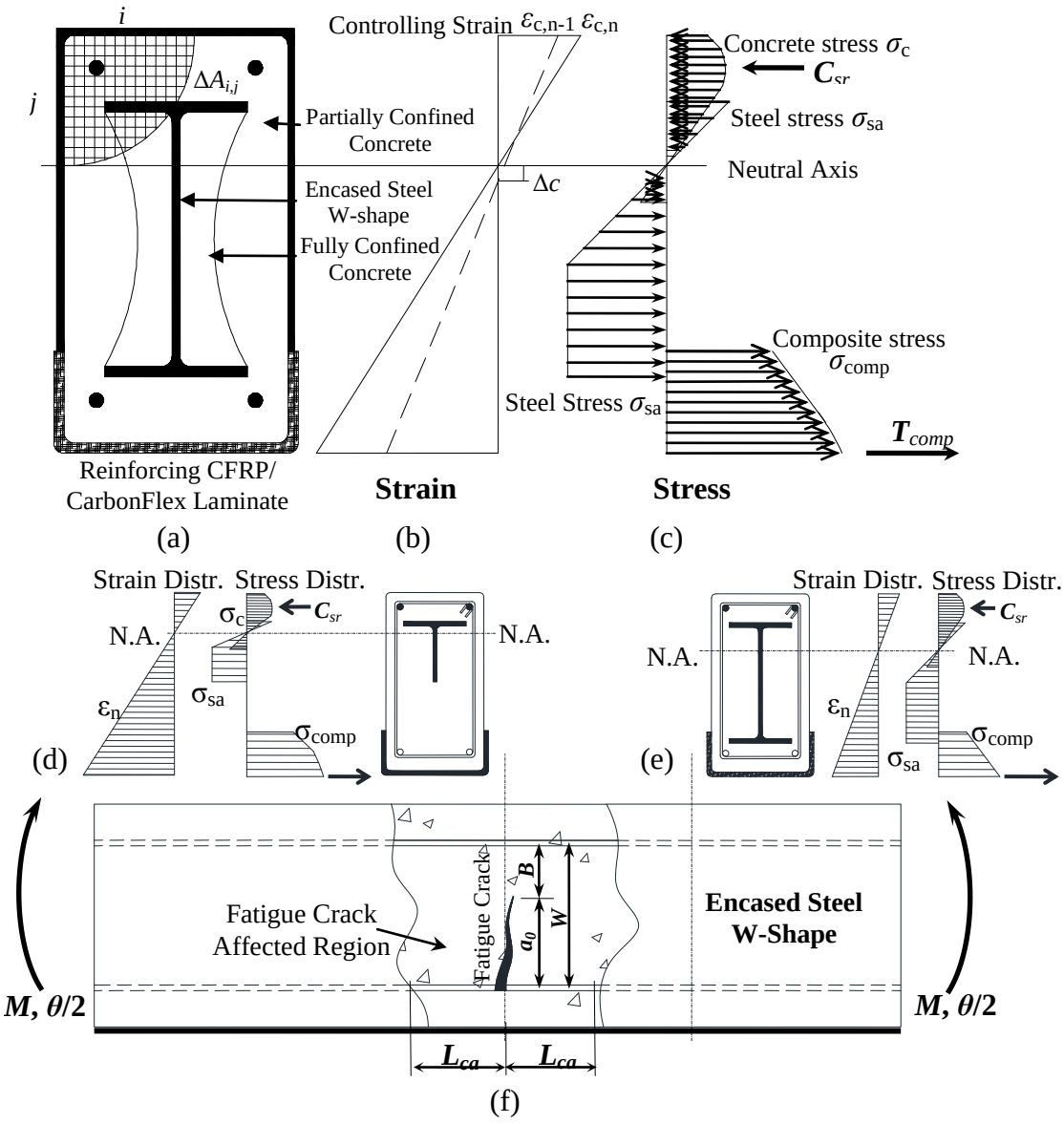

Figure 6.3.1.1. Numerical model for the computational analysis: (a) fiber section analogy of the SRC girders; (b) cross-section strain distribution; (c) cross-section stress distribution; (d) section with fatigue cracked steel; (e) section with intact encased steel; (f) retrofitted SRC girder with the presence of fatigue crack [30][17]

[17] Original figure provided by the author, and reprint with the permission of Elsevier.

6.3.2. Constitutive Models

The concrete- encased steel beams were wrapped around a region of pure bending, i.e., between the two inner point loads, see Figure 6.3.2.1 (a), in order to confine the compression zone of the beams and to enhance the rotational ductility at mid-span. The constitutive equations of concrete used in the analysis were initially proposed by Fafitis and Shah [138;139], which can be used to model the stress-strain behavior in concrete, with and without lateral confinement as shown schematically in Figure 6.3.2.1 (a). The compression part of the model includes a power function of concrete strain $\boldsymbol{\varepsilon_c}$ for the ascending branch followed by an exponential function for the descending branch. The constitutive equations for concrete in compression are expressed in equation (6.3.2.1)

$$f_c = \begin{cases} f_{c,0}\left[1-(1-\varepsilon_c/\varepsilon_{c,0})^A\right], \text{ if } 0<\varepsilon_c<\varepsilon_{c,0} \\ f_{c,0}\exp\left[-k_1(\varepsilon_c-\varepsilon_{c,0})^{k_2}\right], \text{ if } \varepsilon_{c,0}<\varepsilon_c<\varepsilon_{c,u} \end{cases} \quad (6.3.2.1)$$

where $f_{c,0}$ is the peak stress in the stress-strain curve that depends on the confinement stress f_r, and $\varepsilon_{c,0}$ is the corresponding strain; $\varepsilon_{c,u}$ is the ultimate strain. A, k_1, and k_2 are constants controlling the shape of the stress-strain curve which are also functions of f_r , where in the particular case of f_r = 0, equation (6.3.2.1) represents the constitutive behavior of un-confined concrete [138]. Concrete is assumed to remain linear elastic in tension until the failure stress f_t is reached. The steel, i.e., the encased steel and the enclosed rebar, was modeled as elasto-purely plastic.

A linear elastic stress-strain relationship of the unidirectional CFRP laminate was incorporated into CSRAP-Flex. The elastic modulus of the CFRP laminate loaded in tension is 144 GPa, and the ultimate tensile strength is 2548 MPa. The stress-strain

relationship of the CHMC was obtained by the coupon tests according to Dhiradhamvit and Attard [113] which followed the specifications of ASTM D3039. The CHMC behaved linear elastically in tension until approximately 25% of its ultimate tensile strength at which point a nonlinear stress-strain response ensued, see Figure 6.3.2.1 (b). The nonlinear stress-strain behavior in CHMC may be attributed to the high energy dissipation capability of the newly patented polymeric matrix that helps to stabilize crack growth and subsequent fiber damage during loading. The uniaxial stress-strain relationship of CHMC is initially modeled as a linear function of the composite strain ε_{comp} up until the linear-nonlinear transition strain, $\varepsilon_{CF,tran}$ (which may be thought of as the 'yield strain') see Figure 6.3.2.1 (b), followed by an exponential function until the peak stress is reached, and finally by, a linear model that approximate the descending branch until complete failure. The stress-strain relationships of the composites are expressed in Equations (6.3.2.2 a) and (6.3.2.2 b) and are schematically shown in Figure 6.3.2.1 (b) according to previous test results [113]. The compression resistance of either CFRP or CarbonFlex was neglected since the compressive strength of thin layer composites used in structural retrofitting are generally not well defined [43].

$$\text{CFRP: } f_{CFRP} = E_{CFRP}\varepsilon_{comp}, \text{ for } 0 < \varepsilon_{comp} < \varepsilon_{CFRP,u} \tag{6.3.2.2a}$$

$$\text{CarbonFlex: } f_{CF} = \begin{cases} E_{CF}\varepsilon_{comp}, \text{ for } 0 < \varepsilon_{comp} < \varepsilon_{CF,tran} \\ B_1 - B_2\exp(-B_3\varepsilon_{comp}), \text{ for } \varepsilon_{CF,tran} < \varepsilon_{comp} < \varepsilon_{CF,0} \\ f_{CF,0}\dfrac{\varepsilon_{CF,u} - \varepsilon_{CF,0} - C\varepsilon_{comp}}{\varepsilon_{CF,u} - \varepsilon_{CF,0}}, \text{ for } \varepsilon_{CF,0} < \varepsilon_{comp} < \varepsilon_{CF,u} \end{cases} \tag{6.3.2.2b}$$

where E_{CFRP} and E_{CF} are the elastic modulus for CFRP and CarbonFlex, respectively, and B_1-B_3 and C are material constants used in the regression analysis of the test data, where

in this case, E_{CF} =144GPa, $\varepsilon_{CF,tran}$ = 0.0045, $\varepsilon_{CF,0}$ = 0.041, $\varepsilon_{CF,u}$ = 0.057, *B1* = 4062.23MPa, *B2* =3748.91MPa, *B3* =21.664, and *C* = 0.105.

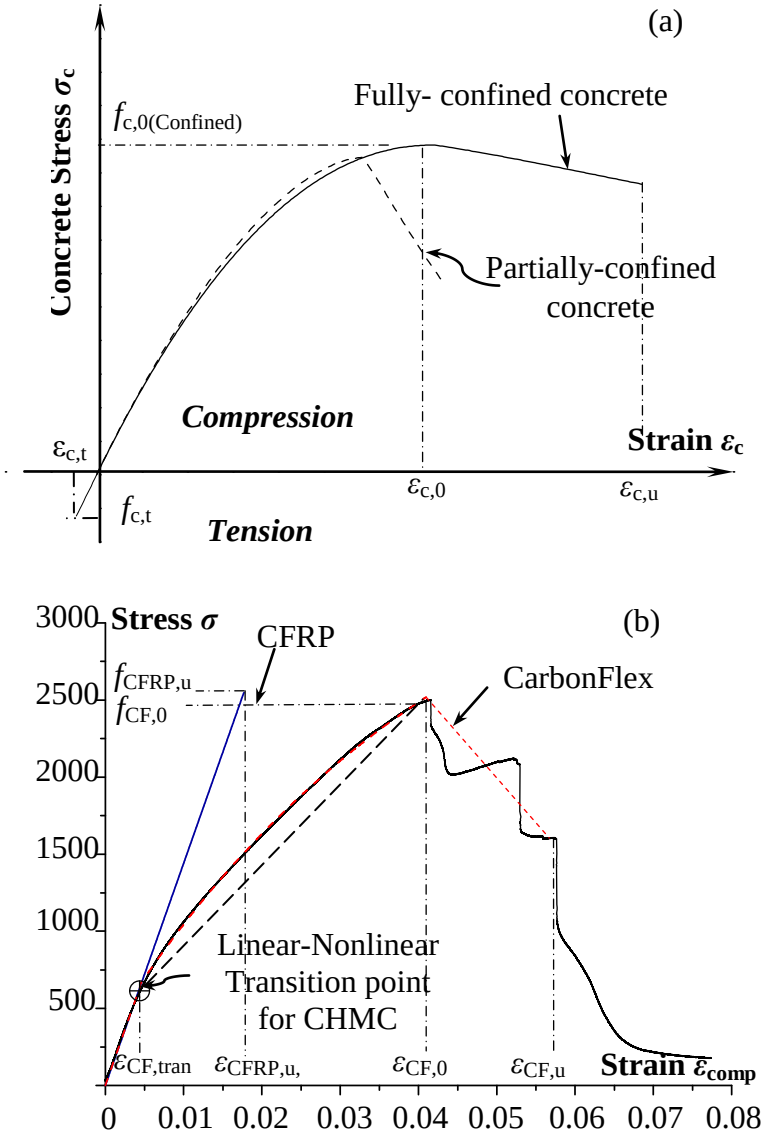

Figure 6.3.2.1. Moment-curvature responses of intact and fatigue damaged sections

6.3.3. Analysis Results and Validations

CSRAP-flex Moment Curvature Analysis of Retrofitted Sections

The results of the numerical analyses using CSRAP-Flex were compared to the experimental test results for the three retrofitted concrete encased steel girders. Moment-curvature relationships were determined for retrofitted beams having existing fatigue cracks in the encased steel and for undamaged beams strengthened by a laminate. Figure 6.3.3.1 (a) compares the cases for CFRP- and CHMC- wrapped beams. Prior to the linear-nonlinear stress transition point in the bottom laminate of the CHMC, see Figure 6.3.2.1 (b), the moment-curvature (M-φ) relationships are identical for sections retrofitted with either CHMC or CFRP. Following this transition point, the stress - strain behavior of CHMC became nonlinear, exhibiting significant ductility and energy dissipation, whereas the CFRP remained linear and was expectedly brittle. This points to two important observations. Although the inelastic modulus of CHMC decrease in comparison to the constant modulus of CFRP, which results in a slightly smaller moment capacity in comparison to the CFRP- retrofitted beam having intact encased steel, see Figure 6.3.3.1 (a), (1) the ductility in the idealized case of the intact encased steel is markedly larger for the CHMC- retrofitted beam than for the CFRP- retrofitted beam, and (2) in the case of the fractured encased steel, the CHMC enables the already damaged concrete- encased steel beam to attain a large moment capacity and exhibit tremendous curvature ductility. The moment capacities were controlled either by fracturing of the weldment (B1 or B2), or propagation of the existing crack (B3). In the experimental tests, failure of the specimens was controlled by rupturing of the composite laminates, as

indicated in Figures 6.3.3.1 (b) - (c), where neither did a plastic hinge develop in the encased steel nor did the concrete crush. However, where the encased steel remained ideally intact, the failure mode is crushing of concrete in compression for CHMC-retrofitted beam. It may then be concluded that the behavior of each specimen leading to failure is clearly distinguished by the retrofitting composite laminates' ability to enhance curvature ductility, sustain moment, and dissipate energy, which, according to Figure 6.3.3.1 (a), is clear verification for using CarbonFlex (in lieu of CFRP) and which complements the experimental test results shown in Figure 6.2.4.1 (a).

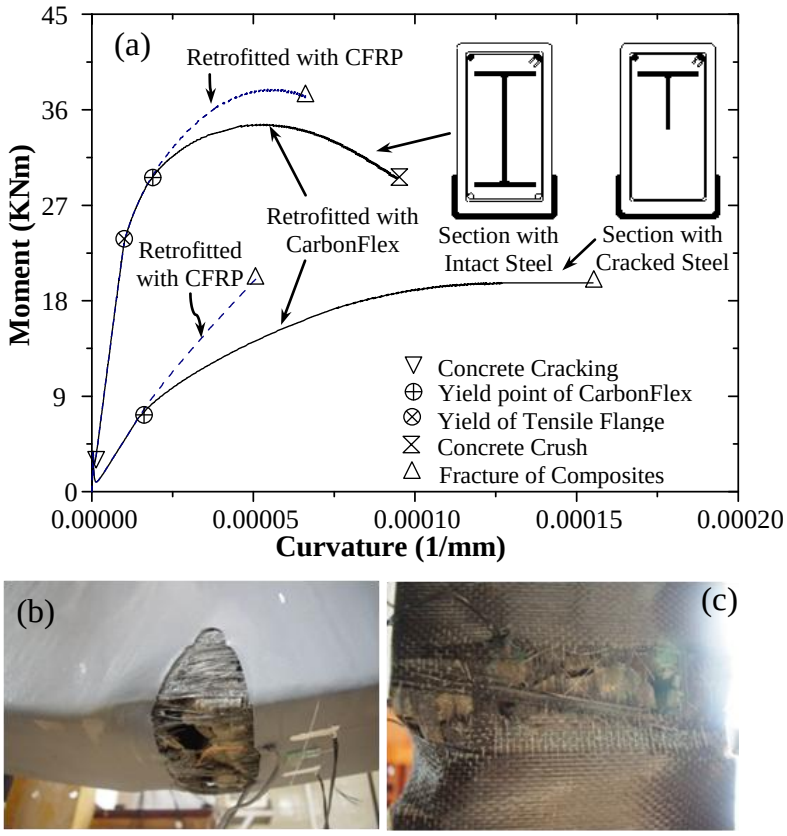

Figure 6.3.3.1. (a) Moment-curvature responses of intact and fatigue damaged sections; (b) picture showing the rupture of the CHMC laminate; (c) picture showing the rupture of the CFRP laminate

Verification of the Load-Deflection Responses and Strains using CSRAP-flex and Experimental Data

The calculated load vs. mid-span deflection responses of the test beams were obtained by integrating the curvature distribution along the length of the beam. The calculated load-deflection responses of each beam using CSRAP-Flex matched very well with the experimental test results, as indicated by Figures 6.3.3.2 (a) , 6.3.3.3 (a) and 6.3.3.4 (a) for beams B1, B2, and B3, respectively. A method of transformed sections was used to analyze the elastic load-deflection response prior to when the concrete cracked (i.e., at about 70kN in Figure 6.2.4.1 (a) or Figures 6.3.3.2 (a) , 6.3.3.3 (a) and 6.3.3.4 (a)). The analysis then correctly identified the sudden re-location of the neutral axis, accompanied by a slight reduction of the flexural stiffness in the retrofitted SRC members. A nearly linear load-deflection relationship was then maintained until the tensile flange of the encased steel section yielded resulting in a nonlinear load-deflection response and a gradual spread of plasticity which is influenced by all constituent materials including the encased steel, concrete, reinforcing rebar, and retrofitting composites. An essentially continuous movement of the neutral axis during loading is also observed due to concrete cracking and its nonlinearity in compression. During the experimental test, the strain in the bottom laminate, which was determined immediately prior to the fracture of the weldment, was measured as 0.0062 in B1 (see Figure 6.3.3.2 (b)), which is 15.1% of the ultimate strain of the CHMC). The analysis using CSRAP-Flex predicted a acceptable strain of 0.0054 (see Figure 6.3.3.2 (b)). In B2, the strain measured in the CFRP laminate was 0.0056 (see Figure 6.3.3.3 (b)), which is 33.5% of

the ultimate strain of CFRP), and the strain predicted by CSRAP-Flex was 0.0051 (see Figure 6.3.3.3 (b)). Prior to reaching the maximum strength in beams B1 and B2, the cracking in the concrete did not result in a significant increase in the laminate strain although after the weldments fractured, the strain gradient was substantial. Unlike its CFRP counterpart, CHMC at this point, helped stabilize the strain energy dissipation corresponding to the crack growth in the concrete and in the encased steel and enabled a significant portion of the post-peak-strength to be sustained under large deformations. A comparison of B3 vs. B1 or B2 (having welded encased steel sections) in terms of the laminate strain vs. mid-span beam deflection relationships (i.e., Figure 6.3.3.4 (a) vs. Figures 6.3.3.2 (a) and 6.3.3.3 (a)) clearly reveals that at a common deflection of about 7.5mm, the deflection in B3 is about 0.006, and it is about 0.0025 for B1 and 0.0015 for B2, thus indicating the increase in laminate strain following fracture of the encased steel. The discrepancy between B1 and B3 is due to the fact that the CHMC laminate in B3 had already been experiencing large strains prior to the peak load, as a result of the repaired encased steel.

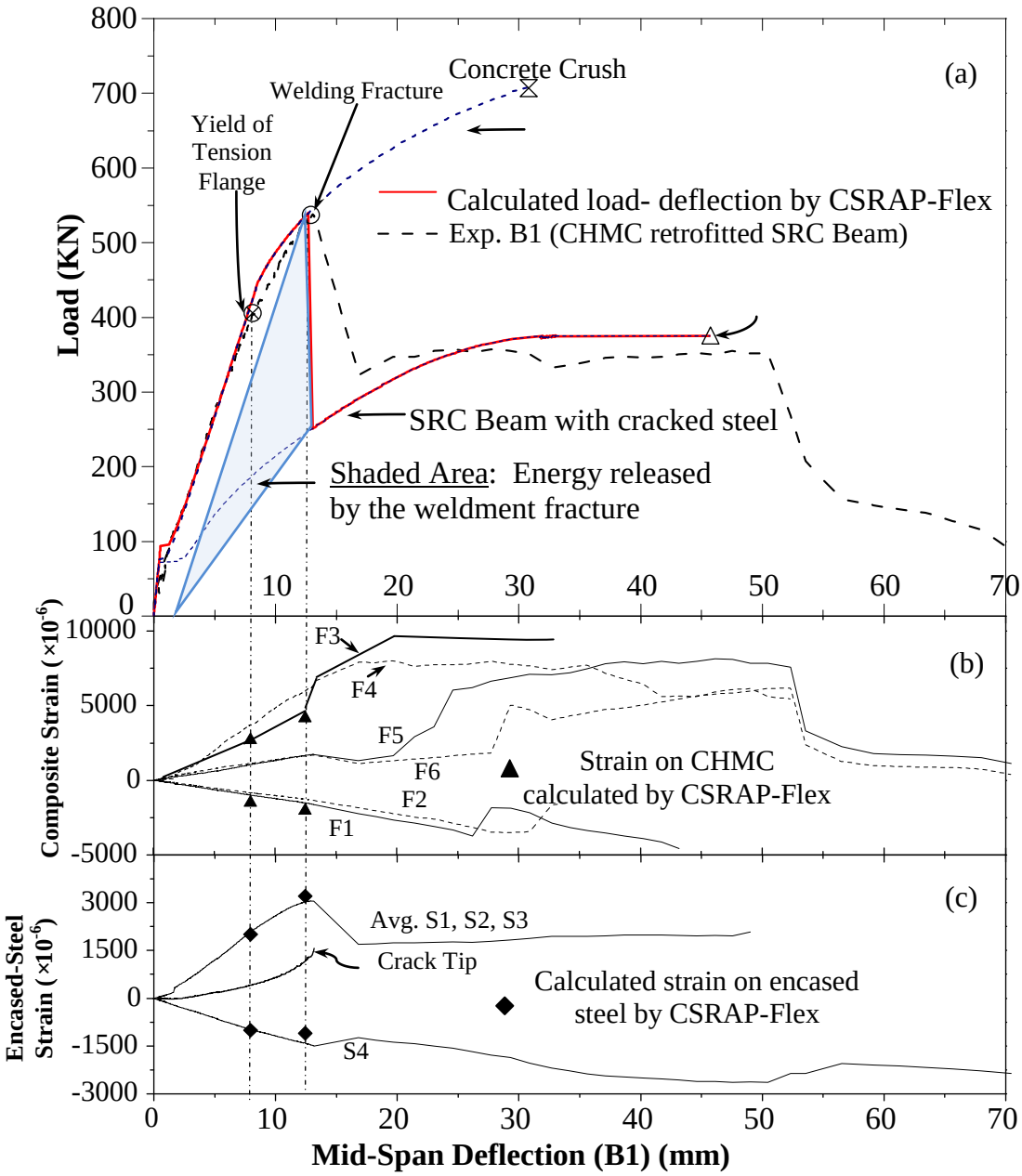

Figure 6.3.3.2. Comparison between experimental and analytical results - specimen B1: CHMC-retrofitted girder with fatigue crack welded: (a) load-deflection; (b) composite strain - deflection; (c) strains on the encased steel [30]

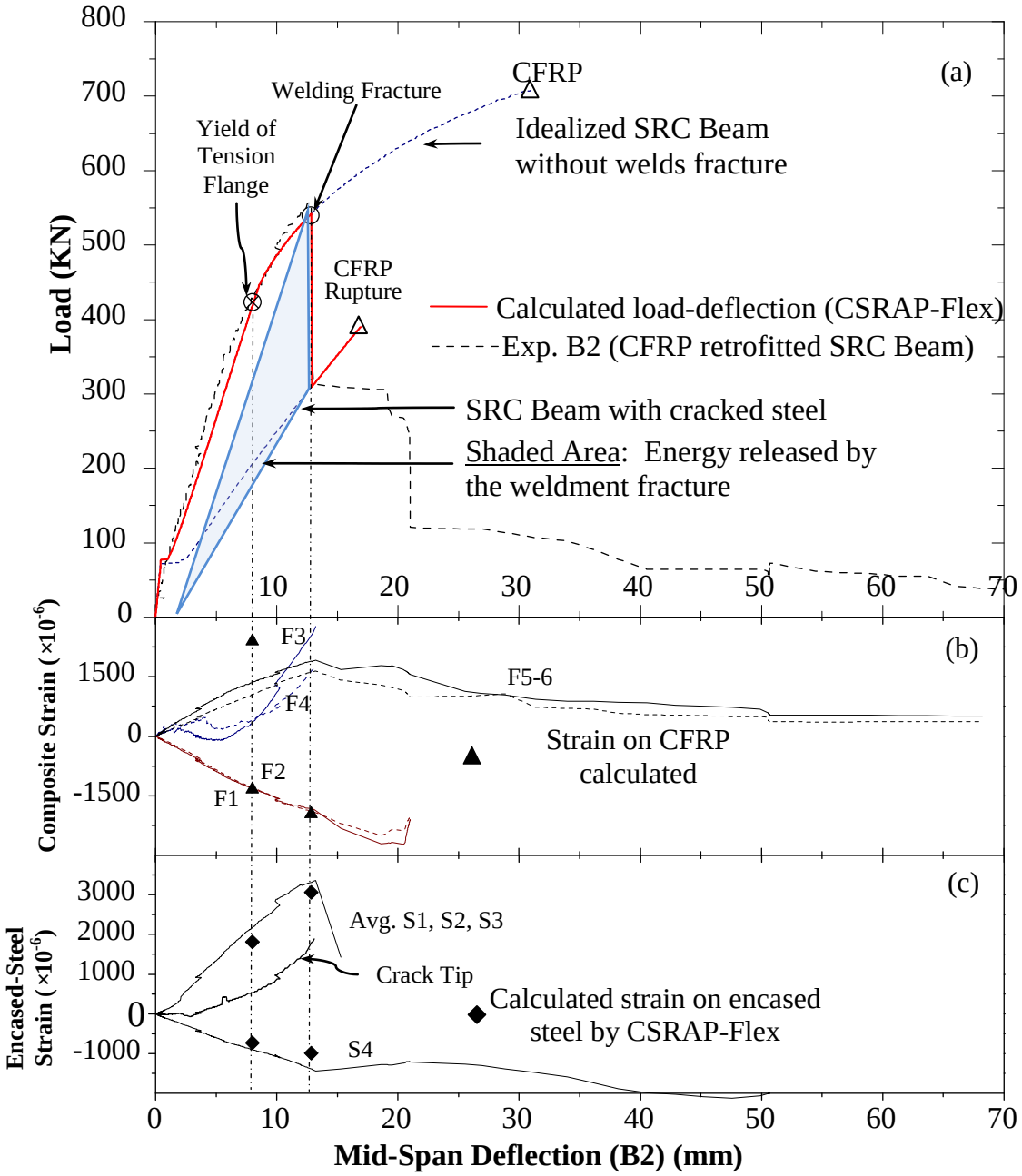

Figure 6.3.3.3. Comparison between experimental and analytical results - specimen B2: CFRP-retrofitted girder with fatigue crack welded: (a) load-deflection; (b) composite strain - deflection; (c) strains on the encased steel [30]

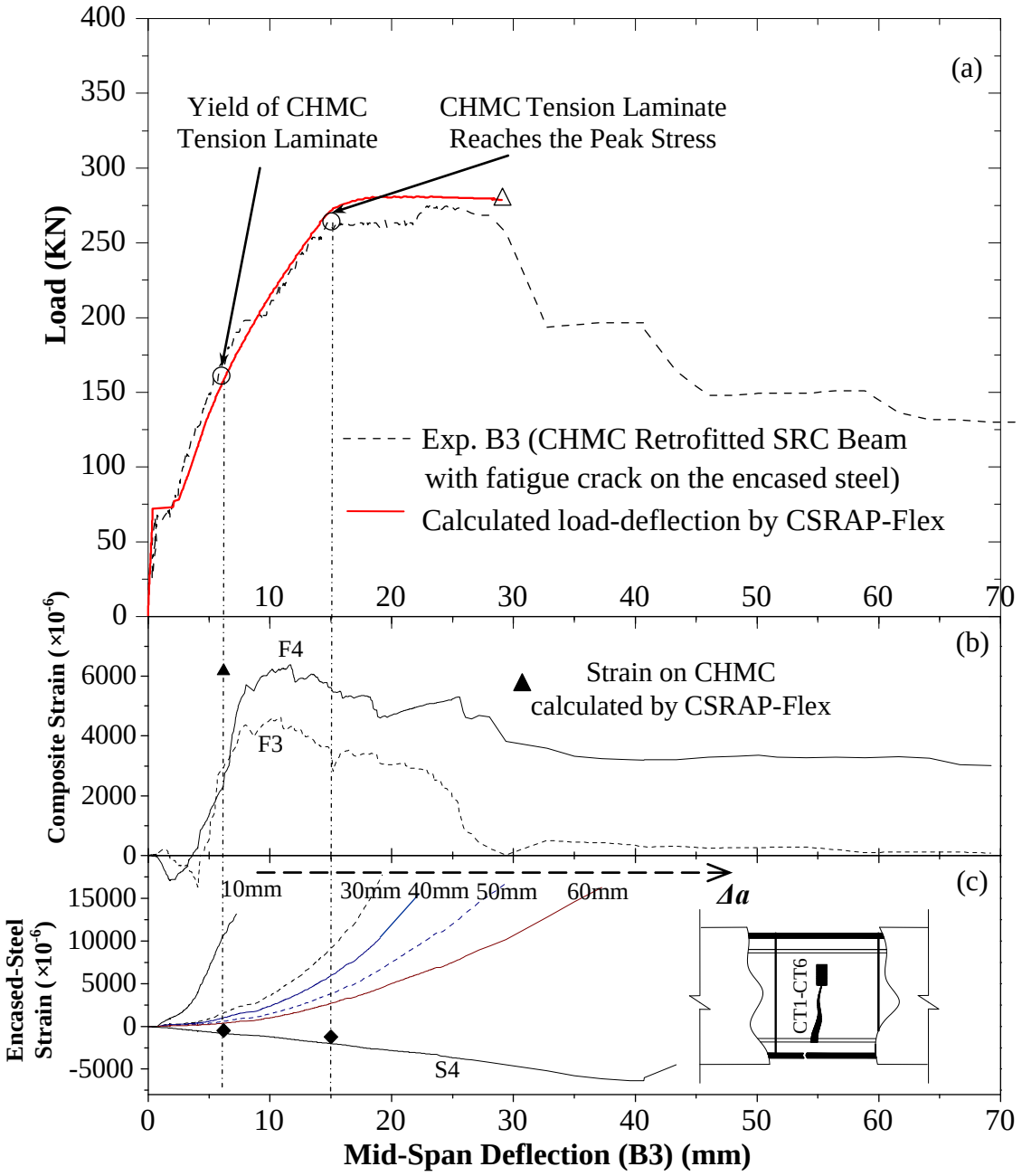

Figure 6.3.3.4. Comparison between experimental and analytical results - specimen B3: CHMC-retrofitted girder with fatigue crack un-welded: (a) load-deflection; (b) composite strain - deflection; (c) strains on the encased steel [30]

CSRAP-Flex is developed as a design tool for engineers that would allow them to assess the potential sustainable strength of already-damaged retrofitted systems. The upper and lower bounds of the strength of retrofitted systems may be defined in terms of their predicted failure modes:

a) *Crushing of concrete* (assuming that the repaired welds do not fracture, see Figure 6.3.3.1 (a) for the intact steel section, or the predicted dotted-line response in Figure 6.3.3.2 (a) labeled "Idealized SRC Beam without welds fracture"). This is an upper bound projection of the strength. In this case, the CHMC laminate does not fracture while dramatically improving the confinement of the beam until the concrete finally crushes.

b) *Rupturing of the CHMC laminate* (assuming that the encased fractured steel was not repaired, e.g., beam B3, see Figure 6.3.3.1 (a) for the cracked steel section, or Figure 6.3.3.4 (a)). This is a lower-bound projection of the strength.

Fracture of the welding seam may be caused by imperfections such as minor surface cracks and residual stresses caused by the welding process. Factors could influence the weldment strength include the weld type, strength and fracture toughness of the weld base material, welding quality, the original defect size, and the residual stresses[131;132;135]. As previously discussed, the weld fracture moment, M_{wf}, is determined experimentally in the current study. The load- deflection relationship after the displacement that corresponds to M_{wf} is reached differed significantly between B1 and B2. Initially, the strain energy being suddenly released was nearly equal, see the shaded areas in Figures 6.3.3.2 (a) and 6.3.3.3 (a), which was characterized by the abrupt decrease in the measured strains from the gauges mounted on the steel tension flange near

the crack location, see Figures 6.3.3.2 (c) and 6.3.3.3 (c). Due to the brittle nature of the carbon fiber and epoxy matrix that help constitute CFRP, this sudden burst of energy may have initiated damage either within the CFRP laminate (for example as either matrix micro-cracking, fiber-matrix debonding, or inter-lamina delamination) [55] or at the adhesive layer region between the CFRP laminate and the concrete substrate which may have later resulted in laminate debonding, see Figure 6.3.3.5 (a). This damage to the CFRP laminate immediately following M_{wf} explains the difference between the experimental and computational results, see the slight increase in the idealized predicted CFRP strength following the fracture of the weldment which leads to the CFRP Rupture point soon thereafter in Figure 6.3.3.3 (a); conversely, the experimental results show a short plateau following the weld fracture, likely a result of the immediate damage to, e.g., the matrix micro-cracking or the adhesive layer of the CFRP laminate, leading to a smaller stress, lower modulus, and subsequent lower load capacity experimentally. A comparison to Figure 6.3.3.2 (a) shows that the strength between the predicted and computational results is more consistent, as a result of there being little to no internal damage (e.g., matrix micro-cracking) to the CHMC.

The CFRP laminate ruptured shortly after the weldment had fractured, which was partially attributable to strain localization, and the unstable release of strain energy, resulting in the progressive formation of new crack surfaces. The CFRP bottom laminate had, at that point, ruptured and debonded from the concrete substrate as did a number of the "U"-shape CFRP jackets that had been provided along the shear span length of the beam in order to support the bottom laminates, see Figure 6.3.3.5 (a). On the other hand, this was not the case in B1 due to the ability of CHMC to absorb and then dissipate the

sudden burst of energy release [113] caused by the sudden fracturing of the weldments. The capability of the CHMC to absorb and dissipate energy has been evident by the impact and vibration tests presented in the previous chapters. Furthermore, there was no debonding between CarbonFlex and the concrete substrate, which was not the case in the CFRP-retrofitted beam. Figure 6.3.3.5 (b) shows no observable composite debonding or delamination which is again attributable to the ability of CarbonFlex to consistently absorb the shock energy from the fracturing steel.

The strain localization caused by the abrupt section change is discussed by Hmidan et al. in a study of notched steel beams retrofitted by CFRP [39]. This phenomenon was idealized as the "fatigue crack affected region" in Figure 6.3.1.1 (f) and was incorporated in CSRAP-Flex, which accurately predicts the larger laminate strains as a result. At the moment when the welds fractured, the resulting redistribution of forces in B1 along the beam re-established equilibrium and led to the subsequent load drop shown in Figure 6.3.3.2 (a). In Figure 6.3.3.2 (b), the strain in the CHMC laminate abruptly increased inside the "fatigue crack affected region", see gauges F3 and F4, while strains in other regions decreased, see the strain readings of gauges F5 and F6. The CHMC laminate stabilized the damaged region in B1 and distributed the strain localized region, thus substantially increasing the ductility of the beam resulting in an ultimate mid-span deflection of 51.2 mm or approximately $1/60^{th}$ of the span length L. In beam B2, the strain localization caused the CFRP bottom laminate to rupture prior to re-establishing equilibrium in the beam where the significant decrease in load was interrupted by a short plateau in Figure 6.3.3.3 (a).

A similar approach was used to analyze the response of B3. Since the pre-existing fracture in B3 was not welded, the crack was expected to propagate at an early load stage. As a result, a series of strain gauges spaced at 10 mm and labeled CT1-CT6 as shown in Figure 6.3.3.4 (c) were mounted along the assumed crack propagation path. Prior to the crack propagation in the encased steel, the near-crack-tip region experienced significant post-elastic deformation. As the crack propagated, a spread of plasticity was observed around each new crack surface, and the "fatigue crack affected region" expanded. The gradual section loss of the encased steel thus lowered the load capacity of B3 following the post-weld fracture.

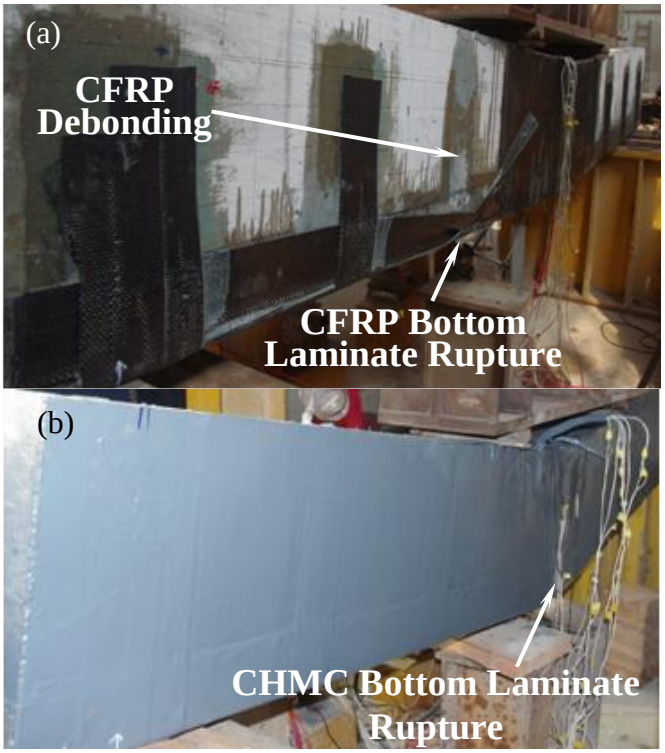

Figure 6.3.3.5. (a) CFRP rupture and debonding (specimen B2); (b) CHMC laminate rupture at failure, no debonding was observed (Specimen B1) [30][18]

[18] Original figure provided by the author, and reprint with the permission of Elsevier.

6.4. Propagation and Stabilization of Crack Growth in the Web of the Encased Steel Section for Specimen B3

The monitored relationship between the crack extension, Δa, in B3 and the calculated moment is shown in Figure 6.4.1.1 (a). The fractured web of the encased steel was analyzed using a linear elastic fracture mechanics (LEFM) approach which is shown in Figures 6.4.1.1 (b) and (c) for an isolated web section. The distribution of stresses on the isolated web is a function of the load and position of the neutral axis. The length along the tension flange at a distance L_{ca} from the crack is ineffective in resisting loads, see Figures 6.3.1.1 (f) and 6.4.1.1 (b). Over the span $2 \times L_{ca}$, the tensile force, F_{tf} is resisted mostly by the CHMC laminate in the case of CHMC retrofitted beam (see Figure 6.4.1.1 (c)), and is transferred into the web in the cased of un-retrofitted beam (see Figure 6.4.1.1 (b)). The net axial force and corresponding pure bending moment that on the *web* portion of the encased steel lying outside the $2 \times L_{ca}$ region are defined as P_{aw} and M_{aw} and may be calculated as:

$$P_{aw} = \begin{cases} t_{aw} \int_{-W/2}^{W/2} \sigma_{aw}(x)dx + F_{tf}, \text{ for non-retrofitted beam} \\ t_{aw} \int_{-W/2}^{W/2} \sigma_{aw}(x)dx + F_{tf} - T_{comp}, \text{ for retrofitted beam} \end{cases} \quad (6.4.1.1)$$

$$M_{aw} = \begin{cases} t_{aw} \int_{-W/2}^{W/2} x\sigma_{aw}(x)dx + \frac{W}{2} F_{tf}, \text{ for non-retrofitted beam} \\ t_{aw} \int_{-W/2}^{W/2} x\sigma_{aw}(x)dx + \frac{W}{2} F_{tf} - \left(\frac{W}{2} + c_{cover} \right) T_{comp}, \text{ for retrofitted beam} \end{cases} \quad (6.4.1.2)$$

where t_{aw} is the thickness of web; W is the height of the web; and x is the distance to the location of plastic centroid of the steel web. It is important to note that equations (6.4.1.1) and (6.4.1.2) are the net section forces and do not account for the concrete in tension. Finally, the first mode stress-intensity factor of an edge-cracked plate subjected to combined bending and tension may be obtained using equation (6.4.1.3) [136]

$$K_I = \frac{1}{t_w\sqrt{W}}\left[P_{aw} f_t\left(\frac{a}{W}\right) + \frac{M_{aw}}{W} f_b\left(\frac{a}{W}\right)\right] \qquad (6.4.1.3)$$

where a is the crack length, and $a=a_0+\Delta a$; a_0 is the initial crack length; and Δa is the crack extension. The terms $f_t(a/W)$ and $f_b(a/W)$ represent geometric factors that are functions of a/W and may be found in [136].

The calculated moment, M_{stable}, under which the existing crack does not grow, in non-retrofitted or retrofitted concrete- encased steel beams having a crack length may be solved by setting K_{I} obtained by equation (6.4.1.3) equal to the critical stress intensity factor K_{Ic} for plane strain condition or K_{c} for plane stress condition for structural steel, where the latter is assumed in the analysis of the web. Figure 6.4.1.1 (a) shows the relationship between the moment M_{stable} of a non-retrofitted and CHMC-retrofitted beam for varying crack length extensions, Δa.

The calculated moment at which crack growth initiates, defined here as $M_{init,}$ (i.e., at $\Delta a \sim 0$) according to the experimental test results of B3, is 89.25 KN-m; this is very reasonably predicted by equation (6.4.1.3), which calculates M_{init} to be 82.07 KN-m, which is 2.54 times larger than the calculated moment for the non-retrofitted beam (32.25 KN-m). Shortly after crack-growth, the value of M_{stable} of the non-retrofitted beam converges to that of the concrete cracking moment, M_{cr}, thus implying that crack in the

encased steel propagates even under minimal load, in a non-retrofitted beam quickly results in imminent beam failure; in fact, this was observed in the CFRP-retrofitted beam (B2), where immediately following the fracture of the weldment, the CFRP laminate ruptured due to a lack of ductility and energy dissipation. Following the rupture of the CFRP laminate, the post-peak response of B2 was very similar to that of a non-retrofitted beam as the crack propagated unstably through the steel web leading to the observed failure.

On the other hand, the calculated moment capacity (144.2 KN-m) according to the experimental test results of the CHMC-retrofitted specimen (B3) was significantly larger than the initial moment of 89.25 KN-m at the time of crack growth initiation. A comparison of the experimental test results of B3 (shown as in Figure 6.4.1.1 (a)) to the calculated results of the LEFM analysis using equation (6.4.1.3) demonstrates significant improvement in the CHMC retrofitted system by stabilizing load-crack extension behavior. An explanation of this improvement, which also helps explain the discrepancy between the experimental results and the results predicted by equation (6.4.1.3), lies in the energy dissipation properties of CHMC which equation (6.4.1.3) does not capture. Equation (6.4.1.3) essentially describes the moment capacity of idealized CFRP-retrofitted sections, which (a) do not exhibit internal damage, such as matrix micro-cracking and (b) do not include a sufficient energy dissipation mechanism. At $\Delta a \sim 0$, there is a close agreement between the result of the experimental test data and the equation (6.4.1.3) prediction. Immediately following fracture of the weldment, this agreement is consistent with the results observed in Figure 6.2.4.1. By dissipating the shock energy after the steel welds had fractured, immediate laminate damage is precluded,

the strain localization near the crack location is adequately distributed, and the ensuing moment and load capacity are subsequently sustained.

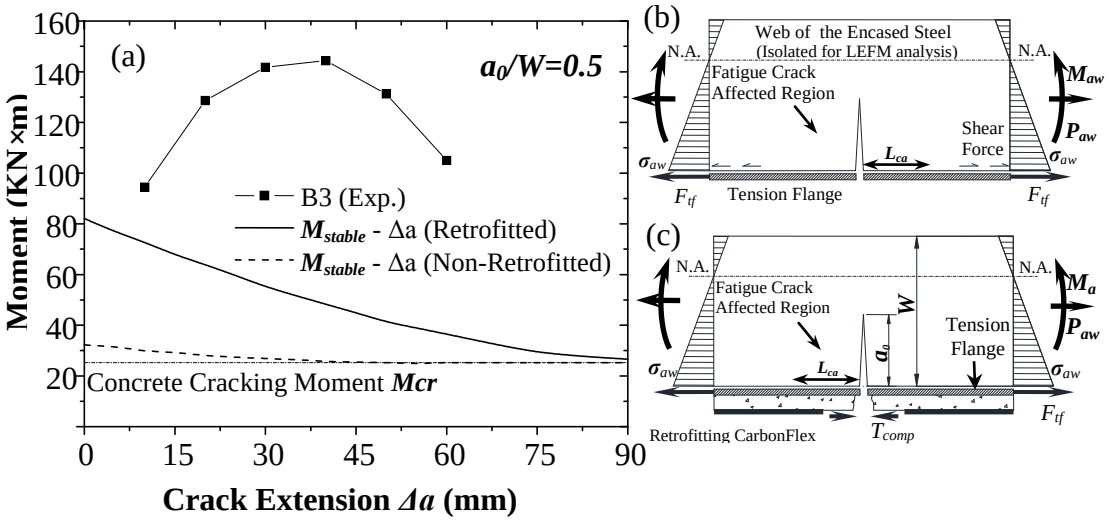

Figure 6.4.1.1. Analysis of crack stabilization using the LEFM approach: (a) moment-crack extension; (b) isolated encased steel web for non-retrofitted beams; (c) isolated encased steel web for retrofitted beam using composite lamimate

6.5. Moment Capacity of CHMC-retrofitted Deeply Cracked Concrete-Encased Steel Sections

6.5.1. Formula Derivation

A numerical example is used to calculate the moment capacity of deeply cracked concrete- encased steel sections retrofitted using either CFRP or CHMC and the applicable formulas are derived. In the derivation, 1) a perfect bond is assumed between composing materials to ensure strain compatibility, 2) an equivalent stress block is used

to represent the stress distribution in the concrete compression zone [125], 3) an elasto-plastic stress-strain relationship is used to model the rebar and the encased steel section, 4) the CFRP laminate is modeled assuming a linearly elastic stress-strain relationship, and 5) for the sake of simplicity resulting in minimal loss of accuracy [113], the constitutive relationship for CHMC is assumed to follow a bi-linear model, as shown in Figure 6.3.2.1 (b).

The analysis determines the failure mode as either crushing of concrete or laminate rupture, where the former occurs when the maximum compressive strain in the concrete, ε_c, reaches the crushing strain (defined as $\varepsilon_{c,u}$ = 0.003 for unconfined concrete and $\varepsilon_{c,u}$ = 0.004 for confined concrete). The moment capacity and force equilibrium for a cross-section may be determined as

$$M_u = (0.85 f_c^{'})(\beta c)(b)(h_0 - \frac{\beta c}{2}) + f_y^{'} A_s^{'}(h_0 - a_{sr}^{'}) + f_{af}^{'} A_{af}^{'}(h_0 - \delta_1 h_0 + 0.5 t_f) + M_{aw} \quad (6.5.1.1)$$

$$(0.85 f_c^{'})(\beta c)(b) + f_y^{'} A_s^{'} + f_{af}^{'} A_{af}^{'} - f_y A_s - T_{comp} + P_{aw} = 0 \quad (6.5.1.2)$$

where c is the distance from neutral axis to the top of the beam; $f_c^{'}$ is the compressive strength of concrete; b is the section width; h_0 is the distance from the location of the centroidal force of the tensile reinforcements and retrofitting composite to the top of the compression zone; $\delta_1 h_0$ and $\delta_2 h_0$ are the distances from the top of the web and the crack tip to the top of the compression zone, respectively, see Table 2; and $f_{af}^{'}$ is the stress in the compression flange. Assuming strain compatibility, the compressive stress in the flange of the encased steel is expressed in terms of the concrete crushing strain $\varepsilon_{c,u}$ as

$$f_{af}^{'} = E_s \frac{c - \delta_1 h_0 + 0.5 t_f}{x} \varepsilon_{c,u} \le f_a \quad (6.5.1.3)$$

where f_a is the yield stress of the encased steel. The terms M_{aw} and P_{aw} are the resultant moment and force, respectively, in the web of the encased steel. In the case of concrete-encased steel beams having deeply cracked encased steel section and where the position of neutral axis may be either below, above, or in the top-flange of the section, the expressions for M_{aw} and P_{aw} are discussed as follows:

<u>*Case1.*</u> In a case where the neutral axis is located in the web - where the web does not yield - a linear stress distribution in the web yields the following:

$$M_{aw} = \frac{1}{2} E_s t_w \varepsilon_{c,u} \left[\frac{(c-\delta_1 h_0)^2}{x} (h_0 - \frac{2}{3}\delta_1 h_0 - \frac{1}{3}c) - \frac{(\delta_2 h_0 - c)^2}{x} (h_0 - \frac{2}{3}\delta_2 h_0 - \frac{1}{3}c) \right] \quad (6.5.1.4a)$$

$$P_{aw} = \frac{1}{2} E_s t_w \varepsilon_{c,u} \left[\frac{(c-\delta_1 h_0)^2}{c} - \frac{(\delta_2 h_0 - c)^2}{c} \right] \quad (6.5.1.4b)$$

<u>*Case2.*</u> If the neutral axis is located in the web and if part of the web yields in tension, then:

$$\begin{aligned} M_{aw} = {} & \frac{1}{2} E_s t_w \frac{(c-\delta_1 h_0)^2}{c} (h_0 - \frac{2}{3}\delta_1 h_0 - \frac{1}{3}c)\varepsilon_{c,u} \\ & - f_a t_w (0.9c^2 - \frac{4}{3}ch_0 + \delta_2 h_0^2 - \frac{1}{2}\delta_2^2 h_0^2) \end{aligned} \quad (6.5.1.5a)$$

$$P_{aw} = \frac{1}{2} E_s t_w \frac{(c-\delta_1 h_0)^2}{c} \varepsilon_{c,u} - f_a t_w (\delta_2 h_0 - \frac{4}{3}c) \quad (6.5.1.5b)$$

<u>*Case3.*</u> If the neutral axis is located either in or above the top flange of the encased steel the resultant moment and force are calculated as:

$$M_{aw} = -\frac{1}{2}(f'_{af} + f_a)(\frac{5}{3}c - \delta_1 h_0)(h_0 - \frac{1}{2}\delta_1 h_0 - \frac{5}{6}c) - f_a t_w (\delta_2 h_0 - \frac{5}{3}c)(h_0 - \frac{1}{2}\delta_2 h_0 - \frac{5}{6}c) \quad (6.5.1.6a)$$

$$P_{aw} = -\frac{1}{2}(f'_{af} + f_a)(\frac{5}{3}c - \delta_1 h_0) - f_a t_w (\delta_2 h_0 - \frac{5}{3}c) \quad (6.5.1.6b)$$

The encased steel is assumed to have not yielded in compression so that the formulas established are suitable for a section having encased steel that may be deeply cracked ($a_0/W \geq 0.5$) by virtue of fatigue or, in some cases, via corrosion.

The tensile force in the retrofitting laminate may be calculated for either CFRP or CHMC as:

For CFRP:

$$T_{comp} = E_{CFRP} t_{comp} \varepsilon_{CFRP} \tag{6.5.1.7a}$$

For CHMC:

$$T_{comp} = \begin{cases} E_{CF} t_{comp} b_{comp} \varepsilon_{CF}, \text{ for } \varepsilon_{CF} < \varepsilon_{CF,t} \\ \dfrac{\varepsilon_{CF}(f_{CF,0} - f_{CF,t}) - \varepsilon_{CF,t} f_{CF,0} + \varepsilon_{CF,0} f_{CF,t}}{\varepsilon_{CF,0} - \varepsilon_{CF,t}} t_{comp} b_{comp}, \text{ for } \varepsilon_{CF,t} < \varepsilon_{CF} < \varepsilon_{CF,0} \end{cases} \tag{6.5.1.7b}$$

in which a bi-linear post-yield stress-strain model is assumed for the CHMC, and

$$\varepsilon_{CF} \text{ or } \varepsilon_{CFRP} = \frac{h-c}{c} \varepsilon_{c,u} \tag{6.5.1.8}$$

The remaining variables in the equations are calibrated to the experimental test results and are shown in Table 6.2.1.2.

6.5.2. A Numerical Example Using the Experimental Specimen

A numerical example using specimen B3 is used to illustrate the calculation of the moment capacity of a pre-cracked section retrofitted with CHMC. Table 6.2.1.2 shows the various parameters used in the calculation.

Since the tensile rebar was cut and removed from the fatigue-damaged section (as discussed earlier), the effective depth, h_0, to the tensile reinforcement (in this case, to the

bottom plate laminate) is equal to the total depth of the section, *h*, where $h_o = h = 400$mm. Furthermore, the failure mode of the section was assumed to be crushing of the concrete, and the neutral axis was assumed to be located in the web, which was further assumed to have not yielded; these assumptions are examined. The stress in the compression flange may be then calculated as

$$f_{af}^{'} = (200000)\frac{(c-70)}{c}(0.004) \quad MPa \tag{6.5.2.1}$$

and the stress in the CarbonFlex tension plate may be calculated as

$$\varepsilon_{CF} = \frac{(400-c)}{c}(0.004) \tag{6.5.2.2}$$

Substituting equation (6.5.2.2) into equation (6.5.1.7b), the tensile force provided by the CHMC laminate is calculated as

$$T_{comp} = (81183.6/c + 216.7 \quad MPa) \times 0.501 \times 300 = 12202000/c + 32571 \quad N \tag{6.5.2.3}$$

and the resultant force contributed by the web is calculated using equation (6.5.1.4b) is

$$P_{aw} = 900000 - 123750000/c \quad N \tag{6.5.2.4}$$

Therefore, the force equilibrium from equation (6.5.1.2) yields the following:

$$\begin{aligned}&(0.85\times 65)(0.725c)(220) + (385)(307) + (200000)\frac{(c-70)}{c}(0.004)(140\times 10)\\ &-0 - (12202000/c + 32571 \quad N) + (900000 - 123750000c) = 0\end{aligned} \tag{6.5.2.5}$$

where, the position of neutral axis may be calculated as $c = 76.64\ mm > \delta_1 h_0 = 75\ mm$. Therefore, the neutral axis is located in web, which meets the stated assumption. Using the value of *c*, the assumed yielding of both the compression rebar and the remaining web section, and the strain of CHMC tension plate are verified. Assuming strain compatibility, the strain in the compression compressive rebar is calculated as:

$$\varepsilon_{sr} = \frac{(76.64-32)}{76.64}(0.004) = 0.0023 > \frac{f_{sr}}{E_s} = 0.0019 \text{ (O.K.)} \quad (6.5.2.6)$$

The strain of the CHMC tension plate is calculated as:

$$\varepsilon_{CF,t} = 0.0045 < \varepsilon_{CF} = \frac{(400-76.64)}{76.64}(0.004) = 0.017 < \varepsilon_{CF,0} = 0.041 \text{ (O.K.)} \quad (6.5.2.7)$$

The strain of the steel web is calculated as:

$$\varepsilon_{wb} = \frac{(200-76.64)}{76.64}(0.004) = 0.0064 > \frac{f_{sr}}{E_s} = 0.0019 \quad (6.5.2.8)$$

Therefore, this assumption is incorrect; i.e., the web is yielded.

Next, the location of the neutral axis is assumed to lie inside the web and part of the web is assumed to yield in tension. Using equation (6.5.1.5b), the resultant force in the web of the encased steel is calculated as:

$$P_{aw} = 3600\frac{(x-75)^2}{x} - 4800x + 720000 \ \ N \quad (6.5.2.9)$$

Substituting equation (6.5.2.9) into equation (6.5.1.2) and solving for ***c***:

$c = 65.12 \ mm < \delta_1 h_0 = 75 \ mm$ Therefore, the assumption is incorrect; i.e., the neutral axis was incorrectly assumed to be in the web. Finally, the location of the neutral axis is assumed to be located either inside or above the top-flange of the encased steel. Therefore, equation (6.5.1.6b) is used to calculate the resultant force in the web as:

$$P_{aw} = 5000x - 2100000/x - 628300 \ \ N \quad (6.5.2.10)$$

Substituting equation (6.5.2.10) into equation (6.5.1.2) and solving again for *c*:

$$c = 63.29 \ mm < \delta_1 h_0 = 75 \ mm \text{ (O.K., neutral axis is above the top flange.)} \quad (6.5.2.11)$$

Next, the yielding strain of the compression steel and the strain in the composite tension laminate are verified:

$$\varepsilon_{sr} = \frac{(63.29-32)}{63.29}(0.004) = 0.00197 > \frac{f_{sr}}{E_s} = 0.0019 \text{ (O.K.)} \qquad (6.5.2.12)$$

The strain in the CHMC tension plate may finally be calculated as:

$$\varepsilon_{CF,t} = 0.0045 < \varepsilon_{CF} = \frac{(400-63.29)}{63.29}(0.004) = 0.021 < \varepsilon_{CF,0} = 0.041 \qquad (6.5.2.13)$$

The magnitude of the strain in the CHMC laminate lies between the transition point and the peak point, which was previously defined in Figure 6.3.2.1 (b).

Therefore, the assumptions are satisfied, and *c* may be substituted into equations (6.5.1.3) - (6.5.1.8) and in equation (6.5.1.1) in order to calculate the moment capacity of the section, which is $M_{u,cal} = 134.0 \text{ K}N \times m$. The moment capacity that is calculated from the experimental test of specimen B3 is $M_{u,\text{expr}} = 141.75 \text{ K}N \times m$, which results in an acceptable error of 5.5%.

6.6. Summary and Conclusions

The experimental test results of three large concrete-encased steel girders retrofitted using CHMC or CFRP laminates are analyzed in the chapter. The girders were repaired and retrofitted following fatigue-induced failure of the embedded steel section. In addition, a Concrete Structural Retrofitting Analysis Program (or CSRAP-Flex) was developed to predict the nonlinear behavior of already-damaged concrete-encased steel girders.

- Concrete- encased steel girders retrofitted with CHMC show significant sustainable high strength (about 68% of the peak strength) with superb ductility. The energy dissipation mechanism that is integrated into the damaged, yet retrofitted, specimens

via the CHMC helps to stabilize the crack growth in the fractured steel weldment, thus controlling the formation of new crack surfaces that would otherwise lead to a brittle-like failure (as in the case of CFRP-retrofitted beams).

- CSRAP-Flex very accurately reproduces the experimental test results of the retrofitted specimens. The arrest and stabilization of the crack growth is investigated via a Linear Elastic Fracture Mechanics (LEFM) approach.

Formulas are derived to estimate the moment capacity of retrofitted deeply cracked concrete-encased steel girders. The results show excellent accuracy (within about 5%) in comparison to the experimental test results.

Chapter 7.

RETROFIT OF SEISMICALLY DAMAGED REINFORCED CONCRETE SHEAR WALL USING THE CHMC

This chapter presents the experimental results of a reinforced concrete shear wall that underwent combined static vertical and quasi-static cyclic lateral loading to simulate the reinforced concrete structures under the seismic environment. Following the test of the "as-built" shear wall, the Carbon-fiber reinforced Hybrid-polymeric Matrix Composite (CHMC) was used to retrofit the damaged structure. The retrofitted shear wall was then re-tested under the same loading condition as the "as-built" control specimen. The experimental test results were presented and discussed.

7.1. Introduction

Reinforced concrete (RC) structural shear wall systems are commonly utilized in regions of high seismicity, where they may comprise the lateral and axial force resistant systems [140]. However, the earlier design provisions of the RC shear walls may not have sufficiently addressed the ductility and stiffness demands, as a consequence, severe damages had been induced in many R/C shear walls by major earthquake events [141;142]. In this light, the repair and retrofit of damaged R/C wall systems following a seismic event remains a preferable alternative to costly and time-consuming demolition and reconstruction. The last 20 years have seen significant research advances using various seismic retrofitting techniques, including the implementation of fiber reinforced polymers (FRPs). While the major failure mechanisms of R/C shear wall systems are

effectively mitigated through reasonable design and careful detailing requirements according to current design code standards, many of these systems remain susceptible to the re-occurrence of severe seismic damage due to the inherent brittle nature of the retrofitting/ reinforcing material. While R/C shear wall systems are designed with sufficient ductility following detailing requirements and improved structural design codes, failures under the combined action of lateral and vertical loads highlight deficient confinement issues [143]. As a result, the effectiveness of shear wall systems, which comprise a significant component of seismic load-resistance used in R/C structures, is underscored by their ductility.

In this chapter, the effectiveness of CHMC is investigated as a retrofit alternative for already-damaged R/C shear walls. A R/C shear wall specimen was retrofitted using the CHMC laminates, following quasi-static cyclical loading under combined lateral-axial effects that resulted in damage to a level at which only 40% of its peak strength remained. The retrofitted R/C shear wall was subsequently re-tested using the same loading environment, and the results of the two tests were compared.

7.2. Quasi-static Pushover Test of the As-built Shear Wall

7.2.1. Specimen Configurations and Test Setup

The experimental testing program of the R/C shear wall was conducted in order to evaluate the effectiveness of utilizing CHMC to retrofit a damaged R/C shear wall under the combined action of cyclical lateral and constant vertical loads. The cross sectional dimension of the scaled as-built shear wall specimen is 450mm by 150mm with

a height of 700mm, see Figure 7.2.1.1 (a). The aspect ratio of the specimen is 1.56, and the details of both vertical reinforcements and horizontal stirrup are presented in Figures 7.2.1.1 (b) and (c). The concrete design-strength used in the construction of the specimen is 30MPa, and the yield stress of the longitudinal reinforcement and stirrups are 318.9 MPa and 385.4 MPa, respectively. In order to prevent rotation and lateral sliding during loading, the shear wall specimen was anchored to the strong floor using two long steel bolts through a foundation block; two steel beams were anchored to the base of the wall in the horizontal direction to prevent lateral sliding. The vertical load was applied via a hydraulic jack that was distributed across a rigid steel beam above the specimen. The lateral load was applied using a displacement controlled actuator which was fixed to a steel loading frame. A series of LVDTs was installed at predetermined locations to measure specimen deformations; strain gauges having a gage length of 2mm were mounted onto the steel reinforcements at various locations in order to measure the rebar strains during loading; in addition, concrete strain gauges having a gage length of 50mm were mounted on the surface of the concrete to detect concrete cracking. The test setup and instrumentation lay-out are illustratively depicted in Figure 7.2.1.2.

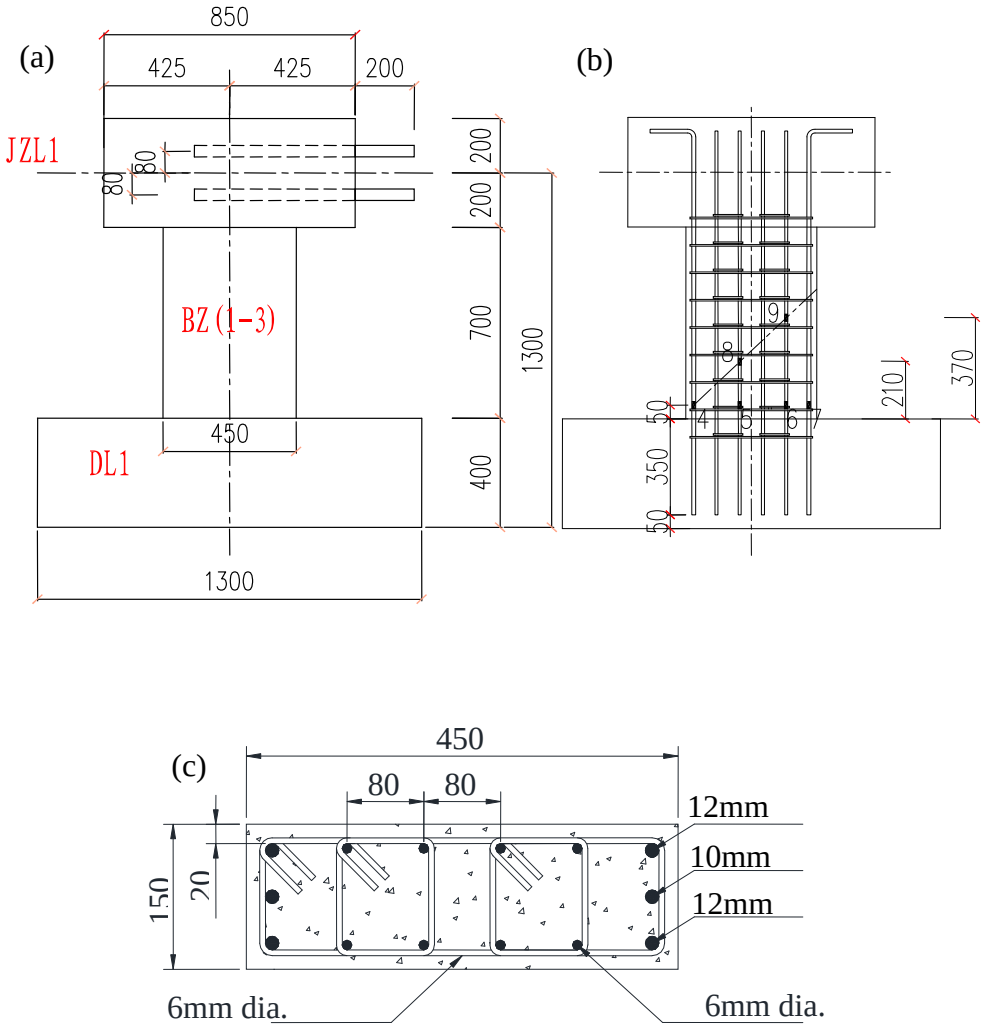

Figure 7.2.1.1. Dimension and reinforcements details for the RC shear wall specimen: (a) specimen dimensions (mm); (b) reinforcements details (elevation view, in mm); (c) cross section dimensions and reinforcements [144][19]

[19] original figures provided by the author and reprint under the license permission of Elsevier.

(a)

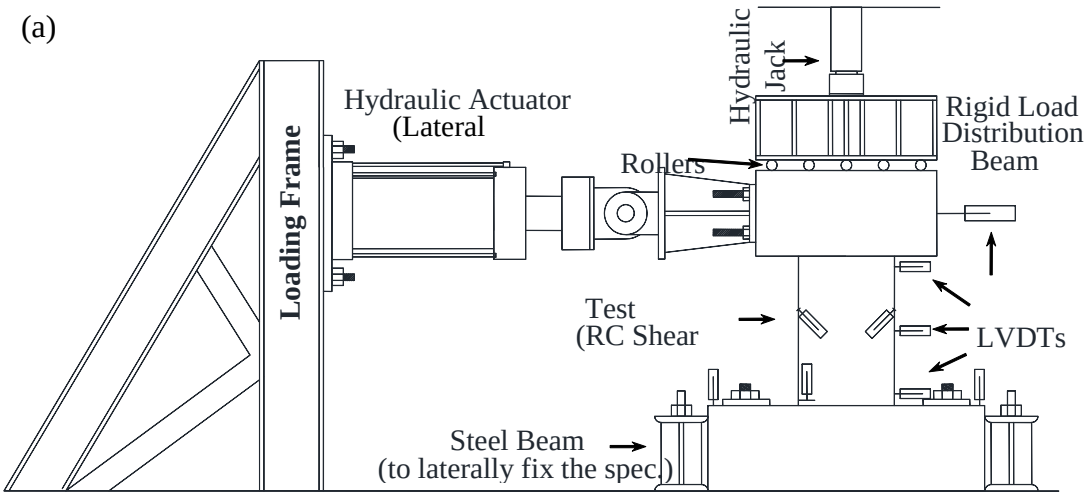

(b)

Figure 7.2.1.2. Experimental setup and instrumentation: (a) schematic figure; (b) picture

7.2.2. Test Results of the As-Built Shear Wall

The as-built shear wall specimen was loaded quasi-statically in displacement control mode for 3 consecutive hysteretic cycles at increments of 3 mm lateral displacement until the remaining strength was about 40% of the peak strength. The wall,

shown in Figure 7.2.1.1, was loaded simultaneously with a vertical load of 300 kN and a varying cyclic lateral load, resulting in an axial compression ratio ($P_{axial}/ f_c'A_{gross}$) of 0.15, i.e., the applied static axial force (P_{axial}) was equal to 15% of the design axial capacity ($f_c'A_{gross}$) of the concrete shear wall, where f_c' is the concrete compressive strength, 30MPa, and A_{gross} is the gross cross-sectional area of the specimen. During the first three loading cycles when the drift ratio (defined as the lateral displacement/ story height) is approximately equal to 0.43%, no visible damage was observed, and the shear wall specimen behaved nearly elastically. Ensuing hair line flexural cracks then started to develop along the height of the specimen after the drift ratio had increased to about 0.71%. Diagonal shear cracks then started to emerge when the drift ratio finally exceeded 1% (corresponding to a lateral displacement of about 8 mm). Soon after this the lateral load capacity of the specimen started to decrease for subsequent loading cycles beyond that maximum point on the backbone curve (as explained later) of the lateral load-deflection hysteresis. Lastly, loading was stopped when the remaining strength of the specimen had fallen to approximately 40% of the peak lateral strength. Some observations of the specimen at this point included severe concentration of damage at the base of the wall, which was signified by spalling and crushing of the concrete at the two footing corners. This resulted in exposure and compressive buckling of the vertical reinforcement due to a lack of sufficient confinement near the base that had been mainly instigated by the substantial vertical load. In addition, a 3mm-wide diagonal-crack had been induced by the lateral load, as shown in Figure 7.2.2.1 (a), which caused yielding of the steel reinforcement rebar. A vertical crack that spanned the height of the wall and in the direction of the vertical reinforcement was also observed whereby the concrete cover

had started to spall, especially at the base of the wall. The damaged R/C shear wall is shown in Figures 7.2.2.1 (a) and (b).

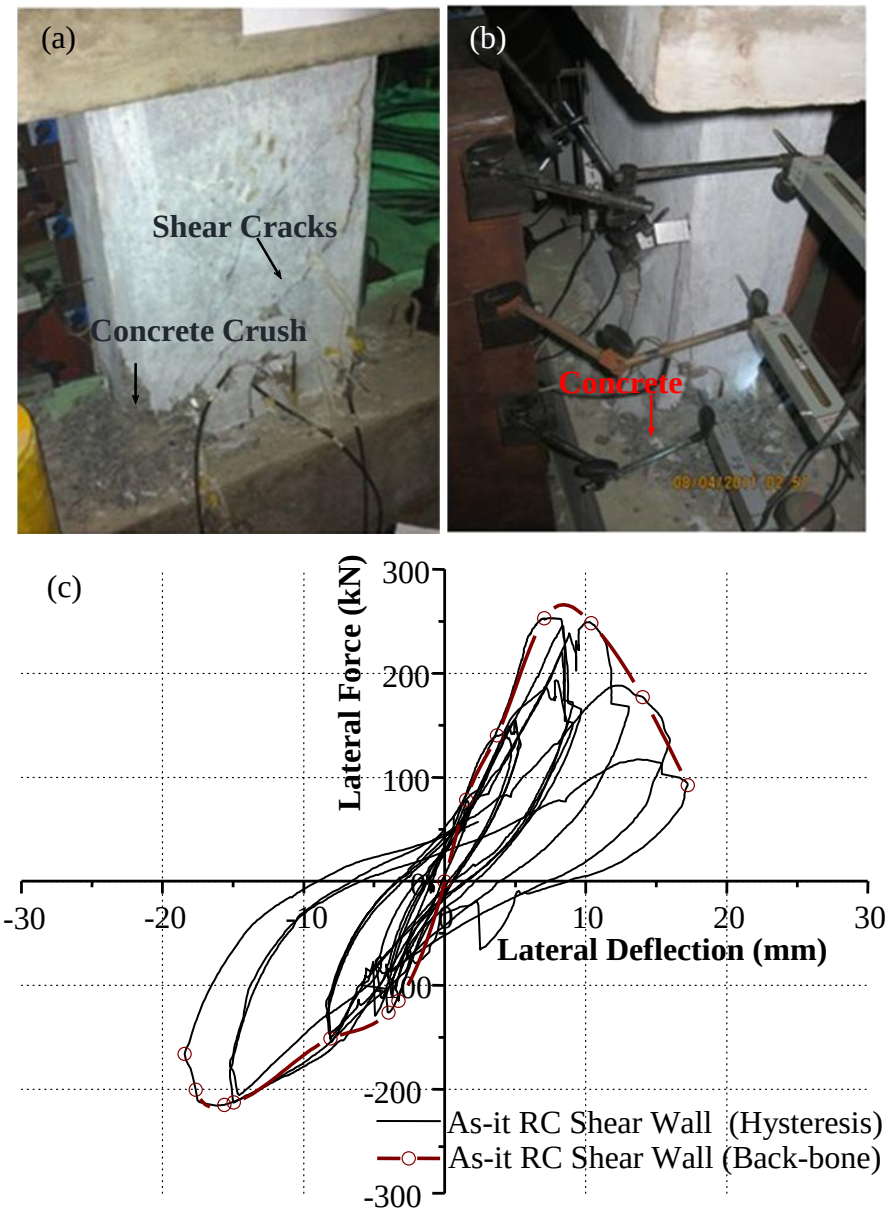

Figure 7.2.2.1. Test results of the as-built shear wall: (a) shear wall damage (front view); (b) shear wall damage (side view); (c) hysteresis and back-bone curves of the lateral load vs. deflection

Figure 7.2.2.1 (c) shows the hysteresis test results of the as-is R/C shear wall. The lateral deformation is defined as the relative lateral displacement between the top and bottom of the shear wall. The backbone curve, which is also plotted in Figure 7.2.2.1 (c) and is configured using the peak points of each hysteresis loop, represents the "envelope curve" of the shear wall's hysteresis; the backbone curve also represents the force-deflection response in specimens loaded monotonically. The maximum lateral load of approximately 265kN occurs at a drift ratio of approximately 1.2%, see Figure 7.2.2.1 (c). This was followed by a relatively sharp decline in the lateral load strength of the specimen, until the terminal load of about 100kN, or 40% of the peak strength, remained. The sudden declination, highlighted by the backbone curve, demonstrates the insufficient ductility inherently present in shear walls loaded bi-axially, mainly a result of the walls' insufficient confinement.

7.3. Retrofit using the CHMC and the Post-retrofit Performance

7.3.1. Repair and Retrofit Procedures

Following the as-is shear wall test and ensuing damage, a multi-step procedure was used to repair and retrofit the wall, including manufacturing and on-site application of the CHMC system to the damaged wall. The repairing procedure involved grouting and crack injection of the damaged wall. The heavily cracked and spalled concrete near the base was removed and replaced using a cementious high-strength grouting material, which had a 3-day strength of 62.5 MPa. In order to maintain reliable bonding between

the grouting material and the existing concrete, the shrinkage of the grout was controlled to be less than 0.1%. The 3 mm-wide diagonal shear cracks were repaired by injecting an epoxy putty, which consisted of a two-component epoxy-based polymer compound with relatively high viscosity. A second two-component epoxy having low viscosity was injected into the remaining hair line cracks. Lastly, the surface of the entire specimen was smoothed over using a grinder in order to provide an ideal surface for applying the subsequent CHMC system. Additionally, the corners of the wall specimen were rounded per specifications of ACI440.2R-08 specification [43] in order to minimize stress concentrations in the retrofitting laminates. Figures 7.3.1.1 (a) and (b) shows the grouting procedure and epoxy crack injections used to repair the damaged concrete.

Figure 7.3.1.1. Repair of the damaged RC shear wall: (a) grouting; and (b) crack epoxy injection [144][20]

[20] original figures provided by the author and reprint under the license permission of Elsevier

Following the repairing stage, the shear wall specimen was strengthened by utilizing the CHMC composite wrap system. The unidirectional woven carbon fiber fabric strips, which provide the base-line strength of the CHMC, were externally mounted to the shear wall specimen surface according to a pre-designed strengthening procedure. The carbon fiber lay-out and strengthening schemes are illustratively shown in Figures 7.3.1.2 (a) – (f), and are described as follows:

- Step 1: Two cross-bracing strips with fiber orientation aligned with the diagonal directions on each side (front and back surfaces) were mounted to increase the shear resistance of the R/C shear wall;

- Step2: Two strips with the carbon fiber oriented vertically were used to assist resisting the flexural stresses, as shown in Figure 7.3.1.2 (a);

- Step 3 utilized two horizontally orientated strips wrapped around the specimen at the top and footing regions, as shown in Figure 7.3.1.2 (b). Step 3 is critical for providing sufficient anchorage for the strengthening laminates for the previous retrofitting steps at the high-stress regions at the top and bottom of the wall; this also helps to sustain a direct transfer of shear force between the wall and footing (which had been anchored to the laboratory's concrete strong floor). Furthermore, it also provided additional confinement for the concrete in these regions which will be discussed in the synthesis of the test results. Figure 7.3.1.2 (c) shows the shear wall specimen with the carbon fiber lay-out at Stage 3;

- The system wrap, Step 4 in Figure 7.3.1.2 (d), ties all the wraps and provides necessary additional confinement in the critical compression zones during lateral loading (namely at the top and bottom regions of the wall). The final carbon fiber layup is shown

in Figures 7.3.1.2 (e) and (f) which provide a close-up of the anchor at the corner of the wall.

The carbon fiber laminates used for the retrofitting steps have a tensile strength of 2550MPa, and a nominal thickness of 0.167mm per ply. The fibers were unidirectionally woven so that the strength of transverse direction (or perpendicular to the fiber direction) strength of each ply was considered to be zero. A completed shear wall specimen is presented in Figure 7.3.1.3.

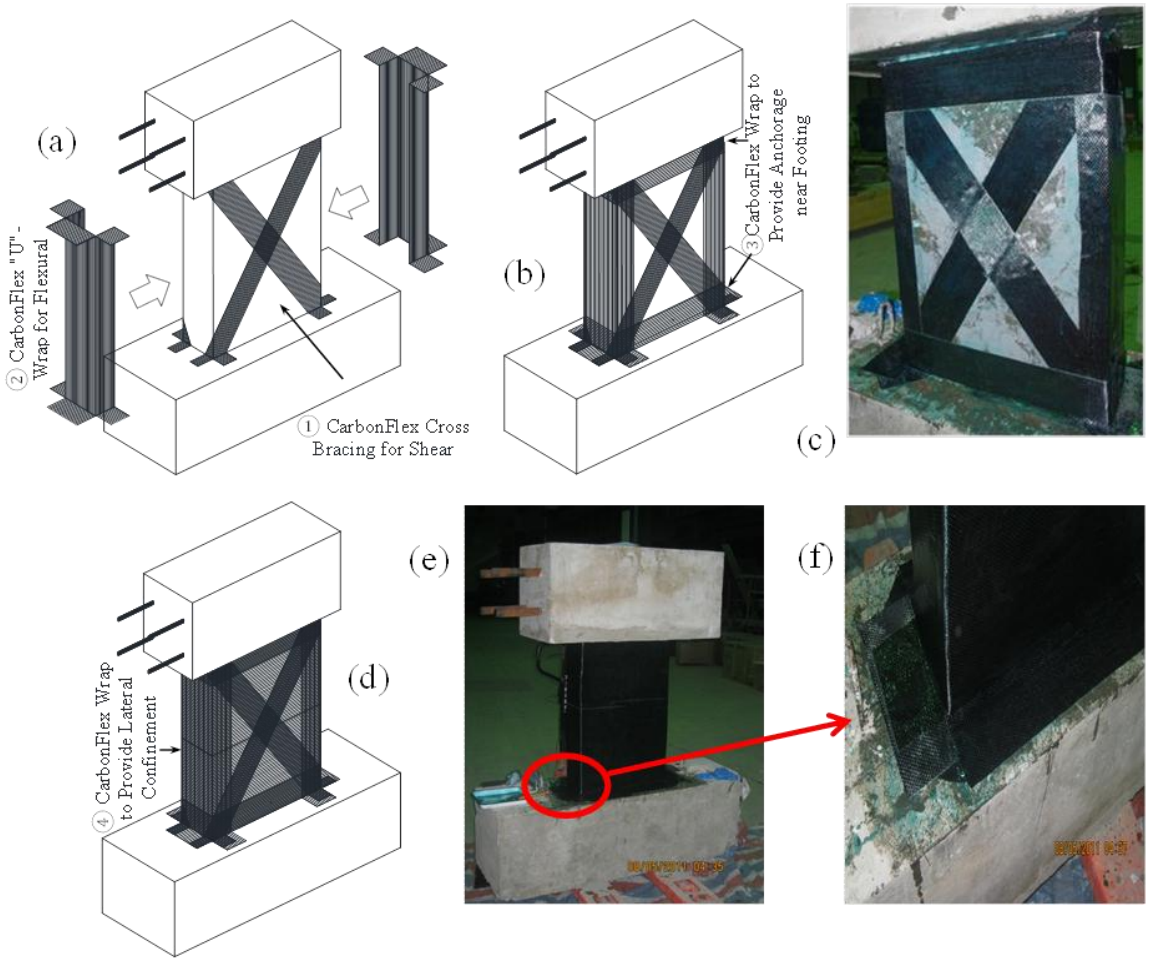

Figure 7.3.1.2. Retrofitting scheme for the damaged R/C shear wall: (a) Shear and flexural resistance applied to shear wall; (b) additional anchoring support at high-stress points near wall base; (c) the shear wall specimen following Step 3; (d) system wrap; (e) final lay-up of base carbon-fiber wrap; and (f) close-up of wrap at base of wall [144][21]

[21] original figures provided by the author and reprint under the license permission of Elsevier

Figure 7.3.1.3. The CHMC retrofitted RC shear wall specimen

7.3.2. Test Results of the CHMC Retrofitted Shear Wall

The R/C shear wall was cured for 3 days following repair and retrofit and was then re-tested under the same load conditions as the as-built specimen, maintaining the 300 kN of vertically applied constant load throughout the testing, again corresponding to $0.15f_c'A_{gross}$. Similar to the as-built specimen, linear variable differential transformers (LVDTs) were installed at various locations in order to measure the in-plane deformation of the shear wall; in particular, two LVDTs were inclined at 57.3 ° with respect to the

horizontal direction in order to measure the shear deformations; the remainder of the vertical LVDTs were mounted to the two sides of the specimen in order to measure the axial deformations near the base, as shown in Figure 7.2.1.2 (a). Electric resistance strain gauges were mounted at various locations on the CarbonFlex laminates in order to monitor the strain states of the retrofitting composite during loading. Figure 7.3.2.1 shows the hysteresis of the lateral force (kN) versus lateral displacement (mm) responses of the retrofitted and as-built specimens. The back-bone curves of both specimens are plotted and compared in Figure 7.3.2.2. For the retrofitted shear wall, approximately 80% of the original peak (positive side) strength, or a 100% increase in the terminal strength (100kN) of the as-built specimen was recovered. On the negative side of yielding of the backbone curve, the peak strength of the retrofitted specimen was about 43% greater than the terminal side (from approximately -175kN to -250kN, where the 'negative sign' represents left-side loading). The initial stiffness, see Figure 7.3.2.2, of the back-bone curves, was nearly 100% recovered in the negative loading direction, and about 80% of the stiffness had been recovered in the positive loading direction. The varying responses in the positive and negative loading directions may have been caused by a redistribution of forces once one side of the as-built specimen first experienced 'significant' damage, resulting in the asymmetrical response, see Figure 7.3.2.3.

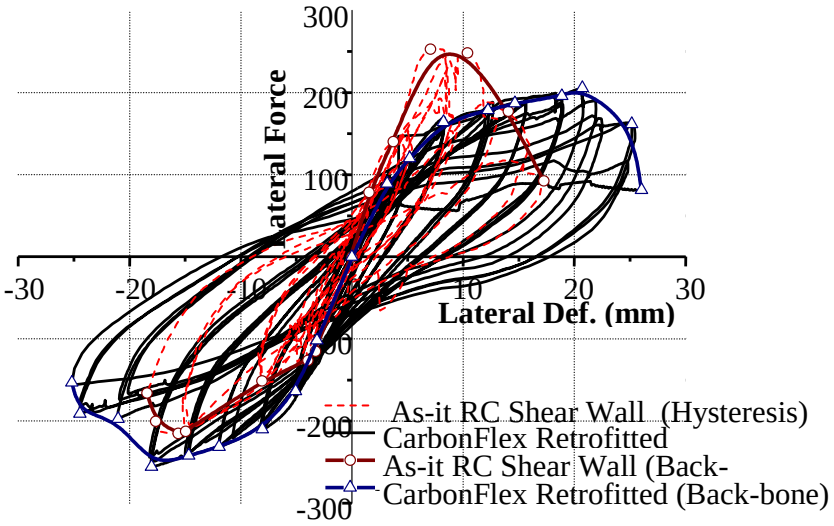

Figure 7.3.2.1. Hysteresis comparison of the as-is and CHMC-retrofitted shear walls

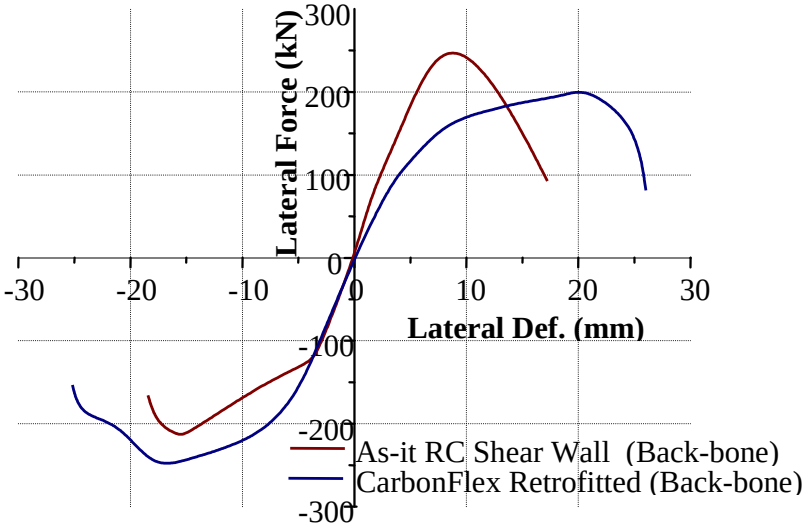

Figure 7.3.2.2. comparison of backbone curves showing large strength recovery and sustainability of the CHMC retrofitted wall

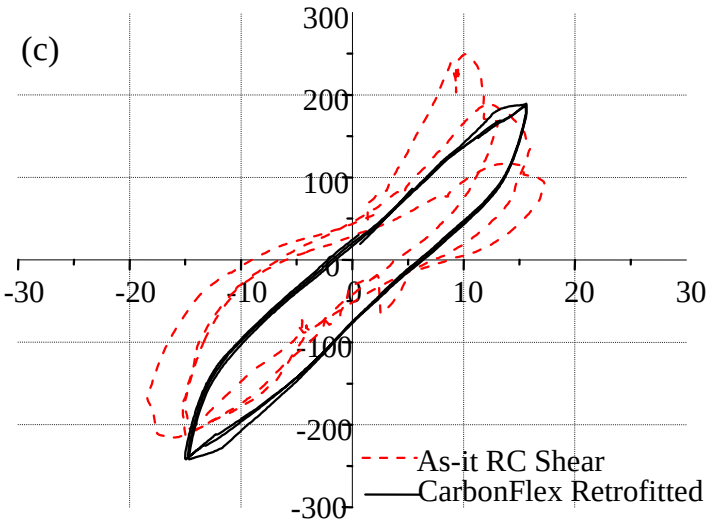

Figure 7.3.2.3. The hysteretic behaviors of as-built and retrofitted specimens at constant displacement range (-15mm to 15mm)

Besides the substantial increase to the strength and stiffness of the retrofitted specimen, the ductility of the wall had also increased dramatically. The hysteresis cycles shown in Figure 7.3.2.1 depict a significant increase in the energy dissipation between the two sets of cycles (as-is vs. CHMC retrofitted walls), which was signified by the total area enclosed by the hysteresis loops. A comparison of the backbone curves in Figure 7.3.2.2 reveals the dramatic increase (approximately 50%) in ductility and the sustainability of the load carrying capacity. This is a clear indication that the damage to the as-built shear wall specimen had been adequately stabilized even under the combined interaction of the axial and lateral loads – the former of which had likely lead to the concrete crushing, thus bringing to light confinement issues that, consequently, limited the ductility capacity of the wall. That said, following the retrofit, the confinement of the retrofitted wall had significantly improved, and the damage, e.g., concrete crack

propagation had been very effectively controlled. In addition, the CHMC-retrofitted specimen exhibited more "stable" hysteretic behavior at a constant displacement range. Figure 7.3.2.3 represents the isolated hysteresis loops when the lateral loading displacement range was -15mm to 15mm. Within this displacement range, the stiffness and load bearing capability of the as-built specimen were degrading significantly following each loading cycle as indicated by Figure 7.3.2.3. Each cycle exhibits a 'transient' component indicating the specimen's inability to adequately dissipate energy from the cracking specimen. Conversely, the CHMC-retrofitted wall exhibited more "stabilized" load-carrying behavior signified by the three over-lapping hysteresis loops, thus implying significant energy dissipation, due to the cracking concrete, via the CHMC system itself. This stabilized hysteretic behavior is also believed to be a result of the adequate confinement provided by the CHMC-at large lateral displacements. This enabled the concrete to sustain higher stresses at large strains, by precluding prevent buckling of the vertical reinforcement.

Figure 7.3.2.4. close-up view of the confined region near the base of the wall right before the test was stopped

Figure 7.3.2.4 (a) emphasizes the significant confinement provided by CHMC to the retrofitted specimen following severe damage, where Figures 7.3.2.5 (a) and (b) show the entire shear wall specimen while it was being loaded towards the end of the testing procedure, near specimen failure. The 'bubbled area' near the base of the wall validates the confinement ability of CHMC due to its higher damage tolerance and higher ductility than ordinary carbon-fiber-reinforced-polymers (CFRPs). Under extreme loading, the wall experienced substantial compressive stresses resulting from the vertical and lateral loads, thus causing large lateral expansion when the resultant compressive strain approached the crushing strain of the concrete, resulting in a Poisson's ratio of concrete that could exceed 0.5 because of the internal micro- and macro- cracks induced by the excessive stresses and, in this case, sustained by the energy dissipating mechanism of the CHMC via the hybrid matrix system and interfacial interactions. This enables a much larger damage tolerance of the specimen (in comparison to conventional CFRP-wrapped specimens) and prevents the sudden brittle rupture of the retrofitting laminate often observed with CFRPs, and thus leading to sudden confinement failure. Consequently, the crack propagation of the retrofitted wall specimen was stabilized and allowed the wall to continue deflecting (laterally) without experiencing a significant decrease in the load. Also, the location of the '*bubble*' as shown in Figure 7.3.2.4, which implies encasement of the severely damaged concrete inside the retrofitting composite wrap, is significant in that it is not at the base of the column where the stresses are largest, but it is rather located at about 10 cm above the column base in the vicinity of where the anchoring carbon-fiber wrap terminates (see Step 2 of the lay-up procedure, Figures 7.3.1.2 (a) and (b)). The significance of this is:

- The additional carbon-fiber anchorage wrap should extend over the entire anticipated plastic hinge region of the shear wall, where the stresses in the unanchored region would have been significant enough to cause damage to the concrete, i.e., the large compressive stresses caused by the combination lateral/ vertical load action that are ordinarily culpable for causing confinement-related damage. In fact, the as-is shear wall experienced the majority of its damage at the base, whereas the retrofitting wraps mitigated the damage above the base where no additional fiber anchorage was used, which emphasizes the ability of CHMC to significantly improve confinement.
- The reaction of the polymeric compound and saturant/ epoxy that creates the CHMC composite system creates an interfacial barrier that dissipates the energy generated by the damaged concrete that may have otherwise resulted in the formation of new crack surfaces, leading to a confinement failure. Instead, the column continued to expand as ensuing energy was dissipated via the CHMC system.

The large compression forces combined with the cyclic - and significantly large - lateral load, which would have, otherwise, caused a retrofitted specimen, e.g., one retrofitted with the brittle CFRP, to fail, were remarkably resisted.

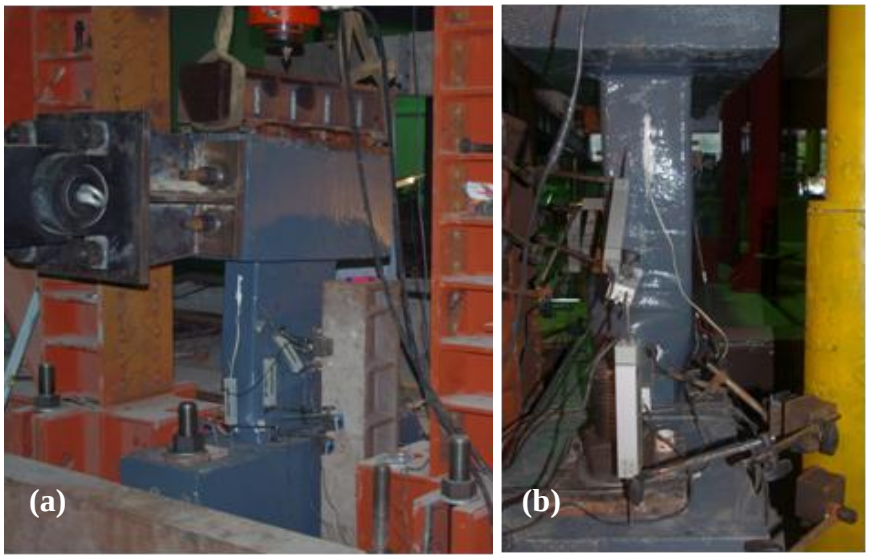

Figure 7.3.2.5. (a) angled view of the column being loaded near failure; and (b) wall with severe "bubble" near its base during loading

7.4. Summary and Conclusion

This chapter presented the experimental test results of a reinforced concrete shear wall retrofitted with CHMC. The shear wall was repaired and retrofitted following bi-axial loading in which large constant vertical and quasi-changing cyclic lateral loads were applied; the wall was damaged to the point where 40% of the peak strength remained before being retrofitted. The results are as follows:

- Following the retrofit of a damaged R/C shear wall using CHMC, the peak strength of the wall elevated to 80% of its peak original strength (after the wall had been damaged to a level where only 40% of its peak strength had been retained). The backbone curve also shows significant strength sustainability and ductility of the retrofitted wall

- The confinement of the wall increased considerably following application of the CHMC system, where the region near the base of the wall had ‘bubbled’ significantly under the combined action of axial and lateral loads but ultimately did not fail. The CHMC system had successfully dissipated the energy that may have otherwise ruptured the carbon fibers, thus enabling the epoxy/ saturant-to-fiber bond to retain its strength even after the concrete had been considerably crushed internally, as indicated by the large expansion of the wall and its significant lateral displacement.

Chapter 8.

SUMMARY AND RECOMMENDATIONS

8.1. Summary of the Current Work

In order to provide a fundamental engineering solution for civil infrastructure damage mitigation and retrofitting, a new **C**arbon-fiber reinforced **H**ybrid-polymeric **M**atrix **C**omposite (CHMC) material was developed. The microstructure behaviors of the newly developed CHMC were investigated using scanning electron microscopy (SEM), and its micromechanical properties were preliminarily characterized via nano-indentation tests that were correlated to macro-scale testing, resulting in a positive outcome but with some margin of error that will be addressed future investigations at the micro- and smaller scales. The scanning electron microscopy (SEM) images showing the microstructures of the CHMC are presented. The proposed multilayered cross-ply texture of CHMC was evidenced by the SEM images. The mechanisms by which CHMC is able to better sustain damage than conventional carbon fiber reinforced epoxies were revealed by performing a series of fractography studies on the fractured composite tensile coupons. The cross-ply modulus profile of the CHMC was obtained using nano-indentation tests, and the indentation results revealed preliminarily positive results related to the visco-elastic/ visco-plastic properties of the constituents of the hybrid matrix system of the CHMC. A simplified analytical model that was based on the micromechanics formulations was proposed for predicting the equivalent modulus of the CHMC laminates; and the model was later validated by the vibration tests.

The dynamic properties of the CHMC and conventional carbon fiber reinforced epoxies (CF/ epoxy) are investigated using free vibration and forced vibration tests. The methodology used to characterize the dynamic performance and provide initial damping

property information of composite materials was presented. The natural frequencies and damping coefficients were calculated for the materials based on the macro-scale vibration responses of tested beams. The test results indicated that the CHMC exhibits significantly greater damping and vibration suppression properties than the conventional CF/ epoxy as both a stand-alone structural material and as a retrofitting system. Generally, the observed damping is higher when CHMC is used as a stand-alone laminate than as a retrofitting material. This may be attributed to the single-side coated lay-up of the retrofitting laminates and the constraint of the substrates and also because of the greater damping the CHMC provides over the steel substrate beam. The influence of the two material processing parameters - h_p and t_c - on the material damping was investigated at the macro-scale level, and the results reveal that, generally, the damping coefficients increase with greater h_p and smaller t_c although the influence of h_p is greater than that of t_c.

The feasibility of using CHMC to retrofit damaged structural systems was investigated via a series of structural component level tests.

The experimental test results of nine notch damaged steel beams retrofitted by CHMC and the conventional carbon-fiber reinforced epoxy revealed that the load capacities of the notched steel beams were increased between the following ranges: 3.8% to 42.9% and 6.9% to 84.9% with respect to the unretrofitted specimens, following a retrofit strategy using CFRP and the CHMC laminates, respectively. In addition, the CHMC-retrofitted beam showed marginal increase in strength recovery, which is defined as the increase in peak strength with respect to the unretrofitted beam. However, the strength sustainability and the displacement ductility (related to the material energy-

dissipation) of the CHMC-retrofitted beams are significantly larger than those of the CFRP-retrofitted beams. In particular, the peak-load deflections of the CHMC-retrofitted beams were between 67.8% to 73.1% higher than those of the CFRP-retrofitted specimens. The comparison between the strain distributions and crack mouth opening distances (CMODs) immediately prior to and after the rupture of the retrofitting laminates indicates the ability of the CHMC (or CarbonFlex) to sustain some strengths after the damage was initiated, while the complete failure of CFRP occurred in an abrupt manner.

The experimental test results of three large concrete-encased steel girders retrofitted using CHMC or CFRP laminates indicated that concrete- encased steel girders retrofitted with CHMC show significant sustainable high strength (about 68% of the peak strength) with superb ductility. The energy dissipation mechanism that is integrated into the damaged, yet retrofitted, specimens via the CHMC helps to stabilize the crack growth in the fractured steel weldment, thus controlling the formation of new cracks that would otherwise lead to a brittle-like failure (as in the case of CFRP-retrofitted beams). A Concrete Structural Retrofitting Analysis Program (or CSRAP-Flex) was developed to predict the nonlinear behavior of already-damaged concrete-encased steel girders. The CSRAP-Flex program very accurately reproduced the experimental test results of the retrofitted specimens. Simplified formulas are derived to estimate the moment capacity of retrofitted deeply cracked concrete-encased steel girders. The results show excellent accuracy (within about 5%) in comparison to the experimental test results.

Lastly, a quasi-static pushover test on the CHMC retrofitted reinforced concrete shear wall further highlighted the CHMC's capacity of enhancing the deformation and energy dissipating potential of damaged civil infrastructure systems.

8.2. Recommendations for Future Works

In the current study, the micromechanical properties of the composite were preliminarily related to its macro-scale mechanical performances via simple micro-mechanics based formulations. However, a more elaborated model should be established from a "multi-scale" perspective that is based on more thorough micro-scale and macro-scale mechanical test results, such that the properties (such as strength, ductility, and damping etc.) of the composite material could be accurately predicted and controlled. The micro-mechanical tests results, such as the nanoindentation results, could be quantitatively related to the material constitutive properties through time-dependent constitutive models. For instance, the creep and visco-elastic/ visco-plastic behavior of the two polymeric matrix phases exhibited in the nanoindentation tests may be used to determined model parameters such as the coefficient of viscosity. The constitutive models obtained using micro-mechanical tests results can then be used to predict the material macro-mechanical properties, such as damping. Furthermore, since the preliminary studies have revealed that the mechanical properties of CHMC, such as damping and impact resistance, are closely related to the interfacial cohesion zone between the two polymeric matrix phases, the fundamental mechanism by which the

polymeric interface, as revealed by the SEM study, is able to influence the material's properties should be more thoroughly understood from the molecular level.

Lastly, in order to implement the newly developed material into commercialized applications, further studies at the structural system level should be carried out to evaluate and qualify the material for structural damage mitigation in a systematic sense. The manufacturing process, construction procedure, and overall project cost etc. should be investigated and compared to those of the traditional structural systems.

REFERENCES

[1] Raizer V. Natural disasters and structural survivability. R&RATA #3 2009;2:7-16.

[2] National Institute of Building Science. Natural hazards and security. http://www.wbdg.org/design/resist_hazards.php . 2013.

[3] Recommended lateral force requirements and commentary. San Francisco, CA: Seismology Committee, Structural Engineers Association of California; 1989.

[4] Shepherd R. The San Salvador earthquake of Oct 10, 1986. 3 ed. EERI; 1987.

[5] Ayscue JK. Hurricane damage to residential structures: risk and mitigation. Boulder, CO: NHRAIC; 1996. Report No.: Natural Hazards Research Working Paper #94.

[6] Mehta KC, Smith DA, Ronald HC. Knowledge-based system for wind damage to buildings. New York, NY: ASCE; 1994. Report No.: Hurricanes of 1992.

[7] Minor JE, Mehta KC. Wind damage observations and implications. J Struct Div ASCE 1979;(105):2279-91.

[8] Minor JE. Windborne debris and the building envelope. J Wind Eng Ind Aerodyn 1994;(53):207-27.

[9] Zhou H, Dhiradhamvit K, Attard TL. Tornado-borne debris impact performance of an innovative storm safe room system protected by a carbon fiber reinforced hybrid-polymer matrix composite. Engineering Structures 2013.

[10] Masters FJ, Gurley KR, Shah N, Fernandez G. The vulnerability of residential window glass to lightweight windborne debris. Eng Struct 2010;32:911-21.

[11] Fernandez G, Masters FJ, Gurley KR. Performance of hurricane shutters under impact by roof tiles. Eng Struct 2010;32(3384):3393.

[12] The effects and economic impact of corrosion. ASM International; 2000. Report No.: #06691G.

[13] Kenney PP. A review of procedures for the analysis and design of concrete structures to resist missile impact effects. Nuclear Eng Design 1976;37(183):203.

[14] Corbett GG, Reid SR, Johnson W. Impact loading of plates and sheels by free-flying projectiles: a review. Int J Impact Eng 1995;18(2):141-230.

[15] Li MO, Reid SR, Wen HM, Telford AR. Local Impact effects of hard missles on concrete targets. Int J Impact Eng 2005;32:141-230.

[16] Fu CC, Burhouse JR, Change GL. Overheight vehicle collision with highway bridges. Transport Res Board 2004;80-8.

[17] Svensson H. Protection of bridge piers against ship collision. Steel Construct 2009;2(1):21-32.

[18] Davidson MT, Consolazio GR, Getter DJ, Shah FD. Probability of collapse expression for bridge subject to barge collision. J Bridge Eng ASCE 2013;18(4):287-96.

[19] Housner GW, Bergman LA. Structural control: past, present, and future. J Eng Mech Div 1997;123(9):897-971.

[20] Teng JG, Chen JF, Smith ST, Lam L. Behaviour and strength of FRP-strengthened RC structures: a state-of-the-art review. Structures & Buildings 156 2003;(1):51-62.

[21] Bakis CE, Bank LC, Brown VL, Cosenza E, Davalos JF, Lesko JJ, et al. Fiber-reinforced polymer composites for construction - state-of-the-art review. J Compos Constr, ASCE 2002;6(2):73-87.

[22] Song W, Ma ZJ. Behavior of honeycomb FRP sandwich structures under combined effects of service load and low temperatures. J Comp Construct ASCE 2011;15(6):985-91.

[23] Buyukozturk O, Hearing B. Failure behavior of precracked concrete beams retrofitted with FRP. J Comp Construct ASCE 1999;2(3):138-44.

[24] Saadatmanesh H, Ehsani MR, Jin L. Repair of earthquake-damaged RC columns with FRP wraps. ACI Struct J 1997;92(2):206-14.

[25] Meier U. Bridge repair with high performance composite materials. Mater & Tech 1987;15:125-8.

[26] Rostasy FS. Bonding of steel and GFRP plates in the area of coupling joints. Braunschweig, Germany: Federal Institute for Mater Testing; 1987. Report No.: 3126/1429.

[27] Fardis MN, Khalili H. Concrete encased in fiberglass reinforced plastic. ACI Struct J 1981;76:440-6.

[28] Gu X, Peng B, Chen G, Li X, Ouyang Y. Rapid strengthening of masonry structures cracked in earthquakes using fiber composite materials. J Comp Construct ASCE 2012;16(5):590-603.

[29] Jesus AMP, Pinto JMT, Morais JJL. Analysis of solid wood beams strengthened with CFRP laminates of distinct lengths. Construct & Building Mater 2012;35:817-28.

[30] Zhou H, Attard TL. Rehabilitation and strength sustainability of fatigue damaged concrete-encased steel flexural members using a newly developed polymeric carbon-fiber composite. Comp Part B: Eng 2013;45:1091-103.

[31] Mukhopadhyaya P, Swamy N. Interface shear stress: a new design criterion for plate debonding. J Compos Constr, ASCE 2001;5(1):35-43.

[32] Chen JF, Teng JG. Shear capacity of fiber-reinforced polymer-strengthened reinforced concrete beams: fiber reinforced polymer rupture. J Struct Eng, ASCE 2003;129(5):615-25.

[33] Aram MR, Czaderski C, Motavalli M. Debonding failure modes of flexural FRP-strengthened RC beams. Compos Part B: Eng 2008;39:826-41.

[34] Lopez A, Nanni A. Composite strengthening technologies: field evaluation and monitoring of five reinforced concrete bridges. Concr Int 2006 Jan;28(1):74-80.

[35] Zhao XL, Zhang L. State-of-an-art review on FRP strengthened steel structures. Eng Struct 2007;29:1808-23.

[36] Lam ACC, Yam MCH, Cheng JJR, Kennedy GD. Study of stress intensity factor of a cracked steel plate with a single-side CFRP composite patching. J Compos Constr, ASCE 2010;14(6):791-803.

[37] Attard TL, Abela CM, Dhiradhamvit K. Seismic FRP retrofit of circular single-column bens using a ductility wrap envelope to alter failure modes. Eng Struct 2011;33:1553-64.

[38] Abela CM, Attard TL. Analytical models and guidelines for ductility enhancement for circular reinforced concrete single-column bents using fiber-reinforced polymers. J Bridge Eng ASCE 2010;16(1):171-6.

[39] Hmidan A, Kim YJ, Yazdani S. CFRP repair of steel beams with various initial crack configurations. J Compos Constr, ASCE 2011;15(6):952-62.

[40] Tavakkolizadeh M, Saadatmanesh H. Fatigue strength of steel girders strengthened with carbon fiber reinforced polymer patch. J Struct Eng, ASCE 2003;129(2):186-92.

[41] Sen R, Liby L, Mullins G. Strengthening steel bridge sections using CFRP laminates. Compos Part B: Eng 2001;32:309-22.

[42] Tavakkolizadeh M, Saadatmanesh H. Repair of damaged steel-concrete composite girders using carbon fiber-reinforced polymer sheets. J Compos Constr, ASCE 2003;7(4):311-22.

[43] ACI Committee 440. ACI 440.2R-08, Guide for the design and construction of externally bonded FRP systems for strengthening concrete structures. Detroit, Michigan: American Concrete Institute; 2008.

[44] Saadatmanesh H, Malek AM. Design guidelines for flexural strengthening of RC beams with FRP plates. J Compos Constr, ASCE 1998;2(4):158-64.

[45] Hamed E, Rabinovitch O. Damping and viscoelastic dynamic response of RC flexural members strengthened with adhesively bonded composite materials. J Eng Mech, ASCE 2007;133(12):1278-89.

[46] Kelly JM. The role of damping in seismic isolation. Earthquake Eng Struct Dyn 1999;28:3-20.

[47] Attard TL, Dansby RE. Evolutionary structural control of elastic and inelastic strains using rehabilitative algorithms in damaged steel buildings. J Mech Mater Struct 2009;4(3):413-24.

[48] Zhang Y, Iwan WD. Active interaction control of tall buildings subjected to near-field ground motions. J Struct Eng, ASCE 2002;128(1):69-79.

[49] Callister WD. Material science and engineering - an introduction. 3rd Edition ed. New York, NY: John Wiley & Sons; 1994.

[50] Donnet J, Wang TK, Peng JCM, Rebouillat S. Carbon fiber. 3rd Edition ed. New York, NY: Marcel Dekker, Inc.; 1998.

[51] Curtis GJ, Milne JM, Reynolds WN. Non-hookean behaviour of strong carbon fibres. Nature 1968;220:1024-5.

[52] Tanabe Y, Yasuda E, Bunseell AR, Favry Y, Inagaki M, Sakai M. The strength of pitch-based carbon fibre at high temperature. J Mater Sci 1991;26:1601-4.

[53] Agarwal B, Broutman LJ, Chandrashekhara K. Analysis and performance of fiber composites. 3rd Edition ed. New York, NY: Jon Wiley & Sons; 2006.

[54] Barbero EJ. Introduction to Composite Materials Design. 2 ed. Boca Raton, FL: CRC, Inc; 2010.

[55] Jones RM. Mechanics of composite materials. 2nd ed. New York: Taylor & Francis Group, LLC; 1999.

[56] Paul B. Prediction of elastic constants of multiphase materials. Transactions of the Metallurgical Society of AIME 1960;36-41.

[57] Hashin Z. The elastic moduli of heterogeneous materials. J App Mech 1962;29:143-50.

[58] Hashin Z, Shtrikman S. A variational approach to the theory of the elastic behavior of multiphase materials. J Mech & Phy Solids 1963;11(2):127-40.

[59] Halpin JC, Tsai SW. Effect of environmental factors on composite materials. Air Force Material Laboratory; 1969. Report No.: AFML-TR-67-423.

[60] Jones RM. Mechanics of composite materials. 2 ed. Philadephia, PA: Taylor & Francis, Inc; 1999.

[61] Hoffman O. The brittle strength of orthotropic materials. J Comp Mater 1967;1(2):200-6.

[62] Tsai SW, Wu EM. A general theory of strength for anisotropic materials. J Comp Mater 1971;5(1):58-80.

[63] Saravanos DA, Chamis CC. Tailoring of composite links for optimal damped elasto-dynamic performance. Washington D.C.: NASA; 1989. Report No.: 102094.

[64] Adams RD, Fox MAO, Flood RJL, Friend RJ, Hewitt RL. The dynamic properties of unidirectional carbon and glass fiber reinforced plastics in torsion and flexure. J Comp Mater 1969;3:594-603.

[65] Adams RD, Bacon DGC. Effect of fibre orientation and laminate geometry on the dynamic properties of CFRP. J Comp Mater 1973;7:402-28.

[66] Gibson RF, Plunkett R. Dynamic mechanical behavior of fiber-reinforced composites: measurement and analysis. J Comp Mater 1976;10:325-41.

[67] Suarez SA, Gibson RF, Sun CT, Chaturvedi SK. The influence of fiber length and fiber orientation on damping and stiffness of polymer composite materials. Exp Mech 1986;26(2):175-84.

[68] Cawse JL, Stanford JL. Rubber-toughened polyurethane network and composite mateirals. Polymer 1987;28:356-67.

[69] Tsai JL, Huang BH, Cheng YL. Enhancing fracture toughness of glass/epoxy composites by using rubber particles together with silica nanoparticles. J Comp Mater 2009;43(25):3107-23.

[70] Parker DS, Sue HJ, Huang J, Yee AF. Toughening mechanisms in core-shell rubber modified polycarbonate. Polymer 1990;31:2267-77.

[71] Yee AF. Modifying matrix materials for tougher composites. Toughened Composites, ASTM STP 937 1987;383-96.

[72] Garcia R, Evans RE, Palmer RJ. Structural property improvements through hybridized composite. Toughened Composites, ASTM STP 937 1987;397-412.

[73] Bakis CE, Nanni A, Terosky JA, Koehler SW. Self-monitoring, pseudo-ductile, hybrid FRP reinforcement rods for concrete applications. Comp Sci Tech 2001;61(815):823.

[74] Hai ND, Mutsuyoshi H, Asamoto S, Matsui T. Structural behavior of hybrid FRP composite I-beam. Construct Building Mater 2010;24:956-69.

[75] Wu ZS, Sakamoto K, Niu HD, Shimada M, Murakami S. Strengthening effects of concrete flexural members retrofitted with hybrid FRP composites. San Francisco, CA: The 3rd Int Conf on Comp in Infrastructures; 2002.

[76] Hu H, Yu S, Wang M, Ma J, Liu K. Tribological properties of epoxy/ polyurea composite. Polymer Adv Techn 2008;20:748-52.

[77] BASF Mbrance CF 130 Data Guide. Shakopee, MN: BASF Construction Chemicals, LLC - Building Systems; 2007.

[78] Nashif AD, Jones DIG, Henderson JP. Vibration damping. New York, NY: Jonh Wiley & Sons; 1985.

[79] Oliver WC, Pharr GM. An improved technique for determining hardness and elastic modulus using load and displacement sensing indentation experiments. J Mater Res 1992;7(6):1564-83.

[80] VanLandingham MR, Villarrubia JS, Guthrie W, Greg FM. Nanoindentation of polymers: an overview. Macromol Symp 2001;167:15-43.

[81] Bhushan B, Li X. Nanomechanical characterisation of solid surfaces and thin films. Int Mater Reviews 2003;48(3):125-63.

[82] Das B, Prasad KE, Ramamurty U, Rao CNR. Nano-indentation studies on polymer matrix composites reinforced by few-layer graphene. Nanotechn 2009;20:1-5.

[83] Kucuk Y, Mollanmahmutoglu C, Wang Y, Lu H. Nonlinear viscoelastic nanoindentation of PMMA under a spherical tip. Exper Mech 2013;53:731-42.

[84] Berthelot JM, Sefrani Y. Damping analysis of unidirectional glass and Kevlar fibre composites. Comp Sci & Tech 2003;64:1261-78.

[85] Suarez SA, Gibson RF, Deobald LR. Random and impulse techniques for measurement of damping in composite materials. Exp Techn 1984;6(2):10-4.

[86] Crane RM, Gillespie JW. Characterization of the vibration damping loss factor of glass and graphite fiber composites. Comp Sci Techn 1991;40:355-75.

[87] Hadi AS, Ashton JN. Measurement and theoritical modelling of the damping properties of a unidirectional glass/epoxy composite. Comp Struct 1996;34:381-5.

[88] Rajoria H, Jalili N. Passive vibration damping enhancement using carbon nanotube-epoxy reinforced composites. Comp Sci Techn 2005;65:2079-93.

[89] Khan SU, Li CY, Siddiqui NA, Kim JK. Vibration damping characteristics of carbon fiber-reinforced composites containing multi-walled carbon nanotubes. Comp Sci Techn 2011;71:1486-94.

[90] Rao SS. Vibration of continous systems. New York, NY: John Wiley & Sons; 2007.

[91] BASF Mbrace Primer Data Guide. Shakopee, MN: BASF, The Chemical Company; 2007.

[92] Gersch W, Sharpe DR. Estimation of power spectra with finite-order autoregression models. IEEE Trans Automat Contr 1973;18(4):367-9.

[93] Evans E, Ritchie K. Dynamic strength of molecular adhesion bonds. Biophys J 1997;72(4):1541-55.

[94] Standard test method for measuring vibration-damping properties of materials. West Conshohocken, PA: ASTM; 2010. Report No.: ASTM E756-05.

[95] Zhao XL, Zhang L. State-of-the-art review on FRP strengthened steel structures. Eng Struct 2007;29:1808-23.

[96] Mertz DR, Gillespie JW. Rehabilitation of steel bridge girders through the application of advanced composite materials . Washington D.C.: Transportation Research Board; 1996. Report No.: NCHRP-93-ID011.

[97] Linghoff D, Al-Emrani M, Kliger R. Performance of steel beams strengthened with CFRP laminate - part 1: laboratory tests. Comp Part B: Eng 2010;41:509-15.

[98] Deng J, Lee MMK, Moy SSJ. Stress analysis of steel beams reinforced with a bonded CFRP plate. Compos Struct 2004;65(205):215.

[99] Wu G, Wang HT, Wu ZS, Liu HY, Ren Y. Experimental study on the fatigue behavior of steel beams strengthened with different fiber-reinforced composite plates. J Comp Construct ASCE 2012;16(2):127-37.

[100] Jiao H, Mashiri F, Zhao XL. A comparative study on fatigue behavior of steel beams retrofitted with welding, pultruded CFRP plates and wet layup CFRP sheets. Thin-Walled Struct 2012;59:144-52.

[101] Kim YJ, Harries KA. Predictive response of notched steel beams repaired with CFRP strips including bond-slip behavior. Int J Struct Stability & Dyn 2012;12(1):1-21.

[102] Kim YJ, Brunell G. Interaction between CFRP-repair and initial damage of wide-flange steel beams subject to three-point bending. Compos Struct 2011;93:1986-96.

[103] El-Hacha R, Mohamed YEA. Anchorage system to prestress FRP laminates for flexural strengthening of steel-concrete composite girders. J Comp Construct ASCE 2013;17(3):324-35.

[104] Lunn DS, Rizkalla SH, Maeda S, Ueda T. FRP anchorage systems for infill masonry structures. 2012 Feb 2; Sapporo, Japan: Hokkaido University; 2012.

[105] Cortes-Puentes WL, Palermo D. Modeling of RC shear walls retrofitted with steel plates or FRP sheets. J Struct Eng ASCE 2012;138(5):602-12.

[106] Zhou H, Attard TL, Wang YL, Wang JA, Ren F. Rehabilitation of notch damaged steel beams using a carbon fiber reinforced hybrid polymeric-matrix composite. Compos Struct 2013;(106):690-702.

[107] Peters WH, Ranson WF. Digital imaging techniques in epxerimental stress analysis. Opt Eng 1981;21:427-31.

[108] Chu TC, Ranson WF, Sutton MA, Peters WH. Application of digital-image-correlation techniques to experimental mechanics. Exp Mech 1985;25:232-44.

[109] Sutton MA, Cheng M, Peters WH, Chao YJ, McNeill SR. Applicaion of an optimized digital correlation method to planar deformation analysis. Image Vis Comput 1986;4:143-50.

[110] Keating TJ, Wolf PR, Scarpace FL. An improved method of digital imaging correlation. Photo Eng Remote Sens 1975;41(8):993-1002.

[111] Pan B, Qian K, Xie H, Asundi A. Two-dimensional digital image correlation for in-plane displacement and strain measurement: a review. Meas Sci Techn 2009;20:1-17.

[112] ABAQUS [computer program]. Version 6.10. Providence, RI: 2010.

[113] Dhiradhamvit K, Attard TL, Zhou H. Development of a new lightweight "Rubberized-Carbon" composite for wood home protection. 2011 Jun 20; Athens, Greece 2011.

[114] Gunes O, Buyukozturk O, Karaca E. A fracture-based model for FRP debonding in strengthened beams. Eng Fract Mech 2009;76:1897-909.

[115] Rice JR. Contained plastic deformation near cracks and notches under longitudinal shear. Int J Fract Mech 1966;2:426-47.

[116] Xia ZC, Hutchinson JW. Crack tip fields in strain cradient plasticity. J Mech Phys Solids 1996;44(10):1621-48.

[117] Jing PH, Khraishi T. Analytical solutions for crack tip plastic zone shape using the Von Mises and Tresca yield criteria: effects of crake mode and stress condition. J Mech 2004;20(3):199-210.

[118] Theocaris PS. Experimental evaluation of the plastic zones for steady mode-III crack growth. Acta Mech 1986;69:271-94.

[119] Liu AF. Mechanics and mechanisms of fracture: an introduction. 1 ed. Materials Park, OH: ASM International; 2005.

[120] Gross B, Srawley JE. Stress-intensity factors for three-point bend specimens by boundary collocation. Washington, DC: National Aeronautics and Space Administration; 1965. Report No.: NASA TN D-3092.

[121] Ricles JM, Pabppjian SD. Seismic performance of steel-encased composite columns. J Struct Eng, ASCE 1994;120(8):2474-94.

[122] El-Tawil S, Deierlein GG. Strength and ductility of concrete encased composite columns. J Struct Eng, ASCE 1999;125(9):1009-19.

[123] Mirza SA, Lacroix EA. Comparative strength analyses of concrete-encased steel composite columns. J Struct Eng, ASCE 2004;130(12):1941-53.

[124] Naito H, Akiyama M, Suzuki M. Ductility evaluation of concrete-encased steel bridge piers subjected to lateral cyclic loading. J Bridge Eng, ASCE 2011;16(1):72-81.

[125] ACI Committee 318. ACI 318-08, Building code requirements for structural concrete. Detroit, Michigan: American Concrete Institute; 2008.

[126] AISC Committee 360. ANSI/AISC 360-05, Specification for structural steel buildings. Chicago, Illinois: American Institute of Steel Construction, INC; 2005.

[127] Hayashi K, Ono S, Nakamura S. Experimental studies on retrofit by partially encased concrete to the steel I-girder subjected to bulckling deformation. Tech Memo Pub Works Res Inst 2003;3920:229-36.

[128] Byers WG, Marley MJ, Mohammadi J, Nielsen RJ, Sarkani S. Fatigue reliability reassessment applications: state-of-the-art paper. J Struct Eng, ASCE 1997;123(3):277-85.

[129] Zhao Z, Haldar A. Bridge fatugue damage evaluation and updating using non-destructive inspecitions. Eng Fract Mech 1996;53(5):775-88.

[130] ASCE Cofafrotcossarotsd. Fatigue reliability 1-4. J Struct Eng, ASCE 1982;108:3-88.

[131] Righiniotis TD, Omer E, Elghazouli AY. A simplified crack model for weld facture in steel moment connections. Eng Struct 2002;24:1133-40.

[132] Chi W, Deierlein GG, Ingraffea A. Fracture toughness damands in welded beam-column moment connections. J Struct Eng, ASCE 2000;126(1):88-97.

[133] Mirza SA, Tikka TK. Flexural stiffness of composite columns subjected to major axis bending. ACI Struct J 1999;96(1):19-28.

[134] Attard TL. Post-yield material nonlinearity: optimal homogeneous shear-frame sections and hysteretic behavior. Int J Solid Struct 2005;42:5656-68.

[135] Toyoda M, Mochizuki M. Control of mechanical properties in structural steel welds by numerical simulation of coupling among temperature, microstructure, and macro-mechanics. Sci Technol Adv Mater 2004;5(255):266.

[136] Anderson TL. Fracture mechanics fundamentals and applications. 3rd ed. Boca Raton, Florida: CRC Press, Taylor & Francis Group, LLC; 2005.

[137] Bae S, Bayrak O. Seismic performance of full-scale reinforced concrete columns. ACI Struct J 2008;105(2):123-33.

[138] Fafitis A, Shah SP. Lateral reinforcement for high strength concrete columns. ACI Spec Publ, SP-87 1985;213-32.

[139] Fafitis A, Shah SP. Constitutive model for biaxial cyclic loading of concrete. J Eng Mech, ASCE 1986;112(8):760-75.

[140] Lefas ID, Kotsovos MD, Ambraseys NN. Behavior of reinforced concrete structural shear wall: strength, deformation characteristics, and failure mechanism. ACI Struct J 1990;87(1):23-31.

[141] Lombard J, Lau DT, Humar JL, Foo S, Cheung MS. Seismic strengthening and repair of reinforced concrete shear walls. Silverstream, New Zealand: New Zealand Society for Earthquake Engineering; 2000.

[142] Li B, Lim CL. Tests on seismically damaged reinforced concrete structural walls repaired using fiber-reinforced polymers. J Comp Construct ASCE 2010;14(5):597-608.

[143] Greifenhagen C, Lestuzzi P. Static cyclic tests on lightly reinforced concrete shear walls. Eng Struct 2005;27:1703-12.

[144] Zhou H, Attard TL, Zhao B, Yu J, Lu W, Tong L. Experimental study of retrofitted reinforced concrete shear wall and concrete-encased steel girders using a new CarbonFlex composite for damage stabilization. Eng Fail Anal 2013;DOI:10.1016/j.engfailanal.2013.01.032.

APPENDIX

Appendix A. Nanoindentation Results

Table A1.
Nanoindentation results within the area A1

hc	h_{max}	hf	**m**	$\mathbf{P_{max}}$	**S**	**A**	**Er**	**H**
nm	nm	nm		μN		nm^2	GPa	GPa
29.35	49.65	0.00	1.86	499.87	18.86	9.23E+04	55.01	5.41
35.28	53.97	0.00	2.21	499.91	20.75	1.14E+05	54.35	4.37
29.10	48.13	0.00	1.93	499.90	20.35	9.14E+04	59.64	5.47
22.71	45.09	0.00	1.51	499.89	16.79	6.85E+04	56.82	7.30
25.61	45.55	0.31	1.72	499.92	19.18	7.88E+04	60.53	6.35
27.42	46.47	0.00	1.85	499.88	20.13	8.53E+04	61.06	5.86
40.76	59.57	7.40	2.13	499.84	20.69	1.36E+05	49.71	3.68
28.82	46.96	0.00	2.16	499.91	24.38	9.04E+04	71.85	5.53
26.18	46.01	1.11	1.72	499.89	19.44	8.08E+04	60.58	6.19
28.49	53.23	5.17	1.47	499.85	15.38	8.92E+04	45.64	5.61
27.81	47.07	0.00	1.85	499.90	19.72	8.67E+04	59.34	5.77
27.86	50.45	1.21	1.64	499.92	16.71	8.69E+04	50.24	5.75
25.14	44.91	0.00	1.74	499.87	19.77	7.71E+04	63.09	6.48
29.23	51.02	0.00	1.77	499.87	17.37	9.19E+04	50.79	5.44
27.24	45.88	0.00	1.87	499.88	20.59	8.46E+04	62.71	5.91
252.8	297.6	141.3	2.58	499.90	8.18	1.96E+06	5.17	0.25
245.0	284.5	140.1	2.70	499.90	9.30	1.86E+06	6.04	0.27
40.11	65.52	0.00	1.93	499.86	14.74	1.33E+05	35.77	3.75
37.42	62.23	0.00	1.83	499.90	14.44	1.23E+05	36.50	4.07
90.22	110.5	18.15	3.33	499.90	17.92	3.81E+05	25.71	1.31
39.27	63.43	0.00	1.96	499.90	15.35	1.30E+05	37.71	3.84
141.2	160.8	0.00	4.55	499.90	13.43	7.46E+05	13.78	0.67
143.5	166.3	67.15	3.20	499.89	16.05	7.65E+05	16.26	0.65

Table A2.
Nanoindentation results within the area A2

hc	h_{max}	hf	**m**	$\mathbf{P_{max}}$	**S**	**A**	**Er**	**H**
nm	nm	nm		μN		nm^2	GPa	GPa
33.72	57.23	0.00	1.81	499.89	15.77	1.09E+05	42.42	4.61
33.15	59.14	5.70	1.57	499.89	14.85	1.06E+05	40.33	4.70
30.89	52.63	0.00	1.81	499.89	17.19	9.80E+04	48.67	5.10
267.3	317.6	139.1	2.65	499.88	7.42	2.17E+06	4.46	0.23
265.0	316.1	152.0	2.38	499.90	7.22	2.13E+06	4.38	0.23
249.5	299.8	140.3	2.35	499.90	7.33	1.92E+06	4.69	0.26
244.5	288.2	138.9	2.53	499.87	8.41	1.85E+06	5.47	0.27
274.9	326.2	165.1	2.34	499.89	7.22	2.28E+06	4.24	0.22
261.7	313.2	148.3	2.38	499.88	7.20	2.09E+06	4.41	0.24
247.7	298.3	135.4	2.39	499.91	7.30	1.89E+06	4.70	0.26
261.7	307.9	155.1	2.46	499.89	8.01	2.09E+06	4.91	0.24
262.8	314.5	148.9	2.38	499.88	7.15	2.10E+06	4.37	0.24
255.3	305.7	0.0	4.07	499.90	6.50	2.00E+06	4.08	0.25
244.8	295.9	133.4	2.36	499.88	7.23	1.86E+06	4.70	0.27
256.4	303.9	146.3	2.46	499.93	7.76	2.01E+06	4.85	0.25
265.0	316.3	155.8	2.33	499.82	7.22	2.13E+06	4.38	0.23
252.6	304.2	138.6	2.38	499.90	7.17	1.96E+06	4.54	0.25
252.7	303.6	140.9	2.38	499.88	7.30	1.96E+06	4.61	0.25
250.9	295.4	145.9	2.47	499.85	8.21	1.94E+06	5.22	0.26
262.6	314.1	152.5	2.34	499.87	7.22	2.10E+06	4.42	0.24
270.1	321.8	160.2	2.33	499.85	7.18	2.21E+06	4.29	0.23
263.5	314.6	152.8	2.36	499.89	7.27	2.11E+06	4.43	0.24
263.8	312.5	153.0	2.42	499.89	7.54	2.12E+06	4.59	0.24

Table A3.
Nanoindentation results within the area A3

hc	h_{max}	hf	**m**	$\mathbf{P_{max}}$	**S**	**A**	**Er**	**H**
nm	nm	nm		μN		nm^2	GPa	GPa
218.1	277.4	113.7	2.05	499.89	6.22	1.52E+06	4.47	0.33
258.0	318.6	143.5	2.16	499.88	6.14	2.04E+06	3.81	0.25
270.7	324.9	157.1	2.31	499.90	6.87	2.21E+06	4.09	0.23
267.0	318.2	150.6	2.43	499.89	7.23	2.16E+06	4.36	0.23
265.5	329.6	144.3	2.15	499.89	5.79	2.14E+06	3.51	0.23
229.1	294.7	124.7	1.94	499.90	5.68	1.66E+06	3.91	0.30
286.7	341.4	172.2	2.30	499.86	6.78	2.45E+06	3.84	0.20
234.7	285.4	124.2	2.37	499.88	7.34	1.73E+06	4.95	0.29
248.5	309.8	137.8	2.09	499.90	6.06	1.91E+06	3.89	0.26
227.7	287.8	125.9	2.01	499.90	6.20	1.64E+06	4.29	0.31
233.4	293.7	124.1	2.10	499.90	6.15	1.71E+06	4.17	0.29
266.6	321.6	157.5	2.22	499.88	6.75	2.16E+06	4.07	0.23
287.3	337.8	173.6	2.42	499.93	7.33	2.46E+06	4.14	0.20
286.4	342.1	181.0	2.15	499.91	6.64	2.45E+06	3.76	0.20
195.0	256.8	98.9	1.90	499.86	6.00	1.26E+06	4.74	0.40
272.8	329.2	161.1	2.22	499.90	6.58	2.24E+06	3.89	0.22
268.6	320.0	156.7	2.37	499.90	7.22	2.18E+06	4.33	0.23
224.4	286.2	136.0	1.82	499.93	6.02	1.60E+06	4.22	0.31
253.3	314.2	140.7	2.12	499.88	6.08	1.97E+06	3.84	0.25
245.3	307.2	138.2	2.04	499.89	6.01	1.86E+06	3.90	0.27
269.2	326.1	159.7	2.19	499.86	6.57	2.19E+06	3.93	0.23
257.0	309.6	149.0	2.27	499.87	7.06	2.02E+06	4.40	0.25

Table A4.
Nanoindentation results within the area A4

hc	h_{max}	hf	**m**	$\mathbf{P_{max}}$	**S**	**A**	**Er**	**H**
nm	nm	nm		μN		nm^2	GPa	GPa
236.8	295.9	140.2	1.96	499.88	6.26	1.75E+06	4.19	0.29
226.8	279.4	122.8	2.22	499.89	7.04	1.63E+06	4.89	0.31
263.4	326.8	155.8	2.01	499.91	5.87	2.11E+06	3.58	0.24
1113.2	1250.2	767.1	2.24	499.89	2.16	3.16E+07	0.34	0.02
531.8	597.4	412.6	2.10	499.84	5.66	7.62E+06	1.82	0.07
1376.2	1675.8	626.5	2.52	499.85	1.18	4.78E+07	0.15	0.01
538.1	601.6	415.8	2.18	499.90	5.86	7.79E+06	1.86	0.06
1492.0	1833.0	736.0	2.33	499.86	1.04	5.61E+07	0.12	0.01
1478.6	1806.2	752.2	2.32	499.89	1.08	5.51E+07	0.13	0.01
1363.2	1677.8	717.4	2.22	499.84	1.14	4.69E+07	0.15	0.01
1212.2	1366.9	829.8	2.19	499.89	1.89	3.73E+07	0.27	0.01
1531.4	1905.1	780.9	2.18	499.88	0.95	5.90E+07	0.11	0.01
1447.4	1780.0	651.6	2.43	499.85	1.06	5.28E+07	0.13	0.01
1401.6	1728.6	691.4	2.30	499.87	1.09	4.96E+07	0.14	0.01
1330.9	1534.2	448.9	3.36	499.86	1.48	4.48E+07	0.20	0.01
1655.6	2043.2	899.7	2.14	499.88	0.92	6.88E+07	0.10	0.01
1520.5	1882.1	805.4	2.16	499.89	0.98	5.82E+07	0.11	0.01
1274.2	1600.3	652.0	2.12	499.87	1.10	4.11E+07	0.15	0.01
1794.1	2224.5	856.4	2.29	499.84	0.82	8.06E+07	0.08	0.01
1706.0	2102.1	898.5	2.19	499.88	0.89	7.30E+07	0.09	0.01
1801.9	2214.7	916.9	2.27	499.87	0.86	8.13E+07	0.08	0.01
1904.8	2299.5	983.2	2.41	499.85	0.90	9.07E+07	0.08	0.01
1537.3	1863.1	672.1	2.59	499.84	1.06	5.94E+07	0.12	0.01

Table A5.
Nanoindentation results within the area A5

hc	h_{max}	hf	**m**	$\mathbf{P_{max}}$	**S**	**A**	**Er**	**H**
nm	nm	nm		μN		nm^2	GPa	GPa
1574	1908	748	2.50	499.89	1.06	6.23E+07	0.12	0.01
1458	1791	658	2.44	499.88	1.06	5.36E+07	0.13	0.01
1446	1777	701	2.34	499.89	1.07	5.27E+07	0.13	0.01
1465	1796	723	2.33	499.84	1.06	5.40E+07	0.13	0.01
1529	1860	804	2.29	499.90	1.06	5.88E+07	0.12	0.01
1447	1774	676	2.41	499.83	1.08	5.28E+07	0.13	0.01
1719	2064	965	2.29	499.87	1.02	7.41E+07	0.10	0.01
1431	1762	721	2.27	499.86	1.07	5.16E+07	0.13	0.01
1414	1749	681	2.30	499.88	1.05	5.04E+07	0.13	0.01
1428	1767	695	2.28	499.83	1.04	5.14E+07	0.13	0.01
1430	1764	674	2.35	499.88	1.05	5.16E+07	0.13	0.01
1426	1762	726	2.24	499.84	1.07	5.13E+07	0.13	0.01
1374	1690	672	2.32	499.89	1.12	4.76E+07	0.14	0.01
1425	1758	703	2.28	499.89	1.06	5.12E+07	0.13	0.01
1416	1758	685	2.26	499.88	1.03	5.06E+07	0.13	0.01
1376	1714	667	2.23	499.90	1.05	4.78E+07	0.13	0.01
1511	1816	934	2.11	499.88	1.17	5.75E+07	0.14	0.01
1436	1767	650	2.41	499.89	1.06	5.20E+07	0.13	0.01
1431	1763	696	2.31	499.90	1.06	5.16E+07	0.13	0.01
1423	1764	683	2.28	499.85	1.04	5.11E+07	0.13	0.01
1415	1744	678	2.33	499.86	1.07	5.05E+07	0.13	0.01
1403	1729	680	2.32	499.86	1.09	4.97E+07	0.14	0.01
1379	1695	667	2.34	499.89	1.12	4.80E+07	0.14	0.01
1425	1761	718	2.24	499.87	1.05	5.12E+07	0.13	0.01
1438	1776	689	2.31	499.84	1.04	5.22E+07	0.13	0.01